

University of Pardubice
Faculty of Chemical Technology
Department of Physical Chemistry

Production of light olefins via (oxidative) dehydrogenation of light alkanes over
nontraditional heterogeneous catalysts

DOCTORAL THESIS

Author: M.Sc. Mehran Sajad

Supervisor: Prof. Ing. Roman Bulanek, Ph.D.

2023

I declare:

The thesis entitled “Production of light olefins via (oxidative) dehydrogenation of light alkanes over nontraditional heterogeneous catalysts” is my own work. All literary sources and information that I used in the thesis are referenced in the bibliography. I have been acquainted with the fact that my work is subject to the rights and obligations arising from Act No. 121/2000 Sb., On Copyright, on Rights Related to Copyright and on Amendments to Certain Acts (Copyright Act), as amended, especially with the fact that the University of Pardubice has the right to conclude a license agreement for the use of this thesis as a school work under Section 60, Subsection 1 of the Copyright Act, and that if this thesis is used by me or a license to use it is granted to another entity, the University of Pardubice is entitled to request a reasonable fee from me to cover the costs incurred for the creation of the work, depending on the circumstances up to their actual amount.

I acknowledge that in accordance with Section 47b of Act No. 111/1998 Sb., On Higher Education Institutions and on Amendments to Other Acts (Act on Higher Education Institutions), as amended, and the Directive of the University of Pardubice No. 7/2019 Rules for Submission, Publication and Layout of Theses, as amended, the thesis will be published through the Digital Library of the University of Pardubice.

In Pardubice, Czech Republic on

.....

Mehran Sajad by own hand

ACKNOWLEDGMENTS

I would like to thank the following people:

My supervisor, prof. Ing. Roman Bulánek, Ph.D., for the scientific and moral support during all the years of my Ph.D. study. I want to thank you for your positive and friendly attitude, for the knowledge and advices you have given. Thank you for the motivation to do high quality research.

The rector of the University of Pardubice, prof. Ing. Libor Čapek, Ph.D., for all your help, and supportive and friendly attitude during all years of my Ph.D. study.

My former colleague and great friend, Ing. Diego Valdés, Ph.D., for being a “dream team” during our work, all of your support, and the great time you have given.

My former colleague and great friend, Ing. Jiří Kotera, for all your help, support, and great time.

My great friend Ing. Zuzana Tuřálková, for all your help, positive energy, and great time you have given.

My great friend, M.Sc. Farshid Farzaneh, for all your help, support, and the great time you have given.

My great friend, M.Sc. Nadi Shojaee, for all your help, support, and great time you have given.

My great friend, M.Sc. Nooshin Jafari, for all your help, support, and great time you have given.

My friend, Raul Zazpe, Ph.D, for all your help, advices, positive energy, and great time you have given.

My colleague and friend Ing. Lada Dubnová, for all your help, support, positive energy, and great days.

My colleague and friend Ing. Vendula Meinhardová, for all your support, positive energy, and great days.

My colleague and friend Ing. Helena Drobná, Ph.D. for all your support, positive energy, and great days.

My former colleague and friend, Dr. Yosra Gherib, for all your help, support, and great days.

My friend, Caroline Novák-Jolly, for all your help, support, and great days.

My colleague and friend, Dr. Safaa Essid, for all your help, support, and great days.

My friend, Hanna Sopha, Ph.D., for all your help, support, and great time you have given.

My former colleague Ing. Jan Vaculík, Ph.D., for all your help.

My colleague Ing. Kateřina Knotková, Ph.D., for all your help.

All members and students of our department for their help and useful discussions.

The financial support by the Czech Science Foundation (project No. 22-23120S) is greatly acknowledged. The Center of Materials and Nanotechnologies of the University of Pardubice is greatly acknowledged for all their supports.

Last but not least, My family for their love and support during my PhD journey.

سپاسگزاری

تقدیر و تشکر بی کران خود را تقدیم میکنم به عزیزانی که در تمام مدت دوره دکتری حمایت بی دریغ ایشان برای من گرما بخش این مسیر طولانی و پر پیچ و خم بوده و از وجود پر مهر ایشان به خود میبالم.

به پاس عاطفه سرشار و گرمای امیدبخش وجودشان، و به پاس قلب های بزرگشان.

این پایان نامه و ماحصل آموخته هایم را تقدیم می کنم:

به مادرمهربان و فداکار و عزیز تر از جانم، که هرچه آموختم در مکتب عشق شما آموختم و هرچه بکوشم قطره ای از دریای بی کران مهربانیتان را سپاس نتوانم بگویم. امروز هستی ام به امید شماست و فردا کلید باغ بهشتم رضای شما. ره آوردی گران سنگ تر از این ارزان نداشتم تا به خاک پایتان نثار کنم، باشد که حاصل تلاشم، نسیم گونه، غبار خستگیاتان را بزداید. بوسه بر دستان پرمهرتان.

به پدرم که مهر آسمانی شان آرام بخش آلام زمینی ام است و استوارترین تکیه گاهم، دستان پرمهرش بود.

به خواهر عزیزم فخری سجاد که همواره با قلبی بزرگ و مهربانی بی انتها یار و یاور من بوده و ذره ای از زحمات گرانقدرش جبران پذیر نخواهد بود.

به برادر عزیزم مهرداد سجاد که همیشه بیش از یک برادر، دوست و رفیق، یار و یاور من بوده است.

به برادر عزیزم محمد سجاد که قلب مهربانش به بزرگی آسمان بی کران است.

به همسر و یار خواهرم رضا صادقی که حضور پر مهرش بی انتها و دلسوزی های برادرانه اش همیشه دل گرم کننده بوده است.

به خواهر زاده عزیزم آرزو صادقی که همچون قلبی دیگر در زندگی من میتپد و دنیاهای گره خورده ما جدا نشدنی است.

به خواهر زاده عزیزم علی صادقی که گویی رفیقی عزیز تر از جان شیرین و برادری همراه تا به انتهای همه مسیر هاست.

از همه شما عزیزان سپاسگزارم و تا ابد قدردان حضور و محبت بی دریغ شما هستم.

مهران سجاد

ABSTRACT

Light olefins are essential feedstock for industrial processes such as the production of polymers, oxygenates, etc. Currently, these olefins are produced mainly via steam cracking and fluid catalytic cracking of petroleum derivatives. However, the present methods are carried out under severe reaction conditions at high temperatures with significant amounts of CO₂ emission. Moreover, the side products of these processes are alkanes that typically burn, while they have great potential for being used in a more helpful way. On the other hand, the abundant discovery of natural and shale gas around the world has provided another source to meet the highly growing global demand for light olefins. Therefore, the (oxidative) dehydrogenation of light alkanes is growing important way to produce olefins more efficiently. Although direct dehydrogenation of light alkanes has found its way into the industry (but suffering from strong deactivation), oxidative dehydrogenation has not yet been industrially implemented because of the low selectivity problem of the available catalysts due to the overoxidation of the products.

Recently, the supported alkali chlorides and hexagonal boron nitride have shown high activity and selectivity in the oxidative dehydrogenation of light alkanes. Meanwhile, supported noble-metal nanoparticles are considered to be active for the direct dehydrogenation of light alkanes. However, a detailed investigation of the structure-activity-stability relationship for their use in the reaction is required. This thesis focuses on studying the catalytic behavior of these three promising catalyst groups for the (oxidative) dehydrogenation of light alkanes and understanding the phenomena that could influence their activity. In this work, critical parameters such as chemical composition, crystallinity, textural properties, reaction conditions, pretreatment/regeneration effect, stability, catalytic activity, and selectivity of the catalysts in olefin production via alkane (oxidative) dehydrogenation were investigated. A comprehensive characterization with fresh and spent catalysts was considered to explore the physicochemical changes that occurred during the reaction.

In the study of supported alkali chlorides, it was found that the high yield of olefin production by the reported catalytic systems, which is due to a molten layer of mixed salts formed at the reaction temperature, is constrained by deactivation. A comprehensive characterization provided insight into the deactivation mechanism and revealed that chlorine loss in some forms of chlorinated hydrocarbons causes the deactivation.

With respect to the supported noble metal nanoparticles, there are several different methods for encapsulating the metal nanoparticles. One of the recent approaches is the assembly disassembly organization reassembly technique, known as ADOR. In this research, the ADOR method was used to encapsulate Pd nanoparticles within IPC-2 and IPC-4 zeolites. It revealed that layered zeolites with thin

layers, such as UTL, are not suitable supports for the confinement of metallic nanoparticles because the zeolite framework cannot tolerate the severe conditions of the cyclic dehydrogenation reaction and regeneration. Nevertheless, metal nanoparticle confinement is an effective way to prevent sintering and improve the catalytic activity of the supported metal nanoparticles compared to conventional impregnation. Therefore, the confinement may result in better stability performance within zeolitic structures having thicker layers.

Lastly, a new promising nonmetallic catalyst, hexagonal boron nitride, was studied systematically in the oxidative dehydrogenation of propane to have a better understanding of the actual driver and the phenomena involved in this complicated system. This catalyst exhibited high activity and selectivity that was accompanied by the production of ethene as a valuable side product, along with low overoxidation of the products. Although the catalysts undergo substantial changes in chemical composition, textural properties, and crystallinity during the reaction, the activity and selectivity remain almost constant. Unlike previous studies that reported the oxygen content as the main factor, in this work it is shown that the reaction is driven mostly by gas-phase chemistry. Therefore, a longer residence time in a larger free space is essential for radical generation and propagation to improve productivity, while oxygen content does not play a key role. In fact, the change in oxygen content is the result of radical formation and not the cause. This catalyst is privileged because a coupled surface-mediated gas-phase mechanism is involved, resulting in higher activity and productivity compared with traditional metallic catalysts in the oxidative dehydrogenation of light alkanes suffering from overoxidation and low selectivity. It seems that one of the actual roles of hBN is to terminate the generated radicals or adsorption of water, which are formed in the gas phase, to form the products or maybe generate the in situ oxygenated species that eventually result in the formation of products. It is hypothesized that in this system, the initiation stage is in the gas phase and not on the surface of the catalyst.

KEYWORDS

Oxidative dehydrogenation, direct dehydrogenation, heterogeneous catalyst, light alkane, light olefin, characterization.

ABSTRAKT

Lehké olefiny jsou nezbytnou surovinou pro průmyslové procesy, jako je výroba polymerů, oxygenátů atd. V současné době se tyto olefiny vyrábějí především parním krakováním a fluidním katalytickým krakováním ropných derivátů. Předkládané způsoby se však provádějí za náročných reakčních podmínek při vysokých teplotách s významným množstvím emisí CO₂. Kromě toho jsou vedlejšími produkty těchto procesů alkanany, které se obvykle spalují, přičemž mají velký potenciál pro užitečnější využití. Na druhou stranu, hojně objevený přírodní a břidlicový plyn po celém světě poskytl další zdroj pro uspokojení vysoce rostoucí celosvětové poptávky po lehkých olefinech. Proto se (oxidativní) dehydrogenace lehkých alkanů stává stále důležitějším způsobem, jak efektivněji vyrábět olefiny. Ačkoli si přímá dehydrogenace lehkých alkanů našla cestu do průmyslu (ale trpí silnou deaktivací), oxidační dehydrogenace dosud nebyla průmyslově implementována kvůli problému s nízkou selektivitou dostupných katalyzátorů v důsledku nadměrné oxidace produktů.

V poslední době nosné alkalické chloridy a hexagonální nitrid boru vykazují vysokou aktivitu a selektivitu při oxidační dehydrogenaci lehkých alkanů. Pro přímou dehydrogenaci lehkých alkanů jsou považovány za aktivní nanosené nanočástice ušlechtilých kovů. Je však zapotřebí podrobného zkoumání vztahu struktura-aktivita-stabilita pro jejich použití v reakci. Tato práce se zaměřuje na studium katalytického chování těchto tří slibných katalytických skupin pro (oxidativní) dehydrogenaci lehkých alkanů a pochopení jevů, které by mohly ovlivnit jejich aktivitu. V této práci byly zkoumány kritické parametry jako chemické složení, krystalinita, texturní vlastnosti, reakční podmínky, efekt předúpravy/regenerace, stabilita, katalytická aktivita a selektivita katalyzátorů při výrobě olefinů prostřednictvím (oxidativní) dehydrogenace alkanů. Byly charakterizovány čerstvé, ale i použité katalyzátory, aby se prozkoumaly fyzikálně-chemické změny, ke kterým došlo během reakce.

Při studiu chloridů alkalických kovů na nosiči bylo zjištěno, že vysoký výtěžek produkce olefinů, který je způsoben roztavenou vrstvou směsných solí vytvořených při reakční teplotě, je omezen deaktivací. Komplexní charakterizace poskytla vhled do mechanismu deaktivace a odhalila, že ztráta chloru v některých formách chlorovaných uhlovodíků způsobuje deaktivaci katalyzátoru.

S ohledem na nanosené nanočástice ušlechtilého kovu existuje několik různých metod pro zapouzdření kovových nanočástic. Jedním z nedávných přístupů je technika opětovného sestavení organizace shromáždění a demontáže, známá jako ADOR. V tomto výzkumu byla použita metoda ADOR k zapouzdření nanočástic Pd v zeolitech IPC-2 a IPC-4. Ukázalo se, že vrstvené zeolity s tenkými vrstvami, jako je UTL, nejsou vhodnými podporami pro zadržení kovových nanočástic, protože zeolitová kostra nemůže tolerovat těžké podmínky cyklické dehydrogenační reakce a regenerace. Nicméně zadržování

kovových nanočástic je účinný způsob, jak zabránit slinování a zlepšit katalytickou aktivitu nanočástic na nosiči ve srovnání s konvenční impregnací. Proto může toto omezení vést k lepší stabilitě v zeolitických strukturách, které mají silnější vrstvy.

Nový slibný nekovový katalyzátor, hexagonální nitrid boru, byl systematicky studován při oxidační dehydrogenaci propanu, aby bylo možné lépe porozumět skutečnému mechanismu a jevům zahrnutým v tomto komplikovaném systému. Tento katalyzátor vykazoval vysokou aktivitu a selektivitu, která byla doprovázena produkcí ethenu jako cenného vedlejšího produktu, spolu s nízkou oxidací produktů směrem k oxidům uhlíku. Přestože katalyzátory během reakce procházejí podstatnými změnami v chemickém složení, texturních vlastnostech a krystalinitě, aktivita a selektivita zůstávají téměř konstantní. Na rozdíl od předchozích studií, které uváděly obsah kyslíku jako hlavní faktor, v této práci se ukazuje, že reakce je řízena převážně chemií v plynné fázi. Proto je delší doba setrvání ve větším volném prostoru nezbytná pro tvorbu a šíření radikálů pro zlepšení produktivity, zatímco obsah kyslíku nehraje klíčovou roli. Ve skutečnosti je změna obsahu kyslíku výsledkem tvorby radikálů a nikoli příčinou. Tento katalyzátor je výsadní, protože se účastní spřaženého povrchově zprostředkovaného mechanismu plynné fáze, což vede k vyšší aktivitě a produktivitě ve srovnání s tradičními kovovými katalyzátory při oxidační dehydrogenaci lehkých alkanů trpících nadměrnou oxidací a nízkou selektivitou. Zdá se, že jednou ze skutečných rolí h-BN je ukončit generované radikály nebo adsorpci vody, které se tvoří v plynné fázi, za vzniku produktů nebo možná generování in situ oksyločených látek, které nakonec vedou k tvorbě produktů. Předpokládá se, že v tomto systému je iniciační stupeň v plynné fázi a ne na povrchu katalyzátoru.

Klíčová slova

Oxidativní dehydrogenace, přímá dehydrogenace, heterogenní katalyzátor, lehký alkan, lehký olefin, charakterizace.

LIST OF PUBLICATION

Paper I:

Mehran Sajad, Oxidative dehydrogenation of propane over the boron-nitride catalysts, Scientific Papers of the University of Pardubice, Series A; Faculty of Chemical Technology, 26 (2020) 195–210.

Paper II:

Mehran Sajad, Roman Bulánek and Stanislav Šlang, Physico-Chemical Changes in the KCl-MgCl₂/La-FAU Composite Catalyst Induced by Oxidative Dehydrogenation of Ethane, Catalysts, 2021, 11 (3), 392. (IF: 3.9, Q2)

Paper III:

Yuyan Zhang, Ang Li, **Mehran Sajad**, Katarína Fulajtarová, Michal Mazur, Martin Kubů, Mariya Shamzhy, Milan Hronec, Roman Bulánek, Jiří Čejka, Imidazolium-type ionic liquid-assisted formation of the MFI zeolite loaded with metal nanoparticles for hydrogenation reactions, Chemical Engineering Journal, 412 (2021), 128599. (IF: 15.1, Q1)

Paper IV:

Mehran Sajad, Yuyan Zhang, Martin Kubů, Michal Mazur, Roman Bulánek, Jiří Čejka, Direct dehydrogenation of propane over Pd nanoparticles encapsulated within IPC zeolites with tunable pore sizes, Applied Materials Today, 29 (2022), 101644. (IF: 8.3, Q1)

Paper V:

Mehran Sajad, Roman Bulánek, Stanislav Šlang, Effect of the catalytic reactor arrangement and catalyst treatment in oxidative dehydrogenation of propane performance over hexagonal boron nitride, will be submitted in “Reaction Chemistry & Engineering”, (IF: 3.9, Q1)

LIST OF ABBREVIATIONS

Abbreviation	Meaning
ADOR	Assembly, disassembly, organization, reassembly
BET	Brunauer-Emmett-Teller
BNNT	Boron nitride nanotube
BN-OH	Hydroxylated boron nitride
COD	Crystallography open database
DDHP	Direct dehydrogenation of propane
DFT	Density functional theory
DH	Direct dehydrogenation
DRIFT	Diffuse reflectance infrared Fourier transform spectroscopy
EDS	Energy dispersive x-ray spectroscopy
FCC	Fluid catalytic cracking
FID	Flame ionization detector
FTIR	Fourier-transform infrared spectroscopy
hBN	Hexagonal boron nitride
ID	Internal diameter
ImILs	Imidazolium type ionic liquids
MS	Mass spectroscopy
NPs	Nanoparticles
ODH	Oxidative dehydrogenation
ODHE	Oxidative dehydrogenation of ethane
ODHP	Oxidative dehydrogenation of propane
RM	Reaction mixture
SC	Steam cracking
STEM	Scanning transmission electron microscopy
SVUV-PIMS	Synchrotron radiation vacuum ultraviolet photoionization mass spectroscopy
TCD	Thermal conductivity detector
TOF	Turnover frequency
TOS	Time on stream
XPS	X-ray photoelectron microscopy
XRD	X-ray diffraction

TABLE OF CONTENTS

INTRODUCTION	12
1. STATE OF ART	13
1.1. Direct dehydrogenation	13
1.1.1 Supported metal nanoparticles.....	13
1.2. Oxidative dehydrogenation.....	14
1.2.1 Alkali and alkaline earth chlorides catalysts	15
1.2.2 Boron nitride	16
2. AIMS AND SCOPE OF RESEARCH	19
3. EXPERIMENTAL.....	20
3.1. Materials	20
3.2. Experiments and characterization	20
3.2.1 Supported alkali and alkaline earth chlorides.....	20
3.2.2 Encapsulated Pd NPs within zeolite	21
3.2.3 hBN.....	21
3.2.4 Calculations	23
4. RESULTS AND DISCUSSION.....	25
4.1. Supported alkali and alkaline earth chlorides.....	25
4.2. Supported metal NPs	30
4.3. Boron nitride	39
CONCLUSION.....	63
REFERENCES	65
APPENDICES	70

INTRODUCTION

Light olefins are one of the most essential feedstocks for a variety of chemical industries around the world. Some examples are the synthesis of polymers (e.g., polyethylene and polypropylene), and oxygenates (e.g., ethylene glycol, acetaldehyde, acetone, and propylene oxide), which are involved in packaging, manufacturing, construction materials, etc., while the global demand for them is continually growing every year [1-3]. These olefins are traditionally produced by petroleum-derived steam cracking (SC) and fluid catalytic cracking (FCC), which are considered highly energy-intensive methods along with low selectivity and significant CO₂ emission. In such a harsh condition, generation of side products (alkanes) is unavoidable, and hence, preventing the wasting of valuable compounds is crucial. Moreover, current processes cannot meet the rapid global demand [1, 4]. Recently, the use of natural gas has become advantageous due to the depletion of fossil fuels and the abundant resources of shale gas explored around the world [5]. Therefore, the development of direct processes by means of catalysts is an interesting field for academic and industrial researchers, as catalysts are able to selectively produce the desired products, minimize the side reactions, avoid undesired environmentally harmful products, decrease the reaction temperature, and suppress the required energy consumption.

This thesis focuses on gaining deeper insight into catalytic systems for the selective production of light olefins such as ethene and propene from natural gas and their behavior. In this work, different types of catalytic systems were studied to gain a deeper understanding of the relationship between catalytic performance and its properties, and to find ways how to improve properties of these catalytic systems.

The parameters that have been considered are based on the type of the reaction (direct nonoxidative and oxidative dehydrogenation), the nature of the catalyst (metal and nonmetal catalysts), and the catalyst support. For this purpose, supported alkali chlorides, supported noble metals, and boron nitride have been studied. The behavior of each system including the catalytic activity, physicochemical changes before and after the reaction, and stability were investigated. Lastly, the advantages and disadvantages of individual systems were investigated, and different parameters that could have had an influence on the dehydrogenation reaction were studied.

1. STATE OF ART

1.1. Direct dehydrogenation

Direct dehydrogenation (DH) of light alkanes ($C_nH_{2n+2} \rightarrow C_nH_{2n} + H_2$) is an endothermic reaction that requires 113-134 kJ/mol to remove two hydrogen from the alkanes depending on the length of the chain. This reaction is equilibrium limited and takes place at relatively high temperatures; however, catalysts are able to decrease the temperature and provide adequate conversion and selectivity towards the desired products. The catalysts most commercially used in industry for the direct dehydrogenation of lower alkanes are based on platinum or chromium and usually necessitate high temperatures (550 to 750 °C). These metals exhibited satisfactory ability to activate the C-H bond while avoiding C-C bond breaking, but apart from required high temperature, sintering and coke formation are inevitable challenge that cause catalyst deactivation [3, 6].

1.1.1 Supported metal nanoparticles

Recently, the use of supported metal nanoparticles (NPs) has been growing due to a better accessibility of the active sites for the feed molecules because the NPs are distributed on a support with a large surface area and subsequently lead to a higher efficiency for the chemical interactions. Furthermore, besides the improved accessibility of metals in these systems, a lower amount of metals is required, which is another reason for the high interest shown by researchers, specifically in the case of noble metals [7]. Hence, using supported noble metal particles is worth trying in the dehydrogenation of light alkanes, as this reaction has been reported to be structure-sensitive (geometric and electronic effect). For instance, intrinsic activity and selectivity of Pt NPs (Pt/Al₂O₃) in propane DH is dependent on their size and vary not in a same way. Smaller Pt particle size result in higher turnover frequency (TOF), but high selectivity and stability are achieved when the particle size is either lower than 1 nm or higher than 3 nm [8]. Also stability is connected with particle size, Campbell et al. reported that thermal stability of different metal species dramatically increased with increasing the particle size from 1 to 6 nm [9, 10]. They also showed that stability of smaller particle (Ag, 2-3 nm) could be preserved by strong bonding to the support, for instance oxygen vacancies in metal oxide supports can provide such strong bonding [11]. Furthermore, the nature of the support and the metal-support interaction will influence the shape, stability and atomic structure of the metallic nanoparticles [12]. Sitja et al. have shown that there is transition point from nonmetallic to metallic properties for Pd and Au around 2 nm. The particles larger than 1.8 nm exhibited a gradual increase in CO adsorption energy with increase in particle size, whereas for the particles below 2 nm there is an irregular oscillation, as the geometric and electronic structure of metal clusters significantly depends on the atomicity [13-15]. When such a small molecule is adsorbed on metal species, there will be also a geometric

deformation which would be dependent on the particle size again. It was reported that a considerable relaxation of Pt-Pt occurs when H₂ or CO are adsorbed on Pt nanoparticles of 1 nm size due to orbital hybridization. But when the size is increased, this adsorbate induced lattice relaxation of Pt nanoparticles is much smaller because of lower number of surface unsaturated Pt atoms [16]. As a result of this interaction effect between metal nanoparticles and the adsorbate molecule, the metal species could go through a dynamic transformation. It has been found that in oxidative atmosphere, Pd nanoparticles transform to smaller particles while after reductive treatment, Pd nanoparticles agglomerate into larger particles [17]. Thus, consecutive treatment that can provides such dynamic structural transformation, assist for the regeneration of deactivated catalysts.

Considering all, the stabilization of NPs against sintering and agglomeration under the severe condition of the dehydrogenation reaction is critical [18], and confinement of the metal NPs within zeolites is helpful solution for stabilizing the supported NPs. The unique properties of zeolites (e.g., crystallinity, ion exchange capacity, tunable porosity, acidity, high surface area, etc.) have enabled metal NPs to be confined in some cavities, layers, pores, or even exact locations inside the zeolite framework. The confinement of NPs within zeolites has shown considerable influence on the activity and stability of NPs compared to their impregnated counterparts, depending on the particle size and electronic construction of the NPs and the zeolite type and their interaction [12, 18-21]. The encapsulation of metals could be done by various approaches, such as post modification strategy (impregnation, Ion-exchange followed by post-treatment, template-guidance approach), and in-situ encapsulation strategy (in-situ hydrothermal synthesis, interzeolite transformation), etc [18]. In general, there are many variables capable of influencing the catalytic behavior of supported metal systems, such as size and shape of the metal nanoparticles, the nature of the support, the interaction between support and the metal nanoparticles, the presence of other metals, etc.

1.2. Oxidative dehydrogenation

Unlike direct dehydrogenation, oxidative dehydrogenation (ODH) of light alkanes ($C_nH_{2n+2} + \frac{1}{2} O_2 \rightarrow C_nH_{2n} + H_2O$) is an exothermic and non-equilibrium limited reaction (-105 and -117 kJ/mol for ethane and propane, respectively) that requires an oxidizing agent and usually takes place at a lower reaction temperature (450-550 °C). However, after more than three decades of research on ODH, a suitable catalyst has not yet been reported to be interesting for industrial implementation. Transition metals, specifically vanadium, have attracted some attention during the last two decades, but the main problems were found to be poor selectivity, overoxidation to CO₂, and coke formation [2, 6, 22]. Nevertheless, interesting activity and selectivity have been reported for supported alkali and alkaline earth chlorides, as well as non-metallic catalysts, which are discussed in the following subsection.

1.2.1 Alkali and alkaline earth chlorides catalysts

Alkali and alkaline earth metal chlorides impregnated on various supports have been reported with encouraging activity and selectivity in the ODH of light alkanes. These modified catalysts exhibited higher activity and selectivity compared to chloride-free catalysts [22, 23]. The addition of mixed chlorides mainly affects the surface structure of the catalyst which means modification of the active centers. Usually, the reaction temperature is higher than the melting point of the eutectic composition of the salts; therefore, in these systems the molten salt layer plays a crucial role as the interface between the solid and gas phases, which is an advantage due to the possibility of working in a wide range of temperature, however these systems become more complicated because the interactions involved are in three phases. Furthermore, it was proposed that a gas-phase radical reaction occurred during the process due to the radical species generated by assistance of chlorine, but the inherent mechanism of chloride-modified catalysts is still the subject of debate [24-32]. Perez-Ramirez et al. showed the vital role of oxyhalogenation by generation of intermediates that could easily convert to valuable olefins. The high electron affinity of halogens for the hydrogen abstraction from hydrocarbons makes them suitable to be used in ODH. This affinity decreases in the order of $\text{Cl} > \text{F} > \text{Br} > \text{I}$ [24]. In another work they showed oxychlorination led to higher olefin productivity compared to the oxybromination over europium oxychloride and europium oxybromide catalysts respectively [33].

There are two main reported reasons for such a high productivity for supported alkali chlorides systems. First, the dynamically rearranging molten interface which create or modify the active centers [22, 25, 27, 34, 35], and second, the hypochlorite species (OCl^-) that have often been hypothesized as the active site on the surface of the overlayer in these systems and as the reason for their observed higher activity and selectivity in the ODH reaction [25, 27, 30, 31, 36]. Lercher et al. proposed a mechanism based on their studied system ($\text{LiCl/MgO/Dy}_2\text{O}_3$), that includes dissolving of oxygen in the molten salt, which results in generation of OCl^- as the active species, then oxygen radical and chlorine radical are formed via OCl^- decomposition, whereas both are able to activate the alkane by hydrogen abstraction. Finally, the alkane radicals react with OH to form alkene and water. The reaction productivity is limited by chlorine concentration and diffusion strains through the molten salt interface [29].

The molten layer as a dynamic interface plays a crucial role in selectivity by facilitating the desorption of olefins. It was shown that ethene is more stable via adsorption at the interface than dissolving in liquid chloride. Moreover, the carbon floats on the surface of molten layer and could be skimmed off easily rather than coke formation [27, 30, 31, 34, 35].

In one of the most promising reports, the study of supported binary alkali and alkaline earth chlorides exhibited 100% selectivity toward ethylene at 40% ethane conversion which seems to be a potential

candidate for future industry [23]. In this report a new catalyst system for activating ethane at very low temperatures was shown, but unfortunately, more detailed characterization of the materials or information on the stability of those systems were not included.

But according to the reports, the unstable behavior is a drawback and reasons depend on the nature of the salts and supports [26, 31, 35, 37-41]. Generally, different pathways of chlorine loss have been considered as the main cause of deactivation [26, 35, 37]. For instance, in metal oxide supports, the interaction between support and chlorine or water and chlorine results in formation of HCl over time and cause deactivation [31, 42]. Also chemical phase transformation during the reaction is one another reported origin [26]. As it is difficult to prevent HCl intermediate from scaping at high temperature, addition of chlorinated compound was suggested for the regeneration [36, 37, 41]. Also, presence of HCl gaseous feed during the reaction was tried on CeO₂-based catalyst and exhibited significant improvement in the activity and selectivity of this system in ODH of ethane [43].

Therefore, investigation of finding an efficient chlorine-promoted catalyst and studying of the deactivation mechanism could be a valuable research to find the way to industry in the future.

1.2.2 Boron nitride

One promising candidate for the nonmetallic group of catalysts in ODH is hexagonal boron nitride (hBN), an analogue of graphite, which is relatively new compared to the others in the field of dehydrogenation[2]. In the past, boron nitride had been considered chemically inert and used as a catalyst diluent due to its high thermal stability and high thermal conductivity, which limits the formation of hot spots, making it appropriate for industrial applications [44]. Firstly, in 2016, Hermans et al. [45] reported their observation about the activity and selectivity of hexagonal boron nitride and boron nitride nanotube (BNNT) for propane ODH which were higher than traditional transition metal catalysts (for e.g. V/SiO₂) and unlike traditional catalysts that produce CO_x as an unavoidable side product, the main side product in this system was ethene which is obviously much more valuable. At the beginning, it was hypothesized that the armchair edges contain B-O-O-N are the active site [45]. Edge-hydroxylated boron nitride (BN-OH) was reported afterward to have a higher activity than any other catalyst at that time, and it was also stable. Density functional theory (DFT) calculations showed that the formation of B-O-B bridges after the dehydration of adjacent B-OH is the key point and is reversible by gaseous water [46]. This idea was clearly in disagreement with the first hypothesis. Since then, there has been a high interest in studying this system and investigating the active site and mechanism. Soon, the first hypothesis about the armchair edges with B-O-O-N structure was invalidated because the catalysts without nitrogen also showed similar activity, and it was concluded that boron is the key element [47]. In that research, a range of metal borides were tested, including NiB, HfB₂, B₄C, TiB₂, WB, hBN, and elemental boron. These primary results and reports led to the conclusion that

boron is oxidized to boron oxide (BO_x) and acts as an essential active site, and the catalytic activity depends on the concentration of boron at the surface [48]. Shi et al. reported a comparison between traditional catalysts and promising boron catalyst for dehydrogenation [49]. Selectivity toward CO_2 , oxygen and alkane reaction order, side products, active sites, and reaction mechanisms were the key points. The negligible selectivity of CO_2 and the long-lasting stable productivity of the boron catalyst make it highly promising for industrial implementation. The presence of oxygen and its role were also discussed, and since it showed a reaction order of 0.5, it suggests the importance of dissociative adsorption of oxygen. Furthermore, unlike metal oxides that function without oxygen, hBN does not exhibit any activity in the absence of oxygen, which means that the active sites are formed under the reaction condition. In another work, it was also shown that the alkane partial pressure has a reaction order of 1 for metal oxides with the Mars-Van Krevelen mechanism, which is not the same as BN with a reaction order of 2 and without lattice oxygen [46], therefore, it is obvious that there are different mechanisms in the boron catalyst compared to the traditional supported metal oxide catalysts. As mentioned above, a valuable side product by using hBN is ethene, meaning that the methyl group formed by the C-C bond cleavage takes different reaction pathways. They can generate C_2H_4 by oxidative coupling that results in better selectivity of C_2 products [50]. Although in situ boron oxide species formation has been hypothesized to be crucial, in the meantime, gas-phase reactions are intensely involved. [51, 52] However, the nature of active sites and the exact mechanisms still need to be unveiled. The first experimental evidence of the gas-phase reaction was the detection of methyl radicals by using synchrotron radiation vacuum ultraviolet photoionization mass spectroscopy (SVUV-PIMS) [52]. The presence of the gas phase radical agrees with the kinetic data on C_2 as the main side product and shows that the methyl radicals contribute to the formation of the C_1 and C_2 products. Surprisingly, no propyl radicals were detected, suggesting that propene is generated via a surface-controlled pathway. Nevertheless, Venegas et al. [53] claimed that if propene formation were surface controlled, the catalytic behavior and selectivity would not be different from vanadium-based catalysts; therefore, they hypothesized that propyl radicals react with HOO^\bullet radicals in the gas phase. This is in direct disagreement with the first report using SVUV-PIMS without detection of propyl radicals. Later, a study of reactor parameters revealed that the change in catalyst mass, reactor diameter, and catalyst dilution resulted in the importance of the gas phase reaction as the main driver and the catalyst surface as the initiator [54]. Recent theoretical studies suggest two approaches regarding how to explain the high activity and selectivity of hBN; first, by detached nano-sized boron oxide clusters that diffuse with the gas flow, and subsequently, the tricoordinated boron site dehydrogenates the alkane. B-O-B sites are claimed to be more reactive than B-OH groups in eliminating alkoxy radicals in the ODH of light alkanes, and the edge boron sites (B-OH) can activate atmospheric dioxygen [55]. The second is about in situ generation of surface boron peroxy species at the B-O-B sites that acts as a mild oxidant and prefer secondary hydrogen over the primary hydrogen, and thus

increases the selectivity by preventing over oxidation [56]. Lastly, a comprehensive study using the operando spectroscopy technique in combination with theoretical calculations detected the presence of short-lived intermediates such as radicals and oxygenates, and concluded that boron peroxy-like species on the surface are responsible for propane activation while radicals are derived from BO dangling sites; after desorption of radicals and oxygenates, gas-phase H-abstraction chemistry will be initiated [57].

Based on this chapter, boron nitride and in general, boron-based catalysts, are highly promising in the field of dehydrogenation but understanding the nature of actual active species and the mechanisms involved during the ODH reaction is still a challenge for researchers and future industrial applications.

2. AIMS AND SCOPE OF RESEARCH

All in all, in the targeted research field of this dissertation thesis (conversion of light alkanes to alkenes), there are still many ambiguous points that are potentially helpful to take the catalysts out of the lab and finally put them into the industry. Therefore, we have tried here to shed light on some of those points. These are included the following questions:

- Is the high activity and selectivity of the supported alkali chlorides stable? And if not, what is the cause?
- How does the encapsulation of noble metal NPs affect their catalytic activity and stability in the dehydrogenation of light alkanes?
- What is the mystery of hBN exceptional productivity in oxidative dehydrogenation of light alkanes?

To address these questions and meet the objectives of the thesis, the following actions were taken:

- Synthesis of some of the most active and selective supported alkali chlorides catalyst, measurement of catalytic activity in ODH of light alkanes. Comprehensive characterization of the fresh and spent catalysts, and identification of the side products and clarifications of the possible deactivation.
- Confinement of noble-metal NPs within various zeolites in collaboration with colleagues at the Faculty of Sciences, Charles University, Prague. Investigation of the catalytic activity and selectivity in dehydrogenation of light alkanes. Cyclic catalytic tests for studying the stability and regeneration capability of the catalysts. Comprehensive characterization of the fresh and spent catalysts, and investigation of the catalyst behavior.
- Studying hBN behavior in oxidative dehydrogenation of light alkanes, including wide range of catalytic test conditions and comprehensive characterization of all the fresh and spent catalysts. Investigation of physicochemical changes on hBN under different reaction atmospheres, time on stream, different pretreatments, total flowrates, temperatures, reactor geometry, catalyst mass, etc., to discover the influence of effective parameters on the catalytic activity. Understanding the role of catalyst based on the obtained results from designed experiments and theoretical studies.

3. EXPERIMENTAL

3.1. Materials

The list of used chemicals in this work are listed in Table 1.

Table 1. List of chemicals

Name	Formula	specification	Supplier
Ammonium Faujasite	NH ₄ -FAU	Si/Al = 2.55	Zeolyst
boric acid	H ₃ BO ₃	99.5 % purity	Sigma-Aldrich
Ethane	C ₂ H ₆	99.5% purity	Linde
Helium	He	99.996% purity	AIRPRODUCTS
Hexagonal boron nitride	hBN	98% purity, 1 um particle size	Sigma-Aldrich
Lanthanum (III) chloride heptahydrate	LaCl ₃ .7H ₂ O	99.999 % purity	Sigma-Aldrich
Magnesium dichloride	MgCl ₂	99.9 % purity	Sigma-Aldrich
Nitrogen	N ₂	99.999 purity	AIRPRODUCTS
Oxygen	O ₂	100% purity	AIRPRODUCTS
Potassium chloride	KCl	99.5 % purity	Sigma-Aldrich
Propane	C ₃ H ₈	99.5% purity	Linde

3.2. Experiments and characterization

3.2.1 Supported alkali and alkaline earth chlorides

To investigate the stability of highly active and selective supported alkali chloride, it was necessary to prepare the catalyst support by solid-state ion exchange of NH₄-FAU zeolite with LaCl₃.7H₂O. The precursors were mechanically mixed and then heated in an atmosphere control furnace at 500 °C for 12 hours under N₂ flow. After that, extensive mixing of KCl and MgCl₂ with La-FAU produced the prepared catalyst. The mechanical mixture was converted to fresh catalyst just before the catalytic test during pretreatment in the flow of helium at 500 °C. The catalytic behavior of the prepared catalyst was then investigated in oxidative dehydrogenation of ethane in a plug-flow fixed-bed tubular-shaped reactor, using desired mass of catalyst with a grain size of 0.35 to 0.50 mm at 500 °C and under atmospheric pressure. The products were analyzed with an online gas chromatograph with a flame ionization detector (FID) and a thermal conductivity detector (TCD). The pretreatment, reaction mixture, total flow rate, blank experiment, and measurement condition details are declared in **Paper II**. As a deactivation trend was observed for this system, the next step was the characterization of the physical mixture, fresh and spent catalysts to study the physicochemical changes before and after the reaction. The analysis of the chemical composition was done by energy-dispersive X-ray spectroscopy (EDS) combined with SEM. In addition, X-ray diffraction (XRD) of spent catalyst was used for monitoring the changes in crystallinity and population of crystal phases. The

products of the ODHP reaction were analyzed by operando mass spectrometry in order to monitor side products of reaction. Furthermore, N₂ physisorption isotherms were used to see changes in textural properties of the physical mixture, fresh and spent catalysts.

3.2.2 Encapsulated Pd NPs within zeolite

The Pd NPs were encapsulated within MFI, IPC-2 and IPC-4 zeolites at the Charles University Center of Advanced Materials via two different approaches; first, using alkoxysilane functional imidazolium-type ionic liquids (ImILs) as assistant agents to protect metal precursors in Pd encapsulated within MFI (**paper III**). And in the second approach, well-dispersed Pd nanoparticles were encapsulated within IPC-2 and IPC-4 zeolites using the Assembly, Disassembly, Organization, and Reassembly (ADOR) process based on the 3D-2D-3D transformation of UTL zeolite (**paper IV**). To investigate the catalytic activity of the encapsulated Pd NPs, the catalysts were measured in direct dehydrogenation of propane in a plug flow fixed-bed tubular shape reactor, using the desired catalyst mass with a grain size of 0.35 to 0.50 mm at 600 °C and under atmospheric pressure. The products were analyzed with an online gas chromatograph with a flame ionization detector (FID) and a thermal conductivity detector (TCD). The pretreatment, reaction mixture, total flow rate, blank experiment, and measurements condition details are declared in **Papers III** and **IV**. A comparison was made between the catalysts by using the rate of propene formation per one gram of Pd in one second, which exhibited different activity of the catalysts, thus it was necessary to test if the catalysts are stable and, if not, how their behavior changes after regeneration, therefore, a cyclic test was designed to repeat the catalytic measurements four times, and after each measurement a regeneration step was done via treating the catalyst under an oxidative atmosphere at reaction temperature. Also, the intrinsic activity of the supported Pd NPs as turnover frequency was studied by considering the average particle size of Pd and assuming that only Pd atoms on the surface of the particles were involved in the reaction. The next step was to understand whether there is any connection between different catalytic results and the size of Pd NPs; therefore, scanning transmission electron microscopy (STEM) was used to show the Pd NP size and distribution before and after the reaction. The other characterization methods that helped to investigate what could possibly occur during the reaction were study of crystallinity by XRD patterns, textural properties by nitrogen physisorption isotherms, and availability of active sites through CO adsorption via collecting diffuse reflectance infrared Fourier transform (DRIFT) spectra through in situ measurements on a spectrometer equipped with a DRIFT cell.

3.2.3 hBN

The catalytic activity and stability of hBN in oxidative dehydrogenation of propane were measured in a plug-flow fixed-bed tubular shape reactor, using desired mass of the catalyst with the grain size of 0.35 to 0.50 mm at 490 °C under atmospheric pressure. Details of the pretreatment, the composition of the reaction

mixture, and measurement condition details are declared in **Paper I**. To investigate the physicochemical changes that occur during the reaction over hBN, the catalyst was treated under various conditions at the reaction temperature (490 °C), including treatment under different atmospheres for two hours (He, He/O₂, He/C₃H₈, He/O₂/C₃H₈, with the flow rates for He: 11, O₂: 3 and C₃H₈: 6 ml min⁻¹), different time on the stream (TOS) in the ODHP atmosphere (He/O₂/C₃H₈) from 15 minutes to 10 hours. The fresh and treated catalysts were characterized by XRD, nitrogen physisorption isotherms, Raman and infrared spectroscopy, and EDS to clarify the changes in crystallinity, textural properties, skeletal vibration, and chemical composition. To understand the role of boron oxide species in this catalytic system, the hBN catalyst was impregnated with boric acid for 5 wt.% via conventional impregnation. Boric acid was dissolved in water by stirring, and then hBN was added to the solution and continued stirring at 75 °C until the solvent was evaporated. Then the powder obtained was dried at 110 °C over night and labeled as impregnated. Later, to measure the catalytic activity of the washed sample, the impregnated hBN was stirred for one hour in methanol, filtered and dried at 110 °C overnight and labeled as washed. Moreover, it was needed to compare the activity of the boron nitride with low specific surface area with another synthesized boron nitride with significantly larger specific surface area. Therefore, the high surface area sample was synthesized by colleagues in “Iran University of Science and Technology” by using guanidine carbonate and boric acid as precursors. After dissolving the precursors in water, the solvent was evaporated at 80 °C over night, and then the white powder was treated at 1000 °C under N₂ atmosphere.

On the other hand, to study the effect of gas phase reaction, a set of reactors with different total volume based on different inner diameter (id: 9, 10, 12.3, 14.5, 15.5 mm) were prepared and the catalytic activity of a similar mass of hBN was measured in all of them in the same condition. To investigate whether the gas-solid interface plays any role, a reactor with the same diameter as the largest reactor (id: 15.5 mm) with a lower height was prepared to provide the same void volume as the smallest reactor (id: 9 mm). Later, different mass of catalyst (50, 100, 150 mg), different total flow rate (15 to 35 ml min⁻¹) and effect of catalyst dilution (with SiC or quartz sand) were also examined to understand what is the main driver of the reaction.

To have a better knowledge of how coupled surface mediated and gas phase reactions are cooperatively involved, the generated products under the reaction condition were monitored in situ via a mass spectrometer. Also, the effect of oxygen presence was investigated by a pulse experiment dosing oxygen and monitoring the change in the detected propane through the mass spectrometer.

3.2.4 Calculations

For evaluating the catalyst activity, it is important to distinguish the overall performance of the catalyst and the intrinsic activity of the active sites. The overall performance includes the alkane conversion, selectivity to products, and products yield.

The alkane conversion was calculated using Equation 1.

$$X_a = \frac{n_i - n_t}{n_i} \times 100 \quad (\text{Equation 1})$$

Where X_a is the conversion of corresponding alkane (%), while n_i is the molar flow of corresponding alkane in inlet gas mixture (mol min^{-1}), and n_t is the molar flow of the alkane at the measured time-on-stream in outlet gas mixture (mol min^{-1}).

The selectivity toward products was calculated based on Equation 2.

$$S_x = \frac{n_x}{n_p} \times 100 \quad (\text{Equation 2})$$

Where S_x is the selectivity of product x (%), n_x is the number of alkane moles converted to product x (nmol), and n_p is the number of alkane moles converted to all products (nmol).

The yield was calculated using Equation 3.

$$Y_x = \frac{X_a \times S_x}{100} \quad (\text{Equation 3})$$

Where Y_x is the yield of product x (%), X_a is the conversion of corresponding alkane (%) base on Equation 1, and S_x is selectivity toward product x (%) according to the Equation 2.

Intrinsic activity of the active phase of catalysts was then expressed as the rate of propene formation over metal NPs mass unity using Equation 4 and turnover frequency that was calculated using Equation 5.

$$R_{alkene} = \frac{F_a \cdot X_a \cdot S_x}{m_{Pd}} \quad (\text{Equation 4})$$

Where R_{alkene} is the rate of alkene formation ($\text{mmol}_{alkene} \text{ s}^{-1} \text{ g}_{pd}^{-1}$), while F_a is the molar flow of corresponding alkane (mmol s^{-1}), X_a is the conversion of alkane (%), S_x is the selectivity towards alkene x (%) and m_{Pd} is the mass of Pd NPs (g).

$$TOF = \frac{F_a \cdot X_a}{n_{Pd}} \quad (\text{Equation 5})$$

Where TOF is turnover frequency (s^{-1}), F_a is molar flow of the corresponding alkane (mol s^{-1}), X_a is the conversion of alkane (%), n_{Pd} is the surface Pd content (mol). The content of Pd surface atoms was obtained based on the Pd face-centered cubic lattice with $a = 0.38907$, where 2 Pd atoms are in the cube wall. Therefore, the surface density (D_s) is:

$$D_s = \frac{2}{0.38907^2} \approx 13.2 \text{ atoms per nm}^2 \quad (\text{Equation 6})$$

And the number of atoms on the surface of the nanoparticle ($n_{Pd/S}$) is:

$$n_{Pd/S} = S_{Pd} \times D_s \quad (\text{Equation 7})$$

Where S_{Pd} is the surface of the Pd NPs calculated from the average particle size obtained by STEM, and D_s is the surface density from equation 7.

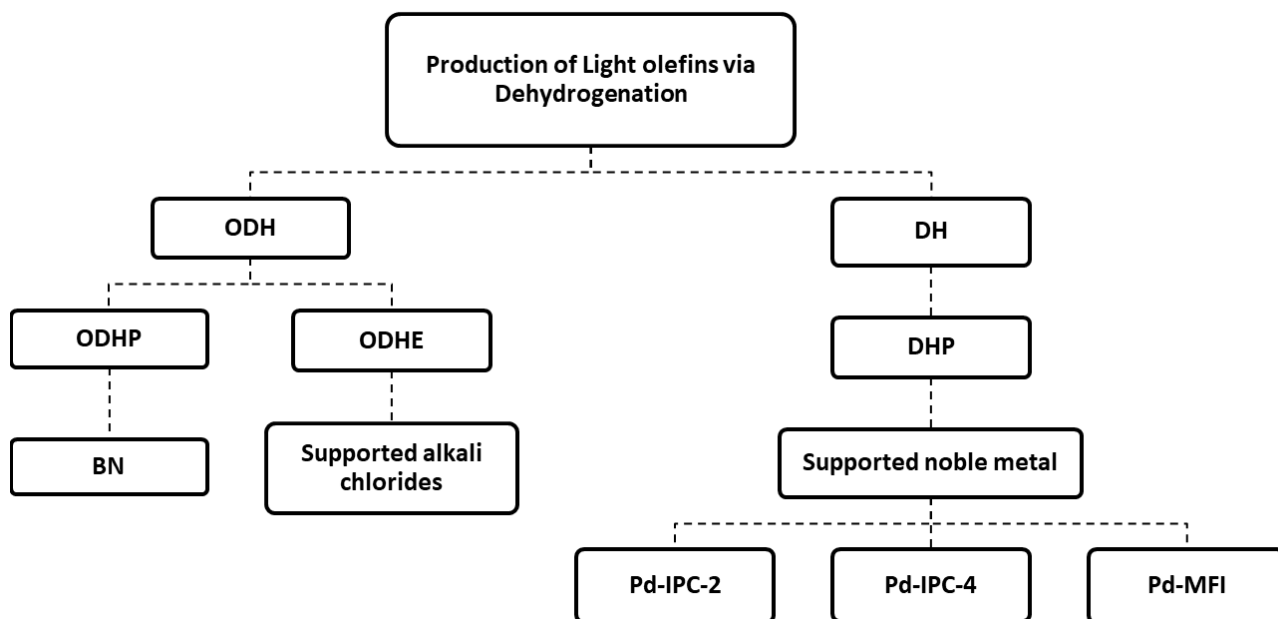
Thus, the amount (mol) of Pd on the surface of the particle (n_{Pd}) is calculated by:

$$n_{Pd} = \frac{n_{Pd/S}}{N_A} \quad (\text{Equation 8})$$

Where $n_{Pd/S}$ is number of Pd surface atoms from equation 7, and N_A is Avogadro number.

4. RESULTS AND DISCUSSION

This chapter is divided into three parts, based on the aims and the questions defined in the chapter 4 of this thesis. Each part discusses and summarizes the published data related to a specific catalyst and its behavior. The studied reactions are oxidative dehydrogenation of ethane (ODHE) by supported alkali chlorides, direct dehydrogenation of propane (DDHP) by supported metal NPs, and oxidative dehydrogenation of propane by boron nitride. Scheme 1 shows how these data are related to the topic of this dissertation thesis.



Scheme 1. The diagram on the relation between studied catalytic systems and the thesis topic.

4.1. Supported alkali and alkaline earth chlorides

In the first part of our research, a range of binary and ternary alkali and alkaline earth chlorides were prepared including $\text{KCl-MgCl}_2/\text{La-FAU}$, $\text{NaCl-MgCl}_2/\text{La-FAU}$, $\text{CsCl-MgCl}_2/\text{La-FAU}$, $\text{RbCl-MgCl}_2/\text{La-FAU}$, $\text{KCl-NaCl-MgCl}_2/\text{La-FAU}$ and tested in the oxidative dehydrogenation of ethane. The catalytic activity of the FAU zeolite and La-FAU supports was measured too, that exhibited very low yield of ethene productivity. Among all the prepared catalysts, the $\text{KCl-MgCl}_2/\text{La-FAU}$ exhibited the highest efficiency (57% yield) in ODH of ethane, therefore it was considered as the representative of this group and has been discussed in this section while more details could be found in **Paper II**. Also, a comparison between this system and similar reports in the literature has been shown in Table 2. In all cases, the addition of chlorides resulted in higher activity and selectivity, compared to the pristine support. However, the studied system in

this work is rather incomparable due to exhibiting high performance at low temperature that is critical for industrial applications. It is noteworthy that for the reports on higher yield of propene formation higher reaction temperature was applied in range of 550-750 °C.

The observed catalytic activity of KCl-MgCl₂/La-FAU was extraordinary, 80% conversion of ethane with 72% selectivity to ethene at 500 °C (Figure 1). Furthermore, a negligible amount of CO₂ and CH₄ was detected without any traces of CO (**Paper II**). This exceptionally low temperature activity was stable for a short time, then the ethane conversion decreased significantly and this is the fact that had not been described previously in the literature. Meanwhile the selectivity towards ethene increased slowly, but there were some side products that could not be identified by gas chromatography, as the column was designed to determine C₁-C₃ alkanes and alkenes, CO_x and O₂ (**Paper II**). Hence, it seemed that the identification of these products could help to find the reasons for the observed deactivation in this system, and it is discussed in the following section.

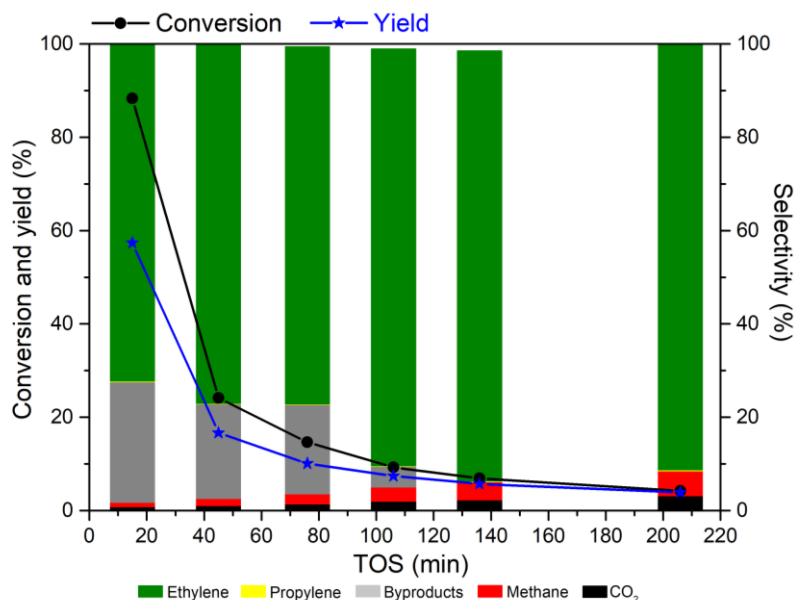


Figure 1. Catalytic activity and stability of KCl-MgCl₂/La-FAU in ODH of ethane as a function of time on stream.

Table 2. A comparison between similar reported study to this work.

Catalyst	Conversion (%)	selectivity (%)	Temperature (°C)	Yield (%)	TOS (min.)	Ref.
KCl-MgCl ₂ /La-FAU	80	72	500	57	15	This work
NaY-La(Cl)-(NaMg)	2	100	500	2	-	[23]
NaY-La(Cl)-(KMg)	27	100	500	27	-	[23]
NaY-La(Cl)-(RbMg)	40	100	500	40	-	[23]
NaY-La(Cl)-(CsMg)	7	100	500	7	-	[23]
NaY-Binary(NaMg)	3	100	500	3	-	[23]
NaY-La(Cl)-(NaKMg)	20	100	500	20	-	[23]
LiCl/SiO ₂	99	79	600	78	5	[26]
NaCl/SiO ₂	88	69	550	61	5	[26]
KCl/SiO ₂	70	75	550	52	5	[26]
LiCl/SZ (sulfated zirconia)	98	70	650	68	1	[38]
LiCl/AZ (amorphous zirconia)	87	60	650	52	1	[58]
LiCl/ZrON	95	71	650	68	1	[58]
LiCl/ZrOCl	28	97	650	27	1	[58]
LiCl/ZrSO ₄	89	83	650	74	1	[58]
LiCl/ SZ (sulfated zirconia)	53	90	650	48	1	[59]
BaCl ₂ -TiO ₂ -SnO ₂	66	93	720	60	30	[39]
Li/Dy/Mg/O/Cl	-	-	650	77	-	[29]
(Li-K)Cl-(Dy ₂ O ₃ /MgO) membrane	34	97	700	33	-	[27]
(Li-K)Cl-(Dy ₂ O ₃ /MgO) membrane	85	75	750	64	-	[27]
KCl-MgCl ₂ /La-FAU	22	77	500	17	45	This work
PbBi ₃ O ₄ Cl ₃	51	88	660	45	60	[37]
KCl-MgCl ₂ /La-FAU	8	89	500	7	106	This work
Li/K/Cl-MgO/Dy ₂ O ₃	5	94	550	5	120	[35]
Li/Na/Cl-MgO/Dy ₂ O ₃	2	75	500	2	120	[35]
Li/Cl-MgO/Dy ₂ O ₃	2	60	500	1	120	[35]
K/Cl-MgO/Dy ₂ O ₃	2	40	500	1	120	[35]
Na/Cl-MgO/Dy ₂ O ₃	2	37	500	1	120	[35]
KCl-MgCl ₂ /La-FAU	4	91	500	4	206	This work
SrBi ₃ O ₄ Cl ₃	20	89	660	17	360	[37]
SrBi ₃ O ₄ Cl ₃ + SrCl ₂	35	89	660	31	360	[37]
SrBi ₃ O ₄ Cl ₃ + 2SrCl ₂	44	90	660	39	360	[37]
SrBi ₃ O ₄ Cl ₃ + KCl	36	96	660	34	360	[37]
SrBi ₃ O ₄ Cl ₃ + SrCl ₂ + KCl	45	92	660	42	360	[37]
SrBi ₃ O ₄ Cl ₃ + SrCl ₂ + LiCl	42	94	660	40	360	[37]
SrBi ₃ O ₄ Cl ₃ + SrCl ₂ + NaCl	41	95	660	39	360	[37]
LiCl/ SZ (sulfated zirconia)	70	66	650	46	900	[38]

The mass spectroscopy (MS) was found to be helpful technique for identifying unknown side products and resulted in finding chlorinated hydrocarbons include chloromethane, ethyl chloride, and chloroethene at the beginning of the reaction (Figure 2). Traces of HCl were also observed that probably act as an unstable intermediate. As time passed and the ethane conversion decreased, the nature of the side products changed (dashed area in Figure 3 and **Paper II**). The new side products consisted of some higher hydrocarbons (C₅) or oxygenates. These include allyl vinyl ether; 1,3-dimethylallene; trans-2-methyl-2-butenal; 2-methyl-2-butenal; 4-pentyne-2-ol; 3-butyric acid; 2-buten-4-olide; 1-ethyl-2-methylacetylene; and 3-methyl-2-butenal.

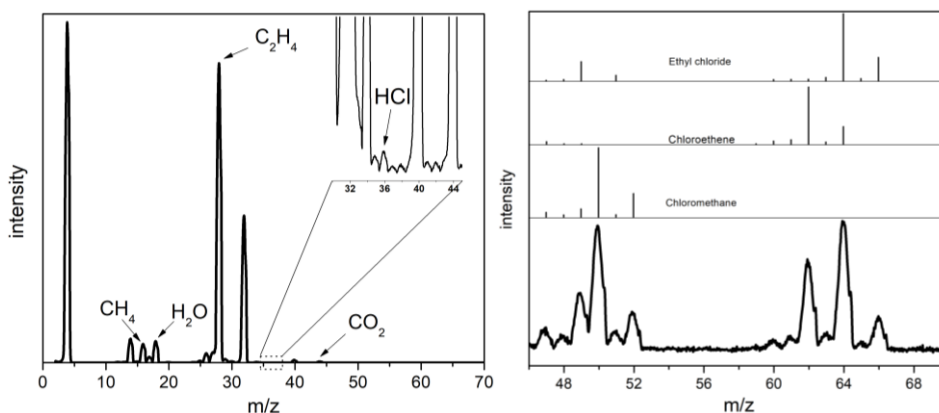


Figure 2. Mass spectrum of the products of the ethane ODH over KCl-MgCl₂/La-FAU (left), and details of low-intensity signals at m/z 46–70 compared to the model spectra of the three most probable chlorinated compounds formed during the reaction.

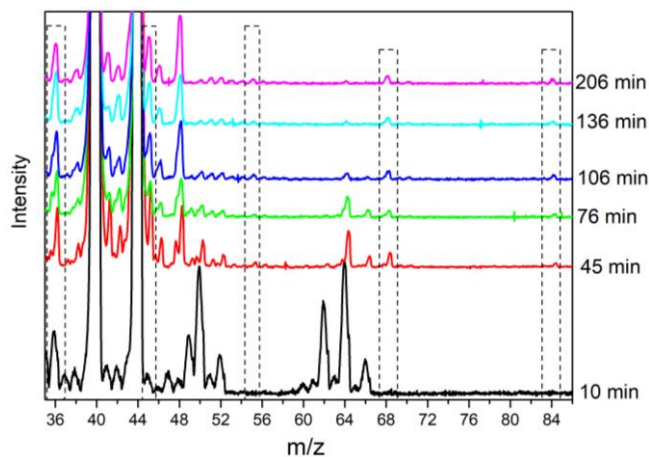


Figure 3. Mass spectra of the side products of ethane ODH over KCl-MgCl₂/La-FAU during the reaction time. The changes in side products over time are indicated by dashed area.

The changes in the chemical composition of the catalyst were tracked by EDS. It was disclosed that the content of alkali and alkaline earth metals remained almost constant for the time under the reaction stream. Meanwhile, the chlorine content had been continuously reduced and finally leveled off by 75% loss of

chlorine which agrees with the observation by mass spectroscopy and formation of chlorinated side products. The 25% remaining were probably inaccessible from the surface to escape or bounded to more stable compounds (**Paper II** and Table 3).

Table 3. Chemical composition of KCl-MgCl₂/La-FAU catalyst measured by EDS based on the atomic percentage of elements.

Element	Spent catalysts, different TOS (min.)					
	Fresh	15	45	76	136	223
O	52.7	57.8	57.6	56.3	57.6	60.0
Na	0.7	0.9	0.9	0.7	0.7	0.7
Mg	9.4	11.6	10.4	13.1	13.2	9.7
Al	3.9	4.4	4.5	4.2	4.0	4.3
Si	9.1	11.1	11.4	10.8	10.4	11.8
Cl	11.5	11.1	7.6	7.1	6.6	6.3
K	5.8	5.5	5.2	5.4	5.1	5.4
La	1.7	2.6	2.5	2.4	2.5	1.9

The XRD patterns revealed that after the treatment at temperature higher than the eutectic point, a solid solution of chlorides was formed because of the dissolution of chlorides in each other (Figure 4). The presence of FAU, LaOCl, and KCl was evidenced before and after the heat treatment, which showed their stability. It is noteworthy that the presence of La in LaOCl means that not all of the lanthanum was in the cationic sites of zeolite. Furthermore, not any form of MgCl₂ was detected after the formation of the molten layer that discloses its lability. After the reaction alongside LaOCl and KCl, more crystalline phases were presented, for instance, SiO₂ and MgO. In the case of MgO, it shows that after chlorine loss during the reaction, its crystallinity changed to a different phase by taking advantage of oxygen as a substitution. More details about changes in crystalline phases, and also the textural properties are discussed in **Paper II**.

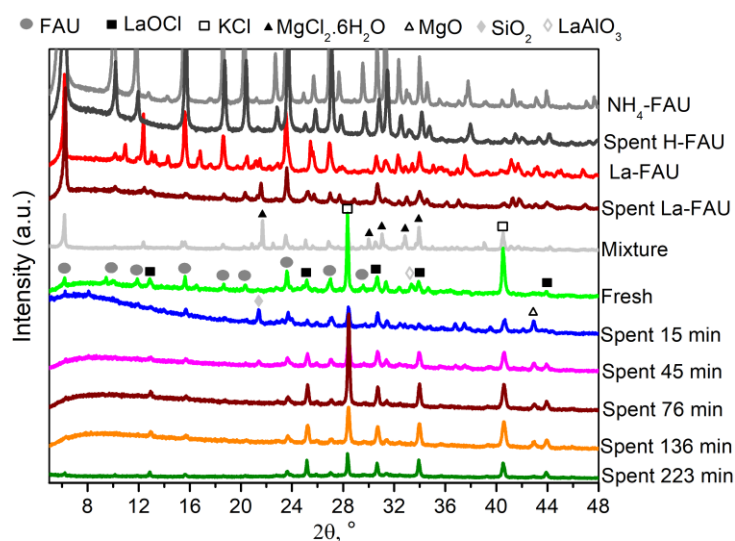


Figure 4. The X-ray diffraction patterns of the support, physical mixture and the catalyst before and after the reaction.

According to this chapter, it could be concluded that the supported alkali and alkaline earth chlorides are highly active and selective in ODH of ethane at fairly low temperature, but not stable enough for long term use to be applicable in the near future. These systems need modification to prevent chlorine loss which cause the deactivation by formation of side products such as chlorinated hydrocarbons, higher hydrocarbons and oxygenates. One option to solve this problem is to dose chlorine gas into the reaction mixture, as in the case of the LiCl/MgO catalyst for oxychlorination, but this would promote the formation of chlorinated hydrocarbons and a corrosive environment

4.2. Supported metal NPs

The confinement of metal nanoparticles within zeolite matrices has garnered significant attention because of its potential applications in catalysis, adsorption, etc. Zeolites, possessing a well-defined porous structure and high thermal stability, offer an ideal environment for the encapsulation and stabilization of metal nanoparticles. This confinement effect can lead to enhanced catalytic properties, such as improved selectivity, increased activity, and a prolonged catalyst lifetime. The interactions between the metal nanoparticles and the zeolite framework play a crucial role in determining the size, distribution, and accessibility of the encapsulated nanoparticles. Understanding the confinement effects at the atomic and molecular levels is of paramount importance for designing novel catalysts with tailored properties. This dissertation aims to investigate the influence of metal nanoparticles confinement within zeolites on catalytic activity, by utilizing advanced characterization techniques to unravel the intricate interplay between the metal nanoparticles and the zeolite framework, and ultimately providing insights for the development of highly efficient catalytic systems. To meet this goal, structures such as MFI, IPC-2 and IPC-4 zeolites were chosen to be tested for Pd NP confinement. For each support, a different method of encapsulation was utilized and an impregnated sample was synthesized by the conventional impregnation method to compare the results.

The Pd NPs were encapsulated within MFI zeolite via a new method by using alkoxy silane functional imidazolium-type ionic liquids (ImILs) as assistant agents to protect the metal precursor against precipitation during the hydrothermal synthesis of the MFI zeolite. The final encapsulated catalyst is labeled as Pd@MFI in this thesis (Pd@MFI_ImILs in **paper III**), and the impregnated catalyst was labeled as Pd/MFI in this thesis (Pd@MFI_Imp in **paper III**).

In the case of IPC-2 and IPC-4 zeolites, the Assembly, Disassembly, Organization, and Reassembly (ADOR) process was used based on the 3D-2D-3D transformation. IPC-2 and IPC-4 zeolites were prepared from an IPC-1P precursor derived from hydrolysis of UTL zeolite using the ADOR approach to encapsulate Pd NPs inside the zeolitic layers (**Paper IV**).

Then the catalytic activity of Pd NPs encapsulated within MFI, IPC-2, and IPC-4 zeolites in direct dehydrogenation of propane was studied and compared to their impregnated counterparts. Interestingly, all encapsulated catalysts exhibited higher rate of propene formation compared to impregnated catalysts (Figure 5). There are several factors involved in the higher activity of the encapsulated catalysts, such as the uniformity of the distribution of Pd NPs within the zeolitic support in the encapsulated catalysts. Also, the size of Pd NPs plays a crucial role, as the smaller NPs provide a higher specific surface area, but in the impregnated samples, the metal NPs form larger sizes, which are not uniformly spread. The STEM images of the encapsulated catalysts exhibited a homogeneous distribution of Pd NPs with a narrow size distribution that shows the successful confinement of the metal NPs within the zeolite. Furthermore, the impregnated samples showed an uneven distribution of Pd NPs with significantly larger particle sizes, which were placed mainly on the external surface of the zeolite crystals (**Paper III, IV**, and Figure 7 and Figure 8). Another effective parameter is the different intrinsic capacity of metal NPs with different arrangements. The electronic structure made by the connection between Pd atoms and the support is potentially one of the most important sources of higher capability of the encapsulated catalysts to catalyze the dehydrogenation reaction in these systems (**Paper III, IV**). The Pd@IPC-2 and Pd@IPC-4 showed higher activity than Pd@MFI, which could be connected to the zeolite structure, and also the aluminosilicate nature of MFI compared to the siliceous nature of IPC zeolites. These parameters will be discussed later in this chapter. It should be mentioned that the activity of Pd@MFI catalyst in DH reaction has not published yet.

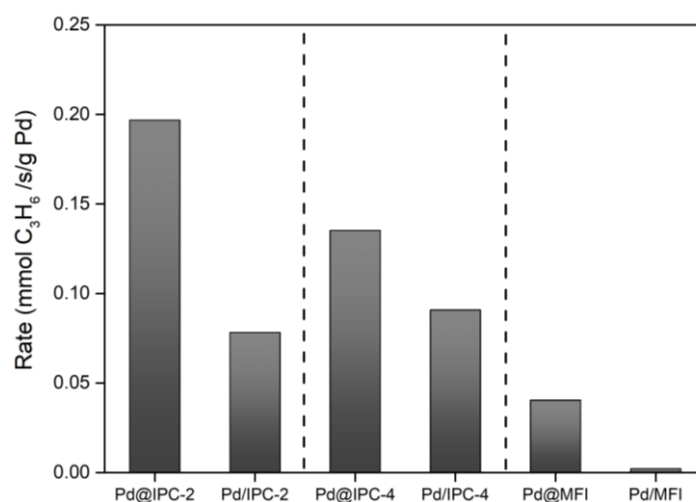


Figure 5. Rate of propene formation for encapsulated (Pd@IPC-2, Pd@IPC-4, Pd@MFI) and impregnated (Pd/IPC-2, Pd/IPC-4, Pd/MFI) catalysts in DH of propane, at 600 °C and TOS: 5 min.

The EDS measurements showed no change in the Pd content before and after the reaction for all the encapsulated and impregnated catalysts; therefore, the metal NPs were not leached out of the catalyst. However, it is known that the metal NPs tend to agglomerate and create larger particles, but in the

encapsulated catalysts, these particles are limited by the space inside the zeolite pores and channels, therefore their size is restricted even after the reaction, whereas the metal NP size of the impregnated catalysts increased significantly under the harsh condition of the reaction (**paper III, IV** and Figure 6). This presents another advantage of NP confinement, which prevents sintering and agglomeration of metal NPs and subsequently deactivation of the catalyst.

Regarding the higher rate of propene formation by Pd@IPC-2 compared to the other encapsulated catalysts (Figure 5), despite the fact that the intrinsic activity of Pd NPs in Pd@IPC-2 and Pd@IPC-4 for propane conversion are comparable (Figure 9) but the propene selectivity was higher for the Pd@IPC-2 catalyst (Figure 10) which resulted in higher rate of propene formation. The structure of the IPC-2 zeolite could explain a better chance for the mass transfer that lead to the higher productivity of Pd@IPC-2. This zeolite has larger pore system (12-ring: 5.6 x 7 Å and 10-ring: 6.1 x 4.7 Å) compared to the other studied zeolites in this study, that is IPC-4 (10-ring: 5.6 x 3.4 Å and 8-ring: 4.7 x 3.5 Å), and MFI (10-ring: 5.5 x 5.1 Å and 10-ring: 5.6 x 5.3 Å) [60]. Therefore, the produced gaseous molecules can escape outside the channels and pores more easily, and it might prevent generation of unwanted products via side reactions such as cracking. Moreover, for the least active encapsulated catalyst (Pd@MFI), there are acidic sites on MFI zeolite as an aluminosilicate structure that favor the side reactions and thus cracking was enhanced and subsequently selectivity to the desired product decreased significantly. It is noteworthy that in Pd encapsulated and impregnated within IPC-2 and IPC-4 supports, the metal NP sizes are similar, nevertheless the activity of metal particles in impregnated samples is significantly lower than the encapsulated ones, which means the activity of Pd NPs was improved in the confined space. In the case of Pd within MFI zeolite, the NP size in the impregnated catalyst is remarkably larger than the encapsulated sample, and due to the much lower specific surface area of the larger particles, there is an important impact on the drop in the activity. Therefore, it could be said that the intrinsic activity of Pd NPs is influenced by several parameters including the NP size, the interaction of the support with the NPs, and the diffusion limitation.

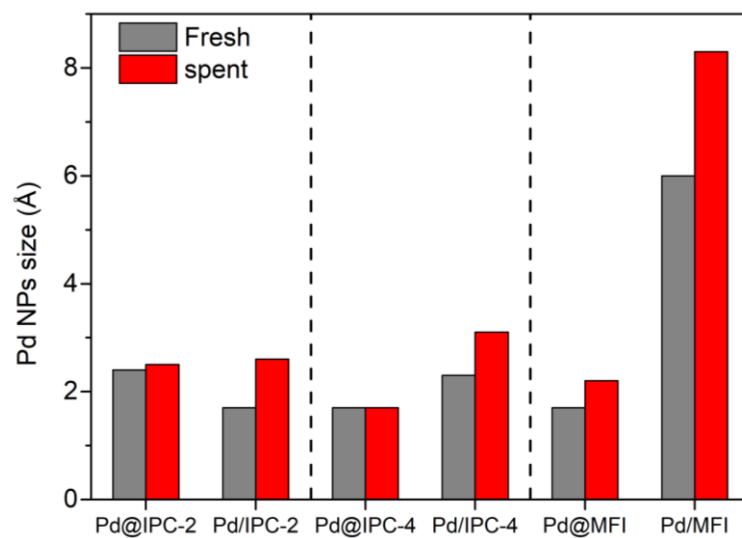


Figure 6. Pd NP size of encapsulated and impregnated catalysts before and after the reaction of propane dehydrogenation.

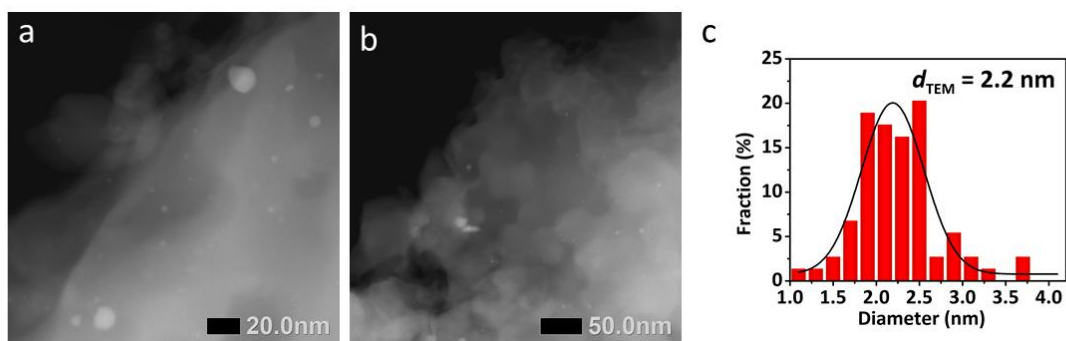


Figure 7. STEM images (a,b), and corresponding particle size histogram (c) of spent Pd@MFI.

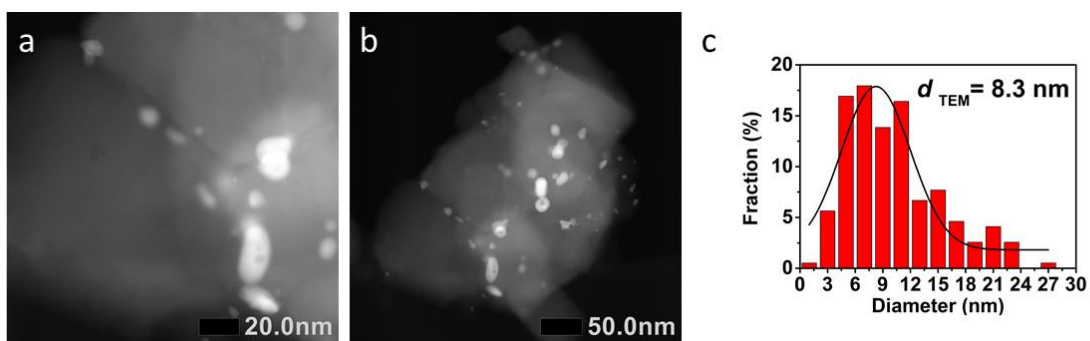


Figure 8. STEM images (a,b), and corresponding particle size histogram (c) of spent Pd/MFI.

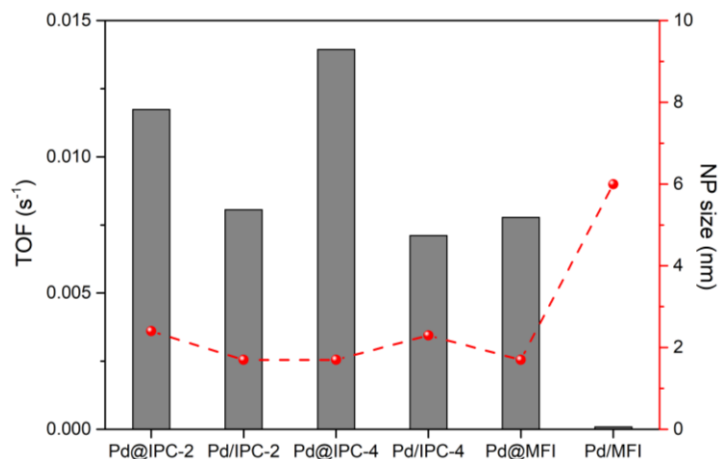


Figure 9. Turnover frequency of propane conversion on the surface atoms of the Pd NPs in encapsulated and impregnated catalysts with a comparison between Pd NP size in each catalyst, for TOS: 5 min

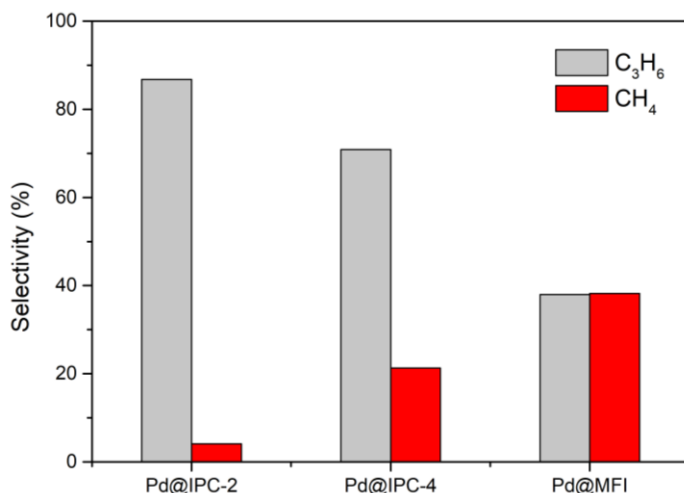


Figure 10. Selectivity toward propene and methane via different encapsulated catalysts, TOS: 5 min.

As expected, the catalysts exhibited a fast deactivation as it is typical for DH catalysts most likely as a result of the formation of carbon deposits at the active sites or in the pores. It could also be related to strongly adsorbed propene on the surface of the Pd NPs. Hence, cyclic catalytic tests become important for investigating the regeneration ability of these systems for long-term use. In the case of MFI zeolite, the encapsulated and impregnated catalysts are compared in Figure 11 and showed that both systems reach a plateau after 4 cycles, but in a way that the productivity and stability of the encapsulated samples are higher than those of the impregnated counterpart. In the encapsulated catalyst, the propane conversion exhibited a similar trend to the propene formation rate, shown in Figure 12. One of the possibilities is that the conversion decreased by enlarging the size of Pd NP during the cyclic tests and therefore blockage of the pores. Also, the dealumination of MFI zeolite during the reaction and regeneration steps could influence the activity by

decreasing the propane conversion. Since the acid sites are strong enough to favor the cracking reaction, dealumination and subsequent removal of the acid sites, resulted in an increase in selectivity towards propene and decrease in methane selectivity (Figure 12). On the other hand, for the impregnated catalyst, propane conversion increased during cycles while propene selectivity decreased (Figure 12). In the case of impregnated catalysts, probably the change in electronic structures of the metal particles on the outer surface of the zeolite assisted by the availability of the acid sites inside the empty pores led to an enhancement in propane conversion and methane selectivity. Nevertheless, eventually the activity (propane conversion and rate of propene formation) was limited maybe due to the dealumination that reduced the number of acid sites and also Pd NPs found an equilibrium size over time. Furthermore, it was observed that, in fact, the cracking, which is a side reaction, was improved, not the propene selectivity (Figure 12). Therefore, in the end, the rate of propene formation for the impregnated catalyst was leveled off under the value for the encapsulated catalyst (Figure 11). Note that the selectivity of propene and methane cannot be compensated by each other, and as the selectivity to ethene was not in line with methane, thus it means when cracking was favored and selectivity towards methane increased, some other carbon side product (which could not be detected by the used GC column) by means of different mechanisms were generated.

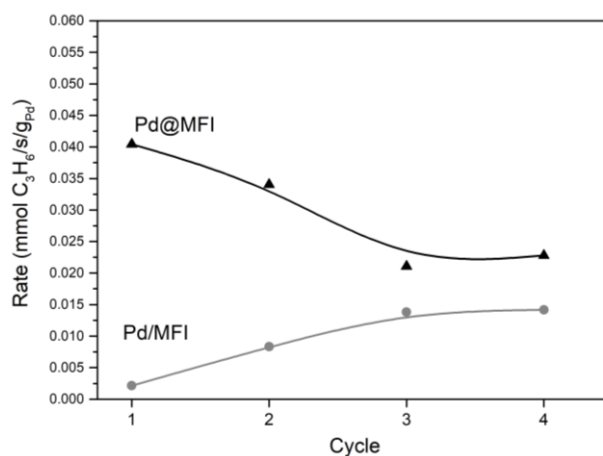


Figure 11. Rate of propene formation for the dehydrogenation catalytic cyclic test of encapsulated (Pd@MFI) and impregnated (Pd/MFI) at TOS: 5 min.

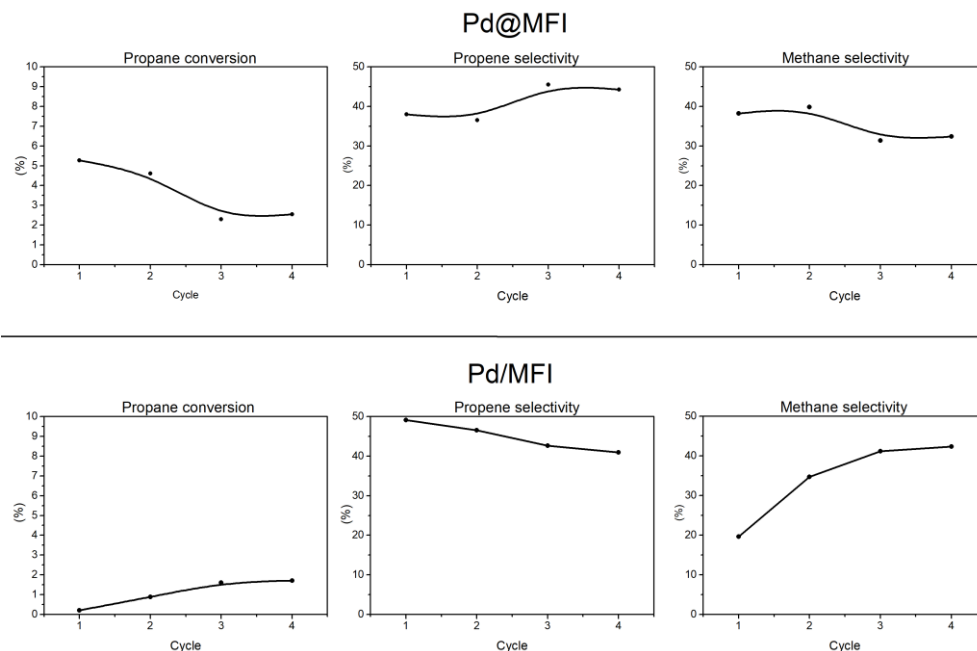


Figure 12. Propane conversion, propene and methane selectivity over the cyclic catalytic test for Pd@MFI and Pd/MFI, TOS: 5 min

Regarding the IPC-2 and IPC-4 zeolites, different behavior was observed. Similarly, the encapsulated catalysts exhibited higher activity in the first cycle, but then dropped sharply after the regeneration, while the impregnated samples exhibited lower activity, but almost without a big change (Figure 13). The XRD patterns revealed that although the transformation from UTL zeolite to IPC-1P and then IPC-2 and IPC-4 took place without any problems and the structure has been preserved after the introduction of the metal NPs (**Paper IV**), the structure of the encapsulated catalysts collapsed under the harsh reaction and regeneration conditions, and at the same time under the stress associated with the presence of Pd NPs between the individual lamellae, as the main peaks at 7.6° and 9.7° 2θ disappeared in the XRD patterns of the spent Pd@IPC-2 and Pd@IPC-4 catalysts, respectively (Figure 14). Thus, structural collapse was the reason for the decreased activity of the encapsulated catalysts after the first cycle of dehydrogenation. Note that Pd in impregnated samples did not cause stress and tensions and the zeolite structure was much more stable. Also, for the MFI catalysts, both encapsulated and impregnated samples exhibited stable structure after the reaction and regeneration step (Figure 15). The higher stability of MFI is caused by the thicker layer of this zeolite compared to the other two, as one unit cell layer is thicker than layer in UTL-derived zeolites, and in addition, MFI sample consists of “layers” containing more than one unit cell, thus the structure is more rigid. Furthermore, there was no peak showing the presence of crystalline Pd in any of the studied catalysts in this work.

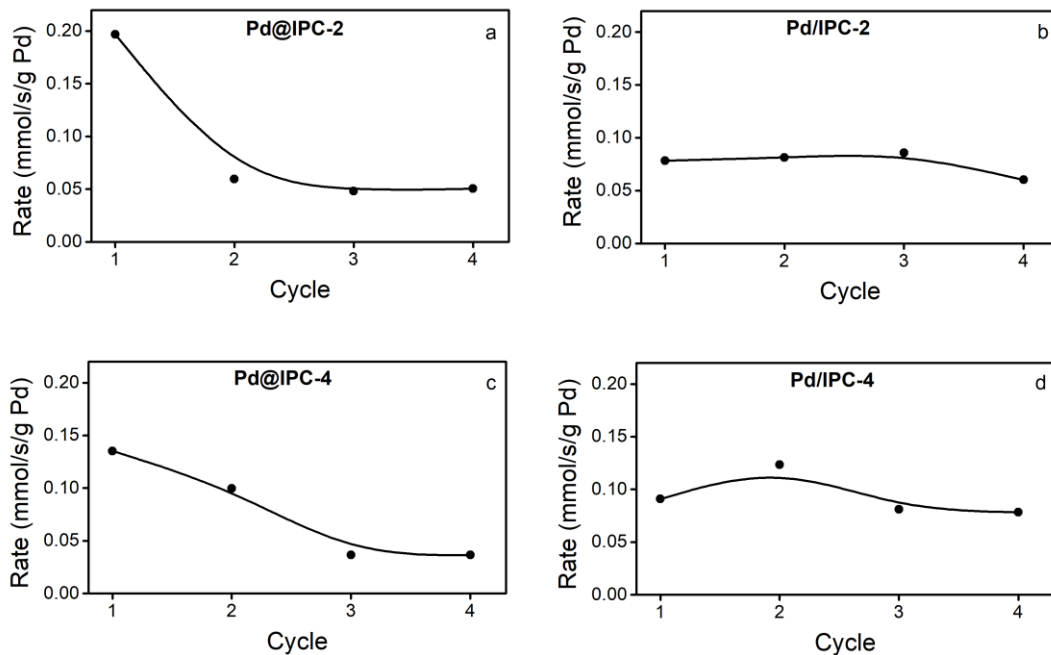


Figure 13. Initial activity of the Pd@IPC-2 (a), Pd/IPC-2 (b), Pd@IPC-4 (c) and Pd/IPC-4 catalysts expressed as the rate of propene production for four cycles.

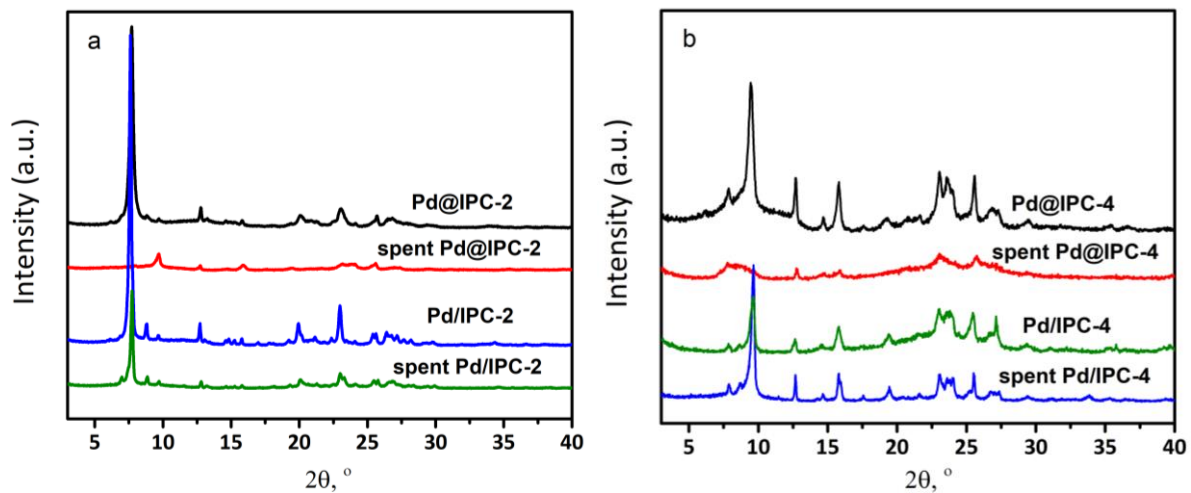


Figure 14. XRD patterns of fresh and spent encapsulated and impregnated Pd-IPC-2 (a), and Pd-IPC-4 (b)

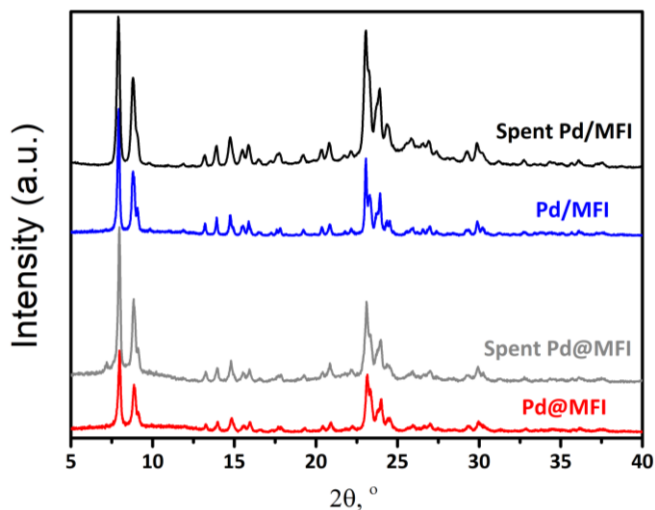


Figure 15. XRD patterns of fresh and spent encapsulated and impregnated supported Pd NPs within MFI zeolite.

The textural properties of the studied catalysts were evaluated using N_2 adsorption-desorption isotherms (**Paper III and IV**), demonstrating type I for microporous materials according to the IUPAC classification [61] and confirmed the reduction of the BET (Brunauer-Emmett-Teller) surface area and micropore volume of the catalysts compared to the parent zeolite. These smaller values are due to the partially occupied pore by the metal NPs. After the reaction, the BET surface area and micropore volume of the spent catalyst (without regeneration) was measured and showed even lower values, but this time as a result of carbon deposit formation during the dehydrogenation reaction which could be the reason for the fast deactivation of the catalyst under the reaction stream (**Papers III and IV** and Figure 16).

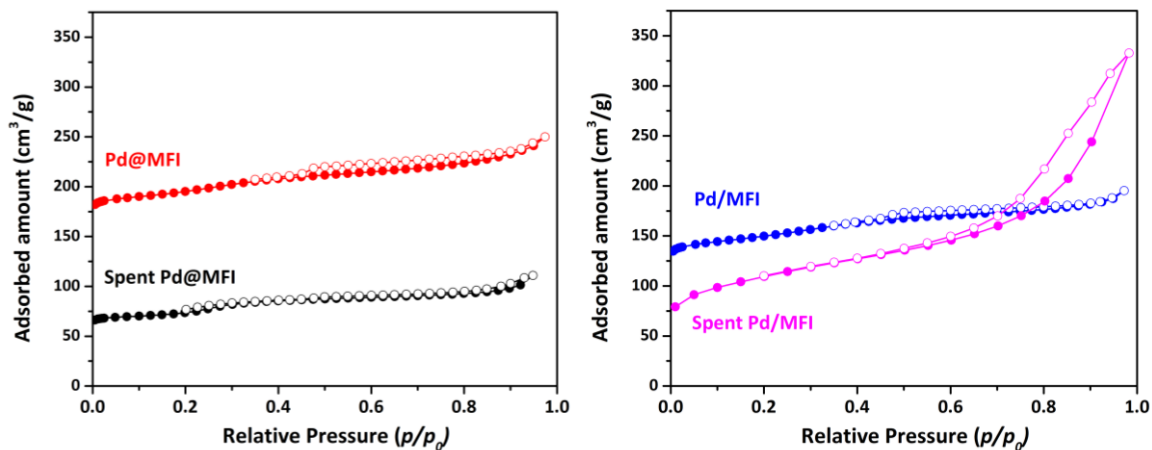


Figure 16. N_2 physisorption isotherms of the fresh and spent encapsulated (left) and impregnated (right) supported Pd within MFI.

As Pd@IPC-2 and Pd@ IPC-4 exhibited higher productivity for the dehydrogenation reaction, more research was performed to study their behavior. For example, different amounts of carbon deposit were

detected by the TG-DSC shown in **Paper IV**. It was discussed that the confinement of the Pd NPs resulted in a lower content of carbon deposit. Also, the diffuse-reflectance FTIR (DRIFT) technique was used to monitor the availability of the active sites by the CO probe molecule. It was observed that there are two absorption bands of carbonyl formed on metallic Pd, linear and bridged carbonyl. The integral intensities of the linear and bridged carbonyls revealed that in the impregnated catalysts the intensity of the linear carbonyls decreased after the reaction, whereas it increased for the bridged carbonyls during the reaction, because Pd NPs tend to form larger particles from unprotected Pd atoms after the reaction on impregnated catalysts, in line with the STEM results of the NPs size evaluation. In the case of the encapsulated catalysts, the intensity of both linear and bridged carbonyls decreased as the active sites are less accessible because the zeolite framework collapsed, as evidenced by changes in XRD and textural properties of spent materials (decrease in the volume of micropores accompanied by increase in external surface area, see **paper IV** Fig. 9) and therefore the probe molecule as well as the reaction feed could not reach the metal NPs.

Based on this section, it could be concluded that in the catalytic activity of Pd NPs encapsulated within MFI, IPC-2 and IPC-4 zeolites in the direct dehydrogenation of propane, there are a couple of effective factors that influence catalyst activity, including the size of the nanoparticles and zeolite channels, electronic structure of the metal NPs, and structure of the support framework. Overall, the encapsulated Pd NPs show a higher propane conversion and propene formation rate compared with their impregnated counterparts, probably because of the smaller size or intrinsic properties of confined Pd NPs. The confinement of Pd NPs within a zeolite framework prevents undesired sintering, whereas their size increases in the impregnated catalysts during the reaction. Furthermore, even though the Pd NPs encapsulated within the IPC-2 and IPC-4 catalysts show a decrease in coke deposition inside the pores, their structures collapsed, meaning that the Pd active sites were inaccessible after the reaction and consequently caused deactivation during cyclic catalytic tests.

4.3. Boron nitride

In this part of the thesis, commercial hexagonal boron nitride was studied as a catalyst for oxidative dehydrogenation of propane due to its high activity and selectivity while preventing overoxidation [45, 48]. The goal was to better understand catalytic behavior of this system as it was reported a high promising catalyst with many unclear aspects. Thus, the catalyst activity was measured under various conditions such as different atmospheres, time on stream, temperatures, catalyst masses, reactor diameters, etc. The fresh and spent catalysts were characterized with a wide range of methods to investigate the physicochemical changes occurring on the catalyst during the reaction, and also to find out the actual role of the catalyst in this system. Our findings were confronted with the views on the reaction mechanism and the role of the hBN catalyst published in the literature. Although it has been firstly hypothesized in the literature that the

boron oxide acts as the active site, and also gas-phase reactions are involved [51, 52], but the knowledge about how active sites function and the mechanisms need to be unveiled. Grant et al. first suggested that $>B-O-O-N<$ was the active site [45] which was invalidated by observation of the oxidized boron structure generated on boron containing materials with similar ODHP activity [47]. Both theoretical and experimental studies on the catalytic activity of hBN catalytic systems identified the oxygenated boron species as active sites [46, 62]. The generation of the oxygenated boron species in this catalytic system is studied and discussed in **Paper I**. It was shown that the oxyfunctionalization of hBN is not limited only to the surface of the catalyst but also a deep penetration into the volume of the particles was observed. Su et al. found that the hBN materials could not be oxidized below 800 °C under an O₂ atmosphere, indicating that with molecular O₂ alone it was difficult to form the proposed B–O species at the armchair edges under ODH reaction conditions [63]. Therefore, as a part of our study, different atmospheres were applied at the reaction temperature (490 °C) to study the possible physicochemical changes in an inert, oxidative, propane and ODHP environment. The results revealed that only the ODHP reaction atmosphere (He/O₂/C₃H₈), which contains propane and oxygen simultaneously, make changes in the chemical composition, crystallinity, and surface area of hBN in agreement with Su's group [63]. Figure 17 shows the changes in chemical composition of hBN treated in different atmospheres. It was observed that neither propane nor oxygen could change the catalyst chemical composition independently, where hBN showed stability on the surface and inside the bulk. The N₂ adsorption-desorption isotherms of the fresh and treated samples, shown in Figure 18, exhibit character similar to type II based on IUPAC classification for non-porous or macro-porous materials [61] and also did not go through significant changes in different single atmospheres. But, when propane and oxygen were fed simultaneously to the reactor, an obvious increase in oxygen content occurs accompanied by a decrease in nitrogen content (Figure 17). The oxygen content on the catalyst surface changes significantly from 5 to 13 at. % for the fresh and activated samples, respectively, confirmed by XPS, while the EDS results showed that it changed slightly from ca. 2 to 5 at. % inside the bulk. Also, the BET surface area declined from 46 to 25 m² g⁻¹. Therefore, it displays that the interaction between reaction precursors and the catalyst, stimulate the catalyst to generate oxygenated species. These changes are more noticeable on the surface of the catalyst based on the XPS data, because the surface is more exposed and is readily available for the feed molecules. As the melting point of the boron oxide is lower than the ODHP reaction temperature, the accessibility of gaseous probe molecule (nitrogen) to the catalyst surface had been reduced on partially fused surface and caused the decrease in BET surface area. Furthermore, the amount of nitrogen declined on the surface from 46 to 40 at. % (XPS) and inside the bulk from 50 to 47 at. % (EDS), whereas boron content was kept almost constant, 47 at. % on the surface and 50 at. % inside bulk. The XRD patterns of the fresh and the treated catalysts (Figure 18) confirmed the formation of crystalline BO₃ only under a reaction atmosphere that agrees with the XPS and EDS results. The diffraction peaks at 14.6 ° and

27.9° 2θ correspond to BO₃ (Crystallography Open Database (COD) code: 2016172), while the peaks at 26.7°, 41.7°, 43.8° and 55° 2θ are related to the hexagonal structure of hBN (COD database code: 9008997). Furthermore, Raman spectra of the treated hBN shown in Figure 19 confirmed the generation of B-O and B-O-B bonds, peaks at 882 and 500 cm⁻¹ Raman shifts, respectively. Their presence is visible only when the treating atmosphere contains propane and oxygen concurrently. The peak at 1367 cm⁻¹ that is related to B-N is clearly observable in all spectra.

Our observation confirms part of Su et al. hypothesis [63], where hBN materials found being not able to be oxidized under an O₂ atmosphere (below 800 °C), indicating that molecular O₂ alone is not able to attack surface of hBN and to form the proposed B-O species at the armchair edges under ODH reaction conditions. Our results show that the oxidation occurs under the ODHP reaction atmosphere and temperature (490 °C) not only at edges, but also gradually inside the bulk hBN (**Paper I**).

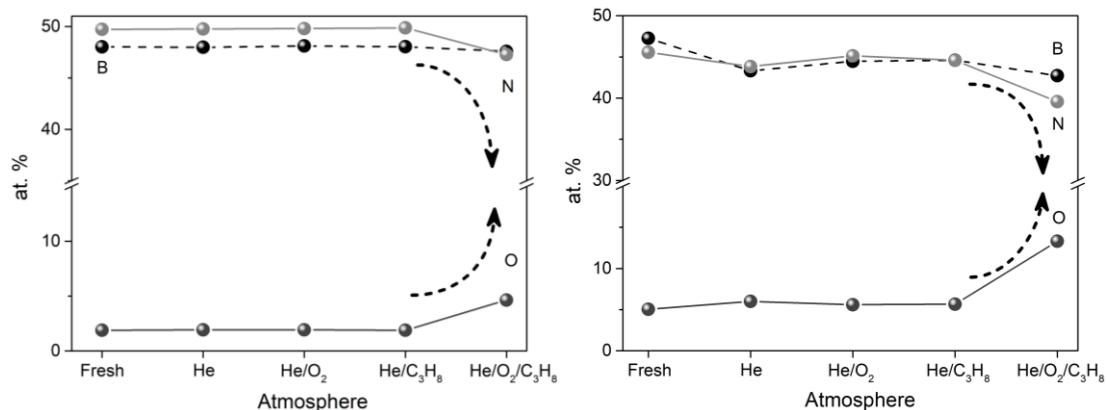


Figure 17. Chemical composition of hBN treated under different atmospheres analyzed by EDS (left) and XPS (right).

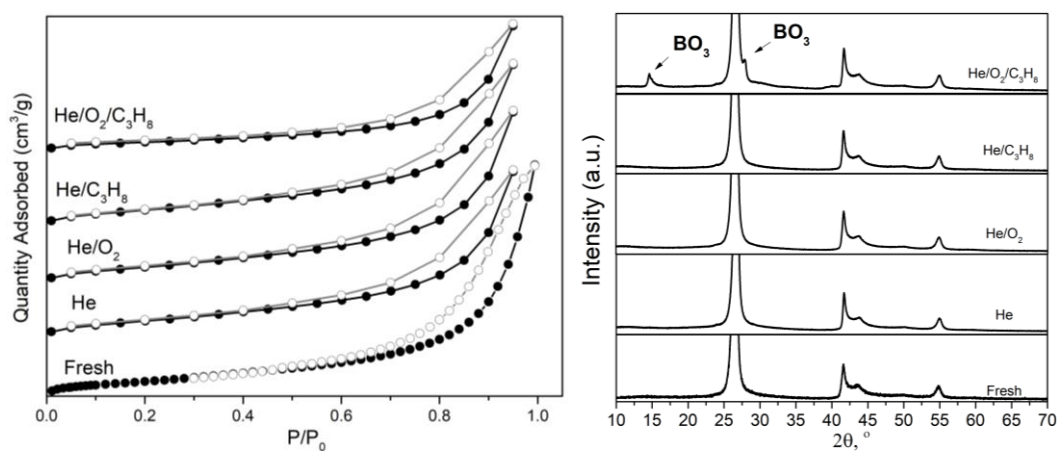


Figure 18. N₂ adsorption-desorption isotherms (left) and X-ray diffraction patterns of the treated hBN under different atmosphere.

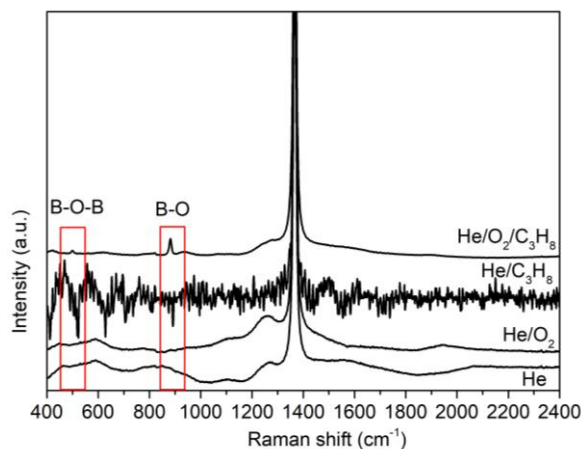


Figure 19. Raman spectra of the treated hBN under different atmospheres.

In some of the first studies, an amorphous boron species like oxyhydroxide ($B(OH)_xO_{3-x}$) layer was identified on the surface of hBN as the active sites [48, 64]. On the other hand Shi et al. proposed that it is the hydroxylated B-OH that acts as the active site [46, 62]. Later it was concluded that the hydroxylated boroxol ring/tri-coordinated planar oxidized boron is the active site and B-OH reacts with O_2 to produce $>B-O-O-B<$ sites that can abstract hydrogen from propane [62, 63]. Shi et al. further studied the participation of BO_x active species in ODHP reaction by using in situ FTIR characterization and isotopic labeling experiments. In situ IR spectroscopy demonstrated that the intensity of B-OH vibration which was claimed to be around 3400 cm^{-1} , continually weakened with the introduction of O_2 to the propane atmosphere. This phenomenon demonstrated that B-OH was an active surface intermediate involved in the reaction network. Isotope labeling experiments discovered that both HDO and D_2O were generated when C_3H_8 and O_2 were introduced into the deuterated BNOD catalyst at $530\text{ }^\circ\text{C}$. The $H_2^{16}O$ and $H_2^{18}O$ signals also appeared after the catalyst was exposed to $^{18}O_2$, indicating that two adjacent B-OH were able to dehydrate and reversibly exchange H and O atoms with gas-phase reactants. A Langmuir-type dependence on oxygen concentration (0.5) and second-order dependence on propane concentration demonstrated that the molecular oxygen was adsorbed or activated on the catalyst surface and that the propane derived from the gas phase directly reacted with the active oxygen species [46].

In our research the functionalities and the skeletal vibration of the hBN catalyst before and after reaction was identified by DRIFT spectroscopy. To make the comparison more visible, the spectra from the spent catalysts are subtracted from the spectra of the fresh hBN and shown in Figure 20. The intensity of the peaks at 732 cm^{-1} and $1200\text{-}1300\text{ cm}^{-1}$, corresponding to B-O vibration, increases by reaction time, which confirms the generation of B-O bond, in agreement with the EDS and XPS results (Figure 21) showing the increment in oxygen content of the catalyst. Also, the XRD patterns (Figure 22) exhibited formation of boron oxide crystalline phase during TOS which is accompanying by increase in boron oxide crystallite size while boron

nitride crystallite size is almost constant (Figure 22). On the other hand, our observation not fully agrees with Shi et al. report discussed above [46]. There are two points where there are disagreement, first the vibration at 3400 cm^{-1} is probably corresponding to N-H [63, 65] and also its intensity is constant over time (Figure 20). Moreover, the O-H vibration is more likely to appear in higher frequency [65], therefore in this research the O-H vibration is considered at 3690 cm^{-1} (Figure 20). Furthermore, the O-H vibration at 3690 cm^{-1} was interrupted in the initial step under the stream and its intensity decreased from the beginning and not gradually, which could be due to formation of the real active sites at the very first stages of the reaction. Hence one scenario could be that the O-H vibration was interrupted because of the interaction with reaction feed or radicals produced in the feed, and thus the O-H group on the surface of the hBN is involved in the reaction. This agrees with the previous researches that announced the participation of oxygen from the edge hydroxylated boron nitride [46, 62, 63], however not a step by step decrease at 3400 cm^{-1} , but an instant decline at 3690 cm^{-1} .

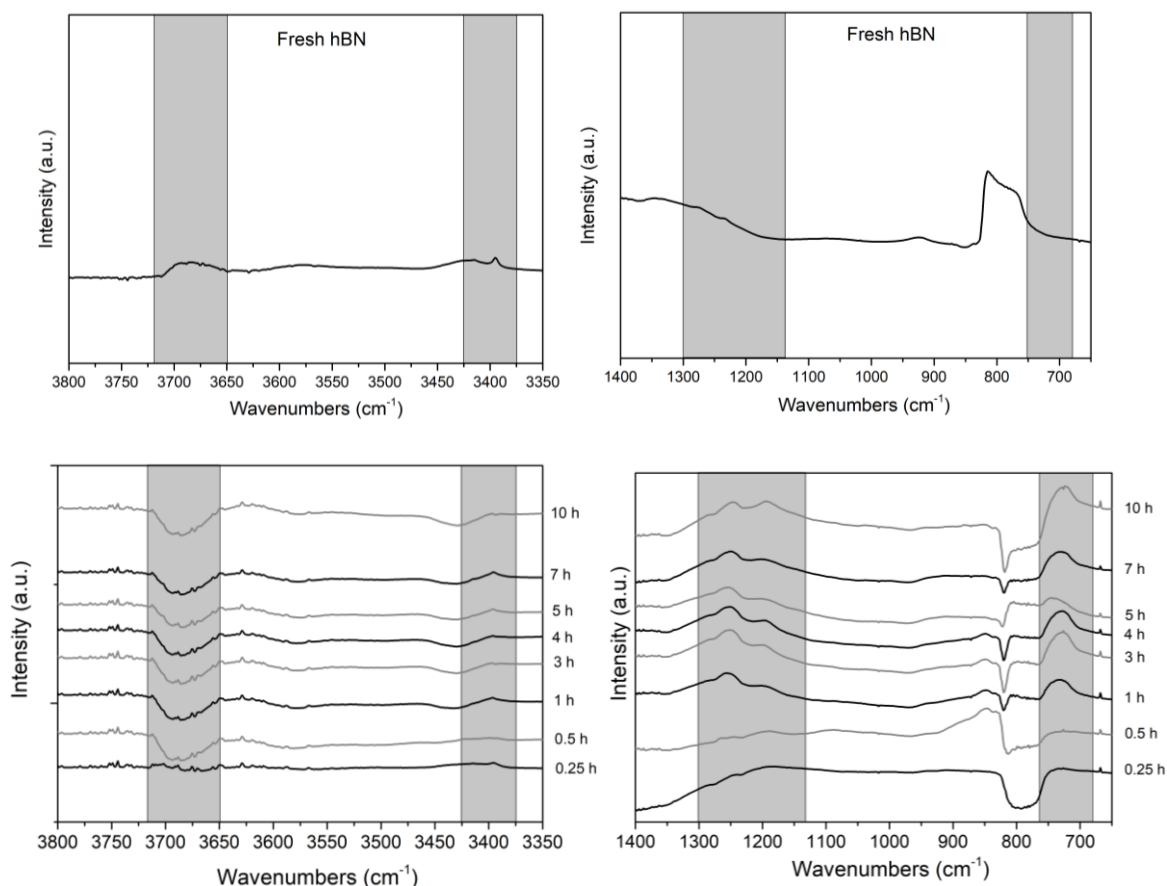


Figure 20. DRIFT spectrum of fresh hBN in the range $650\text{--}1400\text{ cm}^{-1}$ (above right) and $3350\text{--}3800\text{ cm}^{-1}$ (above left). The subtraction of DRIFT spectra collected through spent hBN from the fresh hBN for the corresponding ranges (below).

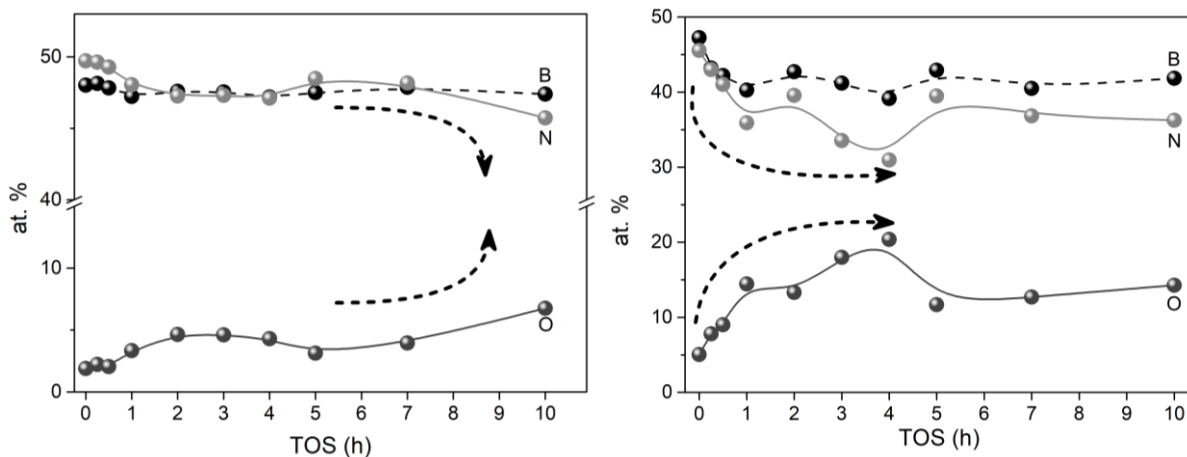


Figure 21. Chemical composition of hBN under the ODHP reaction atmosphere as a function of time on stream analyzed by EDS (left) and XPS (right).

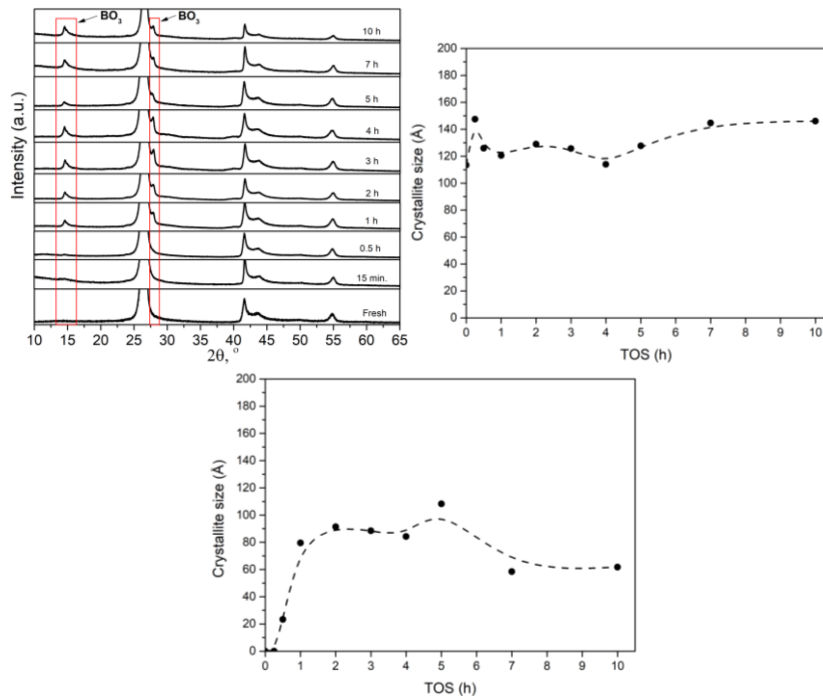


Figure 22. X-ray diffraction patterns of the treated hBN under different time on stream (left), crystallite size of hBN (middle) and BO_3 (right), calculated by Scherrer equation for 2θ : 26.5 and 14.5, respectively.

Later it was reported that propene is mainly generated on the catalyst surface (BO_3 site) while C_2 and C_1 products are formed via both surface-mediated and gas-phase pathways. This was the first direct experimental evidence of gas-phase methyl radicals (CH_3^{\cdot}) in the ODHP reaction over boron-based catalysts that was achieved by using online synchrotron vacuum ultraviolet photoionization mass spectroscopy (SVUV-PIMS), and uncovers the existence of gas-phase radical pathways [52]. Meanwhile, any gas-phase ethyl ($C_2H_5^{\cdot}$) and propyl ($C_3H_7^{\cdot}$) radicals were not detected in this system, meaning the main product

propene, is more likely formed on the catalyst surface, since no gas-phase propyl radicals were observed. [50, 52]. Recently, it was discussed that to initiate the radical chain reactions in the gas phase, O_2 is activated on the boron site to form BOO^{\bullet} which react with propane to generate $C_3H_7^{\bullet}$ and HOO^{\bullet} radicals. Later the former one oxidized by O_2 and the later one act as H-abstractor to react with another propane [66].

After these reports, instant screening of the catalyst behavior and generated products became crucial. Accordingly, the experiments were performed in the presence or absence of O_2 and reaction mixture (RM) by means of mass spectroscopy. The hBN samples (and SiC as a blank test) were treated under the ODHP atmosphere for various time periods in the stream and then the oxygen or reaction mixture was terminated while the changes in products were continuously monitored. The mass spectra disclosed that after termination of the dosing reaction mixture or oxygen over hBN, water formation did not end immediately but decreased gradually over time, unlike in SiC, where water peak intensity dropped immediately (Figure 23). Moreover, the desorption of water from the samples that were treated for longer time, occurred with prolonged delays compared to the ones treated in shorter time. For example, it is clearly visible that water was more easily desorbed from the hBN surface that was treated for 25 minutes rather than 3.5 hours (Figure 23). Therefore, it could be understood that water was formed on the surface of hBN catalyst and that this is the reason why after termination of the reaction mixture or oxygen, water was still detected and was kept desorbing over time. There are a couple of explanations for such different desorption kinetics of each sample, for instance, it could be the fact that a different amount of water was formed on the surface depending on time under the ODHP stream. It also might be related to the different types of adsorption sites which were generated during time; thus, desorption took place with different mechanisms. Moreover, it can be said that due to diffusion limitation, a different time was needed for desorption. It also could be caused by dehydroxylation of the surface at 490 °C, where the OH groups generated during the reaction on the surface are unstable in inert gas stream. On the other hand, when the dosing of the reaction mixture or oxygen was interrupted, the oxygen decreased immediately and dramatically (Figure 23). This means that there was no oxygen adsorbed on the surface of hBN as a molecule that would desorb over time and gradually decrease the detection of oxygen. Therefore the detected oxygen was probably only from the gas phase, while the adsorbed oxygen (which increased the oxygen content of the catalyst after the reaction) probably was dissociatively chemisorbed, in agreement with DFT calculation showing irreversible oxygen functionalization of the fresh edges [67]. Regarding the formation of the products, propene as the main product, ethene as the main side product and methane as the cracking product were also ended rapidly by termination of reaction mixture (Figure 24). But after discontinuing dosing oxygen, these products were still detected for longer time, gradually decreasing before reaching the initial states. Thus, the results revealed that the reaction products are either formed on the surface of the catalyst or they are adsorbed on the surface after being generated in the gas phase and then escaped in the absence of oxygen by the stream, over a short

period of time but not instantly. Furthermore, the combination of these results (showing no detection of O₂ molecule by MS and no change in O content by treatment of hBN only under oxidative atmosphere) disagree with the reports considering the adsorption of the O₂ molecule on the hBN surface as a molecule to generate oxygenated boron species. A complementary experiment of dosing oxygen for a certain short period of time (oxygen pulse dosing while propane was flowing) revealed more important information. The results have shown that when propane and oxygen co-exist in the reaction feed, immediately propane conversion was initiated and reached 17% propane conversion, (Figure 25) which means the reaction starts instantly and independently from the formation of oxygenated boron species over time. This result is against some reports mentioning the idea of necessary induction period for formation of boron oxide as the active site, because in this pulse experiment with short time of dosing oxygen, no induction period was required. Also, in our catalytic measurements any induction period was never observed. Therefore, all together could support the hypothesis that the ODHP reaction starts via formation of radicals in the gas-phase and stand against the frequent report of introducing boron oxide as the main driver in this system. In other words, the gas-phase reaction is the reason for the oxyfunctionalization of a hBN surface and not the consequence of that phenomenon. The reason is probably that the radicals formed in the gas phase activate the hBN surface and result in an increase in the oxygen content on the catalyst surface. This experiment was performed three times, and each time the results were repeated without showing any history effect, revealing that the formation of oxygenated species on the hBN surface does not influence the main driver of the reaction which is the gas phase. It could also be said that at the beginning of the reaction, the catalyst surface might be the location for termination of the generated radicals in the gas phase.

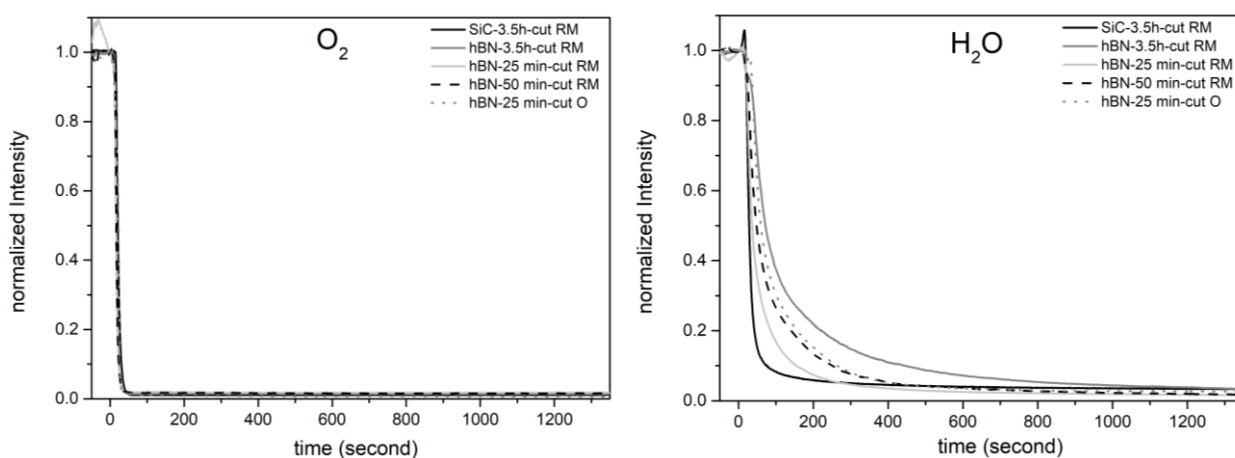


Figure 23. Detection of oxygen (left) and water (right) during ODHP as a function of measurements time in mass spectroscopy after termination of RM and O₂.

Reactor id: 15.5 mm, T: 490 °C, mass of catalysts: 100 mg, He/O₂/C₃H₈ = 11/3/6 ml min⁻¹

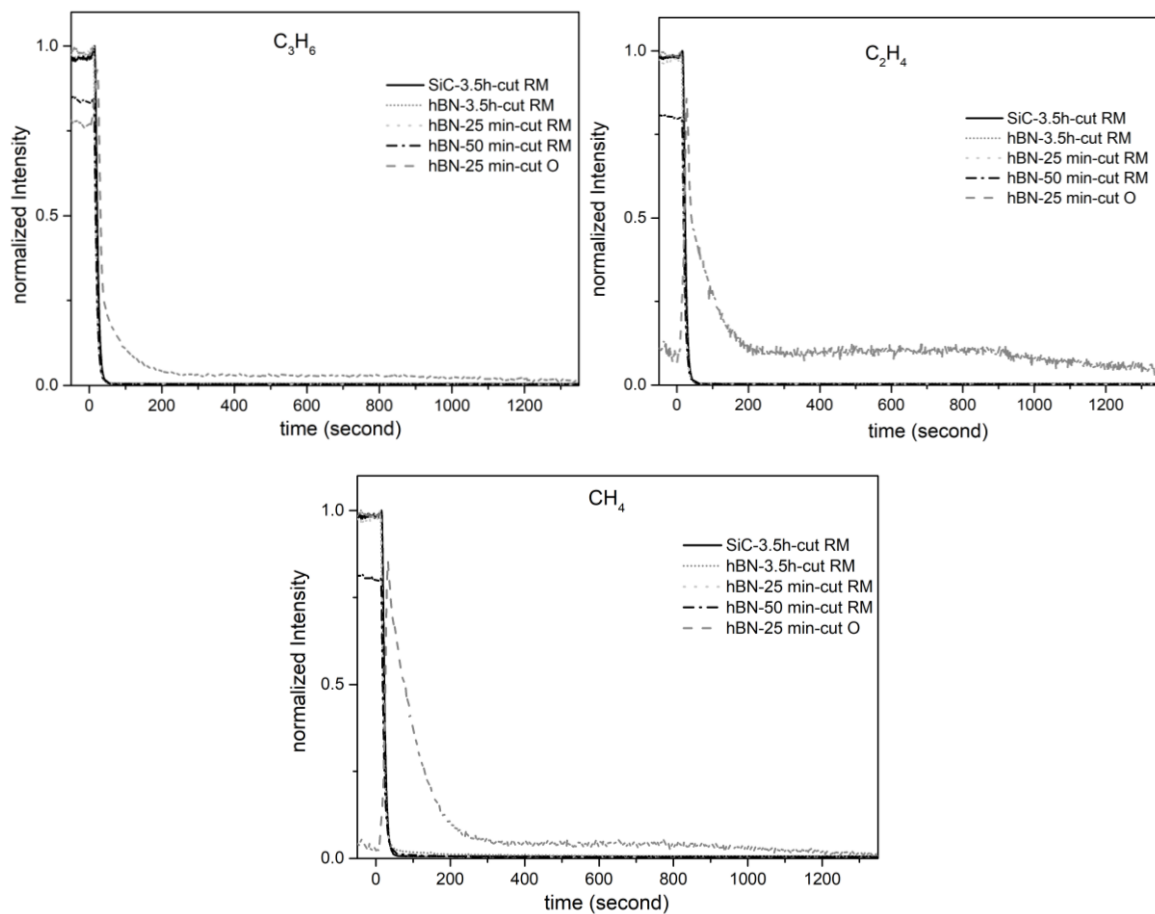


Figure 24. Propene, ethene, and methane mass spectra during ODHP as a function of measurements time in mass spectroscopy after termination of RM and O₂. Reactor id: 15.5 mm, T: 490 °C, mass of catalysts: 100 mg, He/O₂/C₃H₈ = 11/3/6 ml min⁻¹

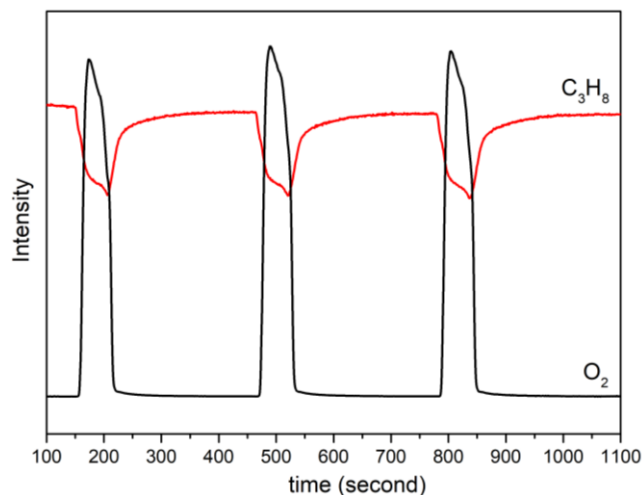
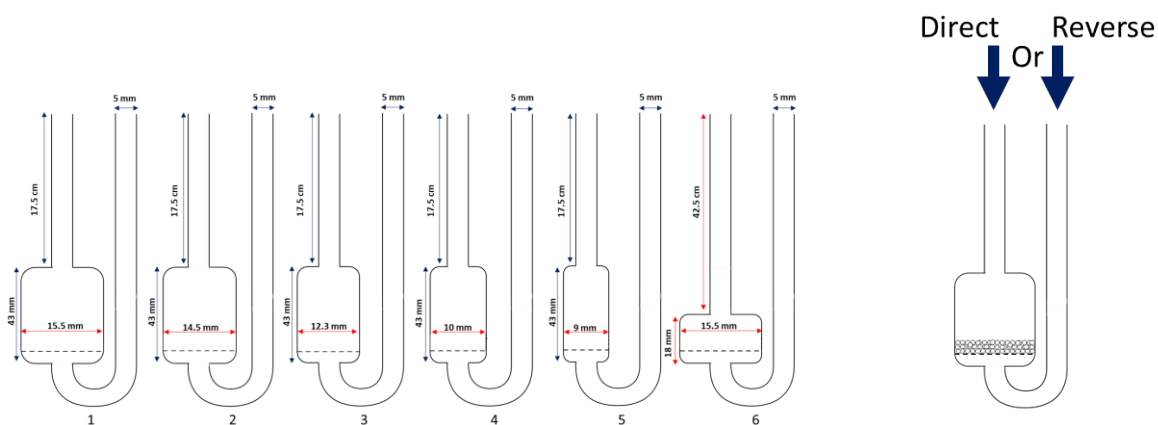


Figure 25. Mass spectra of oxygen and propane when oxygen was dosed as a pulse experiment. Reactor id: 15.5 mm, T: 490 °C, mass of catalysts: 100 mg, He/C₃H₈ = 11/6 ml min⁻¹, O₂: 3 ml min⁻¹

Although several studies have indicated that the ODHP reaction is driven by a combination of surface and gas-phase reactions over boron-based catalysts [48, 51, 53, 54] the exact contribution from each side and the mechanism has not understood yet. The important parameter that has been frequently overlooked is the size and geometry of the reactor and arrangement of the catalytic bed. In fact, this parameter is a representative of available free space for the gas-phase reaction. There are few reports focused on this topic where it was tried to study the effect of free space on hBN activity [54, 66, 68] and they will be compared to our results in the following parts.

In our first step, to understand the influence of reactor and catalytic bed geometry on gas-phase chemistry of reaction, the ODHP reaction over hBN was studied by utilizing different size of reactor and realization of catalyst bed to provide various free space (**Paper V**). Interestingly, the propane conversion increases with changes in product selectivity as a function of reactor free space (Scheme 2, and Figure 26), which agrees with Venegas work reporting decrease in propane conversion by changing the reactor diameter from 8 to 4 mm [54]. To take a step forward, two reactors with the same free volume but different diameter of the catalyst bed (Scheme 2, reactor 5 and 6) were used to test the effect of reactor geometry at constant free volume on course of the ODHP reaction. These two reactors exhibited similar activity regardless of the differences in diameter, therefore it could be said that the gas-solid interface does not play a key role, but in fact the available free space drives the conversion of propane. This phenomenon is connected to the fact that the change in the reactor geometry not only impact the free volume, but also influence the residence time of the reaction mixture within the available space (**Paper V**). Note that although the interaction period with catalysts (contact time) remains the same, the residence time within the space is affected. Therefore, it confirms the vital role of gas-phase reactions and to support this idea, more experiments were carried out. The reactor was also fed by reverse direction (Scheme 2) to check the effect of post-treated free space in the gas-phase reactions, and it confirmed the preliminary observations (Figure 26) but the propane conversion decreased over time which was not observed for direct feeding with free space above the hBN catalyst (Figure 27). The chemical composition analysis of the spent catalysts after 3 hours of reaction by EDS revealed that in both feeding pathways, the oxygen content (which represents the oxygenated boron species) increases as the free space inside the reactor expands (Table 4). In the direct feeding, the lowest amount of oxygen (3.2 at. %) was observed for the smallest reactor with 9 mm diameter, while this value increased step by step for each reactor by enlarging the container and reached 15.6 at. % for the largest reactor with 15.5 mm diameter. The amount of boron was almost constant, while the nitrogen content slowly decreased, probably due to the substitution with oxygen. In general, this trend was also valid for the reverse feeding direction, but with a lower oxygen content that changed from 2.6 to 7 at. % for the smallest and largest reactors, respectively. It seems that the amount of incorporated oxygen is proportional to the amount of converted propane because the lower activity of hBN under the stream due to the deactivation (Figure 27)

is corresponding for the lower content of oxygen in the reverse direction of feeding. Concerning this observation, it also could be deduced that the position of the catalyst bed could influence the activity, and the free space above the catalyst surface provide a better environment for the radicals to attack the catalyst surface and form the products, or maybe generates species that participate in the reaction and enhance the activity. Due to the interaction of feed molecules with each other in the gas phase that results in generation of radicals (probably oxygenated propyl radicals) the hBN surface is activated, but in the reverse feeding with post-treatment free space, the residence time assist only in the formation and propagation of the radicals that not all of them will meet the catalyst surface eventually. Therefore, it was observed that the availability and the position of the free space is evidently crucial and have impact on oxygen content of the catalyst which is a representative of how much gas-surface interaction was involved (**Paper V**).



Scheme 2. Schematic of the prepared reactors for ODHP over hBN (left) and the applied direct and reverse feeding lanes (right).

The free volume above the catalyst bed: Reactor number 1: 5.4 ml, 2: 4.9 ml, 3: 3.4 ml, 4: 2 ml, 5: 1.4 ml, 6: 1.4 ml.

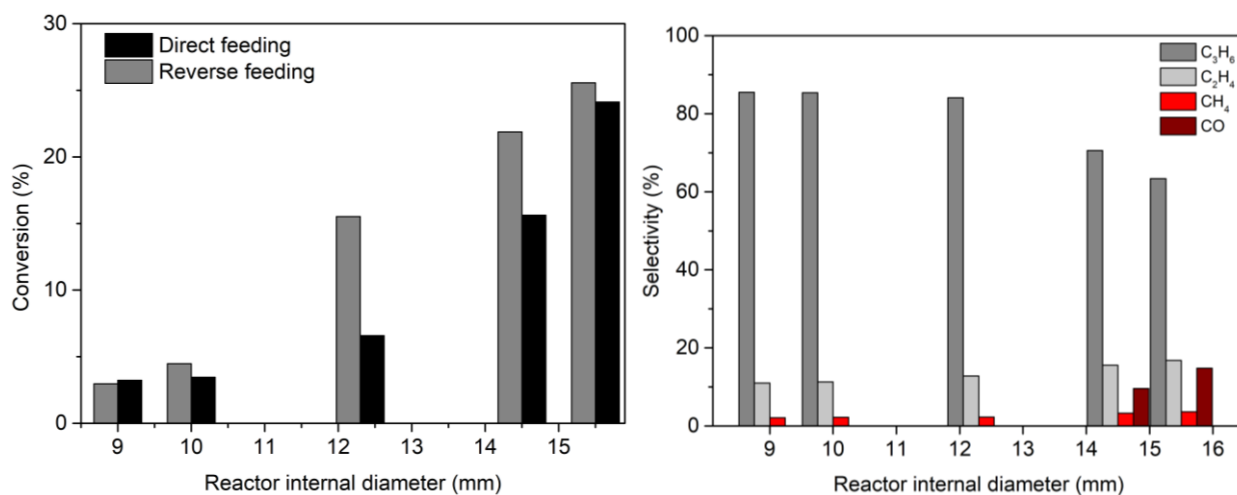


Figure 26. Propane conversion as a function of reactor size in ODHP for direct and reverse feeding direction (left), and products selectivity for the direct feeding (right), T: 490 °C, mass of catalysts: 100 mg, TOS: 15 min., He/O₂/C₃H₈ = 11/3/6 ml min⁻¹

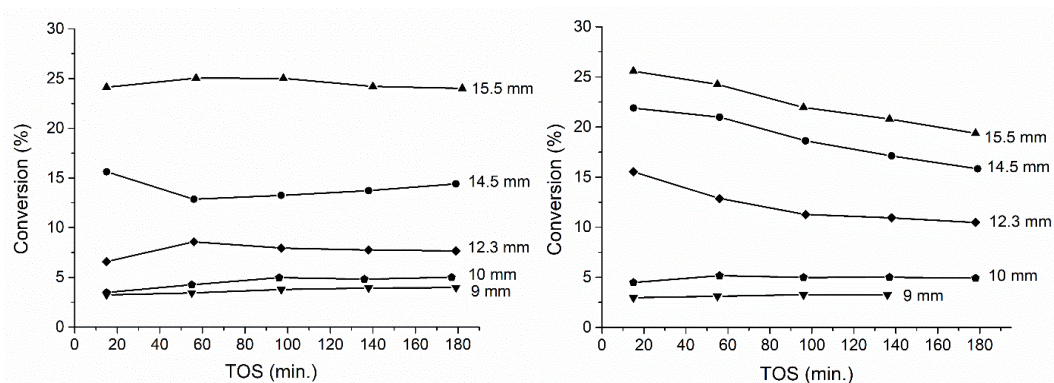


Figure 27. Propane conversion as a function of TOS for different reactor sizes under the ODHP atmosphere, the direct direction of feeding (left), and the reverse direction of feeding (right). T: 490 °C, mass of catalysts: 100 mg, He/O₂/C₃H₈ = 11/3/6 ml min⁻¹

Table 4. Chemical composition of spent hBN after the ODHP reaction via different reactor sizes (Figure 27), TOS: 180 min.

	Reactor diameter (mm)	at. %		
		B	N	O
Direct	15.5	45.1	38.5	15.6
	14.5	47.2	46.0	5.9
	12.3	47.5	47.1	4.5
	10	47.5	47.7	3.7
	9	47.7	48.2	3.2
Reverse	15.5	47.1	45.1	7.0
	14.5	47.3	46.5	5.3
	12.3	47.4	47.2	4.4
	10	47.4	48.7	2.9
	9	47.9	48.9	2.6

Lindstedt et al. further stated that the catalyst is only responsible for initiating the gas-phase chemistry and the gas-phase is responsible for the high selectivity toward olefins [51]. Different radicals desorbed from the surface of catalyst can initiate the gas-phase reactions and influence the product distribution [48, 51, 53, 54, 69]. According to the numerous research that have shown partial oxidation of hBN, it has been frequently reported that the initiation of radicals occurs on the surface of hBN and multiple boron oxide species are proposed as the active sites [64, 67, 70, 71]. Boron peroxy radical (BOO[•]) formed by reaction between O₂ and tri-coordinated boron, is proposed to serve as the initiator of the gas phase radical chain by reacting with propane to form C₃H₇[•] and HOO[•] radicals [71]. In agreement with the hypothesis that states oxidized boron species as the active sites [45, 53, 72, 73], it was reported that either the B₂O₃ has identical catalytic property regardless of supports or the product distribution is determined in the gas phase reaction rather than the B₂O₃ surface [66]. As the boron oxide melting point is lower than the ODHP reaction temperature, it was reported that the presence of dimerized di-coordinated boron radical >B-B< dynamically formed in the liquid boron oxide activates O₂ molecule to form peroxide-like >B-O-O-B< sites. Then propane is oxidized on those sites and form propyl radical loosely bond to B-OH. Finally, the formed >B-

O' dangling bond is critical for the subsequent dehydrogenation or activation. The dehydration of B-OH with desorption of water recover the active site and close the catalytic cycle [74]. In summary, It has been frequently reported that the ODHP over hBN is influenced by both heterogeneous (catalyst surface), homogeneous (gas-phase reactions) and co-existence of heterogeneous-homogeneous mechanism (catalytically initiated gas phase reactions via radicals such as $C_3H_7^*$ and HOO^* desorbing from the hBN surface and reacting in the gas-phase) [48, 52-54, 68].

Based on our observation all of the characterized physicochemical changes during the ODHP reaction over hBN occur without noticeable impact on the catalyst activity, and the stable behavior of hBN was almost preserved in the course of 10 hours under the reaction stream (Figure 28). The catalytic activity of hBN exhibited almost stable behavior in ODHP and showed propane conversion of approximately 25 % with selectivity of ca. 60% toward propene, approximately 17% for both ethene and carbon monoxide, and less than 4 and 2% for methane and carbon dioxide, respectively. Thus, it could be deduced that the boron oxide species that play a key role, are probably formed at the initial states and then the increase in oxygen content is due to formation of other (maybe unimportant) oxygenated boron species or growing the size of boron oxide nanoparticles (or nanoislands on the surface of hBN) that do not interfere in the reaction. However, the experimental evidence of continuously increased boron oxide formation during the ODHP (Figure 21) as well as the enhanced conversion of propane by larger reactors (Figure 26) raised the questions whether the reaction is actually driven by in situ generated boron oxide or the gas-phase chemistry that takes place inside the free space or both. Moreover, whether the free space controls the formation of oxygenated species and subsequently the catalyst activity, or free space and oxygenated species launch as individual phenomena. To answer these questions, two experiments were designed and carried out. The first experiment consisted of three steps: 1: The hBN catalyst was treated in ODHP using a small reactor (9 mm), 2: then the spent catalyst from the small reactor was moved into a larger reactor (15.5 mm), and 3: the spent catalyst from the larger reactor was moved back to the primary small reactor, and in each step the activity of the catalysts was measured in ODHP. As discussed above (Table 4), the fresh catalyst in the small reactor generated a lower oxygen content (3.2 at. %) compared to the larger reactor (15.6 at. %). Therefore, the idea was to see whether the higher content of oxygenated species that was created in the larger reactor results in a higher activity of the catalyst in the smaller reactor or not. The results shown in Figure 29 disclosed that regardless of the amount of oxygen-containing species, the reaction is driven by the empty space because the oxygen content of the spent catalyst in the large reactor which was used for step 3 is five times higher than the oxygen content formed in step 1 using small reactor, but for both steps (1 and 3) the propane conversion is the same (ca. 3%) as the reactor size is identical (9 mm) thus the role of initial oxygenated species is not critical, while the actual driver force is the gas-phase reactions controlled by the free space (**Paper V**).

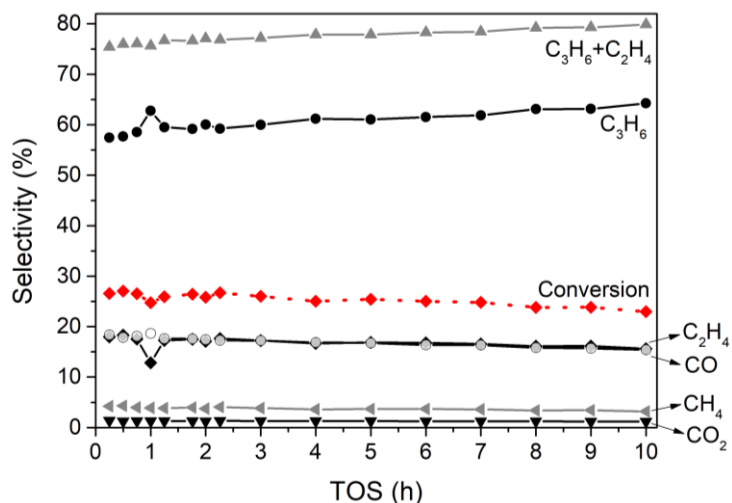


Figure 28. Propane conversion and product selectivity toward products over hBN in ODHP reaction as a function of TOS. Reactor id: 15.5 mm, T: 490 °C, mass of catalysts: 100 mg, He/O₂/C₃H₈ = 11/3/6 ml min⁻¹

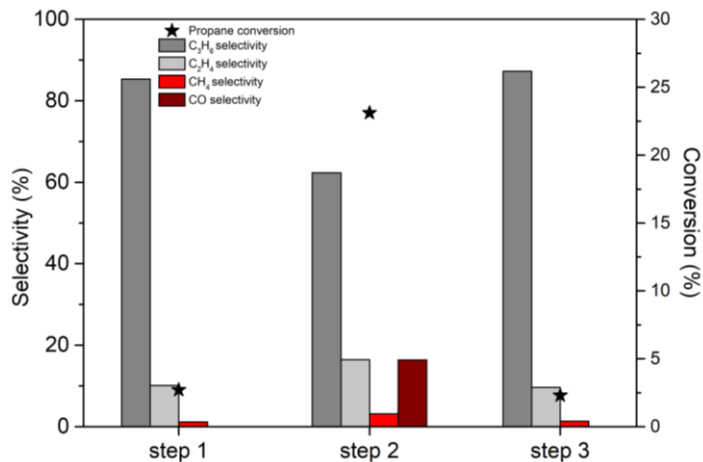


Figure 29. Propane conversion and product selectivity of step 1: fresh hBN in reactor with 9 mm diameter, step 2: the spent hBN from step 1 with O content of 3.2 at. % in reactor with 15.5 mm diameter, step 3: the spent hBN from step 2 with O content of 15.6 at. % in the reactor with 9 mm diameter. The O content after step 3 was measured as 13.7 at. %. T: 490 °C, mass of catalysts: 100 mg, TOS: 15 min., He/O₂/C₃H₈ = 11/3/6 ml min⁻¹

For the second experiment, the catalytic activity of hBN impregnated by boric acid (5 wt.%) was measured in ODHP. Then the catalyst was washed in order to remove the boron oxide and then the catalysts activities were compared (Figure 30). Surprisingly, the impregnated catalyst exhibited 36% less propane conversion compared to fresh hBN, meaning that the pre-formed boron oxide species not only did not improve the activity but also lessened it, probably due to covering the actual active sites or prevention of generating the genuine active sites. After washing the catalyst, the boron oxide was completely removed from the hBN surface and the activity was almost fully recovered. Thus, removing the preformed boron oxide made room for the catalyst to function with the typical access of the gaseous feed to the catalyst surface. The elemental

composition obtained by EDS showed approximately 2 at. % and 12 at. % of oxygen content for the fresh and the impregnated catalyst which decreased to around 2 at. % after washing (Table 5). But interestingly both impregnated and washed catalysts exhibited ca. 12 at. % of oxygen after the reaction, which unveiled that the real active oxygenated species are formed in situ during the reaction and cannot be created by conventional impregnation of boron oxide in advance (**Paper V**). It can be related to the nature of the species or to their sizes. Therefore, these experiments demonstrate that the structure of the active boron oxide is not the same as the preformed added bulk boron oxide. To conclude, the initial amount of boron oxide does not control the reaction pathway but, in fact, the gas-phase reaction is the decisive factor, meaning that the free space, permissible gas-phase reaction chains, and subsequently the interaction of feed with hBN surface for in situ generation of active sites, control the catalytic activity of this system. On the other hand, the activity of the empty reactors without hBN catalyst showed more than 3 % of propane conversion which are only due to formation of radical species in the pure gas-phase reactions. It was also tried to compare the activity of commercial hBN (with 47 m²/g BET surface area) with a high surface area hBN (with 300 m²/g BET surface area, and textural properties between microporous-mesoporous isotherms) and the results showed comparable or even a bit lower activity for the high surface area hBN, even though the later one with high BET surface area exhibited ca. 25 at. % oxygen content. Under the same reaction condition, the propane conversion was ca. 18 and 25 % for the high surface area and the commercial hBN, respectively (Figure 31). Likewise, the selectivity toward products were similar. Therefore, these experimental results doubt the previous reports on considering importance of the catalyst surface (in sense how large surface area is) as the initiator of the gas-phase reaction and introduction of the boron oxide species as the main driver (**Paper V**).

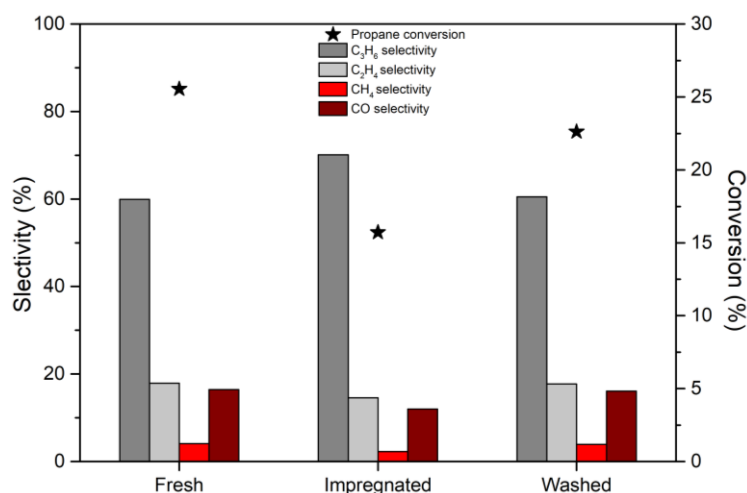


Figure 30. Propane conversion and products selectivity of impregnated BN by boric acid, and after washing, in ODHP, Reactor id: 15.5 mm, T: 490 °C, mass of catalysts: 100 mg, TOS: 15 min., He/O₂/C₃H₈ = 11/3/6 ml min⁻¹

Table 5. Chemical composition of impregnated and washed hBN before and after the ODHP reaction by EDS.

	Impregnated	washed	Spent impregnated	Spent washed
O at. %	12	2	12	12

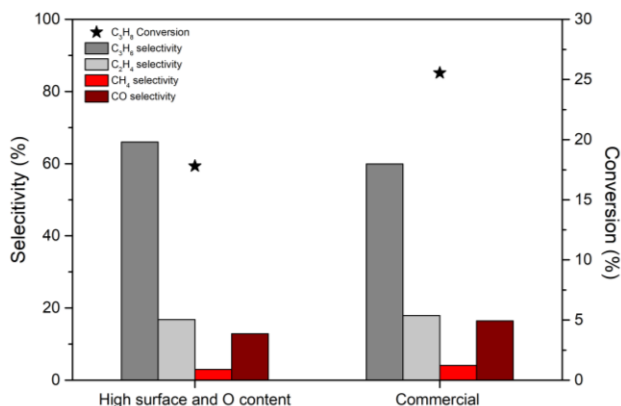


Figure 31. Propane conversion and products selectivity in ODHP over commercial hBN, and the synthesized hBN with higher surface area and oxygen content. T: 490 °C, mass of catalysts: 100 mg, TOS: 15 min., He/O₂/C₃H₈ = 11/3/6 ml min⁻¹

The effect of dilution was studied in this work and it was observed that the presence of SiC did not improve the activity but in contrary delayed reaching the typical level. This induction period was observed only in the presence of SiC, as the hBN catalyst without dilution exhibited stable activity from the beginning without showing induction time (Figure 32). The total volume of the bed (hBN diluted with SiC) was kept constant while changing the mass of hBN catalyst. Even though the initial activity of different masses of hBN catalyst were not the same, but they all reached similar conversion values after 3h under the stream which is in line with previous data showing that in a constant temperature the free space is the main driving force of the reaction, and as the free space was almost identical, the observed activity was similar. The presence of the induction period could be due to the presence of the diluent, because the radicals and intermediates are quenched on those sites. The slightly higher conversion of the hBN without dilution was probably due to the larger free space. The selectivity towards propene as the main product was a reverse trend of propane conversion and it decreased by time and at the end reached the value of 65 % for all the three diluted hBN catalysts (Figure 33). However, the ethene and CO selectivity increased over time with a similar trend as the propane conversion, and reached ca. 16 % for both after 225 minutes under the stream. The selectivity of the undiluted samples kept the same values due to no change in conversion. The existence of an induction period was reported in another work for ODH of ethane to ethene [75], where the catalyst was also diluted as well, and the selectivity towards ethene decreased gradually by the increase in alkane conversion. In their work, it was claimed that the induction period indicate the B–O site needs to be formed under a certain activation and/or reaction condition, but the effect of the diluent was not considered by them. Because when

we tried the ODH reaction over pure hBN without dilution, our observation did not show any induction period neither for propane nor ethane. Thus, as it was mentioned earlier, the induction can be caused by quenching the generated radicals on the diluent surface and delaying reaching the maximum efficiency. Additionally, an experiment was carried out to demonstrate the activity of hBN in the presence of a fully packed reactor by SiC, to eliminate the entire possible free space of the reactor. The observed conversion was less than 2 % during 3 h of TOS whereas the empty reactor with the same geometry exhibited more than 3 % of propane conversion. Thus, it revealed that the hBN without having available free space is almost inactive in ODHP, and displayed again the critical role of the free space within the reactor for the gas phase reactions as the main driver (**Paper V**). This result contradicts the report by Venegas et al. [54] where addition of SiC improved the propane conversion while the remaining free volume of the reactor was filled by quartz chips. In fact, the presence of a diluent accelerates the radical quenching (based on the type of diluent) which means lowering the extent of reaction, even though the diluents or fillers are chemically inert and will not participate in the reaction. Hence accurate interpretation of the results is always important to not confuse the others working in the same field and we tried to clarify some of those.

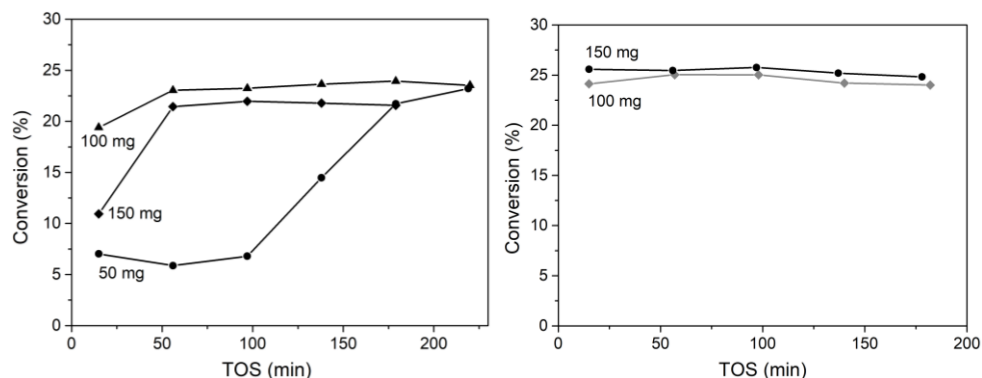


Figure 32. Propane conversion of different hBN masses as a function of time on stream, diluted by SiC (left), undiluted (right). The free volume above the catalyst in reactor with diluted hBN: 5.2 ml, and in reactor without dilution: 5.4 ml for 100 mg and 5.3 ml for 150 mg. Reactor id: 15.5 mm, T: 490 °C, He/O₂/C₃H₈ = 11/3/6 ml min⁻¹

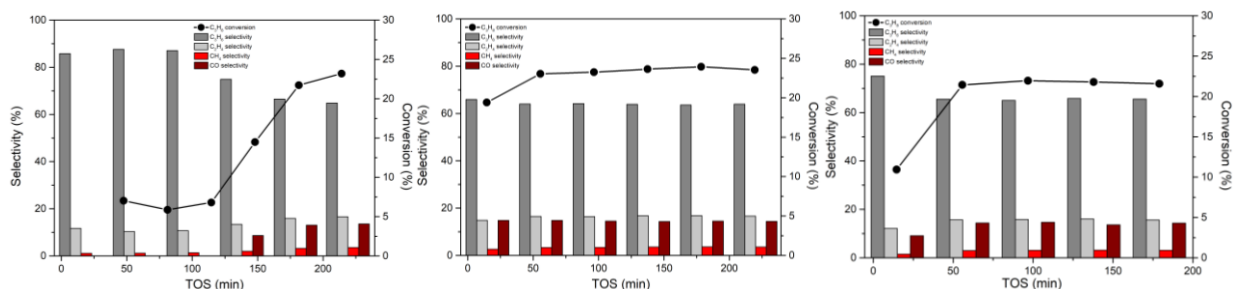


Figure 33. Selectivity towards products for different masses of hBN diluted by SiC, 50 mg (left), 100 mg (middle) and 150 mg (right). The free volume above the catalyst in reactor with diluted hBN: 5.2 ml. Reactor id: 15.5 mm, T: 490 °C, He/O₂/C₃H₈ = 11/3/6 ml min⁻¹

The pure gas phase reactions which were measured in the reactor with 15.5 mm diameter without the catalyst, exhibited 86 % of propene selectivity and 9 % of ethene selectivity with ca. 3 % propane conversion. The CO, methane and CO₂ selectivity were observed as 0, 3 and 1 % respectively. In comparison with the hBN activity in the reactor of 9 mm diameter with similar propane conversion (ca. 3 %) and under the same reaction condition, it could be seen that the selectivity toward products is just slightly higher and almost comparable. Propene, ethene, CO, methane and CO₂ exhibited selectivity of 85, 11, 2, 0 and 2 % respectively. Therefore, it means in such a situation where there is not enough space for an efficient coupled surface-mediated and gas-phase interaction, the reaction is driven only by the gas phase chemistry. Nevertheless, when hBN activity is measured in the larger reactor (id: 15.5 mm) under the same reaction condition, it is clearly visible that along with the increase in propane conversion to ca. 25 % (and O₂ conversion ca. 80 %), the selectivity to propene decreases to almost 60 % while the cracking products become more selective, such as ethene and CO with 17 % selectivity for both. There is no big change in selectivity toward methane and CO₂ as they stay with 4 and 2 %. However

The effect of catalyst mass on this catalytic system was studied in two different reactors with container diameters of 12.3 mm and 15.5 mm. For both of them, the results showed that the change in catalyst mass did not significantly influence conversion of propane, as shown in Figure 34. Note that changes in the free space were negligible with respect to the different masses of catalyst; therefore, it means the same diameter of catalyst bed provided identical interface between the gas and the solid phase in each reactor, and thus similar free space resulted in a comparable propane conversion (**Paper V**). Even though the experiments involved adjusting the contact time between the gaseous feed and the catalyst surface by varying the mass of hBN, they provided confirmation that the reaction is primarily influenced by the available free space, rather than the quantity of catalyst. The selectivity toward products were similar in the same reactor (Figure 34). In reactor with 12.3 diameter, for all three masses of hBN, the propene selectivity was kept approximately 74 % ± 2%, and for the ethene and CO ca. 13 ± 1 and 9 ± 1 %. Methane and CO₂ selectivity were less than 2%. In case of the reaction in the reactor with 15.5 mm diameter, both masses of hBN exhibited 61 % ± 2% of propene selectivity, while ethene, CO, and methane selectivity were 17 ± 1, 16 ± 1, and 4 ± 0.5 %. CO₂ selectivity was 1%.

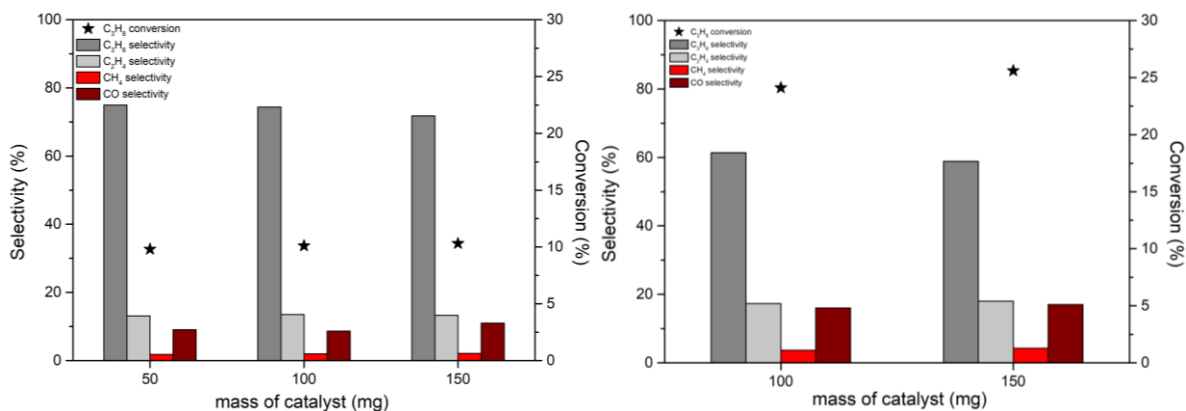


Figure 34. Propane conversion and products selectivity over hBN as a function catalyst mass, reactor diameter: 12.3 mm (left), 15.5 mm (right). The free volume above the catalyst in reactor with 12.3 mm diameter: 50 mg=3.6 ml, 100 mg= 3.4 ml, 150 mg= 3.3 ml, and in reactor with 15.5 mm diameter: 100 mg= 5.4 ml, and 150 mg= 5.3 ml. T: 490 °C, He/O₂/C₃H₈ = 11/3/6 ml min⁻¹

From the experiments described in the previous paragraphs, the essential role of the free space in the reactor emerges. Therefore, we performed another series of experiments with different values of the total flow rate of the reaction mixture, which affects the contact time with the catalyst as well as the total residence time of the gaseous mixture in the reaction zone of the reactor. It was observed that increasing the total flow rate, which is lowering the contact time and also the residence time of the gas in reactor, resulted in a decrease in the catalyst activity (**Paper V**, and Figure 35). Unlike catalyst mass, that did not play a crucial role in activity (due to not altering the free space), changing total flow within a constant free space, changed the time that the feed molecules (radical species) were able to interact with the hBN surface and/or with each other (residence time), therefore it affected the activity. It could be concluded that both larger free space and lower total flow rate increase the interactions between the gaseous species with each other and also with the catalyst surface and therefore push the ODHP reaction toward higher activity.

In another set of experiments, the propane conversion over the same amount of hBN in the same reactor was measured in the presence of quartz sands (particle size: 0.8-3 mm) as layers occupying one quarter, two quarters, three quarters and four quarters of the free space. The volume of the voids between the particles was calculated based on their porosity. The quartz sand particles occupied 0, 14, 31, 47 and 54 % of the space inside the reactor container. The results showed that by depressing the free space, the conversion rate decreased (Figure 36), which agrees with the observation of the change in the reactor size. Although the free space did not change to zero, because the porosity of the quartz sand layers inside the reactor was quite large, but still when the reactor was filled by the quartz sands, the propane conversion dropped to 2.6 %, because the space between quartz particles as voids were not large enough to let the propagation chain of radicals be formed via gas phase chemistry, and in fact the filler particles turned to a place for termination of the radicals (**Paper V**). As the propane conversion decreases by filling quartz sands, the propene selectivity increases from ca. 61 % for zero filling to 86 % with fully occupied reactor space (Figure 36). In

contrary, the selectivity toward ethene and CO decreases from 17 to 11 and 16 to 0, respectively. Methane selectivity went through a smaller decrease from 4 to 1% while CO₂ selectivity was kept on 1%.

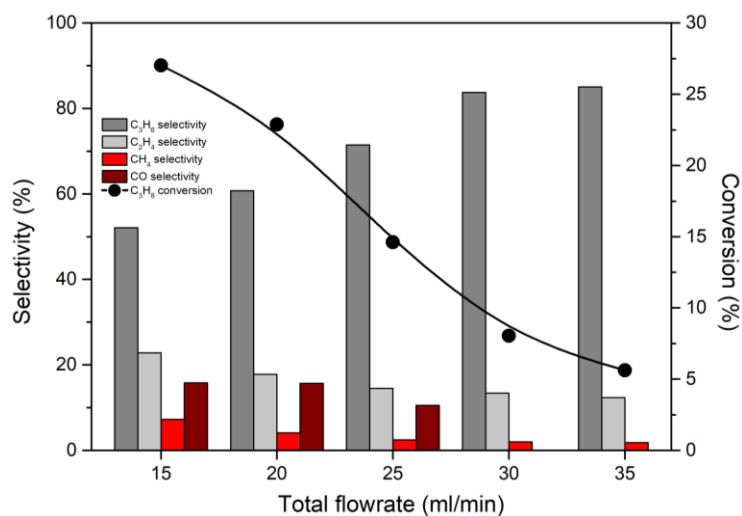


Figure 35. Propane conversion and product selectivity over hBN as a function total flow rate. Reactor id: 15.5 mm, T: 490 °C, mass of catalysts: 100 mg, He/O₂/C₃H₈ = 55/15/30 %

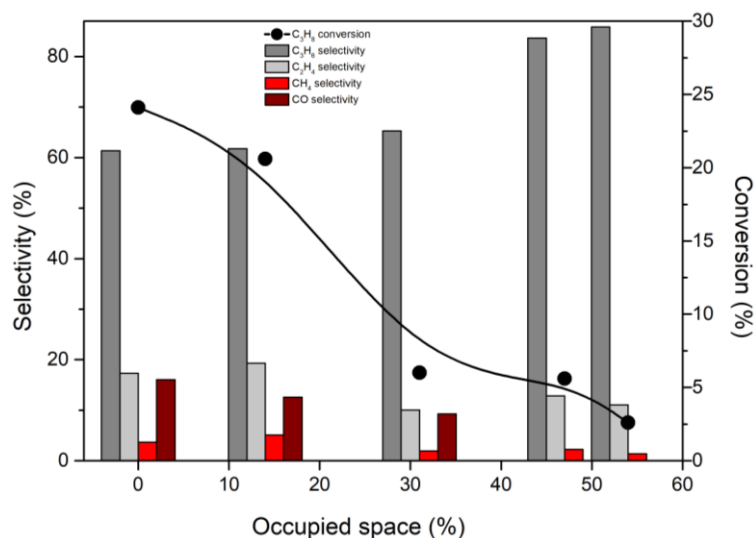


Figure 36. Propane conversion and product selectivity over hBN in ODHP reaction as a function of occupied reactor space by quartz sands. Reactor id: 15.5 mm, T: 490 °C, mass of catalysts: 100 mg, He/O₂/C₃H₈ = 11/3/6 ml min⁻¹

A combination of results from experiments with changing reactor size, free volume in the reactor by filler and change in flowrate revealed the dependency of reaction rate on residence time shown in Figure 37. It disclosed how propane conversion depends on residence time and supports the hypothesis mentioned above which showed the gas-phase is the main driving force the reaction in this system (**Paper V**).

As the final part of studying hBN behavior, the change in reaction temperature (Figure 38) as well as the changes of products selectivity as a function of conversion were investigated (Figure 39). As it was expected, a higher reaction temperature resulted in higher propane conversion but it also revealed that regardless of how the propane conversion was changed, the selectivity to propene was always a reverse function of the propane conversion, irrespective of whether the size of the reactor was changed, or the temperature, or the amount of catalyst, or the gaseous feed flowrate, etc., the selectivity responded only to the conversion value and possibly took the same pathway. This trend was opposite for the other products which means in the case of ethene, methane and CO, the selectivity increases as the propane conversion was improved.

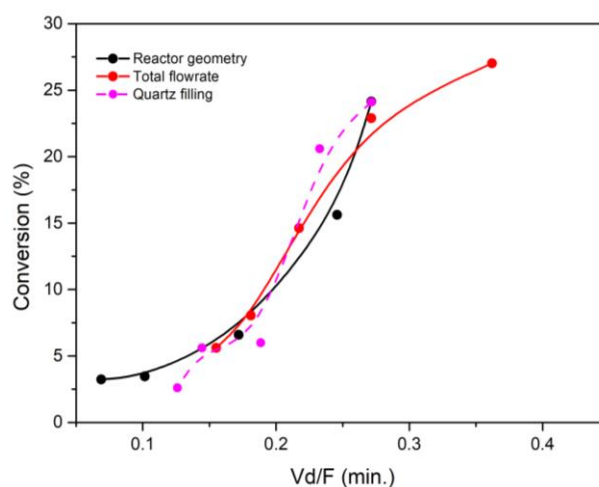


Figure 37. Propane conversion as a function of residence time (free space (or dead volume)/flowrate). Reactor id: 9, 10, 12.3, 14.5 and 15.5 mm, T: 490 °C, mass of catalysts: 100 mg, He: O₂: C₃H₈= 55/3/6 %, total flow: 15, 20, 25, 30, 35 ml min⁻¹, quartz filling: 0, 14, 31, 47, 54 %.

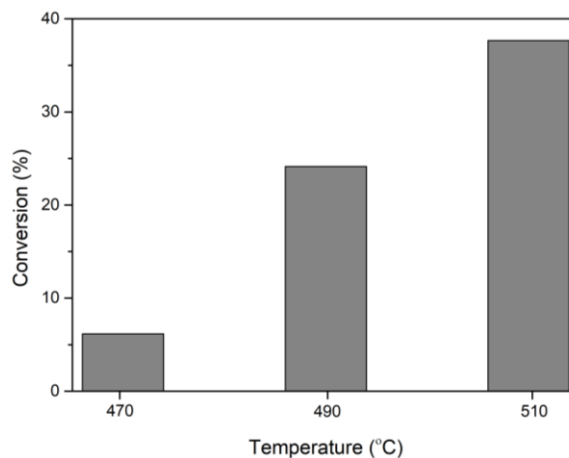


Figure 38. Change of propane conversion in different reaction temperature. Reactor id: 15.5 mm, mass of catalysts: 100 mg, He/O₂/C₃H₈= 11/3/6 ml min⁻¹

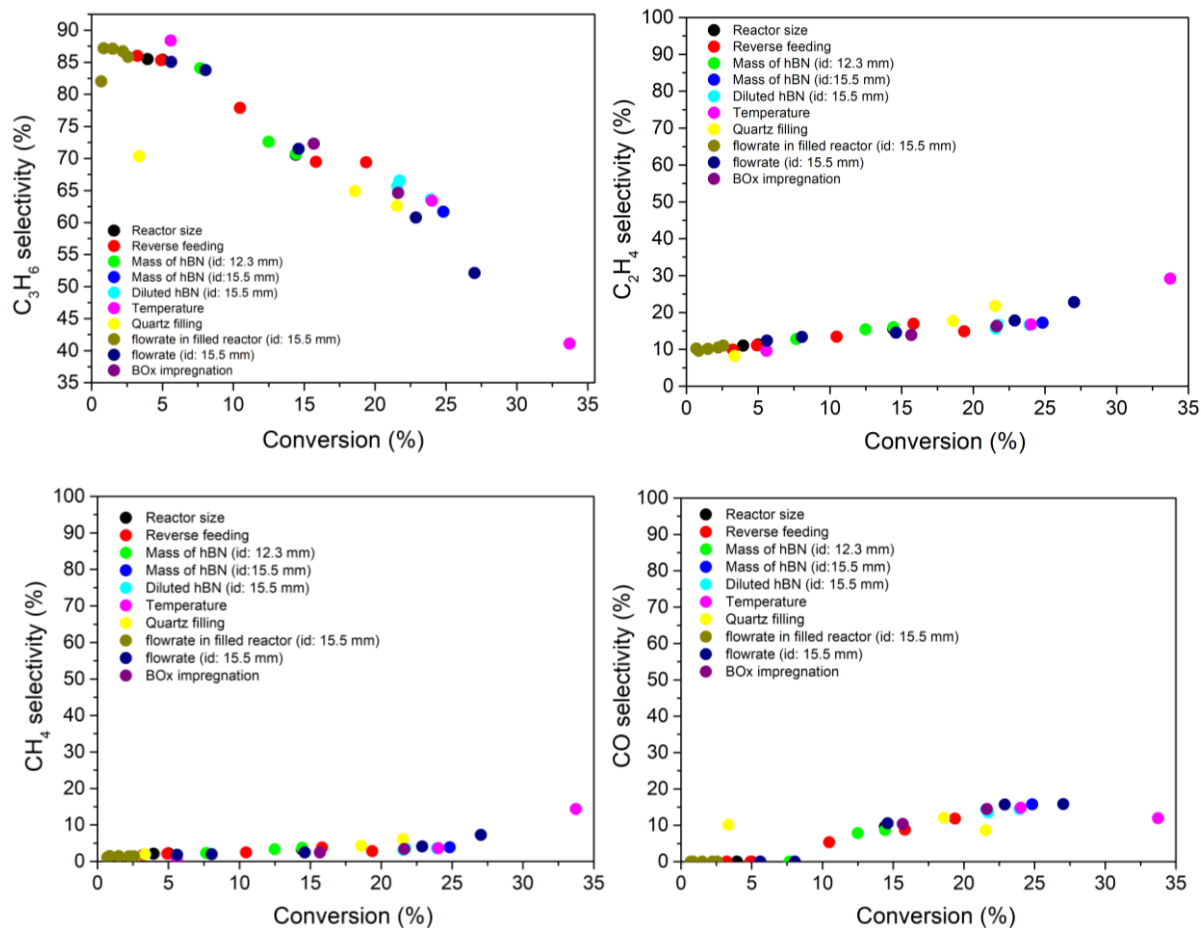


Figure 39. Selectivity towards products as a function of propane conversion.

Herein, the main hypothesis from the literature related to the three topics of reaction initiation, dehydrogenation of propane and selectivity, are discussed and then inspect regarding our observation. In the initiation step, according to the previous studies, the feed molecules are being activated on the surface to form radicals (intermediates), which then continue to propagate in a chain reaction and finally the dehydrogenation of propane takes place [51, 52]. The mixed heterogeneous–homogeneous ODH mechanism has been proposed, which can be described as the boron oxide/hydroxide phase on the surface of the hBN catalyst acting as an initiator to form alkyl radicals, which further react in the gas phase [76]. After oxygen functionalization of boron on the hBN catalyst surface, BO^* is formed with the generation of important gas radical HOO^* because O_2 could be activated on the catalyst surface and form peroxy-like >BO-OB< species which results in BO^* after O-O cleavage. On the other hand, in parallel, the boron surface sites generate B–OH and B–H active species, and then the formed B–H will react with O_2 from HOO^* , which is the main reactive radical for the gas reaction [53, 76, 77]. Wang et al. [78] proposed different viewpoints, considering the abundant thermodynamically stable B–O–B bridges in tricoordinated B_2O_3

units that could be hydrolyzed to generate more B–OH under ODH conditions. The H abstraction of B–OH occurred in the presence of O₂. The highly reactive species of BO• and •OOH radicals formed by H abstraction of B–OH by O₂ could invoke the dehydrogenation of propane via the surface channel and gas channel, respectively. The aforementioned reaction processes were reported as the initiation stages during which the radical species are generated.

During the ODHP reaction, the dehydrogenation of propane mainly occurs via the abstraction of hydrogen from propane by the reactive species of BO• and •OOH radicals [76]. The second hydrogen could be abstracted by the same mean or by O₂. Meanwhile, a part of propene is formed by the direct cleavage of the C–H bond of propyl and isopropyl radicals. As the main byproduct during the ODHP reaction, ethene is mainly derived from C–C bond cleavage and the coupling reaction of C₁ species.

Concerning selectivity, different nature of the propyl radicals was studied to have different effect on selectivity. The n-propyl radicals desorb from the hBN surface favor formation of ethene and CO_x, while iso-propyl radicals are mainly generated during the gas-phase propagation and result in production of propene [56, 57, 68]. By using density functional theory, researchers also suggested that the tricoordinated B–OH could adsorb the oxygenated radicals under ODH conditions, for example, •OC₃H₇ and •OH, rather than alkyl radicals, for example, •C₃H₇, which effectively detained the alkoxy radicals on the surface and freed the alkyl radicals in the gas phase [76-78] and that is the reason for low selectivity to CO_x.

Nevertheless, the experimental results obtained during this study from observation of different characterization of the hBN catalyst under various range of experiments that was discussed during this chapter let us to disagree with some of the previous works and speculate a new pathway. With respect to the reports about how boron sites such as BO, BOH, BH, BOB, etc. are involved in the initiation stage and during the ODHP reaction, then the reaction rate would have to depend also on the amount of the catalyst and/or its specific surface, which is not quite the case as it was shown and discussed earlier. It is clear that the detected oxygenated boron species are not the decisive parameter to form the radicals via boron oxide on the hBN surface (at least for the initiating the reaction), but contrariwise, it seems that the oxygen and propane interaction in the gas-phase form radicals that attack the catalyst surface, and either form the products or generate in-situ boron oxide moieties which could enhance the extent of the reaction. To support this idea, it was shown that the empty reactor without catalyst exhibited some small activity in ODHP reaction. There is a research supporting this hypothesis and results, an old work reporting the reaction of propane and oxygen in the gas-phase taking place at temperature as low as 318 °C with product distribution similar to selectivity of the ODH reaction over hBN [79]. Furthermore, our results disclosed that the specific surface area, oxygen content and the amount of hBN catalyst do not play a critical role as far as the available free space is not influenced significantly, because in fact the reaction is driven by the residence time.

Additionally, the hBN catalyst was stable under oxidative atmosphere, therefore the reaction of surface with molecular oxygen is not probable at the reaction temperature. Moreover, it was seen that O₂ molecule was not adsorbed on the surface, monitored by MS, thus oxygen adsorption probably is in dissociative chemisorption pathway. According to this research, the free space role is to provide environment for radical propagation as the main driver of the reaction, and then those radicals could be terminated on the catalyst surface, as products such as propene, water, ethene and methane were desorbed even without presence of oxygen when they were continually detected by MS. Another possible role of hBN might be to terminate radicals on the catalyst surface that results in oxygenated moieties which could enhance the propane conversion.

As this complicated system has attracted increasing attention recently due to its high productivity but meanwhile with complex coupled surface-mediated gas-phase chemistry, there have been numerous controversial works that are confusing for any concrete conclusion. Therefore, this study tried to experimentally clarify the vague points and help to understand the real role of hBN between massive number of proposals, while still more investigations are going on by our group.

CONCLUSION

This thesis focused on a detailed investigation of three catalytic systems that are known to be active for (oxidative) dehydrogenation of light alkanes. Supported alkali chlorides and hBN were studied in the oxidative dehydrogenation of ethane and propane, respectively, while encapsulated Pd NPs within MFI, IPC-2, and IPC-4 zeolites were studied in direct dehydrogenation of propane. The aim was to gain a better understanding of their function, activity, selectivity, stability, physicochemical changes during the reaction, active sites, and involved phenomena. The crucial parameters that define the structural properties of the catalysts as well as the factors that could influence the catalytic behavior or possible deactivation were investigated and discussed in detail on the basis of complex characterization of the fresh and spent catalysts.

It is concluded that although the studied supported alkali chlorides exhibit high selectivity and productivity at relatively low temperature, which was also reported previously, this catalyst suffers from deactivation as a result of chlorine loss. Chlorine is removed from the catalyst in the form of chlorinated hydrocarbons such as chloromethane, ethyl chloride, and chloroethene. Therefore, due to the lack of chlorine, some chlorides convert to oxygenates, which results in the decrease in catalyst activity. The XRD analysis evidenced that MgCl_2 is more prone to exchange chlorine for oxygen, thus the activity of the catalyst is tightly connected with the presence of MgCl_2 . However, it seems that the generation of molten layer salt at the reaction temperature probably provides the conditions for chlorine lability.

Regarding the confinement of Pd NPs within MFI, IPC-2, and IPC-4 zeolites, the results showed that the new approaches used for the encapsulation of metal NPs provided a well distribution of Pd NPs and prevent sintering or leaching of the metal NPs under the reaction condition. Moreover, the encapsulation of metal NPs improved the rate of the desired product formation in all the catalysts compared to that of their impregnated counterparts. Furthermore, the intrinsic activity of Pd NPs with similar size was enhanced by their confinement. Therefore, it is concluded that besides the metal NP size, the activity of Pd NPs is also influence by their interactions with zeolitic support and the structure of pores and channels in the used zeolite. The larger size of metal NPs decrease the metal surface area which has a negative impact on the activity. Nevertheless, the size of zeolite channels, and the structure of the framework play a critical role in mass transfer with diffusion limitations and acceleration of the side reactions such as cracking which should be considered. The Pd NPs encapsulated within IPC-2 and IPC-4 exhibited higher productivity compared to Pd@MFI; nevertheless, it turned out that the ADOR approach, which was used for the encapsulation process of Pd@IPC-2 and Pd@IPC-4, is not a suitable method for zeolites with thin layers such as UTL. The low structural stability of IPC-2 and IPC-4 under the cyclic catalytic test and the tension caused by replacement of Pd NPs resulted in structural collapse.

In the last part, the study of hBN as a promising nonmetallic catalyst in oxidative dehydrogenation of propane revealed that, contrary to the previous reports, the boron oxide species detectable after the reaction do not play the key role. The catalytic activity and selectivity remain almost constant, while the catalyst crystalline phases, textural properties, and chemical composition undergo significant changes mainly due to the presence of oxygenated species within several hours of the reaction. Yet, the results obtained in this investigation revealed that the oxygen content does not control the reaction and in fact the gas-phase chemistry is the main driver in the oxidative dehydrogenation of propane over hBN. Thus, the available free space is a critical parameter because the residence time controls the radical formation/propagation in the gas phase. It could also be stated that the changes in the oxygen content of the catalyst are the result of interaction between activated oxygen in form of radicals and the hBN catalyst. According to our results we can hypothesize that one of the actual roles of hBN catalyst could be to terminate the generated radicals in the gas phase, and form the products. Also, it might result in formation of in situ oxygenated species that ultimately enhance formation of the products. On the other hand, the generated water in the gas phase also can be adsorbed on the hBN surface and produce oxygenated species which might participate in the reaction. Although a final precise mechanism cannot be proposed yet due to the complication of this system, but we have clarified that in contradiction with many reports in the literature, the initiation stage of the reaction in this system is not taking place on the surface of this catalyst, indeed it starts in the gas phase and then the surface contribution comes afterwards.

I believe that these findings helped fill the research gap and that they represent a valuable basis for further investigation of future catalysts as an efficient alternative to traditional catalysts in industrial olefin production as the vital globally required feedstock for chemical industries.

REFERENCES

1. Sattler, J.J.H.B., Ruiz-Martinez, J., Santillan-Jimenez, E., and Weckhuysen, B.M., *Catalytic dehydrogenation of light alkanes on metals and metal oxides*. Chemical Reviews, 2014. 114(20): p. 10613-10653.
2. Sheng, J., Yan, B., Lu, W.-D., Qiu, B., Gao, X.-Q., Wang, D., and Lu, A.-H., *Oxidative dehydrogenation of light alkanes to olefins on metal-free catalysts*. Chemical Society Reviews, 2021. 50: p. 1438-1468.
3. Carter, J.H., Bere, T., Pitchers, J.R., Hewes, D.G., Vandegehuchte, B.D., Kiely, C.J., Taylor, S.H., and Hutchings, G.J., *Direct and oxidative dehydrogenation of propane: from catalyst design to industrial application*. Green Chemistry, 2021. 23(24): p. 9747-9799.
4. Zhang, Y., Yao, W., Fang, H., Hu, A., and Huang, Z., *Catalytic alkane dehydrogenations*. Science Bulletin, 2015. 60(15): p. 1316-1331.
5. Grant, J.T., Venegas, J.M., McDermott, W.P., and Hermans, I., *Aerobic Oxidations of Light Alkanes over Solid Metal Oxide Catalysts*. Chemical Reviews, 2017. 118(5): p. 2769-2815.
6. James, O.O., Mandal, S., Alele, N., Chowdhury, B., and Maity, S., *Lower alkanes dehydrogenation: strategies and reaction routes to corresponding alkenes*. Fuel Processing Technology, 2016. 149: p. 239-255.
7. Liu, J., *Catalysis by supported single metal atoms*. ACS Catalysis, 2017. 7(1): p. 34-59.
8. Zhang, W., Wang, H., Jiang, J., Sui, Z., Zhu, Y., Chen, D., and Zhou, X., *Size dependence of Pt catalysts for propane dehydrogenation: from atomically dispersed to nanoparticles*. ACS Catalysis, 2020. 10(21): p. 12932-12942.
9. Campbell, C.T., *The energetics of supported metal nanoparticles: relationships to sintering rates and catalytic activity*. Accounts of Chemical Research, 2013. 46(8): p. 1712-1719.
10. Campbell, C.T., Parker, S.C., and Starr, D.E., *The effect of size-dependent nanoparticle energetics on catalyst sintering*. Science, 2002. 298(5594): p. 811-814.
11. Farmer, J.A. and Campbell, C.T., *Ceria maintains smaller metal catalyst particles by strong metal-support bonding*. Science, 2010. 329(5994): p. 933-936.
12. Liu, L. and Corma, A., *Metal catalysts for heterogeneous catalysis: from single atoms to nanoclusters and nanoparticles*. Chemical Reviews, 2018. 118(10): p. 4981-5079.
13. Sitja, G., Le Moal, S., Marsault, M., Hamm, G., Leroy, F., and Henry, C.R., *Transition from molecule to solid state: reactivity of supported metal clusters*. Nano letters, 2013. 13(5): p. 1977-1982.
14. Meier, D.C. and Goodman, D.W., *The influence of metal cluster size on adsorption energies: CO adsorbed on Au clusters supported on TiO₂*. Journal of the American Chemical Society, 2004. 126(6): p. 1892-1899.
15. Yudanov, I.V., Genest, A., Schauermaun, S., Freund, H.-J., and Rösch, N., *Size dependence of the adsorption energy of CO on metal nanoparticles: a DFT search for the minimum value*. Nano letters, 2012. 12(4): p. 2134-2139.
16. Lei, Y., Zhao, H., Rivas, R.D., Lee, S., Liu, B., Lu, J., Stach, E., Winans, R.E., Chapman, K.W., and Greeley, J.P., *Adsorbate-induced structural changes in 1–3 nm platinum nanoparticles*. Journal of the American Chemical Society, 2014. 136(26): p. 9320-9326.
17. Newton, M.A., Belder-Coldeira, C., Martínez-Arias, A., and Fernández-García, M., *Dynamic in situ observation of rapid size and shape change of supported Pd nanoparticles during CO/NO cycling*. Nature materials, 2007. 6(7): p. 528-532.
18. Ou, Z., Li, Y., Wu, W., Bi, Y., Xing, E., Yu, T., and Chen, Q., *Encapsulating subnanometric metal clusters in zeolites for catalysis and their challenges*. Chemical Engineering Journal, 2022. 430: p. 132925.

19. Zhang, Y., Li, A., Sajad, M., Fulajtárová, K., Mazur, M., Kubů, M., Shamzhy, M., Hronec, M., Bulánek, R., and Čejka, J., *Imidazolium-type ionic liquid-assisted formation of the MFI zeolite loaded with metal nanoparticles for hydrogenation reactions*. Chemical Engineering Journal, 2021. 412: p. 128599.
20. Farrusseng, D. and Tuel, A., *Perspectives on zeolite-encapsulated metal nanoparticles and their applications in catalysis*. New Journal of Chemistry, 2016. 40(5): p. 3933-3949.
21. Liu, L., Diaz, U., Arenal, R., Agostini, G., Concepcion, P., and Corma, A., *Generation of subnanometric platinum with high stability during transformation of a 2D zeolite into 3D*. Nature materials, 2017. 16: p. 132-138.
22. Gärtner, C.A., van Veen, A.C., and Lercher, J.A., *Oxidative Dehydrogenation of Ethane: Common Principles and Mechanistic Aspects*. ChemCatChem, 2013. 5(11): p. 3196-3217.
23. Ayari, F., Charrad, R., Asedegbega-Nieto, E., Mhamdi, M., Delahay, G., Farhat, F., and Ghorbel, A., *Ethane Oxidative Dehydrogenation over ternary and binary mixtures of alkaline and alkaline earth chlorides supported on zeolites*. Microporous and Mesoporous Materials, 2017. 250: p. 65-71.
24. Lin, R., Amrute, A.P., and Perez-Ramirez, J., *Halogen-mediated conversion of hydrocarbons to commodities*. Chemical Reviews, 2017. 117(5): p. 4182-4247.
25. Gärtner, C.A., van Veen, A.C., and Lercher, J.A., *Oxidative dehydrogenation of ethane on dynamically rearranging supported chloride catalysts*. Journal of the American Chemical Society, 2014. 136(36): p. 12691-12701.
26. Wang, S.B., Murata, K., Hayakawa, T., Hamakawa, S., and Suzuki, K., *Oxidative dehydrogenation of ethane over alkali metal chloride modified silica catalysts*. Energy & Fuels, 2000. 14(4): p. 899-903.
27. Li, M. and van Veen, A.C., *Selective production of ethylene via continuous oxidative dehydrogenation of ethane in (Dy₂O₃/MgO)-(Li-K) Cl composite membrane reactor*. Chemical Engineering Journal, 2019. 365: p. 344-350.
28. Zichittella, G., Luthi, J., Paunovic, V., and Perez-Ramirez, J., *Alkane Functionalization via Catalytic Oxychlorination: Performance as a Function of the Carbon Number*. Energy Technology, 2020. 8(8): p. 1900622.
29. Gaab, S., Find, J., Grasselli, R., and Lercher, J., *Oxidative ethane activation over oxide supported molten alkali metal chloride catalysts*. Studies in Surface Science and Catalysis, 2004, Elsevier. p. 673-678.
30. Tope, B., Zhu, Y., and Lercher, J.A., *Oxidative dehydrogenation of ethane over Dy₂O₃/MgO supported LiCl containing eutectic chloride catalysts*. Catalysis Today, 2007. 123(1-4): p. 113-121.
31. Gärtner, C.A., van Veen, A.C., and Lercher, J.A., *Highly selective supported alkali chloride catalysts for the oxidative dehydrogenation of ethane*. Topics in Catalysis, 2014. 57(14-16): p. 1236-1247.
32. Kristoffersen, H.H. and Metiu, H., *Chemistry of solvated electrons in molten alkali chloride salts*. The Journal of Physical Chemistry C, 2018. 122(34): p. 19603-19612.
33. Zichittella, G., Puértolas, B., Paunović, V., Block, T., Pöttgen, R., and Pérez-Ramírez, J., *Halogen type as a selectivity switch in catalysed alkane oxyhalogenation*. Catalysis Science & Technology, 2018. 8(8): p. 2231-2243.
34. Kristoffersen, H.H. and Metiu, H., *Molten LiCl layer supported on MgO: its possible role in enhancing the oxidative dehydrogenation of ethane*. The Journal of Physical Chemistry C, 2015. 119(16): p. 8681-8691.
35. Kumar, C.P., Gaab, S., Müller, T.E., and Lercher, J.A., *Oxidative dehydrogenation of light alkanes on supported molten alkali metal chloride catalysts*. Topics in Catalysis, 2008. 50(1-4): p. 156-167.
36. Gaab, S., Machli, M., Grasselli, R., and Lercher, J., *Oxidative dehydrogenation of ethane over novel Li/Dy/Mg mixed oxides: structure-activity study*. Topics in Catalysis, 2003. 23(1-4): p. 151-158.
37. Ueda, W., Lin, S.W., and Tohmoto, I., *Highly selective oxidative dehydrogenation of ethane to ethene over layered complex metal chloride oxide catalysts*. Catalysis Letters, 1997. 44(3-4): p. 241-245.

38. Wang, S., Murata, K., Hayakawa, T., Hamakawa, S., and Suzuki, K., *Lithium-chloride-promoted sulfated zirconia catalysts for the oxidative dehydrogenation of ethane*. *Catalysis Letters*, 1999. 59: p. 173-178.
39. Wang, Z., Chen, L., Zou, G., Luo, X., Gao, R., Chou, L., and Wang, X., *A novel BaCl₂-TiO₂-SnO₂ catalyst for the oxidative dehydrogenation of ethane*. *Catalysis Communications*, 2012. 25: p. 45-49.
40. Zichittella, G., Aellen, N., Paunović, V., Amrute, A.P., and Pérez-Ramírez, J., *Olefins from natural gas by oxychlorination*. *Angewandte Chemie International Edition*, 2017. 56(44): p. 13670-13674.
41. Leveles, L., Fuchs, S., Seshan, K., Lercher, J.A., and Lefferts, L., *Oxidative conversion of light alkanes to olefins over alkali promoted oxide catalysts*. *Applied Catalysis A: General*, 2002. 227(1-2): p. 287-297.
42. Conway, S.J. and Lunsford, J.H., *The oxidative dehydrogenation of ethane over chlorine-promoted lithium-magnesium oxide catalysts*. *Journal of Catalysis*, 1991. 131(2): p. 513-522.
43. Yu, F., Wu, X., Zhang, Q., and Wang, Y., *Oxidative dehydrogenation of ethane to ethylene in the presence of HCl over CeO₂-based catalysts*. *Chinese Journal of Catalysis*, 2014. 35(8): p. 1260-1266.
44. Weng, Q., Wang, X., Wang, X., Bando, Y., and Golberg, D., *Functionalized hexagonal boron nitride nanomaterials: emerging properties and applications*. *Chemical Society Reviews*, 2016. 45(14): p. 3989-4012.
45. Grant, J.T., Carrero, C.A., Goeltl, F., Venegas, J., Mueller, P., Burt, S.P., Specht, S.E., McDermott, W.P., Chieregato, A., and Hermans, I., *Selective oxidative dehydrogenation of propane to propene using boron nitride catalysts*. *Science*, 2016. 354(6319): p. 1570-1573.
46. Shi, L., Wang, D., Song, W., Shao, D., Zhang, W.P., and Lu, A.H., *Edge-hydroxylated Boron Nitride for Oxidative Dehydrogenation of Propane to Propylene*. *ChemCatChem*, 2017. 9(10): p. 1788-1793.
47. Grant, J.T., McDermott, W.P., Venegas, J.M., Burt, S.P., Micka, J., Phivilay, S.P., Carrero, C.A., and Hermans, I., *Boron and boron-containing catalysts for the oxidative dehydrogenation of propane*. *ChemCatChem*, 2017. 9(19): p. 3623-3626.
48. Venegas, J.M., McDermott, W.P., and Hermans, I., *Serendipity in catalysis research: Boron-based materials for alkane oxidative dehydrogenation*. *Accounts of Chemical Research*, 2018. 51(10): p. 2556-2564.
49. Shi, L., Wang, Y., Yan, B., Song, W., Shao, D., and Lu, A.-H., *Progress in selective oxidative dehydrogenation of light alkanes to olefins promoted by boron nitride catalysts*. *Chemical communications*, 2018. 54(78): p. 10936-10946.
50. Tian, J., Tan, J., Xu, M., Zhang, Z., Wan, S., Wang, S., Lin, J., and Wang, Y., *Propane oxidative dehydrogenation over highly selective hexagonal boron nitride catalysts: The role of oxidative coupling of methyl*. *Science Advances*, 2019. 5(3): p. eaav8063.
51. Kraus, P. and Lindstedt, R.P., *It's a gas: Oxidative dehydrogenation of propane over boron nitride catalysts*. *The Journal of Physical Chemistry C*, 2021. 125(10): p. 5623-5634.
52. Zhang, X., You, R., Wei, Z., Jiang, X., Yang, J., Pan, Y., Wu, P., Jia, Q., Bao, Z., and Bai, L., *Radical Chemistry and Reaction Mechanisms of Propane Oxidative Dehydrogenation over Hexagonal Boron Nitride Catalysts*. *Angewandte Chemie International Edition*, 2020. 59(21): p. 8042-8046.
53. Venegas, J.M., Zhang, Z., Agbi, T.O., McDermott, W.P., Alexandrova, A., and Hermans, I., *Why Boron Nitride is such a Selective Catalyst for the Oxidative Dehydrogenation of Propane*. *Angewandte Chemie International Edition*, 2020. 59(38): p. 16527-16535.
54. Venegas, J.M. and Hermans, I., *The influence of reactor parameters on the boron nitride-catalyzed oxidative dehydrogenation of propane*. *Organic Process Research & Development*, 2018. 22(12): p. 1644-1652.

55. Liu, Y., Liu, Z., Wang, D., and Lu, A.-H., *Suppressing Deep Oxidation by Detached Nano-sized Boron Oxide in Oxidative Dehydrogenation of Propane Revealed by the Density Functional Theory Study*. The Journal of Physical Chemistry C, 2022. 126(50): p. 21263-21271.
56. Liu, Y., Liu, Z., Lu, W.-D., Wang, D., and Lu, A.-H., *In Situ Generated Boron Peroxo as Mild Oxidant in Propane Oxidative Dehydrogenation Revealed by Density Functional Theory Study*. The Journal of Physical Chemistry Letters, 2022. 13: p. 11729-11735.
57. Zhang, Z., Tian, J., Wu, X., Surin, I., Pérez-Ramírez, J., Hemberger, P., and Bodi, A., *Unraveling Radical and Oxygenate Routes in the Oxidative Dehydrogenation of Propane over Boron Nitride*. Journal of the American Chemical Society, 2023. 145(14): p. 7910-7917.
58. Wang, S., Murata, K., Hayakawa, T., and Suzuki, K., *Oxidative Dehydrogenation of Ethane Over Zirconia-Supported Lithium Chloride Catalysts*. Chemical Engineering & Technology: Industrial Chemistry-Plant Equipment-Process Engineering-Biotechnology, 2000. 23(12): p. 1099-1103.
59. Wang, S., Murata, K., Hayakawa, T., Hamakawa, S., and Suzuki, K., *Performance of metal-oxide-promoted LiCl/sulfated-zirconia catalysts in the ethane oxidative dehydrogenation into ethene*. Catalysis Letters, 1999. 62: p. 191-195.
60. *Database of Zeolite Structures: <http://www.iza-structure.org/databases/>*.
61. Thommes, M., Kaneko, K., Neimark, A.V., Olivier, J.P., Rodriguez-Reinoso, F., Rouquerol, J., and Sing, K.S.W., *Physisorption of gases, with special reference to the evaluation of surface area and pore size distribution (IUPAC Technical Report)*. Pure and Applied Chemistry, 2015. 87(9-10): p. 1051-1069.
62. Shi, L., Wang, D., and Lu, A.-H., *A viewpoint on catalytic origin of boron nitride in oxidative dehydrogenation of light alkanes*. Chinese Journal of Catalysis, 2018. 39(5): p. 908-913.
63. Huang, R., Zhang, B., Wang, J., Wu, K.H., Shi, W., Zhang, Y., Liu, Y., Zheng, A., Schlögl, R., and Su, D.S., *Direct insight into ethane oxidative dehydrogenation over boron nitrides*. ChemCatChem, 2017. 9(17): p. 3293-3297.
64. Love, A.M., Thomas, B., Specht, S.E., Hanrahan, M.P., Venegas, J.M., Burt, S.P., Grant, J.T., Cendejas, M.C., McDermott, W.P., and Rossini, A.J., *Probing the transformation of boron nitride catalysts under oxidative dehydrogenation conditions*. Journal of the American Chemical Society, 2018. 141(1): p. 182-190.
65. Huang, M.T. and Ishida, H., *Surface study of hexagonal boron nitride powder by diffuse reflectance Fourier transform infrared spectroscopy*. Surface and Interface Analysis, 2005. 37(7): p. 621-627.
66. Tian, H., Liu, Y., and Xu, B., *Kinetic investigations of oxidative dehydrogenation of propane on boron oxide in confined spaces*. Catalysis Today, 2023. 420: p. 114048.
67. Li, H., Zhang, J., Wu, P., Xun, S., Jiang, W., Zhang, M., Zhu, W., and Li, H., *O₂ activation and oxidative dehydrogenation of propane on hexagonal boron nitride: mechanism revisited*. The Journal of Physical Chemistry C, 2019. 123(4): p. 2256-2266.
68. Nadjafi, M., Cui, Y., Bachl, M., Oing, A., Donat, F., Luongo, G., Abdala, P.M., Fedorov, A., and Müller, C.R., *On the Importance of Benchmarking the Gas-Phase Pyrolysis Reaction in the Oxidative Dehydrogenation of Propane*. ChemCatChem, 2023. 15(9): p. e202200694.
69. Altvater, N.R., Dorn, R.W., Cendejas, M.C., McDermott, W.P., Thomas, B., Rossini, A.J., and Hermans, I., *B-MWW Zeolite: The Case Against Single-Site Catalysis*. Angewandte Chemie International Edition, 2020. 132(16): p. 6608-6612.
70. Zhang, Z., Jimenez-Izal, E., Hermans, I., and Alexandrova, A.N., *Dynamic phase diagram of catalytic surface of hexagonal boron nitride under conditions of oxidative dehydrogenation of propane*. The Journal of Physical Chemistry Letters, 2018. 10(1): p. 20-25.
71. Tian, H. and Xu, B., *Oxidative co-dehydrogenation of ethane and propane over h-BN as an effective means for C-H bond activation and mechanistic investigations*. Chinese Journal of Catalysis, 2022. 43(8): p. 2173-2182.

72. Dorn, R.W., Cendejas, M.C., Chen, K., Hung, I., Altvater, N.R., McDermott, W.P., Gan, Z., Hermans, I., and Rossini, A.J., *Structure Determination of Boron-Based Oxidative Dehydrogenation Heterogeneous Catalysts With Ultrahigh Field 35.2 T 11B Solid-State NMR Spectroscopy*. ACS Catalysis, 2020. 10(23): p. 13852-13866.
73. McDermott, W.P., Cendejas, M.C., and Hermans, I., *Recent Advances in the Understanding of Boron-Containing Catalysts for the Selective Oxidation of Alkanes to Olefins*. Topics in Catalysis, 2020. 63: p. 1700-1707.
74. Tian, J., Collinge, G., Yuk, S.F., Lin, J., Glezakou, V.-A., Lee, M.-S., Wang, Y., and Rousseau, R., *Dynamically Formed Active Sites on Liquid Boron Oxide for Selective Oxidative Dehydrogenation of Propane*. ACS Catalysis, 2023. 13(12): p. 8219-8236.
75. Zhou, Y.L., Lin, J., Li, L., Pan, X.L., Sun, X.C., and Wang, X.D., *Enhanced performance of boron nitride catalysts with induction period for the oxidative dehydrogenation of ethane to ethylene*. Journal of Catalysis, 2018. 365: p. 14-23.
76. Gao, X., Liu, M., Huang, Y., Xu, W., Zhou, X., and Yao, S., *Dimensional Understanding of Boron-Based Catalysts for Oxidative Propane Dehydrogenation: Structure and Mechanism*. ACS Catalysis, 2023. 13: p. 9667-9687.
77. Liu, Z., Xu, D., Xia, M., Lu, W.-D., Lu, A.-H., and Wang, D., *Understanding the unique antioxidation property of boron-based catalysts during oxidative dehydrogenation of alkanes*. The Journal of Physical Chemistry Letters, 2021. 12(36): p. 8770-8776.
78. Liu, Z., Lu, W.-D., Wang, D., and Lu, A.-H., *Interplay of on-and off-surface processes in the B₂O₃-catalyzed oxidative dehydrogenation of propane: a DFT study*. The Journal of Physical Chemistry C, 2021. 125(45): p. 24930-24944.
79. Knox, J.H., *The gaseous products from the oxidation of propane at 318° C*. Transactions of the Faraday Society, 1960. 56: p. 1225-1234.

APPENDICES

Paper I:

Mehran Sajad, Oxidative dehydrogenation of propane over the boron-nitride catalysts, Scientific Papers of the University of Pardubice, Series A; Faculty of Chemical Technology, 26 (2020) 195–210.

Paper II:

Mehran Sajad, Roman Bulánek and Stanislav Šlang, Physico-Chemical Changes in the KCl-MgCl₂/La-FAU Composite Catalyst Induced by Oxidative Dehydrogenation of Ethane, Catalysts, 2021, 11 (3), 392. (IF: 3.9, Q2)

Paper III:

Yuyan Zhang, Ang Li, **Mehran Sajad**, Katarína Fulajtarová, Michal Mazur, Martin Kubů, Mariya Shamzhy, Milan Hronec, Roman Bulánek, Jiří Čejka, Imidazolium-type ionic liquid-assisted formation of the MFI zeolite loaded with metal nanoparticles for hydrogenation reactions, Chemical Engineering Journal, 412 (2021), 128599. (IF: 15.1, Q1)

Paper IV:

Mehran Sajad, Yuyan Zhang, Martin Kubů, Michal Mazur, Roman Bulánek, Jiří Čejka, Direct dehydrogenation of propane over Pd nanoparticles encapsulated within IPC zeolites with tunable pore sizes, Applied Materials Today, 29 (2022), 101644. (IF: 8.3, Q1)

Paper V:

Mehran Sajad, Roman Bulánek, Stanislav Šlang, Effect of the catalytic reactor arrangement and catalyst treatment in oxidative dehydrogenation of propane performance over hexagonal boron nitride, will be submitted in “Reaction Chemistry & Engineering”, (IF: 3.9, Q1)

Paper I

Oxidative dehydrogenation of propane over the boron-nitride catalysts

Mehran Sajad*

Department of Physical Chemistry, The University of Pardubice,
CZ–532 10 Pardubice, Czech Republic

Received: June 18, 2020; Accepted: August 17, 2020

Boron nitride (BN) has been found as a competitor for currently used catalysts employed in the oxidative dehydrogenation (ODH) of light alkanes, offering a high productivity of their transformation into olefins, low CO₂ emission, and thermal stability under the oxidative atmosphere. In this research, different BNs were synthesized by thermal treatment of different mixtures of precursors at different temperatures. For comparison, commercial BNs were tested as well. Catalytic behavior in propane ODH was investigated for the reaction mixture at atmospheric pressure. BN-based catalysts were characterized by powder XRD, SEM, EDS, XPS, Raman spectroscopy, and N₂-adsorption/desorption isotherms, in order to obtain details on crystallinity, morphology, surface chemistry, chemical analysis, textural properties, etc. The productivity obtained for the prepared catalysts reached 1.4 g_{olefins} h⁻¹ g_{cat}⁻¹, exhibiting higher values for the desired products, compared to the other studies with commercial products.

Keywords: Oxidative dehydrogenation of propane; Boron nitride; Catalyst; Propene

Introduction

Light olefins are one of the crucial feeds with high consumption in chemical industries, where global demands for these substances are rising every year due to their widespread use. Light olefins are usually produced by steam cracking of various feedstock containing a large portion of saturated hydrocarbons (such as naphtha, or LPG) that are broken down into smaller and often unsaturated,

* Corresponding author, ✉ mehran.sajad@student.upce.cz

hydrocarbons. This petrochemical process inevitably needs a very high temperature at around 800 °C, which means tremendous energy consumption. Fluid catalytic cracking (FCC) of heavy gas oil (a portion of crude oil with boiling point above 340 °C), is the second more frequently used process to produce olefins at about 540 °C but regeneration of the spent catalysts is carried out at temperature up to 760 °C. Current conventional processes for the olefin production suffer from numerous limitations related to their high energy necessities (endothermic reactions), coke formation, selectivity control, and thermodynamic constraints [1–6]. In such a condition, the formation of other light alkanes is unavoidable, therefore, to take advantage of the produced light alkanes and convert them into olefins that are more practical, a finding of an efficient catalyst is interesting for researchers at universities and in the industry. Except for high-temperature requirements, the substitution of fossil fuels by natural gas as another abundant source is nowadays also highly desirable for the olefin production [7] as a more ecological way.

For this purpose, the oxidative dehydrogenation is one of the most promising alternatives. ODH does not suffer from the drawbacks of traditional methods, as well as its nonoxidative competitor. As an exothermic process, ODH can overcome the thermodynamic limitations of the non-oxidative dehydrogenation by the formation of water, as a stable product. Moreover, ODH displays highly positive equilibrium constant, decreasing at higher temperatures. Furthermore, the presence of oxygen minimizes undesirable coking, thus extending the catalyst usage. Moreover, light paraffins ODH can be operated at lower temperatures than those of either the thermal or the non-oxidative catalytic dehydrogenation. Then, ODH can thus offer a potential increase in the yield and energy savings while producing the desired olefins, even though a valuable product — hydrogen — is burned [6,8,9]. Approximately, up to 45 % of energy can be saved if the dehydrogenation (DH) process is substituted by ODH, for propane [10,11]. The reaction of the ODH type has been extensively studied by metal oxide-based catalysts [7,12–14]. But there remains left the most difficult challenge, which is an over-oxidation to CO_x because this reaction is more thermodynamically favorable, olefins are more reactive and as a consequence, the over-oxidation by metal oxide-based catalysts decreases the olefin selectivity [11,15]. For example, in the case of propane, the reaction enthalpies of ODH and most frequent accompanying reactions are [16]:



Vanadium and molybdenum-based catalysts were frequently studied for ODH, but they suffer from poor selectivity at conversion higher than 20 % [17]. Moreover, the catalysts based on alkali chlorides, another group of catalysts investigated for ODH reactions, have shown a high tendency to deactivate [18]. Yet another choice is a carbon material as a metal-free catalyst.

But it shows a very low reaction rate for ethane and propane conversion at the temperature lower than 500 °C, and at higher temperatures, carbon materials are not stable due to oxidation [1]. Carbon nanotubes have also been tested for this reaction, exhibiting a very low degree of propane conversion of about 5 %, while it is not appropriate to be used at a higher temperature in presence of oxygen [17].

Boron nitride (BN) is an analogue of graphene predominantly used for its electronic, thermoelectric, and mechanical properties and applicable also as special final products (so far, for instance, fillers, insulators, or lubricants [19]). Recently, BN has been showing significant catalytic activity in the ODH reaction [1,11,15]. The BN-based catalyst produces propene as the main product and ethylene as a by-product which is more desired than CO_x. Recently, a couple of research groups reported their work on this catalyst [11,16,17,20,21], among others, Herman's group proposed it for a 14% propane conversion over a hexagonal BN catalyst with 79% selectivity to propylene and 12% to ethylene. It is supposed that oxygen bonded to boron and nitrogen in an armchair edge, behaves as an active site in ODH.

It has been suggested that dehydrogenation starts with the withdrawal of the hydrogen atom from the secondary carbon of propane by the active sites, followed by breaking the O-O bond and the subsequent formation of B-OH and one nitroxyl radical. In a subsequent step, water desorption regenerates the active site (B-O-O-N). Apparently, this behavior distinguishes BN from traditional metal oxide-supported catalysts with Mars-van Krevelen mechanism [11]. Also, the hydroxylated h-BN, prepared by targeted modification of h-BN by treatment in the sodium-assisted high-temperature steam activation process, has been reported as an efficient catalyst for propane ODH, with high selectivity of around 80 % at 20% conversion and releasing a negligible amount of CO₂ [1].

It is another proof about BN's ability to suppress over-oxidation to CO₂ which has always been a negative aspect of this reaction. Later, Grant et al. have reported that the boron-containing materials, namely (B₄C), (TiB₂), (NiB), (Co₂B/Co₃B), (HfB₂), (WB), and the elemental boron itself, are active for the ODH of propane when showing the same product trends as boron nitride [22]. Therefore, it was concluded that boron was the necessary element to achieve the high olefin selectivity. Based on the results from X-ray photoelectron and IR-spectroscopy, they suggested the formation of an analogous surface-stabilized BO_x active site for all the boride catalysts tested. This observation contradicts the previous mechanistic hypotheses postulating that edge sites on the boron nitride would be the active ones [17].

In this paper, attention was focused on the study of physicochemical changes in the BN structure during the catalytic reaction. For this purpose, selected samples of both commercial h-BN and laboratory-prepared boron-based materials were subjected to chemical, structural, and textural characterization both before application in ODH propane and after 4 hours under reaction conditions (at 490 °C in a reaction mixture stream containing C₃H₈/O₂/He = 30/15/55 vol. %). Subsequent comparison of the information obtained has revealed that oxygen-containing boron species are the functional active sites and, unlike the reported data in the literature, the active sites are available not only at the edges and at the surface of BN, but chemical changes take also place inside the bulk of BN, showing that the B-O bond plays more crucial role than that of the B-N bond for ODH of propane.

Materials and methods

Catalysts

This research was focused on a set of samples, comprising two commercial BNs and three synthesized specimens; all being analyzed by different methods. h-BN was purchased from Sigma-Aldrich (purity: 98%, particle size: 1 μm), and Np-BN was acquired from Alfa Aesar (particle size: 5–20 nm). The BN (550) was prepared at 550 °C using the following procedure: 3.71 g boric acid + 3.78 g melamine were thoroughly mixed in 100 mL distilled water under stirring at 85 °C, giving rise, after evaporation, to a white solid. This product was dried at 85 °C for 12 h and, afterward, calcinated in a quartz crucible inside a furnace at the rate of 3 °C min⁻¹ up to 550 °C in the flow of N₂ (100 L h⁻¹) for 3 h and, finally, cooled down in ambient air [23]. BN (1050) and BN (1050 M) were prepared with the same method but differing in the precursors used. In typical synthesis, two mixtures of urea and boric acid were mutually mixed and ground. In BN (1050 M), melamine was also added to the boric acid and urea, as a secondary source of nitrogen. The molar ratio of urea-to-boric acid was 5 : 1, while that of melamine to boric acid remained 1 : 1. The prepared mixtures were placed in an alumina boat-shaped crucible and heated up to 1050 °C (10 °C min⁻¹) in the stream of N₂ gas with 50 mL min⁻¹ flow rate. The temperature was held at 1050 °C for 3.5 hours, and the furnace then allowed to cool naturally, again, under the atmosphere of N₂ [24]. The prepared catalysts and their labels are shown in Table 1.

Catalytic behavior of each sample in propane ODH was investigated in plug-flow fixed-bed tubular shape reactor, using 100 mg of catalyst at 490 °C under atmospheric pressure with WHSV = 7.1 h⁻¹, in a reaction mixture consisting of C₃H₈/O₂/He = 30/15/55 % (v/v). Before each test, the sample was pretreated by He (11 mL min⁻¹) at 490 °C for 2 h. The U-shape reactor used in this study had an inner diameter of 5 mm. Products were analyzed with an on-line gas chromatograph (Agilent Technologies, Palo Alto, CA, USA) coupled with a flame

ionization detector (GC-FID mode) and a thermal conductivity detector (GC-TCD). The Carboxen[®] 1000 column (60 m long with a diameter of 320 μm) was used for the separation of compounds. The injector and oven temperature was 150 $^{\circ}\text{C}$ and the detector temperature in the GC-TCD mode 270 $^{\circ}\text{C}$. Helium was used as carrier gas with a flow rate of 3 mL min^{-1} .

Table 1 Prepared catalysts and their specification

Sample	Label / type	Product number	Precursors, molar ratio
Hexagonal BN (Sigma Aldrich)	h-BN	255475	–
Nanopowder BN (Alfa Aesar)	Np-BN	44999	–
BN prepared at 550 $^{\circ}\text{C}$	BN (550)	–	boric acid : melamine 2 : 1
BN prepared at 1050 $^{\circ}\text{C}$	BN (1050)	–	boric acid : urea 1 : 5
BN prepared at 1050 $^{\circ}\text{C}$	BN (1050 M)	–	boric acid : urea : melamine 1 : 5 : 1

Characterization

Adsorption-desorption isotherms of nitrogen at -196 $^{\circ}\text{C}$ were measured using an ASAP 2020 instrument. Before each adsorption measurement, the sample was degassed to attain a slow removal of pre-adsorbed water at low temperatures. The temperature was slowly increased with a slope of 0.5 $^{\circ}\text{C min}^{-1}$ up to 110 $^{\circ}\text{C}$ and then 1 $^{\circ}\text{C min}^{-1}$ until 250 $^{\circ}\text{C}$. The sample was degassed at this temperature under a turbo molecular vacuum pump for 8 h. X-ray powder diffraction data were recorded on a D8 X-ray powder diffractometer (Bruker; Karlsruhe, Germany) equipped with a graphite monochromator and a position-sensitive detector (Vantec-1) using Cu $K\alpha$ radiation (at 40 kV and 30 mA) in Bragg–Brentano geometry. The surface chemical state of the samples was monitored by an X-ray photoelectron spectroscopy (XPS, model ESCA2SR; Scienta-Omicron; Uppsala, Sweden) using a monochromatic Al $K\alpha$ X-ray source (with 1486.7 eV). The binding energy scale was referred to appendant carbon (284.8 eV). The quantitative elemental composition of the surface was further evaluated using a scanning electron microscope (LYRA 3; Tescan, Brno, Czech Republic) equipped with an EDS analyzer (model AZtec X-Max 20; Oxford Instruments, High Wycombe, UK) at an acceleration voltage of 20 kV. Raman spectra were recorded by using a Nicolet DXR SmartRaman spectrometer (Thermo Fisher Scientific, Waltham, MA, USA) equipped with a 532 nm laser and 10 mW power. All the measurements were carried out at ambient conditions using finely ground samples without dilution. The spectrum was recorded by an accumulation of 300 scans with integration time 1 s, between 50–3300 cm^{-1} using the Omnic Software package.

Results and discussion

All the prepared BN-based catalysts exhibited stable catalytic activity in propane ODH for more than 200 min, without showing any deactivation tendency (Fig. 1). However, the individual catalysts had differed in the activity. After 25 min under the stream, BN (1050) and (1050 M) samples revealed a capability to convert propane from around 50 % with the highest production value for the propene and ethene, $1.4 \text{ g}_{\text{olefin}} \text{ h}^{-1} \text{ g}_{\text{cat}}^{-1}$ despite low selectivities (cf. Table 2). The BN (550) demonstrated significantly lower efficiency, reaching approx. 31% conversion, besides similar propene and olefin productivity with h-BN. Even though the propene productivity of all the catalysts was comparable (except Np-BN), but the olefin productivity of BN (1050) and (1050 M) had reached higher values than those for commercial BNs.

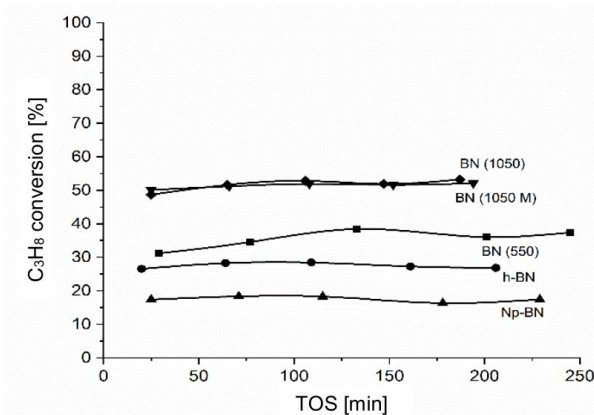


Fig. 1 Propane conversion as a function of time on stream (TOS) in ODH reaction at 490 °C in the flow of 20 mL min^{-1} of the mixture consisting of $\text{C}_3\text{H}_8/\text{O}_2/\text{He} = 30/15/55 \%$ (v/v)

Table 2 Propane conversion, selectivity, and productivity of the catalysts at TOS = 25 min

Sample	Propane conversion [%]	Productivity		Selectivity [%]					
		$[\text{g}^{\text{a}} \text{ h}^{-1} \text{ g}_{\text{cat}}^{-1}]$	$[\text{g}^{\text{b}} \text{ h}^{-1} \text{ g}_{\text{cat}}^{-1}]$	C_3H_6	C_2H_4	C_2H_6	CH_4	CO_2	CO
h-BN	26.6	0.9	1.1	51.2	11.8	0.4	1.8	1.1	14.5
Np-BN	17.4	0.7	0.8	63.1	10	0.4	1.4	0.8	0
BN (550)	31.1	0.9	1.1	44.7	10.3	0.3	1.6	3.4	9.9
BN (1050)	48.7	0.9	1.4	28.4	19	1.3	8.1	0	15.2
BN (1050 M)	50.1	0.9	1.3	26.2	19.9	1.6	9.5	0	14.8

^a propene; ^b propene + ethene

The limit value below which the productivity is too low to be interesting for commercial applications is $1 \text{ g}_{\text{olefin}} \text{ h}^{-1} \text{ g}_{\text{cat}}^{-1}$ [13]. The selectivity varies by time on stream for different catalysts (e.g. for different steady-state propane conversions; Fig. 2). The degree of the CO_2 selectivity was kept negligible, below 3.4 % but the CO selectivity showed a wider range from 0 to 15.2 % for a product studied (Fig. 3). The methane and ethane selectivity changed between 1.4–9.5 % and 0.3–1.6 %, respectively. A relatively high production of methane has indicated a non-negligible rate of cracking reaction. For simplicity, in Table 2, the number of unknown by-products is not mentioned.

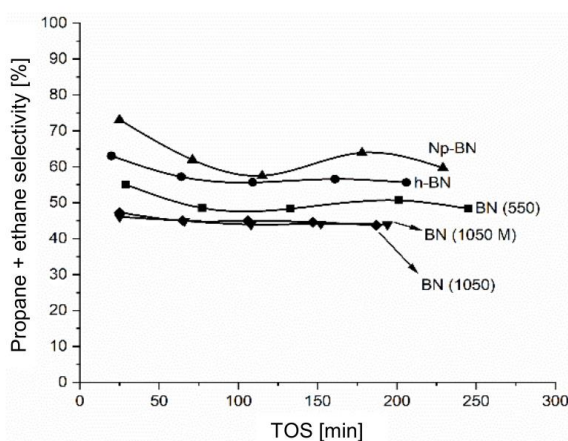


Fig. 2 Propene and ethene selectivity as a function of TOS at 490 °C in the flow of 20 mL min^{-1} of the mixture consisting of $\text{C}_3\text{H}_8/\text{O}_2/\text{He} = 30/15/55 \%$ (v/v)

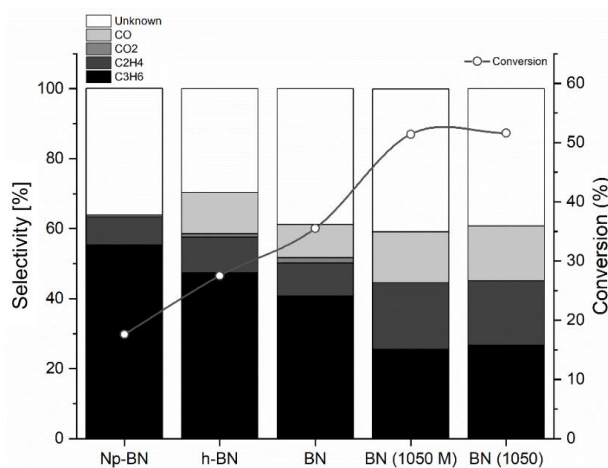


Fig. 3 Average conversion and selectivity for all the products after propane ODH at 490 °C in the flow of 20 mL min^{-1} of the mixture consisting of $\text{C}_3\text{H}_8/\text{O}_2/\text{He} = 30/15/55 \%$ (v/v)

Textural properties of the samples were studied to obtain the BET surface area and porosity of the catalysts. The surface area varied widely from 3, 8, 34, 46 for BN (550), BN (1050 M), BN (1050), h-BN up to 200 m² g⁻¹ for Np-BN. Followed by N₂ adsorption-desorption isotherms depicting the macroporosity for Np-BN based on the IUPAC isotherms of the type II (Fig. 4), h-BN also showed macro/mesopore structure. In contrast, non-commercial samples exhibited almost non-porous textural properties. After the ODH reaction, catalysts have revealed a high decrease in surface area (Fig. 5), for instance, h-BN, Np-BN, and BN (1050M) exhibited 17, 2, and 2 m² g⁻¹ correspondingly. Clearly, all the catalysts showed similarly a very low surface area for the spent samples, indicating quite distinct changes in the structure and morphology. It should be mentioned that catalytic activity did not change during the time of reaction, thus, it can be suggested that the change in surface area is very fast and has happened entirely immediately after starting the reaction or the surface area is not a determinative factor being able of controlling the activity and productivity of the catalysts.

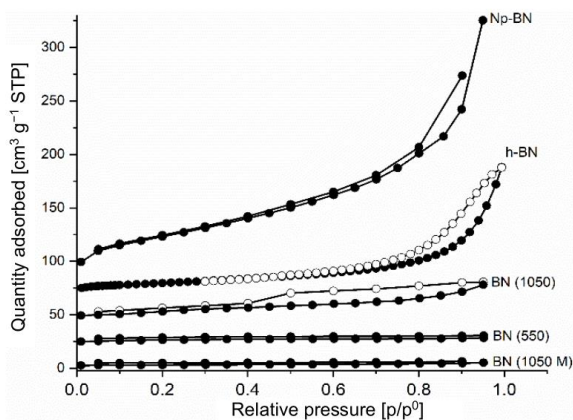


Fig. 4 N₂ adsorption-desorption isotherms of BN samples

Isotherms are shifted along the y-axis by an increment of 25 cm³ g⁻¹

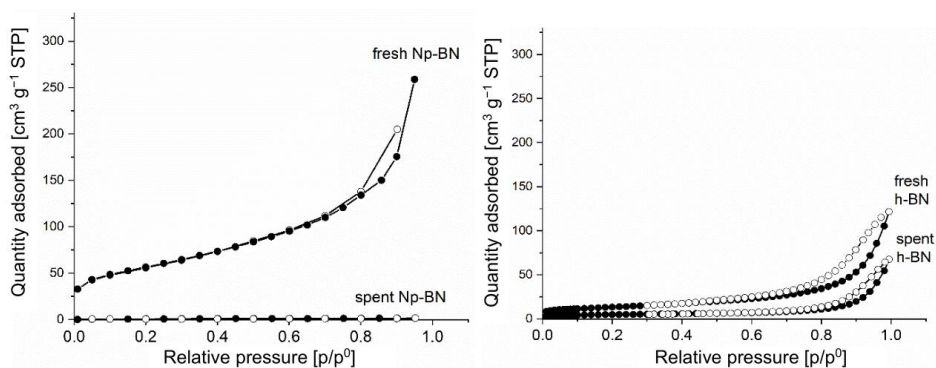


Fig. 5 Comparison of N₂ adsorption-desorption isotherms of Np-BN and h-BN samples before and after the reaction

The crystallinity and structure of BNs were investigated by the X-ray diffraction (see Fig. 6). Commercial h-BN, as expected, had shown typical hexagonal structure, whereas Np-BN and BN (550) were of amorphous structure. BNs (1050) and (1050 M) exhibited both a similar structure with broad peaks showing smaller crystallite size compared to h-BN, as the peak width is inversely proportional to crystallite size. The difference in the structure after the ODH reaction is well illustrated in Fig. 7. An appearance of few new peaks, related to the BOx compound after ODH reaction was a sign of such a difference.

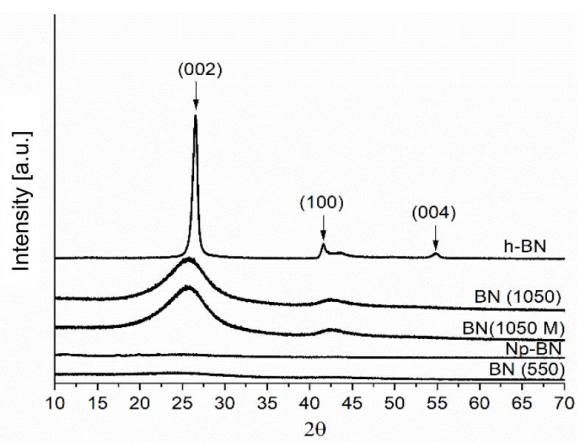


Fig. 6 X-ray diffraction pattern of BN catalysts

Diffraction patterns are shifted along the y -axis by an increment of 2000 a.u.

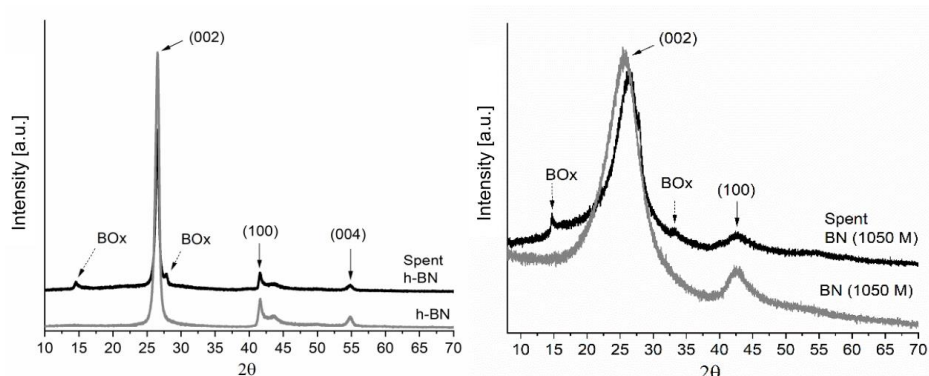


Fig. 7 X-ray diffraction pattern of h-BN (top panel) and BN (1050 M) (bottom panel), before and after ODH of propane

Diffraction pattern of h-BN is shifted along the y -axis by an increment of 1500 a.u.

The most convincing evidence of chemical changes in BN is the result of EDS analysis (Table 3). The data measured for chemical composition present a big difference in the atomic percentage of the oxygen content for the samples studied. h-BN exhibited almost stable atomic ratio of boron and nitrogen, with an increase in the post-reaction oxygen content. Np-BN was not as stable as the other commercial sample. Fresh Np-BN has already gotten a lower amount of nitrogen and a higher content of oxygen; nevertheless, the spent sample showed a large rise in the oxygen content besides removing a large amount of nitrogen. In the other hand, fresh BN (1050 M) gaining a ratio of B : N almost 1 : 1 and, in addition, 20 at. % of oxygen ($O/B = 0.5$), as the corresponding catalyst had reached one of the highest productivity for propene and ethene, and it was therefore considered as a representative for synthesized catalysts.

Table 3 The ratio between the atomic percentage of the elements by EDX

Sample	Fresh				Spent			
	B	N	O	C	B	N	O	C
h-BN	1	1	0	0	1	0.9	0.3	0
Np-BN	1	0.5	0.4	0.1	1	0.1	0.9	0.1
BN (550)*	1	1	1.1	0.4	–	–	–	–
BN (1050)*	1	0.9	0.4	0.2	–	–	–	–
BN (1050 M)	1	0.9	0.5	0.3	1	0.5	1.1	0.4

* no available data for spent samples

Mostly, the amount of carbon was preserved for the spent samples. It seems that the role of oxygen in the enhancement of productivity is about to form BO_x species, but not always via the increase of its amount because, in the case of BN (550), a very high amount of oxygen (31 at. %) was detected whereas its activity was lower than those for BN (1050) and (1050 M), and this phenomenon needs to be more investigated.

The results obtained by X-ray photoelectron spectroscopy analysis of the samples illustrate the different oxygen content, for example in case of fresh h-BN (Fig. 9), the ratio between the elements was found to be $B/N/O = 1/1/0.1$, which means that oxygen was acting at the surface of the fresh sample from the beginning, compared to the EDX results without oxygen detection in the bulk, due to differences in the depth of the surface of the material from which the information about composition could be obtained. The XPS data for the spent h-BN sample showed a lower oxygen content in the surface than bulk measured by EDX, $B/N/O = 1/0.9/0.2$. As a result, the B-O active sites were not formed only in the edges of the layers, and they also existed inside the bulk. This was a finding that did not correspond to the previous works reported in the literature.

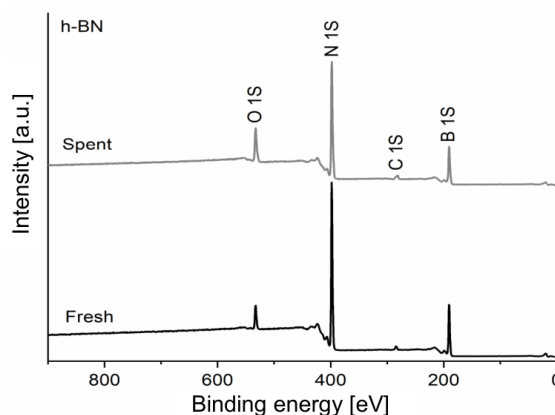


Fig. 9 XPS results for fresh and spent h-BN
Shifted along the y -axis by an increment of 124000 a.u.

Accordingly to the literature [1,11,20–21,26], it has been observed in this research that the oxygen-containing boron species on the surface of boron nitride and also inside the layers, seem to be one of the hot candidates for the active sites of BN-based materials in the ODH reaction of light alkanes. A new and a relatively simple reaction pathway proposing a redox reaction cycle based on B-OH sites [21], can be applied here as well, for the ODH of propane. The B-OH sites initially react with molecular oxygen, leading to the B–O–O–B intermediates (oxidation step) that further withdraw the hydrogen atoms from the alkane, then forming an olefin and water (reduction step), and finally rearranging into the B–OH sites with the participation of water. This mechanism can meet a majority of the experimental facts reported by different research groups [11,20,21]. Thus, maximization of the number of OH-containing boron sites is considered to be the most effective pathway to improve the catalytic activity of the ODH reaction. In one hand, a combination of X-ray photoelectron spectroscopy (XPS) and energy-dispersive X-ray spectroscopy (EDS) measurements showed the emergence of the B–O functional groups for the increased activity of BN material in the ODHP reaction, but in second hand, the incorporation of oxygen takes place also in the bulk and not only in the surface layer.

In order to complete the picture of changes in catalysts during the reaction, micrographs of catalyst surfaces before and after the reaction, the SEM imaging was performed and the results presented here in Fig. 10. The morphology of all the catalysts changed after the ODH reaction compared to the fresh ones. A molten layer was formed on the surface of the spent catalyst, which is in accordance with N_2 adsorption-desorption isotherms and a low BET surface area for spent catalysts.

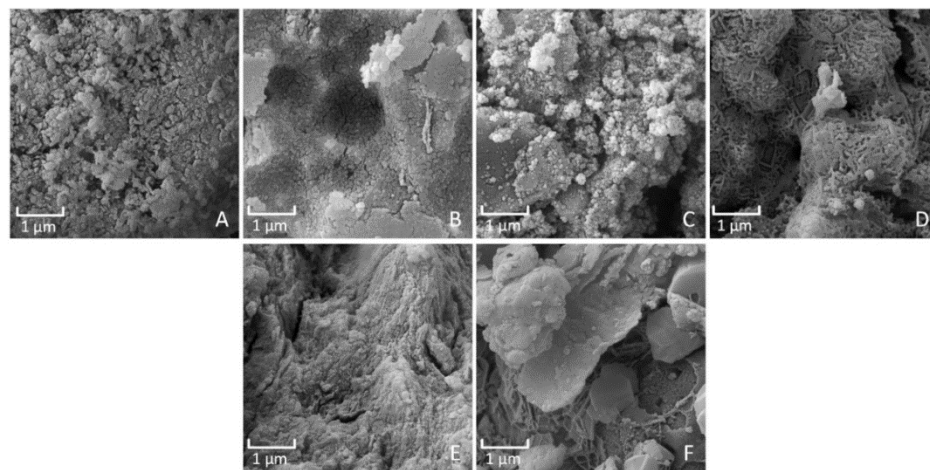


Fig. 10 SEM images of A. fresh h-BN, B. spent h-BN, C. fresh Np-BN, D. spent Np-BN, E. fresh BN (1050 M), F. spent BN (1050 M)

It seems that the formation of new compounds, i.e. boron oxide (BO_x) species on the surface just after started reaction, has changed the morphology and the catalysts then work differently based on available active sites. This interpretation is also in agreement with XRD patterns about the formation of BO_x species and the EDS results for different compositions after the propane ODH.

A comparison between the productivity of different boron nitride- and boron-based catalysts with traditional ODH catalysts reported in the literature [11,18,22,25–28], could be useful to build a new mindset about this type of catalyst (see Table 4).

Table 4 The productivity of BNs and other types of known catalysts used for propane ODH

Catalyst	Productivity [g _{propene} h ⁻¹ g _{cat} ⁻¹]	Ref.	Catalyst	Productivity [g _{propene} h ⁻¹ g _{cat} ⁻¹]	Ref.
h-BN	0.92	This work	BNOH *	5.9	[26]
Np-BN	0.74	This work	hBN	0.4	[22]
BN (550)	0.94	This work	NiB	0.5	[22]
BN (1050)	0.93	This work	TiB ₂	0.6	[22]
BN (1050 M)	0.89	This work	B ₄ C	0.65	[22]
hBN	0.75	[11]	(V ₂ O ₅ /ZrO ₂)	0.29	[27]
BNNT	0.6	[11]	(V ₂ O ₅ /TiO ₂)	0.21	[27]
BN	0.06	[17]	(Mg-Dy-Li)	0.14	[18]
B/SiO ₂	1.04	[28]	(Mg-Dy-Li-Cl)	0.12	[18]
B ₂ O ₃ /SBA-15	1.82	[25]			

* Measured at 530 °C

The propene productivity of different BNs in this work had varied between 0.89 to 0.94 $\text{g}_{\text{propene}} \text{h}^{-1} \text{g}_{\text{cat}}^{-1}$, which was at least three times higher than the well-known transition metal supported and alkali chloride catalysts. A report on the $\text{B}_2\text{O}_3/\text{SBA-15}$ [25] quotes a propene productivity at 500 °C being higher than the others, around 1.8 $\text{g}_{\text{propene}} \text{h}^{-1} \text{g}_{\text{cat}}^{-1}$, which has verified data in this research showing on the importance of BO_x compared to the B-N bond.

Conclusions

In this research, an investigation on different BNs for the ODH reaction of propane has been reported. The BNs prepared showed productivity as high as 1.4 $\text{g}_{\text{olefin}} \text{h}^{-1} \text{g}_{\text{cat}}^{-1}$ through propene and ethene, even higher than that of commercial BN. In general, BN's productivity is more promising in the industrial scale compared to the conventional transition metal oxide-based catalysts.

The study has revealed that the O-containing boron sites generated in the catalysts during the reaction are decisive for the unique catalytic function in the ODH reaction. A deeper characterization of the spent catalysts has revealed that boron nitride is subject to significant chemical and morphological changes which are not limited to the surface layer, but also indicate a deep penetration into the volume of the particles. These changes have led to a significant increase in the oxygen content and a decrease in the nitrogen content. It is hypothesized that some boron oxide-like phase or species are being formed. Thus, the findings reported here indicate that BO_x moieties could be responsible for the catalytic activity. It is suggested to obtain more experimental material on the BO_x species formed on the surface and inside the bulk, which controls the activity. In overall, from the viewpoints of activity, selectivity, and stability, there is still a lot to improve in the catalytic efficiency of boron-based catalyst in the ODH reaction. This newly developed catalyst system not only opens up a research direction of metal-free catalysts in selective cleavage of C-H bonds of alkanes, but it can also enrich our fundamental understanding of active sites of this type of non-metallic catalysts.

Acknowledgments

This work was supported by the Ministry of Education, Youth, and Sports for financial grant under project No. SGS 2020008. The XPS, SEM, and furnace facilities at CEMNAT institute were employed in this study, when financial support under project LM2018103 is also highly acknowledged. Furthermore, Filip Dvořák and Jhonatan Rodriguez Pereira are kindly acknowledged for their

help with the measurement of XPS, Stanislav Šlang for SEM and EDX analyses, Max Fraenkl for materials synthesis, Ludvik Benes for XRD, and Helena Drobná for Raman spectroscopy experiments.

Last but not least, my special thanks belong also to Roman Bulánek from the Department of Physical Chemistry, the University of Pardubice for his assistance during the entire study.

References

- [1] Shi L., Yan B., Shao D., Jiang F., Wang D., Lu A.-H.: Selective oxidative dehydrogenation of ethane to ethylene over a hydroxylated boron nitride catalyst. *Chinese Journal of Catalysis* **38** (2017) 389–395.
- [2] Gärtner C.A., van Veen A.C., Lercher J.A., Oxidative dehydrogenation of ethane: Common principles and mechanistic aspects. *ChemCatChem*. **5** (2013) 3196–3217.
- [3] Bodke A., Olschki D.A., Schmidt L.D., Ranzi E.: High selectivities to ethylene by partial oxidation of ethane. *Science* **285** (1999) 712–715.
- [4] Sattler J.J.H.B., Ruiz-Martinez J., Santillan-Jimenez E., Weckhuysen B.M.: Catalytic dehydrogenation of light alkanes on metals and metal oxides. *Chemical Reviews* **114** (2014) 10613–10653.
- [5] Vogt E., Weckhuysen B.: Fluid catalytic cracking: recent developments on the grand old lady of zeolite catalysis. *Chemical Society Reviews* **44** (2015) 7342–7370.
- [6] Al-Ghamdi S., Volpe M., Hossain M.M., de Lasa H.: VO_x/c-Al₂O₃ catalyst for oxidative dehydrogenation of ethane to ethylene: Desorption kinetics and catalytic activity. *Applied Catalysis A: General* **450** (2013) 120–130.
- [7] Grant J.T., Venegas J.M., Venegas J.M., McDermott W.P., Hermans I.: Aerobic oxidations of light alkanes over solid metal oxide catalysts. *Chemical Reviews* **118** (2018) 2769–2815.
- [8] Grabowski R.: Kinetics of oxidative dehydrogenation of C₂-C₃ alkanes on oxide catalysts. *Catalysis Reviews* **48** (2006) 199–268.
- [9] Bhasin M.M., McCain J.H., Vora B.V., Imai T., Pujadó P.R.: Dehydrogenation and oxydehydrogenation of paraffins to olefins. *Applied Catalysis A: General* **221** (2001) 397–419.
- [10] Rightor E.G., Tway C.L.: Global energy & emissions reduction potential of chemical process improvements. *Catalysis Today* **258** (2015) 226–229.
- [11] Grant J.T., Carrero C.A., Goeltl F., Venegas J., Mueller P., Burt S.P., Specht S.E., McDermott W.P., Chierigato A., Hermans I.: Selective oxidative dehydrogenation of propane to propene using boron nitride catalysts. *Science* **354** (2016) 1570–1573.
- [12] Bulánek R., Čičmanec P., Sheng-Yang H., Knotek P., Čapek L., Setnička M.: Effect of preparation method on nature and distribution of vanadium species in vanadium-based hexagonal mesoporous silica catalysts: Impact on catalytic behavior in propane ODH. *Applied Catalysis A: General* **415** (2012) 29–39.

- [13] Cavani F., Ballarini N., Cericola A.: Oxidative dehydrogenation of ethane and propane: How far from commercial implementation? *Catalysis Today* **127** (2007) 113–131.
- [14] Bulánek R., Kalužová A., Setnička M., Zukal A., Čičmanec P., Mayerová J.: Study of vanadium based mesoporous silicas for oxidative dehydrogenation of propane and n-butane. *Catalysis Today* **179** (2012) 149–158.
- [15] Gärtner C.A., van Veen A.C., Lercher J.A., Oxidative dehydrogenation of ethane on dynamically rearranging supported chloride catalysts. *Journal of the American Chemical Society* **136** (2014) 12691–12701.
- [16] Tian J., Lin J., Xu M., Wan S., Lin J., Wang Y.: Hexagonal boron nitride catalyst in a fixed-bed reactor for exothermic propane oxidation dehydrogenation. *Chemical Engineering Science* **186** (2018) 142–151.
- [17] Chaturbedy P., Ahamed M., Eswaramoorthy M.: Oxidative dehydrogenation of propane over a high surface area boron nitride catalyst: Exceptional selectivity for olefins at high conversion. *ACS Omega* **3** (2018) 369–374.
- [18] Leveles L., Fuchs S., Seshan K., Lercher J.A., Lefferts L.: Oxidative conversion of light alkanes to olefins over alkali promoted oxide catalysts. *Applied Catalysis A: General* **227** (2002) 287–297.
- [19] Lin Y., Connell J.W.: Advances in 2D boron nitride nanostructures: nanosheets, nanoribbons, nanomeshes, and hybrids with graphene. *Nanoscale* **4** (2012) 6908–6939.
- [20] Shi L., Wang Y., Yan B., Song W., Shao D., Lu A.-H.: Progress in selective oxidative dehydrogenation of light alkanes to olefins promoted by boron nitride catalysts. *Chemical Communications* **54** (2018) 10936–10946.
- [21] Shi L., Wang D., Lu A.-H.: A viewpoint on catalytic origin of boron nitride in oxidative dehydrogenation of light alkanes. *Chinese Journal of Catalysis* **39** (2018) 908–913.
- [22] Grant J.T., McDermott W.P., Venegas J.M., Burt S.P., Micka J., Phivilay S.P., Carrero C.A., Hermans I.: Boron and boron-containing catalysts for the oxidative dehydrogenation of propane. *ChemCatChem* **9** (2017) 3623–3626.
- [23] Liu T., Li Y.-L., He J.-Y., Hu Y., Wang C.-M., Zhang K.-S., Huang X.-J., Kong L.-T., Liu J.-H.: Porous boron nitride nanoribbons with large width as superior adsorbents for rapid removal of cadmium and copper ions from water. *New Journal of Chemistry* **43** (2019) 3280–3290.
- [24] Marchesini S., McGilvery C.M. Bailey, J., Petit C.: Template-free synthesis of highly porous boron nitride: insights into pore network design and impact on gas sorption. *ACS Nano* **11** (2017) 10003–10011.
- [25] Lu W.-D., Wang D., Zhao Z., Song W., Li W.-C., Lu A.-H.: Supported boron oxide catalysts for selective and low-temperature oxidative dehydrogenation of propane. *ACS Catalysis* **9** (2019) 8263–8270.
- [26] Shi L., Wang D., Song W., Shao D., Zhang W.-P., Lu A.-H.: Edge-hydroxylated boron nitride for oxidative dehydrogenation of propane to propylene. *ChemCatChem* **9** (2017) 1788–1793.

- [27] Christodoulakis A., Machli M., Lemonidou A.A., Boghosian S.: Molecular structure and reactivity of vanadia-based catalysts for propane oxidative dehydrogenation studied by in situ Raman spectroscopy and catalytic activity measurements. *Journal of Catalysis* **222** (2004) 293–306.
- [28] Love A.M., Cendejas M.C., Thomas B., McDermott W.P., Uchupalanun P., Kruszynski C., Burt S.P., Agbi T., Rossini A.J., Hermans I.: Synthesis and characterization of silica-supported boron oxide catalysts for the oxidative dehydrogenation of propane. *The Journal of Physical Chemistry C* **123** (2019) 27000–27011.

Paper II

Article

Physico-Chemical Changes in the KCl-MgCl₂/La-FAU Composite Catalyst Induced by Oxidative Dehydrogenation of Ethane

Mehran Sajad ^{1,*}, Roman Bulánek ¹ and Stanislav Šlang ²

¹ Department of Physical Chemistry, Faculty of Chemical Technology, University of Pardubice, Studentska 573, 532 10 Pardubice, Czech Republic; Roman.Bulanek@upce.cz

² Center of Materials and Nanotechnologies, Faculty of Chemical Technology, nám. Čs. Legií 565, University of Pardubice, 532 10 Pardubice, Czech Republic; stanislav.slang@upce.cz

* Correspondence: Mehran.Sajad@student.upce.cz; Tel.: +420-777956079

Abstract: In this research, a binary eutectic composition of KCl and MgCl₂ supported over lanthanum exchanged FAU (faujasite) zeolite has been investigated for the oxidative dehydrogenation (ODH) of ethane. The catalyst was prepared by the thermal treatment of La-FAU with a mechanical mixture of alkali chlorides under a flow of helium at 500 °C. The eutectic mixture of alkali chlorides formed at this temperature and a molten layer were spread over the support. Synthesized fresh and spent catalysts were characterized to obtain information about changes in crystallinity, textural properties, phase content, chemical composition, and morphology of the catalyst over the reaction time. The initial conversion of ethane was 80% with ethene as the main product (65% yield). The catalyst deactivation has been demonstrated over time on the stream (TOS). The characterization methods confirmed that the chlorine was being removed from the catalyst. The side products detected by mass spectroscopy, including chlorinated hydrocarbons, have been found as a key pathway of chlorine removal from the catalyst. The exchange of chlorine for oxygen in the catalyst led to a significant decrease in the activity and production of higher hydrocarbons and their oxygenates as side products of the ODH reaction.

Keywords: oxidative dehydrogenation; alkali chlorides; ethane; ethylene



Citation: Sajad, M.; Bulánek, R.; Šlang, S. Physico-Chemical Changes in the KCl-MgCl₂/La-FAU Composite Catalyst Induced by Oxidative Dehydrogenation of Ethane. *Catalysts* **2021**, *11*, 392. <https://doi.org/10.3390/catal11030392>

Academic Editor: Changzhi Li

Received: 25 February 2021

Accepted: 16 March 2021

Published: 19 March 2021

Publisher's Note: MDPI stays neutral with regard to jurisdictional claims in published maps and institutional affiliations.



Copyright: © 2021 by the authors. Licensee MDPI, Basel, Switzerland. This article is an open access article distributed under the terms and conditions of the Creative Commons Attribution (CC BY) license (<https://creativecommons.org/licenses/by/4.0/>).

1. Introduction

Currently, ethene is mainly produced by cracking of naphtha, as one of the main feedstocks for petrochemistry, whereas due to the depletion of fossil fuels and the global demand growth for this olefin [1,2], it is necessary to find a new pathway for the efficient production of ethene. Ethane, a significant by-product of cracking processes that accompanies the production of its olefin, is mainly implemented as fuel due to its lower reactivity, albeit oxidative dehydrogenation is a thermodynamically accessible route to convert this alkane into more valuable olefin. ODH has advantages compared to its non-oxidative competitor that makes it very attractive, comprising the fact that ODH reaction is exothermic and not equilibrium limited [2–6].

Several catalytic systems have been studied in oxydehydrogenation reactions in recent decades. Among the systems that attract the most attention are supported or mixed oxides (mainly vanadium-, molybdenum-, phosphorus, or boron-based ones) [7–9], metal-free carbon-based [10], and chloride-based materials [5,11]. Concerning the last group, it was first found that the addition of a small amount of chlorine or organochlorides to the gas phase significantly affects the activity and selectivity of the oxydehydrogenation reactions over the oxide catalysts [12]. These additives mainly affected the structure of the catalyst surface—the interaction of chlorinated hydrocarbons or chlorine with the surface produced chlorides, which modified the properties of the active centers of the

catalyst. Furthermore, the radical species generated by the assistance of chlorine could influence the rate of the reaction. Later, it was shown that supported chloride catalysts are one of the promising candidates for oxidative dehydrogenation of light alkanes to olefins [6,13–27]. The advantage of using a mixture of molten salts is the ability to work in a wide temperature range if the salts make eutectics that melt at low temperatures [27,28].

Different explanations were stated to illustrate the reasons for the higher activity and selectivity caused by the presence of alkali chlorides. For instance, it was suggested that the alkali chlorides applied to different zirconia-based catalysts and metal oxides (for instance, MgO, TiO₂, SiO₂, and Dy₂O₃/MgO) provide a dynamically rearranging reaction interface and therefore create new sites and increase the number of active sites for ODH [5,6,14,16,18,24,25,27,29]. Hypochlorite (OCl[−]) has been suggested frequently as the active species on the surface of the overlayer in supported alkali chloride catalysts [6,8,16,24,27,29]. The mechanism proposed by Lercher et al. (based on a study of LiCl/MgO/Dy₂O₃ catalytic system) suggested that gaseous oxygen dissolves dissociatively in LiCl, forming OCl[−] as the active species on the chlorinated support, and then the decomposition of OCl[−] produces oxygen and chlorine radicals, where both activate alkanes via homolytic hydrogen abstraction. The formed alkane radical reacts further with OH to form an appropriate alkene. The activity becomes higher by increasing Cl[−] concentration but becomes limited by the availability of OCl[−] diffusing through the molten layer [22].

Along with the increase in catalyst activity, increased selectivity has been observed as well. The higher selectivity was also found to be connected to the presence of the mentioned dynamic interface [24,25,27]. Ethene as the desired product is more stable via adsorption at the interface than the dissolved in liquid chloride, indicating that the interface plays an important role and the molten salt surface facilitates olefin desorption/release [14,16,18,24,25,29]. Moreover, molten salts prevent coke formation because the carbon floats on the surface of the melt where it could be skimmed off, which is a big problem in the traditionally supported metal oxide catalysts [2,7,8,30,31].

However, the unstable character of the supported alkali chloride systems has been observed and reported several times, but the reasons rely on the nature of the salts and supports [13–15,17,25–27,32,33]; therefore, more research studies are needed to clarify the ambiguous aspects. The varying degrees of retention of Cl[−] suggest that the support material and its reaction with Cl[−] are associated with the loss of chlorine. For metal oxide supports, it has been suggested that the formation of HCl causes deactivation over time in the materials prepared by chloride deposition. In MgO and MgO/Dy₂O₃, OH groups on the surface of the supports react with cations in the molten alkali chloride film, and the released H⁺ forms dissolved HCl, which after enhancing the activity is depleted over time into the gas phase [27]. However, in another study for LiCl/MgO, a reaction between water and chlorine to produce HCl was suggested as the reason for the loss of chlorine, and water produced during the reaction promotes the loss of chlorine from the catalyst [34]. Even though it is not easy to detect HCl as an intermediate, a small amount of hydrogen chloride in the outlet was found during the ethane ODH reaction over metal chloride oxides consisting of bismuth, alkali, and alkaline earth chlorides [13]. Moreover, the chemical phase transformation along with the loss of chlorine that occurred during the reaction with alkali (Li, K, Na) chlorides/silica catalysts was reported to cause the deactivation together [15].

Preventing the loss of chlorine from the active catalyst might be very challenging because HCl is a likely intermediate in the reaction path and will tend to escape at high temperature [29]; thus, instead, regeneration was suggested by the addition of a Cl-containing compound [33]. Interesting research on ODH of ethane was done by using a set of various metal oxides in the presence of HCl in the gaseous feed, to avoid the loss of Cl[−], even though chlorine may cause corrosion problems. CeO₂-based catalysts exhibited the highest yield and besides, in the absence of HCl, CO₂ was the main product, but immediately upon increasing the partial pressure of HCl, the CO_x selectivity decreased sharply

and the selectivity to C_2H_4 increased, and the catalyst was stable over time [35]. In addition to using chlorine in the gaseous feed, the addition of chlorine in a catalyst as different alkali chlorides has been examined. The addition of $SrCl_2$ and KCl improved the catalytic yield of ethene by $SrBi_3O_4Cl_3$ expressively in the oxidative dehydrogenation of ethane, as is shown in Table 1 [13].

Recently, Ayari et al. [26] have reported an outstanding activity of binary and ternary mixtures of alkali and alkaline earth chlorides with the eutectic composition supported over lanthanum exchanged Na-Y zeolite in ODH of ethane. These catalysts were very active, the ethane conversion reached up to 40% with 100% selectivity to ethylene at relatively low temperature (500 °C) compared with other reported chloride-based systems mentioned above. Ayari's short communication reported a very interesting and new catalyst system capable of activating ethane at very low temperatures, but unfortunately, a more detailed characterization of the materials or information on the stability of these systems was not included in this communication.

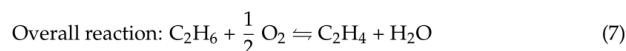
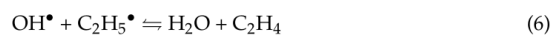
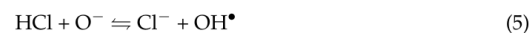
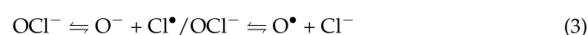
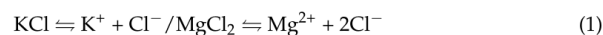
Considering this introduction, it is evident that Cl-based catalysts are promising for ODH reaction; nevertheless, they suffer from deactivation. Thus, the long-term stability of the catalysts must be evaluated and knowledge about the deactivation mechanism could be useful for preparing the Cl-based catalyst with prolonged stability. Therefore, in this study, a binary eutectic mixture of KCl and $MgCl_2$ supported on La-FAU zeolite (supported alkali chlorides labeled as S-ACL), as one of the best representatives for alkali and alkaline earth chloride in Ayari's work [26], has been investigated as a catalyst for the ODH of ethane in more details with emphasis on the study of stability. This study brings detailed structural and compositional analysis of the pristine and spent catalysts, as well as information on catalyst stability and deactivation processes, kinetics, and character. Despite the promising short time activity and selectivity toward ethene, deactivation was found to be significant. The deactivation is connected with the loss of chlorine during the ODH reaction due to the formation of chlorinated hydrocarbons.

2. Results and Discussion

2.1. Catalytic Activity

In oxidative dehydrogenation of ethane, the catalyst reached the high initial ethane conversion of 80% after 15 min of feeding at 500 °C (see Table 1 and Figure 1). The oxygen is in great excess in the reaction mixture, so its conversion is only 8%, and thus, there is not any limitation for the conversion of ethane due to the lack of oxidizing reactants. Even though oxygen is in large excess, the main product is ethene with selectivity around 72%, while CO_2 and CH_4 selectivity was negligible (below 1%). No CO production was observed during the whole reaction.

According to the related reports in the literature, we can propose that a similar to well-known reaction mechanism [25,29,36] works in this system for ethylene formation, with an overall enthalpy of $\Delta_f H(298) = -105.5 \text{ kJ mol}^{-1}$ [5].



Unfortunately, this exceptional low-temperature activity of the catalyst is not stable, as demonstrated by the conversions measured over the next 200 min on stream. The conversion of ethane declined sharply to ca. 22% after 45 min on the stream (Figure 1) and reduced to less than 10% after 100 min under the stream. The selectivity to ethene began to slowly increase to values around 91% under 206 min of time on the stream (TOS). The change in methane and CO₂ selectivity was kept below 3 and 5% during the reaction, but both slightly increased in selectivity. The measured activities of the FAU and La-FAU support exhibited negligible yield of 0.4 and 2.4%, respectively; thus, the observed activity is related to the catalytic system.

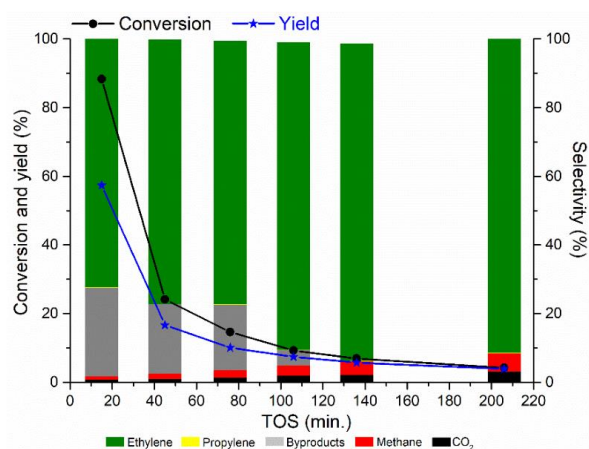


Figure 1. Conversion, yield, and selectivity dependence of ethane ODH as a function of time on stream for S-ACI.

Based on the carbon balance, we found that we are not able to analyze some of the products using gas chromatography (GC), because GC analysis was optimized for the determination of the main compounds of the reaction mixture (i.e., C₁–C₃ alkanes and alkenes, CO, CO₂, O₂, etc.). Missing reaction products based on gas chromatography analysis represented approximately 26% of selectivity at the initial period of the reaction and decreased to almost zero at 136 min of TOS. Therefore, the identification of the side products of the reaction generated on the surface of the catalyst is essential. Hence, the mass spectra of the outlet gases were measured in various times on stream. The mass spectra showed a fingerprint of the main products, as is ethylene, and water vapor accompanied by a low amount of CO₂ and methane. The presence of propane and propylene was detected as well with the selectivity below 1% (based on GC analysis) (Figure 2a). Molecular oxygen, ethane, and helium were detected also in large quantities. In addition to these major, and in gas chromatography detected substances, the species with a mass (*m/z* ratio) higher than 45 were detected in the effluent gas (Figure 2b). At low reaction time (TOS = 10 min), the mass signals at 49, 50, 52, 62, 64, and 66 were clearly visible. The comparison of the experimental mass spectrum with reference mass spectra [37] resulted in that the peaks matched with *m/z* ratios 50, 62, and 64 correspond to chlorinated hydrocarbons comprising chloromethane, ethyl chloride, and chloroethene, respectively. A very low amount of HCl (*m/z* = 36), was also observed, perhaps playing an unstable intermediate role in the reaction formed by available Cl[−] and H⁺ from any source.

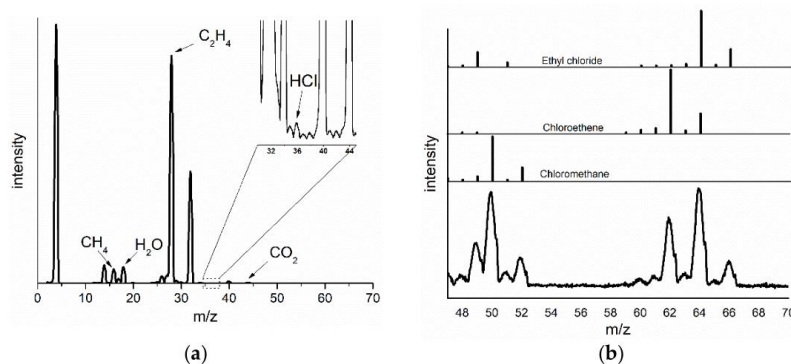


Figure 2. (a) Mass spectrum of the product of ethane oxidative dehydrogenation (ODH) over S-ACI, full-spectrum, and (b) details of low-intensity signals at m/z 45–70. At the bottom is displayed the experimental mass spectrum, above that are the model spectra of the three most probable chlorinated compounds formed during the reaction.

With increasing time on stream, the conversion of ethane decreased as well as the amount of side products. In addition, the nature of the side products changes, as can be seen in the changes of mass spectra character (Figure 3). Intensity of the main fragments of the chlorinated hydrocarbons disappeared during the first hour, and new signals at $m/z = 45, 46, 47, 48, 68,$ and 84 were detected. These new by-products were comprised of some higher hydrocarbons (C_5) or oxygenates. The most possible compounds based on comparison with the reference mass spectra are allyl vinyl ether; 1,3-dimethylallene; trans-2-methyl-2-butenal; 2-methyl-2-butenal; 4-pentyne-2-ol; 3-butyneic acid; 2-buten-4-olide; 1-ethyl-2-methylacetylene; and 3-methyl-2-butenal [37].

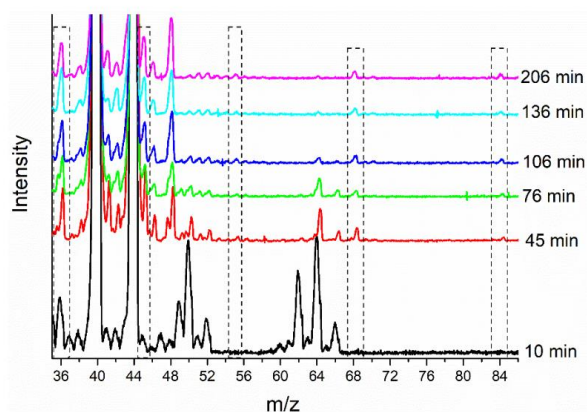


Figure 3. Mass spectra of the side products of ethane ODH over S-ACI during the reaction time including low-intensity signals at m/z 35–86.

Comparing the behavior of different catalytic systems reported in the literature is not entirely easy due to the use of often very different conditions. However, we tried to summarize the available data from the literature (Table 1). Chloride-based catalysts are very frequently studied in ethane ODH at temperatures higher than $500\text{ }^\circ\text{C}$, mostly $650\text{ }^\circ\text{C}$, and even higher [14,15,17,21,38]. The reported ethene yields for these works vary in a wide range from around 2 to 74%. Different alkali metals were exploited so far, for instance, Li [14,15,21,22,25,38], Na [13,25,26], K [13,16,25,26], Ba [17], Sr [13]. These alkali chlorides

have been used on various supports including silica, zirconia, Dy₂O₃, MgO, and other metal oxides. In general, different forms of zirconia as support exhibited higher activity and yields than the other supports. In all cases, the addition of chlorides resulted in higher activity and selectivity compared to pristine support. A similar catalyst as the one in this research was studied in Ayari's work, reporting 27% yield compared to 66% reported here for 15 min of TOS at the same temperature, although the time on stream for the measurements in Ayari's work is not mentioned. There are several reports on measuring at diverse longer TOS and higher temperatures [13,14,16,22,25], which have been compared with similar TOS in this research.

Table 1. Comparison of the catalyst's behavior in similar research with this study.

Catalyst	X *	S [†] (C ₂ H ₄)	T #	Y ‡	TOS	Ref.
S-ACl	80	72	500	57	15	This work
NaY-La(Cl)-(NaMg)	2	100	500	2	-	[26]
NaY-La(Cl)-(KMg)	27	100	500	27	-	[26]
NaY-La(Cl)-(RbMg)	40	100	500	40	-	[26]
NaY-La(Cl)-(CsMg)	7	100	500	7	-	[26]
NaY-Bin(NaMg)	3	100	500	3	-	[26]
NaY-La(Cl)-(NaKMg)	20	100	500	20	-	[26]
LiCl/SiO ₂	99	79	600	78	5	[15]
NaCl/SiO ₂	88	69	550	61	5	[15]
KCl/SiO ₂	70	75	550	52	5	[15]
LiCl/SZ (sulfated zirconia)	98	70	650	68	1	[14]
LiCl/AZ (amorphous zirconia)	87	60	650	52	1	[21]
LiCl/ZrON	95	71	650	68	1	[21]
LiCl/ZrOCl	28	97	650	27	1	[21]
LiCl/ZrSO ₄	89	83	650	74	1	[21]
LiCl/ SZ (sulfated zirconia)	53	90	650	48	1	[38]
BaCl ₂ -TiO ₂ -SnO ₂	66	93	720	60	30	[17]
Li/Dy/Mg/O/Cl	-	-	650	77	-	[22]
(Li-K)Cl-(Dy ₂ O ₃ /MgO) membrane	34	97	700	33	-	[16]
(Li-K)Cl-(Dy ₂ O ₃ /MgO) membrane	85	75	750	64	-	[16]
S-ACl	22	77	500	17	45	This work
PbBi ₃ O ₄ Cl ₃	51	88	660	45	60	[13]
S-ACl	8	89	500	7	106	This work
Li/K/Cl-MgO/Dy ₂ O ₃	5	94	550	5	120	[25]
Li/Na/Cl-MgO/Dy ₂ O ₃	2	75	500	2	120	[25]
Li/Cl-MgO/Dy ₂ O ₃	2	60	500	1	120	[25]
K/Cl-MgO/Dy ₂ O ₃	2	40	500	1	120	[25]
Na/Cl-MgO/Dy ₂ O ₃	2	37	500	1	120	[25]
S-ACl	4	91	500	4	206	This work
SrBi ₃ O ₄ Cl ₃	20	89	660	17	360	[13]
SrBi ₃ O ₄ Cl ₃ + SrCl ₂	35	89	660	31	360	[13]
SrBi ₃ O ₄ Cl ₃ + 2SrCl ₂	44	90	660	39	360	[13]
SrBi ₃ O ₄ Cl ₃ + KCl	36	96	660	34	360	[13]
SrBi ₃ O ₄ Cl ₃ + SrCl ₂ + KCl	45	92	660	42	360	[13]
SrBi ₃ O ₄ Cl ₃ + SrCl ₂ + LiCl	42	94	660	40	360	[13]
SrBi ₃ O ₄ Cl ₃ + SrCl ₂ + NaCl	41	95	660	39	360	[13]
LiCl/ SZ (sulfated zirconia)	70	66	650	46	900	[14]

* Conversion (%), † Selectivity (%), # Temperature (°C), ‡ Yield (%).

Among the systems reported in Table 1, LiCl/SiO₂ exhibited a large decrease in activity in a way that the conversion declined to 5% of the initial value after 15 h [15]. Exceptionally, LiCl supported on sulfated zirconia had been almost stable after 25 h under the stream [38], which contrasts with almost all other systems that exhibit deactivation in different trends.

2.2. Changes in the Catalyst during Pretreatment and ODH Reaction

To gain information about the changes of physico-chemical properties of the catalyst, the N₂ adsorption–desorption isotherms, scanning electron microscopy (SEM), energy-dispersive X-ray spectroscopy (EDX), and X-ray diffraction (XRD) were measured on the catalyst precursor, pretreated and spent catalysts (at various TOS). The prepared catalyst has shown different textural properties before and after the pretreatment as well as the ethane ODH reaction. The N₂ adsorption–desorption isotherms (Figure 4) of the zeolitic support and the mechanical mixture of the support and alkali chlorides have shown microporous features, whereas the fresh catalysts (after pretreatment by He, at 500 °C) and the spent catalysts have exhibited a non-porous character. The textural parameters of all measured samples obtained from N₂ adsorption isotherms are summarized in Table 2. The N₂ adsorption–desorption isotherms and textural properties of the pristine supports before and after the reaction showed no important differences, meaning any change in the textural properties of the catalyst is due to the presence of alkali chlorides. The difference in textural properties of the H-FAU before and after the reaction is due to the presence of carbon deposits after the reaction. It was proved by measuring N₂ adsorption–desorption isotherms of the spent H-FAU after calcination that exhibited similar textural properties to the fresh H-FAU before the reaction. The measured BET (Brunauer-Emmett-Teller) and external surface areas for the pristine support (La-FAU) were 450 and 8 m²/g, respectively, with a pore volume of 0.19 cm³/g. Considering the mass fraction of the La-FAU support in the catalyst, which was 50 wt%, and the fact that chlorides are non-porous materials with relatively large particle sizes, the textural properties of the physical mixture of La-FAU support with the eutectic mixture of MgCl₂ and KCl can be expected to be approximately equal to 50% of the values for the support in good agreement with the experimental results. The pretreatment of the mechanical mixture of support and alkali chlorides in helium flow at 500 °C (denoted as fresh catalyst), which is higher than the eutectic temperature of the mixture of alkali chlorides (473 °C) led to the chlorides melting and the formation of a uniform molten layer of salts on the support particles. Thus, the pretreated fresh catalyst exhibits non-porous character due to blocking of the entrance windows to the support pores by the molten salts layer, resulting in a drop of BET surface area to 7.7 m²/g, which is a value very close to the external surface of the support particles. The N₂ adsorption isotherms of catalysts working under the reaction conditions for different times (Figure 2b) show that the textural properties of the catalyst are not influenced by the reaction and they correspond to the properties of the fresh catalyst (cf. data in Table 2).

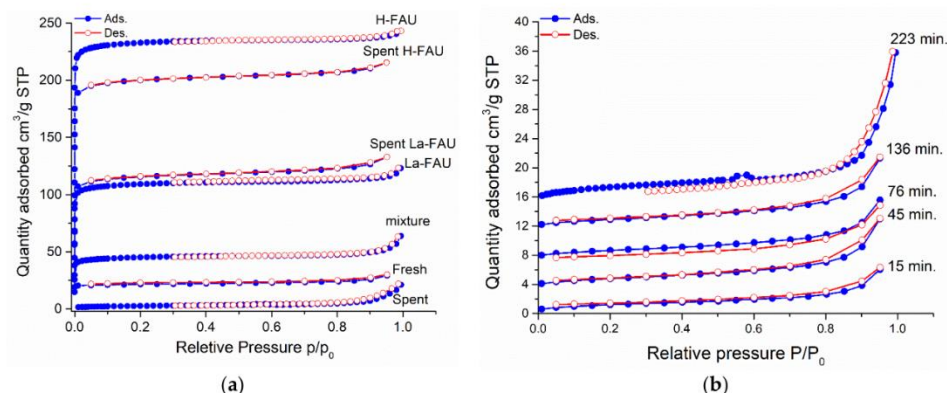


Figure 4. N_2 adsorption–desorption isotherms of (a) the fresh and spent pristine supports, physical mixture of S-ACI, the fresh catalyst before and after reaction (time on the stream (TOS): 223 min) in ethane ODH (isotherms corresponding to the fresh catalyst shifted along the y-axis by an increment of $20 \text{ cm}^3/\text{g}$), (b) the spent catalysts after different TOS under reaction atmosphere (isotherms are shifted along the y-axis by an increment of $4 \text{ cm}^3/\text{g}$).

Table 2. Textural properties of the support (La-FAU), mechanical mixture of S-ACI, fresh, and spent catalyst after the ethane ODH reaction in different TOS.

	S_{BET} (m^2/g) ^a	$S_{\text{ext.}}$ (m^2/g) ^b	$V_{\text{mic.}}$ (cm^3/g) ^c	V_{p} (cm^3/g) ^d
H-FAU	965	16	0.34	0.38
Spent H-FAU	769	16	0.30	0.33
La-FAU	450	8	0.17	0.19
Spent La-FAU	442	16	0.17	0.21
Mechanical mixture	179	4	0.07	0.10
Fresh	7.7	7.7	0	0.015
TOS: 15 min.	5.9	5.9	0	0.010
TOS: 45 min.	7.9	7.9	0	0.016
TOS: 76 min.	6.8	6.8	0	0.014
TOS: 136 min.	7.8	7.8	0	0.016
TOS: 223 min.	10	10	0	0.03

^a BET surface area, ^b External surface area, ^c Micropore volume, ^d Total pore volume.

The SEM images of the parent FAU zeolite, La-FAU support, and fresh and spent catalysts under various time on stream are reported in Figure 5. The parent zeolite of the FAU structure exhibits polyhedral particles of ca. 500 nm in size. La-FAU support, fresh, and even spent catalysts exhibited no big difference in the morphology of the particles. It means that the zeolite support particles are quite stable and the molten salts form a surface layer on the external surface of the zeolitic support. Based on calculations, the thickness of the molten salts layer should be between 30 and 50 nm, according to the volume of the molten alkali chlorides (obtained from the related density) and the suggestion that the whole salt spreads over the external surface of the support or fills the micropores (by intrusion) and the rest of the salt spreads over the surface, respectively. If the whole external surface of the zeolite particles will be evenly covered, it does not cause any significant changes in the shape or size of the particles.

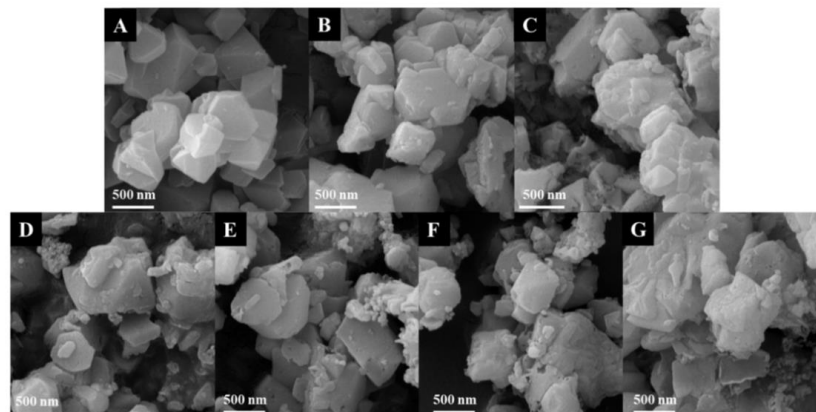


Figure 5. SEM images of (A) NH_4 -FAU, (B) La-FAU, (C) Fresh catalyst, (D–G) Spent catalyst after 15, 45, 76, and 136 min under the reaction atmosphere, respectively.

The chemical composition of the materials investigated was determined by EDX spectroscopy. To obtain representative results, the composition was determined by averaging ten EDX measurements at different points of the sample on an area of at least $400 \times 400 \mu\text{m}^2$. Results (in atomic %) are summarized in Table 3. The parent NH_4 -FAU zeolite has an Si/Al ratio of 2.55, and it is not changed with the preparation of catalysts and its working under reaction conditions for various TOS. La-FAU support prepared by solid-state reaction between NH_4 -FAU and LaCl_3 exhibited an La/Al ratio of 0.52, which is slightly lower compared to the theoretical one (0.61), which can be ascribed to eventual partial sublimation, as was previously observed in the literature [39]. Surprisingly, the content of chlorine in the fresh catalyst after heat treatment at 500°C in helium flow is ca. half compared to the theoretical expectation. We can speculate that during the heat treatment, the reaction between chlorides and moisture evaporated from the zeolite can lead to the partial conversion of chlorides to oxides. Nevertheless, the chlorine content has been reduced continuously during the reaction, decreasing from 11.5 to 6.3 at. %. At TOS = 223 min, almost 75% of chlorine is missing, but it seems that the content of chlorine levels off to approximately 25 rel.% of the original content. This part of chlorine is probably inaccessible from the surface (maybe inside the original zeolite channels) or is bound to more stable compounds. Simultaneously with the decrease in Cl content, an increase in oxygen content is noticeable. The content of alkali and alkaline earth metals remained almost constant.

Table 3. Chemical composition of S-ACl catalyst measured by energy-dispersive X-ray spectroscopy (EDX) based on the atomic percentage (at. %) of elements.

Element	Nominal	NH_4 -FAU	La-FAU	Fresh	Spent Catalysts, Different TOS (Min.)				
					15	45	76	136	223
O	44.3	64.4	64.2	52.7	57.8	57.6	56.3	57.6	60.0
Na	0.1	1.4	1.1	0.7	0.9	0.9	0.7	0.7	0.7
Mg	8.3	0.0	0.0	9.4	11.6	10.4	13.1	13.2	9.7
Al	3.8	7.9	7.1	3.9	4.4	4.5	4.2	4.0	4.3
Si	9.8	20.2	17.9	9.1	11.1	11.4	10.8	10.4	11.8
Cl	24.3	0.0	5.9	11.5	11.1	7.6	7.1	6.6	6.3
K	7.6	0.0	0.0	5.8	5.5	5.2	5.4	5.1	5.4
La	1.7	0.0	3.7	1.7	2.6	2.5	2.4	2.5	1.9
N	0	6.1	0	0	0	0	0	0	0

X-ray diffraction patterns of the prepared catalyst exhibited the expected phases including FAU zeolite and alkali chlorides (Figure 6). According to the obtained XRD patterns, the mechanical mixture of the catalyst consists of crystalline KCl (Sylvite, Crystallography Open Database (COD) code: 9008651, lattice planes (002), (022) at 28.4° and 40.5°), $\text{MgCl}_2 \cdot 6\text{H}_2\text{O}$ (Bischofite, COD: 9011352, lattice planes (111), (310), (220), (11-2), (22-1) at 21.7°, 29.9°, 31°, 32.8°, and 33.9°, respectively), FAU zeolite (Faujasite, COD: 1507214, lattice planes (111), (022), (113), (133), (115), (044), (226), (137), (337) at 6.1°, 10°, 11.8°, 15.5°, 18.5°, 20.1°, 23.6°, 27.4°, and 29.3°, respectively), and LaOCl (Lanthanum–oxychloride, tetragonal, COD: 2101549, lattice planes (001), (011), (110), (012), and (020) at 12.8°, 25.2°, 30.7°, 33.9°, and 43.9°), meaning that the catalyst contains an excess of La; thus, not all La is in the cationic sites of zeolite and part of the lanthanum form oxychloride. Unlike KCl, the MgCl_2 showed a different crystalline structure ($\text{MgCl}_2 \cdot 6\text{H}_2\text{O}$, Bischofite) as its original form before mixing with the support. After the heat treatment at 500 °C, a solid solution of chlorides formed on the surface of the catalyst due to the dissolving of chlorides into each other; therefore, the changes in the quantity and intensity of the diffraction patterns are expected. The fresh catalyst exhibited the presence of FAU, LaOCl, and KCl, but not any form of MgCl_2 anymore. Furthermore, a new phase formed in the fresh catalyst, LaAlO_3 (lanthanum aluminum trioxide, COD: 2206576, lattice plane (011) at 33.4°). In the spent catalysts, besides LaOCl and KCl, SiO_2 (Cristobalite, COD: 9008233 (111) at 21.5°) is also present, whereas the presence of MgO (Periclase, COD: 9000501, lattice plane (002) at 42.9°) instead of its chloride form, showing the change in crystallinity after chlorine lost from the beginning of the reaction. It means that La-oxychloride and KCl are quite stable compounds, but MgCl_2 is highly labile. The intensity of the main diffraction line of FAU zeolite in low angles is decreased with time, which could be due to lowering its crystallinity. Additionally, the spent pristine support includes H-FAU and La-FAU have not exhibited important differences compared to the fresh ones, showing they are rather stable during the reaction.

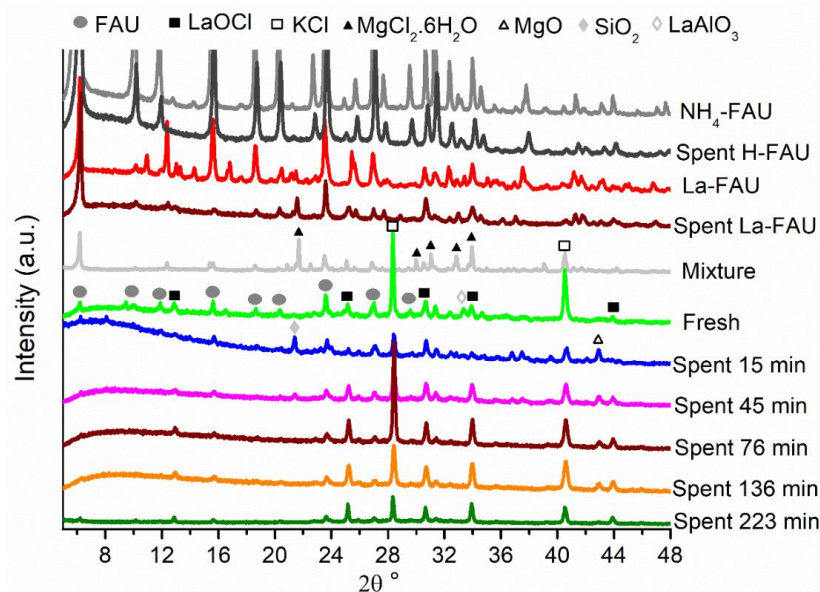


Figure 6. X-ray diffraction patterns of FAU-zeolite, La-FAU, as well as S-ACI catalyst before and after the ethane ODH reaction in TOS: 15, 45, 76, 136, and 223 min (patterns are shifted along the y-axis by an increment of 2500 a.u.).

3. Materials and Methods

3.1. Catalysts Preparation

The catalyst support (La-FAU) was prepared by solid-state ion exchange of 1 g NH₄-FAU zeolite (Zeolyst, Kansas City, KS, USA, Si/Al = 2.55) with 2 mmol LaCl₃·7H₂O (Sigma-Aldrich spol. s.r.o., Prague, Czech Republic). Precursors were mechanically mixed in an agate mortar and then were heated in an atmosphere control furnace by 2 °C min⁻¹ heating rate to 500 °C for 12 h under N₂ flow (30 cm³ min⁻¹). After that, the catalyst was prepared by extensively mixing KCl (Sigma-Aldrich spol. s.r.o., Prague, Czech Republic) and MgCl₂ (Sigma-Aldrich spol. s.r.o., Prague, Czech Republic), (mole fraction: 0.416 and 0.584, respectively, eutectic temperature: 473 °C) with La-FAU (salts-to-zeolite support mass ratio = 1:1) in an agate mortar. The mechanical mixture was converted to fresh catalyst just before the catalytic test (the material was heated in the flow of helium (27.3 cm³ min⁻¹) to 500 °C with the heating rate 5 °C min⁻¹ and kept at this temperature for 2 h). The catalyst is labeled S-ACl (supported alkali chlorides) in this study.

3.2. Catalytic Test

The catalytic activity of the sample for ethane ODH was tested in a plug-flow fixed-bed tubular reactor at atmospheric pressure. Typically, 200 mg of the catalyst was loaded in the glass tube reactor with an inner diameter of 5 mm (the grain size of the catalyst was between 0.35 to 0.5 mm). The pretreatment was performed at 500 °C by using 27.3 cm³ min⁻¹ of He for 2 h. Subsequently, the reaction was performed in a reaction mixture consisting of C₂H₆/O₂/He = 3/15/82 vol % with a total flow of 33.33 cm³ min⁻¹ STP at 500 °C. Products were analyzed with an online gas chromatograph (Agilent 7890A, Agilent Corporation, Santa Clara, CA, USA) equipped with a flame ionization detector (FID) and a thermal conductivity detector (TCD) connected in series. The GS-Carbonplot GC column (60 m long with a diameter of 320 μm) was used for the separation of the gas mixture component. To analyze the essence of the by-products, a sample of gas products was collected at various time on stream into a glass sampling ampule and then analyzed by a quadrupole mass spectrometer OmniStar GDS 300 (Pfeiffer Vacuum, Aßlar, Germany).

3.3. Characterization

The catalyst support, fresh and spent catalysts were characterized by N₂ adsorption-desorption isotherms, XRD, and EDX/SEM. N₂ adsorption-desorption isotherms were measured at -196 °C, using an ASAP 2020 instrument. Before each adsorption measurement, the sample was degassed to allow a slow removal of pre-adsorbed water at low temperatures. The temperature was slowly increased with a temperature ramp of 0.5 °C min⁻¹ up to 110 °C and evacuated at this temperature for 1 h; then, the temperature was increased with the rate of 1 °C min⁻¹ until 250 °C was achieved. The sample was degassed at this temperature under a turbo molecular pump vacuum for 8 h. The surface area was obtained by using the BET model, the total volumes were estimated based on the adsorbed amount at a relative pressure of 0.99, micropore volume and external surface area were determined via the t-plot method employing a Harkins-Jura thickness curve. X-ray powder diffraction data were recorded on a Bruker D8 X-ray powder diffractometer equipped with a graphite monochromator and a position-sensitive detector (Vantec-1) using Cu K α radiation (at 40 kV and 30 mA) in Bragg-Brentano geometry. The quantitative elemental composition of the catalysts was further evaluated using a scanning electron microscope (LYRA 3, Tescan, Brno-Kohoutovice, Czech Republic) equipped with EDX analyzer AZtec X-Max 20 (Oxford Instruments, Prague, Czech Republic) at an acceleration voltage of 20 kV. The morphology of particles in the sample was characterized by field emission scanning electron microscopy (LYRA 3, Tescan) at an acceleration voltage of 10 kV.

4. Conclusions

In this work, the catalytic activity and physico-chemical changes induced by ODH reaction in a binary eutectic mixture of KCl and MgCl₂ supported on La-FAU zeolite as

one of the best representatives for alkali and alkaline earth chloride catalysts reported previously by Ayari's group has been studied. This catalytic system exhibits high activity, as well as high selectivity in a short time on the stream, and a negligible formation of CO₂. Yield of the ethene reached up to 65%. The changes that occurred on the catalyst were studied and disclosed that the interaction between the formed molten layer and feed changed the properties of the catalyst over time, including porosity, phase content, and chemical composition. Loss of catalyst activity in TOS is associated with the loss of chlorine from the catalyst evidenced by EDX analysis of catalysts working in the reaction for various times. It is surprising that the loss of chlorine was observed even during high-temperature treatment in helium, which was very probably due to the reaction of desorbed water vapor with the chlorides. XRD analysis evidenced that MgCl₂ is more prone to exchange chlorine for oxygen. Chlorine is removed from the catalyst in the form of chlorinated hydrocarbons such as chloromethane, ethyl chloride, and chloroethene. Surprisingly, the exchange of chlorine for oxygen occurs not only under catalytic reaction but also under the helium flow, which was probably due to the reaction of chlorides at high temperature with traces of water vapor desorbed from the zeolite support. It indicates high lability of the catalyst. As chlorine is the crucial element to form hypochlorite anions, subsequently, a dropping in the amount of available active species happens. It is interesting that approximately 25 rel.% of chlorine remained in the catalyst even after 223 min in the reaction. This part of chlorine is probably inaccessible from the surface (maybe inside the original zeolite channels) or is bound to more stable compounds (probably KCl or LaOCl). It means that activity of the catalyst is tightly connected with the presence of MgCl₂. We believe that this research clarifies an obstacle in the discussed catalytic system, and it is a step forward to find the solution to build an appropriate catalyst.

Author Contributions: Conceptualization, R.B. and M.S.; methodology, M.S.; validation, R.B., M.S., and S.Š.; formal analysis, M.S.; investigation, M.S. and S.Š.; data curation, M.S.; writing—original draft preparation, M.S.; writing—review and editing, R.B.; visualization, M.S.; supervision, R.B.; All authors have read and agreed to the published version of the manuscript.

Funding: This research was funded by University of Pardubice, grant number “SGS_2021_006”.

Data Availability Statement: Publicly available datasets were analyzed in this study. These data can be found here: DOI: <https://doi.org/10.18434/T4D303>, and <http://www.crystallography.net/cod/> (accessed on 18 March 2021).

Acknowledgments: This work was supported by the Ministry of Education, Youth, and sports with financial support under project No. SGS_2021_006. The SEM and EDX facilities at CEMNAT institute were employed in this study with financial support under project No. LM2018103. Ludvík Beneš was kindly acknowledged for helping XRD measurements.

Conflicts of Interest: The authors declare no conflict of interest. The funders had no role in the design of the study; in the collection, analyses, or interpretation of the data; in the writing of the manuscript, or in the decision to publish the results.

References

1. James, O.O.; Mandal, S.; Alele, N.; Chowdhury, B.; Maity, S. Lower alkanes dehydrogenation: Strategies and reaction routes to corresponding alkenes. *Fuel Process. Technol.* **2016**, *149*, 239–255. [[CrossRef](#)]
2. Sattler, J.J.H.B.; Ruiz-Martinez, J.; Santillan-Jimenez, E.; Weckhuysen, B.M. Catalytic Dehydrogenation of Light Alkanes on Metals and Metal Oxides. *Chem. Rev.* **2014**, *114*, 10613–10653. [[CrossRef](#)] [[PubMed](#)]
3. Blasco, T.; Galli, A.; Nieto, J.L.; Trifiró, F. Oxidative Dehydrogenation of Ethane and n-Butane on VO_x/Al₂O₃ Catalysts. *J. Catal.* **1997**, *169*, 203–211. [[CrossRef](#)]
4. Ciambelli, P.; Lisi, L.; Pirone, R.; Ruoppolo, G.; Russo, G. Comparison of behaviour of rare earth containing catalysts in the oxidative dehydrogenation of ethane. *Catal. Today* **2000**, *61*, 317–323. [[CrossRef](#)]
5. Gärtner, C.A.; van Veen, A.C.; Lercher, A.J. Oxidative Dehydrogenation of Ethane: Common Principles and Mechanistic Aspects. *ChemCatChem* **2013**, *5*, 3196–3217. [[CrossRef](#)]
6. Gärtner, C.A.; Van Veen, A.C.; Lercher, J.A. Oxidative Dehydrogenation of Ethane on Dynamically Rearranging Supported Chloride Catalysts. *J. Am. Chem. Soc.* **2014**, *136*, 12691–12701. [[CrossRef](#)] [[PubMed](#)]

7. Bañares, M.A. Supported metal oxide and other catalysts for ethane conversion: A review. *Catal. Today* **1999**, *51*, 319–348. [[CrossRef](#)]
8. Cavani, F.; Ballarini, N.; Cericola, A. Oxidative dehydrogenation of ethane and propane: How far from commercial implementation? *Catal. Today* **2007**, *127*, 113–131. [[CrossRef](#)]
9. Carrero, C.; Schlögl, R.; Wachs, I.; Schomaecker, R. Critical literature review of the kinetics for the oxidative dehydrogenation of propane over well-defined supported vanadium oxide catalysts. *ACS Catal.* **2014**, *4*, 3357–3380. [[CrossRef](#)]
10. Navalon, S.; Dhakshinamoorthy, A.; Alvaro, M.; Garcia, H. Carbocatalysis by Graphene-Based Materials. *Chem. Rev.* **2014**, *114*, 6179–6212. [[CrossRef](#)]
11. Ronghe Lin, A.P.A.; Pérez-Ramírez, J. Halogen-Mediated Conversion of Hydrocarbons to Commodities. *Chem. Rev.* **2017**, *117*, 4182–4247.
12. Burch, G.D.S.R.; Tsang, S.C. Comparative study of catalysts for the oxidative coupling of methane. *Appl. Catal. A Gen.* **1988**, *43*, 105–116. [[CrossRef](#)]
13. Ueda, W.; Lin, S.-W.; Tohmoto, I. Highly selective oxidative dehydrogenation of ethane to ethene over layered complex metal chloride oxide catalysts. *Catal. Lett.* **1997**, *44*, 241–245. [[CrossRef](#)]
14. Wang, S.; Murata, K.; Hayakawa, T.; Hamakawa, S.; Suzuki, K. Lithium-chloride-promoted sulfated zirconia catalysts for the oxidative dehydrogenation of ethane. *Catal. Lett.* **1999**, *59*, 173–178. [[CrossRef](#)]
15. Wang, S.; Murata, K.; Hayakawa, T.; Hamakawa, S.; Suzuki, K. Oxidative Dehydrogenation of Ethane over Alkali Metal Chloride Modified Silica Catalysts. *Energy Fuels* **2000**, *14*, 899–903. [[CrossRef](#)]
16. Li, M.; van Veen, A.C. Selective production of ethylene via continuous oxidative dehydrogenation of ethane in (Dy₂O₃/MgO)-(Li-K) Cl composite membrane reactor. *Chem. Eng. J.* **2019**, *365*, 344–350. [[CrossRef](#)]
17. Wang, Z.; Chen, L.; Zou, G.; Luo, X.; Gao, R.; Chou, L.; Wang, X. A novel BaCl₂-TiO₂-SnO₂ catalyst for the oxidative dehydrogenation of ethane. *Catal. Commun.* **2012**, *25*, 45–49. [[CrossRef](#)]
18. Kristoffersen, H.H.; Metiu, H. Molten LiCl Layer Supported on MgO: Its Possible Role in Enhancing the Oxidative Dehydrogenation of Ethane. *J. Phys. Chem. C* **2015**, *119*, 8681–8691. [[CrossRef](#)]
19. Zichittella, G.; Lüthi, J.; Paunović, V.; Pérez-Ramírez, J. Alkane Functionalization via Catalytic Oxychlorination: Performance as a Function of the Carbon Number. *Energy Technol.* **2020**, *8*. [[CrossRef](#)]
20. Wang, D.J.; Rosynek, M.P.; Lunsford, J.H. The effect of chloride ions on a li+mgo catalyst for the oxidative dehydrogenation of ethane. *J. Catal.* **1995**, *151*, 155–167. [[CrossRef](#)]
21. Wang, S.; Murata, K.; Hayakawa, T.; Suzuki, K. Oxidative Dehydrogenation of Ethane over Zirconia-Supported Lithium Chloride Catalysts. *Chem. Eng. Technol.* **2000**, *23*, 1099–1103. [[CrossRef](#)]
22. Gaab, S.; Find, J.; Grasselli, R.; Lercher, J. Oxidative ethane activation over oxide supported molten alkali metal chloride catalysts. In *Catalyst Deactivation, Proceedings of the 7th International Symposium, Edinburgh, UK, 24–25 May 2004*; Elsevier: London, UK, 2004; Volume 147, pp. 673–678.
23. Yuan, X.H.; Zhao, Y.B.; Jin, Y.X.; Weng, W.Z.; Wan, H.L. Oxidative dehydrogenation of ethane to ethylene over LiCl/SO₄²⁻-ZrO₂ catalyst. *Chin. J. Catal.* **2006**, *27*, 79–85.
24. Tope, B.; Zhu, Y.; Lercher, J.A. Oxidative dehydrogenation of ethane over Dy₂O₃/MgO supported LiCl containing eutectic chloride catalysts. *Catal. Today* **2007**, *123*, 113–121. [[CrossRef](#)]
25. Kumar, C.P.; Gaab, S.; Muller, T.E.; Lercher, J.A. Oxidative Dehydrogenation of Light Alkanes on Supported Molten Alkali Metal Chloride Catalysts. *Top. Catal.* **2008**, *50*, 156–167. [[CrossRef](#)]
26. Ayari, F.; Charrad, R.; Asedegbega-Nieto, E.; Mhamdi, M.; Delahay, G.; Farhat, F.; Ghorbel, A. Ethane Oxidative Dehydrogenation over ternary and binary mixtures of alkaline and alkaline earth chlorides supported on zeolites. *Microporous Mesoporous Mater.* **2017**, *250*, 65–71. [[CrossRef](#)]
27. Gärtner, C.A.; Van Veen, A.C.; Lercher, J.A. Highly Selective Supported Alkali Chloride Catalysts for the Oxidative Dehydrogenation of Ethane. *Top. Catal.* **2014**, *57*, 1236–1247. [[CrossRef](#)]
28. Kristoffersen, H.H.; Metiu, H. Chemistry of Solvated Electrons in Molten Alkali Chloride Salts. *J. Phys. Chem. C* **2018**, *122*, 19603–19612. [[CrossRef](#)]
29. Gaab, S.; Machli, M.; Find, J.; Grasselli, R.; Lercher, J. Oxidative Dehydrogenation of Ethane Over Novel Li/Dy/Mg Mixed Oxides: Structure–Activity Study. *Top. Catal.* **2003**, *23*, 151–158. [[CrossRef](#)]
30. Grant, J.T.; Venegas, J.M.; McDermott, W.P.; Hermans, I. Aerobic Oxidations of Light Alkanes over Solid Metal Oxide Catalysts. *Chem. Rev.* **2018**, *118*, 2769–2815. [[CrossRef](#)]
31. Bulánek, R.; Čičmanec, P.; Sheng-Yang, H.; Knotek, P.; Čapek, L.; Setnička, M. Effect of preparation method on nature and distribution of vanadium species in vanadium-based hexagonal mesoporous silica catalysts: Impact on catalytic behavior in propane ODH. *Appl. Catal. A: Gen.* **2012**, *415–416*, 29–39. [[CrossRef](#)]
32. Zichittella, G.; Aellen, N.; Paunović, V.; Amrute, A.P.; Pérez-Ramírez, J. Olefins from Natural Gas by Oxychlorination. *Angew. Chem. Int. Ed.* **2017**, *56*, 13670–13674. [[CrossRef](#)] [[PubMed](#)]
33. Leveles, L.; Fuchs, S.; Seshan, K.; Lercher, J.A.; Lefferts, L. Oxidative conversion of light alkanes to olefins over alkali promoted oxide catalysts. *Appl. Catal. A: Gen.* **2002**, *227*, 287–297. [[CrossRef](#)]
34. Conway, S.J.; Lunsford, J.H. The oxidative dehydrogenation of ethane over chlorine-promoted lithium-magnesium oxide catalysts. *J. Catal.* **1991**, *131*, 513–522. [[CrossRef](#)]

35. Yu, F.; Wu, X.; Zhang, Q.; Wang, Y. Oxidative dehydrogenation of ethane to ethylene in the presence of HCl over CeO₂-based catalysts. *Chin. J. Catal.* **2014**, *35*, 1260–1266. [[CrossRef](#)]
36. Gaab, S.; Find, J.; Muller, T.E.; Lercher, J.A. Kinetics and mechanism of the oxidative dehydrogenation of ethane over Li/Dy/Mg/O/(Cl) mixed oxide catalysts. *Top Catal.* **2007**, *46*, 101–110. [[CrossRef](#)]
37. NIST Mass Spectrometry Data Center, W.E.W. Director, “Mass Spectra”. In *NIST Chemistry WebBook*; NIST Standard Reference Database Number, 69; Linstrom, P.J., Mallard, W.G., Eds.; National Institute of Standards and Technology: Gaithersburg, MD, USA, 2005; p. 20899. retrieved March 18, 2021. [[CrossRef](#)]
38. Wang, S.B.; Murata, K.; Hayakawa, T.; Hamakawa, S.; Suzuki, K. Performance of metal-oxide-promoted LiCl/sulfated-zirconia catalysts in the ethane oxidative dehydrogenation into ethene. *Catal. Lett.* **1999**, *62*, 191–195. [[CrossRef](#)]
39. Schüßler, F.; Pidko, E.A.; Kolvenbach, R.; Sievers, C.; Hensen, E.J.M.; Van Santen, R.A.; Lercher, J.A. Nature and Location of Cationic Lanthanum Species in High Alumina Containing Faujasite Type Zeolites. *J. Phys. Chem. C* **2011**, *115*, 21763–21776. [[CrossRef](#)]

Paper III



Contents lists available at ScienceDirect

Chemical Engineering Journal

journal homepage: www.elsevier.com/locate/cej

Imidazolium-type ionic liquid-assisted formation of the MFI zeolite loaded with metal nanoparticles for hydrogenation reactions

Yuyan Zhang^a, Ang Li^a, Mehran Sajad^b, Katarína Fulajtárová^c, Michal Mazur^a, Martin Kubů^a, Mariya Shamzhy^a, Milan Hronec^c, Roman Bulánek^b, Jiří Čejka^{a,*}

^a Department of Physical and Macromolecular Chemistry, Faculty of Science, Charles University, Hlavova 2030/8, 128 43 Prague, Czech Republic

^b Department of Physical Chemistry, Faculty of Chemical Technology, University of Pardubice, Studentská 573, 532 10 Pardubice, Czech Republic

^c Department of Organic Technology, Slovak University of Technology, Radlinského 9, 812 37 Bratislava, Slovakia

ARTICLE INFO

Keywords:

MFI zeolite
Alkoxyisilane functional imidazolium-type ionic liquids
Pt nanoparticles
Pd nanoparticles
Hydrogenation reactions

ABSTRACT

Zeolites loaded with metal nanoparticles (NPs) stand out for their distinct activity and selectivity as heterogeneous catalysts. However, the poor stability of metal species limits their applications. Herein, we report a novel synthetic strategy for stabilizing metal nanoparticles inside the MFI zeolite. For the first time, alkoxyisilane functional imidazolium-type ionic liquids (ImILs) were used as assistant agents to protect metal precursors (Pt and Pd) against precipitation during the hydrothermal synthesis of the MFI zeolite. The positively charged imidazolium groups in ImILs interact with the negatively charged metal precursors (PtCl_4^{2-} , PdCl_4^{2-} etc.), while the alkoxyisilane groups participate in zeolite crystallization. Scanning transmission electron microscopy images indicate that most of the Pt and Pd nanoparticles (average diameters of approximately 1.0 nm and 1.7 nm, respectively) are confined in channels or intersections of the MFI zeolite. The shape-selectivity effect on nitroarene hydrogenation over Pt@MFI_ImILs confirmed the successful encapsulation of metal NPs into the MFI matrix. The conversion of the small molecule 4-nitrotoluene is >99%, whereas the bulky 1,3-dimethyl-5-nitrobenzene shows 5.8% conversion. Simultaneously, the Pd@MFI_ImILs catalyst affords a higher reaction rate (25 mmol/s/g_{Me}) than the impregnated Pd@MFI_imp catalyst (9 mmol/s/g_{Me}) in propene hydrogenation, which is ascribed to the uniform distribution of Pd nanoparticles. The ImIL-assisted synthesis strategy can be therefore successfully used to confine small metal nanoparticles in the MFI zeolite while maintaining its high catalytic activity and shape-selectivity.

1. Introduction

Zeolites are crystalline aluminosilicates with well-defined three-dimensional frameworks. Thanks to their pore systems of molecular dimensions, zeolites are able to catalyze chemical reactions with unique reactivity and selectivity [1–3]. Moreover, zeolite pore systems are suitable for encapsulating metal nanoparticles (NPs) [4–6]. Once the metal NPs are confined in the zeolite channel system, their mobility is reduced, thereby preventing aggregation [7–10]. Some of the most commonly used supports for metal NPs are non-porous oxides [11,12] but zeolites have an advantage over non-porous supports because their porosity provides shape-selectivity in adsorption and catalysis [13–15]. As such, the size and shape of their pores limit the diffusion of excessively bulky molecules (reactants, intermediates or products) in the channels, which provides zeolites with a unique shape-selective

catalytic performance [16,17].

The most frequently reported method for metal NP encapsulation in zeolites is post-synthetic modification, e.g., ion exchange or impregnation. However, the resulting catalysts consist of non-uniform and unevenly dispersed metal NPs [18–20]. An alternative synthetic strategy consists of using the 2D-to-3D zeolite transformation, which effectively confines metal NPs inside the pore system of zeolites. However, this method can only be applied to specific zeolite frameworks with layered precursors [21–23]. Another method is to encapsulate metal NPs within zeolites during the hydrothermal crystallization process [24,25]. For this purpose, metal precursors are introduced into the aluminosilicate reaction gel. Then, the building units of the zeolites are assembled around such metal precursors under hydrothermal conditions [26,27]. In this one-pot method, the encapsulation of metal precursors is synchronized with zeolite crystallization. Thus, this approach is not

* Corresponding author.

E-mail address: jiri.cejka@natur.cuni.cz (J. Čejka).

<https://doi.org/10.1016/j.cej.2021.128599>

Received 9 November 2020; Received in revised form 13 January 2021; Accepted 15 January 2021

Available online 21 January 2021

1385-8947/© 2021 Elsevier B.V. All rights reserved.

restricted by zeolite topology, yet most metal precursors are cations and hence can easily precipitate as large colloidal metal hydroxides in the alkaline aluminosilicate gel, thereby preventing their encapsulation as nanoparticles [28,29]. Consequently, developing protective agents to stabilize metal precursors against precipitation, such as S- and N-containing ligands, [30,31] requires considerable time and effort. Choi et al. have used bifunctional 3-mercaptopropyltrimethoxysilane ligand for stabilization of different metal cations (Pt, Pd, Ir, Rh, and Ag) upon hydrothermal crystallization of NaA zeolite with encapsulated metal nanoparticles [32]. However, such mercaptosilane-assisted synthesis is usually complicated by poor solubility of mercaptosilanes in aqueous medium leading to inhomogeneous distribution of metal-sulfur complexes in reaction mixture and, as a result, poor reproducibility of the method [5]. Iglesias and colleagues have reported the use of organic amine ligands-stabilized metal precursors for the direct synthesis of small-pore SOD and ANA zeolites with encapsulated Rh, Ru, Pd, and Pt clusters [28]. However, the use of such hydrophilic cationic metal complexes characterized by limited thermal stability, was successful only for crystallization of Al-rich zeolites formed at relatively low temperatures ($T < 390$ K). Notwithstanding recent achievements of ligand-assisted synthesis of metal nanoparticles confined in zeolites, protective agents must still be developed to stabilize metal precursors during the hydrothermal crystallization to control the size and dispersion of the resulting metal catalyst.

Ionic liquids are a class of ionic, salt-like materials that remain in liquid state at unusually low temperatures [33,34]. Many metal-containing ionic liquids are widely used in numerous reactions, such as coupling reactions [35–37]. Morris and colleagues synthesized the aluminophosphate zeotype (SIZ series) using imidazolium-based ionic liquids as both solvent and template simultaneously [38,39]. Ivanova et al. prepared BEA, MFI, and ANA zeolites using 1-butyl-3-methylimidazolium methane-sulfonate ionic liquid as a template [40]. On the other hand, such ionic liquids are frequently used for stabilization colloidal suspensions of metal nanoparticles against aggregation [41–43]. Accordingly, imidazolium-type ionic liquids may be used as protective agents for metal precursors without affecting zeolite crystallization. However, to our best knowledge, the preparation of zeolite-confined metal catalysts *via* ImILs-assisted crystallization has not been attempted yet.

Herein, we firstly report on the synthesis of MFI-confined Pt and Pd catalysts by steam-assisted zeolite crystallization aided by alkoxy silane-functionalized imidazolium-type ionic liquid (ImILs) (Scheme 1). The prepared supported catalysts were thoroughly characterized by a combination of relevant experimental techniques (XRD, N_2 physisorption, SEM, STEM, solid state NMR) and tested in hydrogenation of model compounds, such as nitroarenes and propene. The results of this study unambiguously evidence ImILs-assisted crystallization is an efficient method for encapsulation of metal NPs into zeolite matrix providing highly active and shape-selective metal catalysts with improved size stability.

2. Experimental section

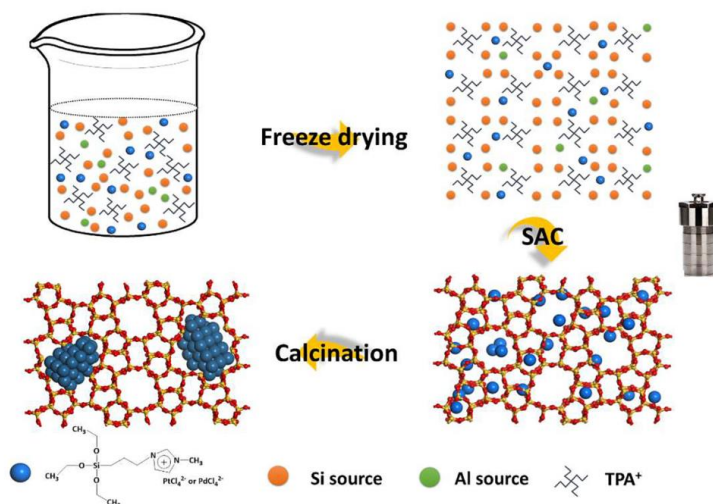
2.1. Chemicals

All reagents were purchased from commercial suppliers and used without further purification. Tetraethyl orthosilicate (TEOS, Sigma Aldrich), aluminum nitrate nonahydrate ($Al(NO_3)_3 \cdot 9H_2O$, Sigma Aldrich), sodium hydroxide solution (NaOH, 50%, Merck), tetrapropylammonium hydroxide solution (TPAOH, 40% solution in water, Sigma Aldrich), (3-chloropropyl)triethoxysilane (95%, Sigma Aldrich), 1-methylimidazole (99%, Alfa Aesar), toluene (>99.5%, Carl Roth), potassium tetrachloroplatinate(II) (98%, K_2PtCl_4 , Sigma Aldrich), sodium tetrachloropalladate(II) ($\geq 99.99\%$, Na_2PdCl_4 , Sigma Aldrich), nitroarenes (Sigma Aldrich), amines (Sigma Aldrich), propene (99.97%, Linde Gas) and *n*-octane (99.5%, VWR Chemicals), silicon carbide (Korund Benátky, s.r.o.) were used as received.

2.2. Catalysts synthesis

2.2.1. Synthesis of 1-methyl-3-(triethoxysilyl propyl) imidazolium chloride

1-methyl-3-(triethoxysilyl propyl) imidazolium chloride (ImILs) was synthesized according to the literature [37,44,45]. In total, 10 mmol (3-chloropropyl)triethoxysilane and an equimolar amount of 1-methylimidazole were dissolved in toluene. The mixture was stirred under N_2 atmosphere at 70 °C for 18 h. The crude product was precipitated in cold diethyl ether and collected by centrifugation. For further purification, ImILs were dissolved in dichloromethane and precipitated in cold



Scheme 1. Schematic illustration of the encapsulation process for ImIL-assisted metal encapsulation during zeolite crystallization. SAC refers to steam-assisted crystallization.

diethyl ether. The final product was dried in a vacuum oven, at room temperature, overnight. Successful synthesis of the ImILs was confirmed by ^1H NMR spectra after dissolution in D_2O (Fig. S1).

2.2.2. Synthesis of standard MFI with TPAOH

The MFI zeolite was synthesized using the steam-assisted crystallization method according to the procedure described in literature [46–48]. In a typical preparation, 0.19 g of $\text{Al}(\text{NO}_3)_3 \cdot 9\text{H}_2\text{O}$ and 0.14 g of NaOH were dissolved in 3.58 g of water containing 3.84 g of 40% TPAOH water solution. After stirring for 15 min, 6.25 g of TEOS was added at the following molar gel composition: 1 SiO_2 :0.0083 Al_2O_3 :0.03 Na_2O :0.25 TPAOH:15 H_2O . The reaction mixture was stirred (500 rpm) at room temperature for 12 h and then dried overnight to obtain a dry solid by lyophilization. Subsequently, the solid was grounded into a fine powder and transferred to a glass vial, which was placed in a 100 mL Teflon-lined autoclave containing 1 mL of deionized water on the bottom (steam-assisted crystallization). The autoclave was placed in an oven at 170 °C for 3 days. Then, the autoclave was cooled down, and the resulting solid was washed by deionized water, centrifuged three times and dried at 60 °C in the oven. Finally, the sample was calcined in air at 550 °C for 6 h.

2.2.3. Synthesis of MFI with ImILs

Synthesis of MFI with ImILs was performed according to the procedure for standard MFI extended by adding 0.33 g ImILs. The sample was designated as MFI_{ImILs}.

2.2.4. Synthesis of metal@MFI with TPAOH

The metal@MFI catalysts were synthesized by following the procedure used for standard MFI extended by introduction of metal precursors. The metal NPs were generated by adding the water solution of the metal sources (21.3 mg of K_2PtCl_4 or 27.3 mg of Na_2PdCl_4) to the reaction mixture. The procedure continued as performed for standard MFI. The synthesized samples were named as Pt@MFI and Pd@MFI.

2.2.5. Synthesis of metal@MFI with ImILs

Metal@MFI with ImILs were prepared by following the procedure used to synthesize metal@MFI extended by adding ImILs. Metal sources and ImILs (0.33 g) were dissolved in deionized water, subsequently adding this solution to the reaction mixture. The procedure continued as performed for standard MFI. The products were designated as Pt@MFI_{ImILs} and Pd@MFI_{ImILs}.

2.2.6. Synthesis of metal@MFI_{Imp} via impregnation

In total, 10.6 mg of K_2PtCl_4 or 13.6 mg of Na_2PdCl_4 was dissolved into 25 mL of deionized water and mixed with 1 g of MFI_{ImILs}, followed by drying in the oven and calcination under the conditions mentioned above and designated as Pt@MFI_{Imp} and Pd@MFI_{Imp}.

2.3. Characterization

List of all samples investigated is shown in Table 1. Powder X-ray diffraction (PXRD) measurements were taken on a Bruker AXS D8 Advance diffractometer with a graphite monochromator and a position

Table 1
The list of investigated samples.

Name	Metal precursors	SDA
Standard MFI	–	TPAOH
MFI _{ImILs}	–	ImILs/TPAOH
Pt@MFI	✓	TPAOH
Pd@MFI	✓	TPAOH
Pt@MFI _{ImILs}	✓	ImILs/TPAOH
Pd@MFI _{ImILs}	✓	ImILs/TPAOH
Pt@MFI _{Imp}	✓	ImILs/TPAOH
Pd@MFI _{Imp}	✓	ImILs/TPAOH

sensitive detector Vantec-1 in the Bragg–Brentano geometry using $\text{CuK}\alpha$ ($\lambda = 0.1542$ nm) radiation with a speed of 0.25 ($2\theta/\text{min}$).

^1H NMR spectra were recorded on a Varian UNITYINOVA 400 instrument. Chemical shifts are reported in ppm (δ) relative to tetramethylsilane (1H) and referenced to the solvent signal (δ): 4.75 ppm (D_2O).

Nitrogen sorption isotherms were measured using a Micromeritics ASAP 2020 static volumetric apparatus at -196 °C. The surface area, S_{BET} , was calculated using adsorption data in the range of relative pressures $p/p_0 = 0.05$ – 0.2 . The external surface area (S_{ext}) of the samples was evaluated using the t -plot method. The adsorbed amount at relative pressure $p/p_0 = 0.97$ reflects the total adsorption capacity (V_{tot}). The NLDFT algorithm using standard Micromeritics software for cylindrical pores was applied to estimate micropore volumes (V_{mic}). Pore size distributions were calculated using the BJH model.

Solid-state ^{29}Si and ^{27}Al MAS NMR spectra were measured on an Avance III HD (Bruker) spectrometer working with a 9.4 T standard-bore superconducting magnet.

The Pt and Pd loading of the catalysts were determined by ICP-OES (ThermoScientific iCAP 7000) analysis.

The size and shape of the crystals were measured by scanning electron microscopy (SEM), under a JEOL JSM-5500LV microscope. In each measurement, the sample was coated with a thin platinum (~ 10 nm) layer by sputtering in the vacuum chamber of a BAL-TEC SCD-050.

STEM images were acquired on a JEOL NeoARM 200F operated at 200 kV. The surface-weighted mean nanoparticle diameter was calculated by $d_{\text{TEM}} = \sum n_i d_i^3 / \sum n_i d_i^2$, where n_i is the number of metal nanoparticles with diameter d_i .

2.4. Nitroarene hydrogenation

The hydrogenation reaction was performed in a 50 mL stainless steel reactor with a flexible metal capillary connected to a hydrogen supply system, which recorded the consumption of hydrogen. Before the reaction, the catalysts were reduced in H_2 atmosphere at 250 °C for 2 h. Then, the catalysts (Pt@MFI_{ImILs} or Pt@MFI_{Imp}, 50 mg), n -octane (5 mL), and nitroarenes (1.5 mmol) were loaded into the reactor. Once sealed, the reactor was purged by flushing two times with 0.3 MPa of hydrogen, pressurized to 0.6 MPa, and placed in an oil bath. After reaching the desired temperature (100 °C), the reactor was shaken using a vibrator. After finishing the reaction, the reaction mixture was analyzed by gas chromatography (Hewlett Packard 5990 with FID detector, column 0.3×60 cm packed with 10% SE 30 on Chromaton N AW). The recycling study of the Pt@MFI_{ImILs} was performed using the following method. After the reaction, the catalyst was collected, washed with 5 mL of n -octane for two times and used for the next cycle. After the 4th cycle, the Pt@MFI_{ImILs} was washed with 5 mL of cyclopentyl methyl ether and used for the 5th cycle. For identification purposes, retention times of the various reactants and products within the gas chromatogram were compared with those of commercially available standards. Conversion and selectivity were calculated from the corresponding GC areas.

The initial reaction rate was calculated as follows: $r = \frac{N_0 - N_{r(t)}}{t \cdot m_{\text{Pt}}}$

where N_0 is the initial molar amount of reactant, $N_{r(t)}$ is the molar amount of reactant at a specific time, m_{Pt} is the amount of Pt in the catalyst based on the ICP-OES measurement, $m_{\text{Pt}} = m_{\text{cat}} \cdot \text{Pt}_{\text{content}}$, and t is the reaction time to reach $\sim 20\%$ conversion.

2.5. Propene hydrogenation

The catalytic activity of the Pd@MFI_{ImILs} and Pd@MFI_{Imp} was studied in hydrogenation of propene on a plug-flow fix-bed vertical tubular shape reactor at atmospheric pressure. We used 10 mg of the catalysts with the desired grain size of 0.35–0.50 mm, added to 20 mg of SiC, with the same grain size, as an inert matrix to have an appropriate catalytic bed. Before each catalytic test, the catalysts were pretreated by

heating them in the flow of He/H₂ gas mixture (at 32.7 and 6 mL min⁻¹ flow rates, respectively) with a heating rate of 5 °C min⁻¹ to 400 °C, keeping the catalyst at this temperature for 2 h. After cooling down, the catalytic test started when adding 2 mL·min⁻¹ of propene to the feed (C₃H₆/H₂/He = 5/15/80 vol%) with a total flow rate of 40.7 mL min⁻¹. The variation of catalyst activity as a function of time-on-stream was tested at 20 °C. The catalytic activity was analyzed under steady-state conditions (first run after 25 min in stream), regenerating the catalyst between consecutive cycles by using He and O₂, at a flow rate of 32.7 and 1.7 mL min⁻¹ (He/O₂ = 95/5 vol%), respectively, at 500 °C (with heating rate 5 °C min⁻¹), for 1 h. The initial reaction rates were calculated as described for nitroarene hydrogenation.

3. Results and discussion

The powder X-ray diffraction (PXRD) patterns of the resulting catalysts indicated the formation of a typical MFI zeolite structure without any phase impurity [49] (Fig. 1a and b), in addition to the presence of ImLs during the synthesis, which had no obvious effect on the crystallization of the MFI zeolite. Notably, no peaks assigned to Pt (39.8° and 46.2°) [50] or Pd (39.9°, 46.4°) [51] phases were present in the diffractograms, thus indicating that no large Pt and Pd species were formed.

Solid ²⁹Si MAS NMR and ²⁷Al MAS NMR spectra of the Pt@MFI_ImLs and Pd@MFI_ImLs catalysts and standard MFI (without the addition of metal precursors and ImLs) are shown in Fig. S2. A broad resonance in

the range from -106 ppm to -116 ppm was observed in the ²⁹Si MAS NMR spectra. The proof of the presence of AlOSi(OSi)₃ and/or HOSi(OSi)₃ sites in MFI framework is in the resonance between -106 ppm and -109 ppm. The resonance centered at -110 ppm indicated the existence of Si(OSi)₄ groups [52,53]. The ²⁷Al MAS NMR exhibited a dominant resonance at 55 ppm, which originated from tetrahedrally coordinated Al [54,55]. These results revealed negligible lattice distortion after Pt and Pd NP encapsulation into the MFI zeolite. This distortion may be caused by framework defects resulting from the encapsulation of nanoparticles larger than the zeolite pores.

The textural properties of metal-supported and standard MFI samples were evaluated by N₂ sorption at -196 °C (Fig. 1c, d and Table 2). The standard MFI sample showed a type I isotherm, which is

Table 2
Textural parameters, metal loading and Si/Al ratio of the investigated samples.

Samples	S_{BET} m ² g ⁻¹	V_{mic} cm ³ g ⁻¹	V_{tot} cm ³ g ⁻¹	Metal loading (wt%)	Si/Al ratio
Pt@MFI	425	0.14	0.30	0.42	57
Pd@MFI	422	0.13	0.31	0.59	63
Pt@MFI_ImLs	326	0.09	0.22	0.40	66
Pd@MFI_ImLs	324	0.08	0.23	0.53	56
Pt@MFI_imp	333	0.08	0.23	0.64	62
Pd@MFI_imp	345	0.09	0.22	0.68	62
MFI_ImLs	383	0.14	0.20	-	58
Standard MFI	383	0.14	0.23	-	61

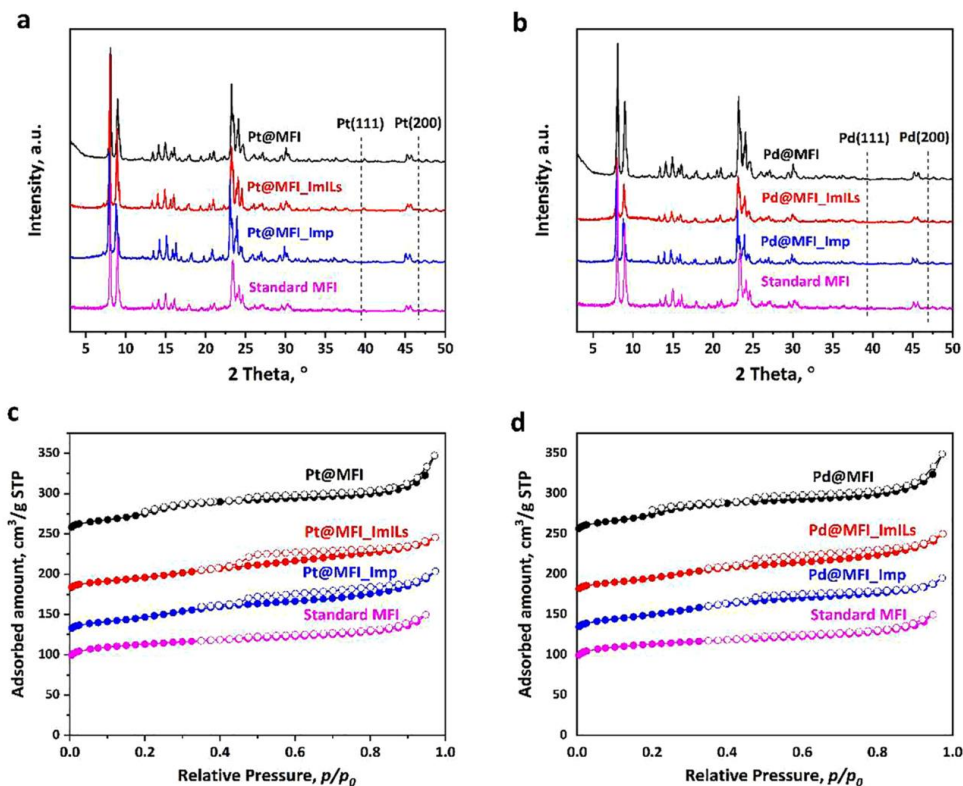


Fig. 1. PXRD patterns (a, b) and nitrogen adsorption (●) and desorption (○) isotherms (c, d) of MFI-supported Pt (a, c) and Pd (b, d) catalysts vs. standard MFI. The isotherms for metal@MFI, metal@MFI_ImLs and metal@MFI_imp were offset vertically by 150, 100 and 50 cm³ g⁻¹ STP, respectively.

characteristic of microporous materials. After introducing the metal precursors during zeolite crystallization, the adsorption isotherms of Pt- and Pd-supported MFI samples maintained their character, with some adsorption also in the interparticle space. Interestingly, no difference in textural properties was observed among samples prepared with and without ImILs. The micropore volumes (Table 2) of metal@MFI_ImILs and metal@MFI_Imp were $0.08\text{--}0.09\text{ cm}^3\text{ g}^{-1}$. These values were smaller than the micropore volume of standard MFI ($0.14\text{ cm}^3\text{ g}^{-1}$) due to partial pore blocking with encapsulated metal NPs. The Pt and Pd loading in metal@MFI_ImILs were approximately 0.40 and 0.53 wt%, as estimated based on ICP-OES measurements (Table 2). In turn, metal@MFI_Imp were characterized by higher metal loadings (0.64 and 0.68 for Pt and Pd, respectively).

Scanning electron microscope (SEM) images of metal-supported MFI catalysts showed that all the resulting catalysts had spherical crystals with sizes ranging from 0.5 to 2 μm (Fig. S3). Figs. 2 and 3 show STEM images of metal@MFI, metal@MFI_ImILs and metal@MFI_Imp (metal = Pt or Pd).

STEM images of Pt@MFI_ImILs and Pd@MFI_ImILs catalysts synthesized with the protection of metal precursors by ImILs are shown in Figs. 2a, b and 3a, b. Catalysts prepared without the ImILs as well as impregnated zeolites were compared (Fig. 2e, f and 3e, f) to describe the effect of ImILs on the properties of the final catalysts. Analysis of the STEM images showed that the sizes of Pt and Pd NPs (visible as white, bright spots) in Pt@MFI and Pd@MFI were relatively large, with average diameters of $\sim 4\text{ nm}$ and $\sim 18\text{ nm}$, respectively and were located mostly on the surface of MFI zeolite crystals. STEM images of catalysts prepared with the ionic liquids (Figs. 2a, b and 3a, b) show that Pt@MFI_ImILs and Pd@MFI_ImILs contained relatively small metal NPs distributed throughout zeolite crystals. The calculated surface-weighted mean nanoparticle diameters, d_{TEM} , were approximately 1.0 nm for Pt@MFI_ImILs and 1.7 nm for Pd@MFI_ImILs (see histograms in the Figs. 2c and 3c). The nanoparticle size distribution is relatively narrow indicating that method utilizing ImILs, and their protecting effect, is

suitable to produce material with smaller metal clusters than in the case of metal@MFI prepared without the ImILs or impregnated MFI. In addition, the STEM images in Figs. 2a and 3a showing lattice fringes confirm the ordered porous structure of MFI zeolite. The corresponding STEM-EDS analysis of Pt@MFI_ImILs and Pd@MFI_ImILs (Figs. 2d and 3d, respectively) confirmed the presence of metal nanoparticles and revealed the homogeneous distribution of Pt and Pd elements in the samples. The large-scale EDS elemental maps of Pt@MFI_ImILs and Pd@MFI_ImILs are presented in Figs. S4 and S5. These results proved the protective effect of ImILs on metal precursors during zeolite crystallization. The catalysts prepared with ImILs are small and well-dispersed metal nanoparticles, which are primarily located in the zeolite matrix. The MFI pore system is 3-dimensional and consists of 10-ring pores. It contains two intersecting channels: straight parallel to [010] and sinusoidal, along [100] having channel diameter 0.54–0.56 nm (based on oxygen radii of 0.135 nm) [49]. The observed d-spacing of approximately 0.55 nm (Fig. 4a, b) confirms the structure of the MFI zeolite. Noticeably, the sizes of the Pt and Pd NPs were larger than sinusoidal and intersectional channels ($\sim 0.9\text{ nm}$) of MFI [30]. The Pt and Pd NPs likely settled in the spaces between two interconnected channels and overgrown by the zeolite during the crystallization process, as shown in Fig. 4. Zeolite crystallizes around the formed metal clusters which most probably creates some local framework defects where NPs are positioned. This explains why some metal species are bigger than zeolite voids. Inevitably, some metal NPs were also present on the surface of the catalysts. In contrast to samples prepared with the protection of ImILs (Pt@MFI_ImILs and Pd@MFI_ImILs), the impregnated catalysts (Pt@MFI_Imp and Pd@MFI_Imp) showed an uneven distribution of Pt and Pd NPs in Fig. 2f and 3f. Moreover, the average diameters of the metal NPs in impregnated catalysts were significantly larger (approximately 5 nm and 6 nm for Pt and Pd, respectively). In addition, STEM images (Figs. 2f and 3f) clearly show that most metal NPs were situated on the external surface of the impregnated zeolite crystals.

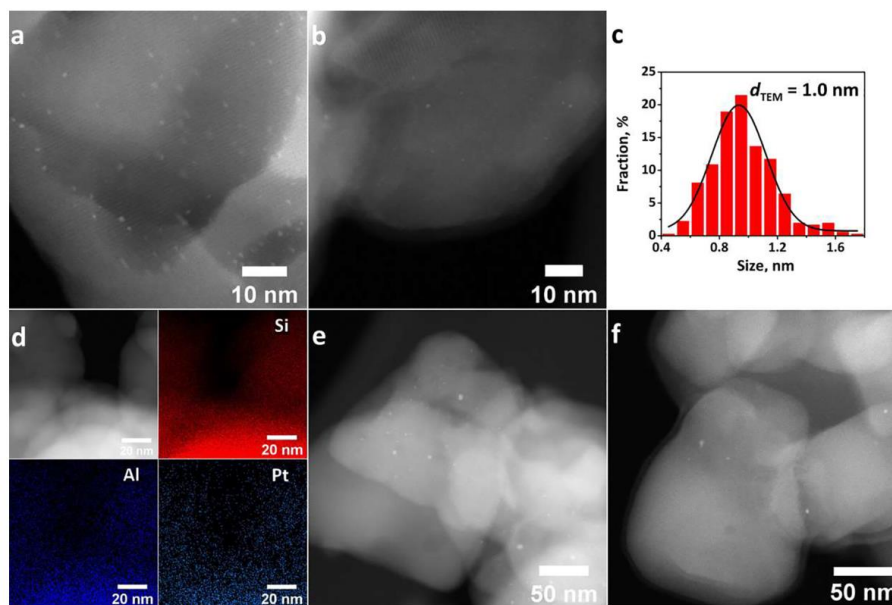


Fig. 2. STEM images (a, b), corresponding particle size histogram (c), and EDS maps of Si, Al, and Pt element distribution of Pt@MFI_ImILs (d); STEM images of Pt@MFI (e) and Pt@MFI_Imp (f).

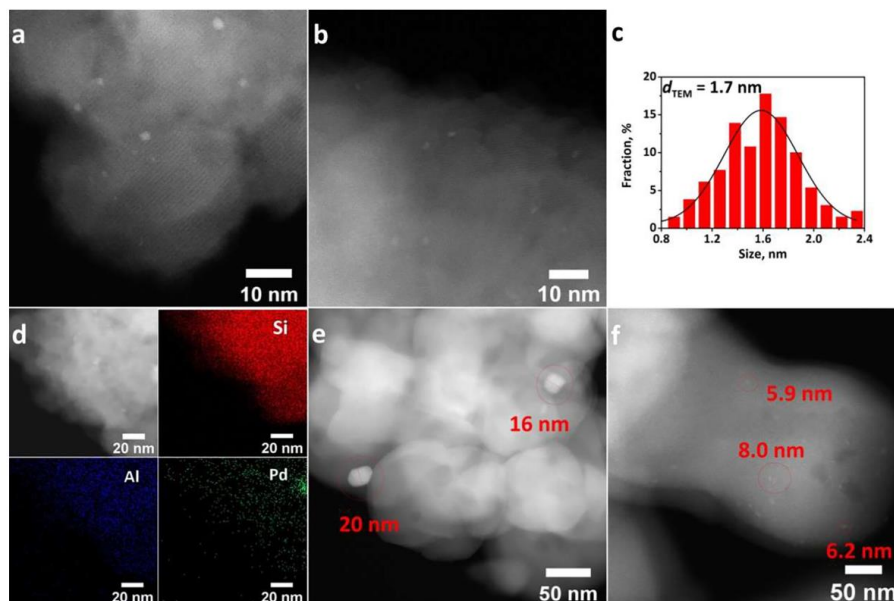


Fig. 3. STEM images (a, b), corresponding particle size histogram (c), and EDS maps of Si, Al, and Pd element distribution of Pd@MFI_Imls (d); STEM images of Pd@MFI (e) and Pd@MFI_Imp (f).

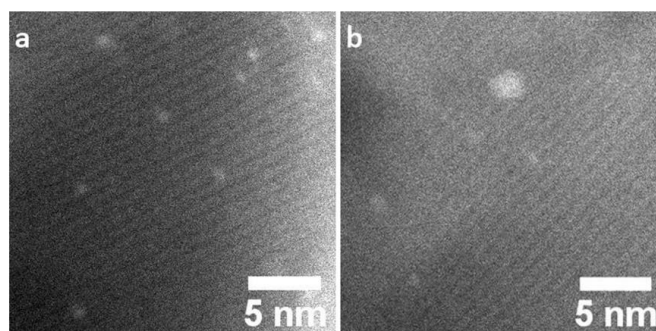


Fig. 4. STEM images of Pt@MFI_Imls (a), Pd@MFI_Imls (b) showing Pt and Pd NPs confined in the MFI zeolite matrix.

3.1. Nitroarene hydrogenation

Nitroarene hydrogenation (see Table 3) was chosen as model reaction to evaluate the catalytic performance of Pt@MFI_Imls. Pt@MFI_Imp with similar textural properties was used for comparison. The functionalized anilines are key intermediates in the industrial production of pharmaceuticals, agrochemicals, pigments, dyes, and polymers [56,57]. Nitroarene hydrogenation is a sustainable, well-established synthetic method, considering its environmental friendliness and atomic efficiency [58]. Besides industrial importance, nitroarene hydrogenation is an excellent model reaction to validate confinement of metal NPs in zeolite support [59]. For that, nitroarenes with different sizes, namely, 4-nitrotoluene (kinetic diameter of 0.45×0.65 nm) and 1,3-dimethyl-5-nitrobenzene (kinetic diameter of 0.60×0.65 nm) in *n*-octane were hydrogenated to investigate the shape-selectivity of Pt@MFI_Imls and Pt@MFI_Imp catalysts. The

concentrations of metal nanoparticles in metal@MFI_Imls are rather low (less than one nanoparticle per hundreds of unit cells), thus the effect of NPs presence on the diffusion of reactants/products is not expected.

4-Nitrotoluene can access Pt NPs located on both internal and external surfaces of the MFI zeolites with a pore size of 0.54–0.56 nm [60] whereas the bulky 1,3-dimethyl-5-nitrobenzene can only access Pt NPs located on the external surface. Pt@MFI_Imls exhibited excellent reagent size-dependent selectivity (Fig. 5), thus supporting encapsulation of most Pt NPs in zeolite matrix upon Imls-assisted crystallization. The reduction of nitro group in 4-nitrotoluene reached >99% conversion. In contrast, 1,3-dimethyl-5-nitrobenzene conversion was only 5.8%. This hydrogenation was selective because the access of the bulky substrate to the catalytically active Pt NPs was hindered by the zeolite channel entrances. The 5.8% conversion of 1,3-dimethyl-5-nitrobenzene over Pt@MFI_Imls was perhaps hydrogenated by the tiny amount of Pt

Table 3

Hydrogenation of nitroarenes over the Pt@MFI_ImlLs and Pt@MFI_Imp catalysts, reaction conditions: 100 °C temperature; 0.6 MPa hydrogen pressure; 5 mL *n*-octane; 1.5 mmol nitroarenes, ~50 mg catalyst.

Entry	Substrates	Products	Catalysts	Time ^a (min)	Max. Conversion (%)	Selectivity ^b (%)
1			Pt@MFI_ImlLs	2	>99	>99
2			Pt@MFI_Imp	3	>99	>99
3			Pt@MFI_ImlLs	18	5.9	>99
4			Pt@MFI_Imp	6	94.8	>99

^a Time to reach 50% conversion.

^b Selectivity at maximum conversion (%).

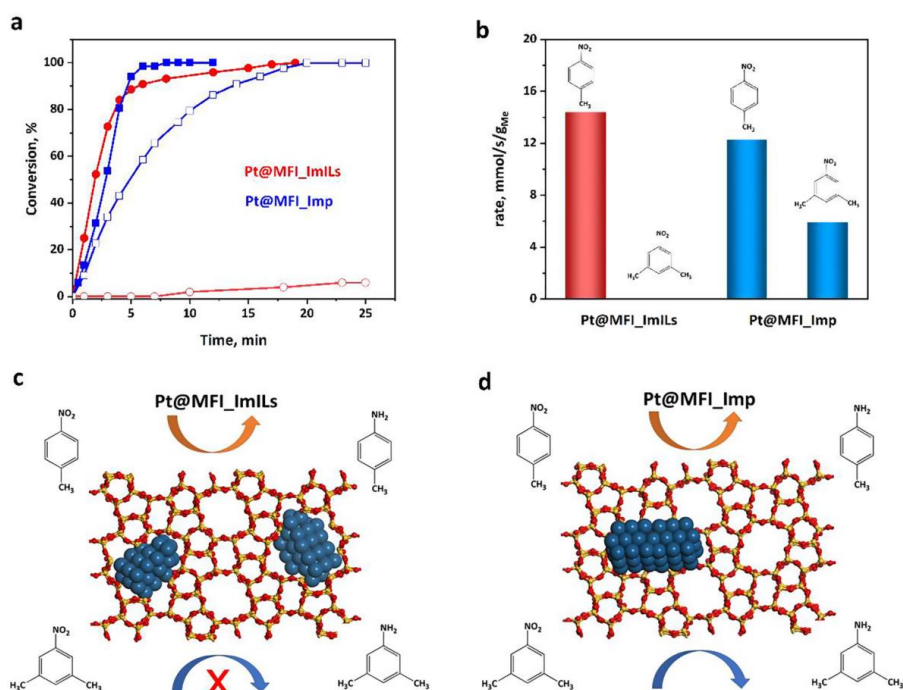


Fig. 5. Nitroarene hydrogenation over Pt@MFI_ImlLs and Pt@MFI_Imp catalysts. 4-Nitrotoluene (● and ■) and 1,3-dimethyl-5-nitrobenzene (○ and □) conversion over Pt@MFI_ImlLs (red) and Pt@MFI_Imp (blue) (a), the corresponding initial reaction rates (b), the reaction schemes for the hydrogenation of 4-nitrotoluene and 1,3-dimethyl-5-nitrobenzene over Pt@MFI_ImlLs (c) and Pt@MFI_Imp catalysts (d).

NPs situated on the entrances of zeolite channels. Conversely, both 4-nitrotoluene and 1,3-dimethyl-5-nitrobenzene were easily hydrogenated over Pt@MFI_Imp catalyst, achieving conversions >99% and 94.8%, respectively, which indicates that the Pt NPs are located mostly on the

external surface, thus allowing 4-nitrotoluene and 1,3-dimethyl-5-nitrobenzene to access the active sites. The shape-selective catalytic performance of Pt@MFI_ImlLs unambiguously demonstrated that the Pt NPs were confined in the pores of the MFI zeolite prepared using the method

reported here *via* protection of Pt precursors with ImILs. Furthermore, the higher initial reaction rate of the 4-nitrotoluene hydrogenation over Pt@MFI_ImILs than over Pt@MFI_Imp (14.5 vs. 12.3 mmol/s/g_{Me}) agrees with the smaller size of the Pt NPs in the former catalyst. The catalytic performances of 4-nitrotoluene hydrogenation on various catalysts according to studies recently published in the literature are outlined in Table S1.

The size stability of Pt NPs in Pt@MFI_ImILs and Pt@MFI_Imp was further investigated after one cycle of 4-nitrotoluene hydrogenation. As shown in Fig. S6a, the size of the Pt NPs in the spent Pt@MFI_ImILs catalyst remained almost unchanged due to the confinement effect of the rigid MFI zeolite framework. After treating Pt@MFI_Imp under the same reaction conditions, the metal NPs readily aggregated into large metal nanoparticles with a diameter of approximately 4–12 nm (Fig. S6b) due to their location on the external surface.

The reusability of the Pt@MFI_ImILs catalyst was investigated by performing the recycle tests in a series of consecutive 4-nitrotoluene hydrogenation cycles (Fig. 6). After three cycles, the conversion and reaction rates decreased to 16.9% and 0.2 mmol/s/g_{Me}, respectively. Once washed with cyclopentyl methyl ether overnight, the conversion reached 80.4%, and the reaction rate reached 7.7 mmol/s/g_{Me}. The STEM images and size distribution of the 4-fold recycled and subsequently regenerated Pt@MFI_ImILs catalyst are shown in Fig. 7. The average size of Pt NPs did not change significantly, increasing from approx. 1.0 nm (fresh catalyst) to 1.1 nm (spent catalyst). Furthermore, the spent Pt@MFI_ImILs catalyst preserved the MFI structure, thus showing no structure collapse under these reaction conditions. These results demonstrated that the Pt@MFI_ImILs catalyst was most likely deactivated by polymeric or condensation by-products which were not completely washed with cyclopentyl methyl ether. As a result, the activity of Pt@MFI_ImILs catalyst was only partially recovered after catalyst regeneration (Fig. 6a, b). The elemental analysis showed that the Pt content in the spent catalyst is 0.380 wt%, while in the fresh catalyst was 0.396 wt%. The relative change of the Pt concentration is less than 5% which confirms a negligible leaching of the metal during the reaction.

3.2. Propene hydrogenation

Simultaneously, we chose propene hydrogenation as model reaction to evaluate the catalytic performance of Pd@MFI_ImILs [61–63]. For comparison purposes, the Pd@MFI_Imp catalyst was also tested under the same mild reaction conditions (C₃H₆/H₂/He = 5/15/80 vol%; total flow rate: 40.7 mL min⁻¹, atmospheric pressure, 20 °C), propane was the only reaction product detected by the GC. With a kinetic diameter of 0.42 × 0.32 nm, the propene molecule can easily diffuse through 10-rings of MFI and reach the active sites of the Pd NPs effortlessly.

Undoubtedly, propane (0.46 × 0.30 nm) can also smoothly diffuse away from the active sites. Fig. 8a, c shows the time-on-stream (TOS) plot of propene conversion over the Pd@MFI_ImILs and Pd@MFI_Imp catalysts utilized for three cycles.

At the first cycle, propene conversion reached approximately 96% over Pd@MFI_ImILs, with minor deactivation (the conversion decreased to 88% at TOS = 105 min). The spent catalysts were regenerated by calcination at 500 °C in the flow of 5 vol% of oxygen in He for 1 h and then subjected to another catalytic cycle. In subsequent cycles, propene conversion over Pd@MFI_ImILs remained approximately 80%. Despite lower values of propene conversion were achieved over Pd@MFI_Imp catalyst, it remained at approximately 40% for three cycles. The variation of the reaction rates of propene hydrogenation as a function of TOS over the Pd@MFI_ImILs and Pd@MFI_Imp catalysts follows similar trend as propene conversion (Fig. 8b and d). The reaction rate on the Pd@MFI_ImILs catalyst was approximately 30 mmol/s/g_{Me} at TOS = 105 min for the first cycle, remained at approximately 25 mmol/s/g_{Me} in subsequent cycles. In contrast, Pd@MFI_Imp exhibited lower hydrogenation propene activity than Pd@MFI_ImILs and maintained similar reaction rates (around 9 mmol/s/g_{Me}) for three cycles.

Generally, the size and dispersion of metal NPs play a key role in the catalytic performance of metal-based catalysts. The low-coordinated metal atoms can be regarded as the catalytically active sites in various hydrogenation reactions. Consequently, the specific activity per metal atom usually increases with decreasing size of the metal nanoparticles [64,65]. The activity of Pd@MFI_ImILs was higher than that of Pd@MFI_Imp in propene hydrogenation, which was apparently caused by the small Pd NPs confined within the MFI framework, as confirmed in the STEM images (Figs. 3 and S5). Both Pd@MFI_ImILs and Pd@MFI_Imp showed slightly reduced catalytic activities at TOS in each cycle, which was likely caused by the formation of some carbon deposit or propene strongly adsorbed on the surface of the Pd NPs. For Pd@MFI_ImILs catalyst, the deactivation after the first cycle can be explained by the slight aggregation of Pd NPs (due to the high temperature treatment before next catalytic test). In the following cycles, we observed similar propene conversions, which suggest that the nanoparticles maintained their size (approximately 2 nm), as shown in Fig. 9. In contrast, the size of the Pd NPs in Pd@MFI_Imp increased from approximately 6 nm to 10 nm (Fig. S8). These results confirmed that, with the protection effect of ImILs, the Pd NPs confined evenly in the MFI zeolite, thereby limiting the aggregation during the reaction and regeneration process.

4. Conclusions

We proposed a new strategy for the protection of metal NPs during the hydrothermal synthesis of zeolites. This method provides the

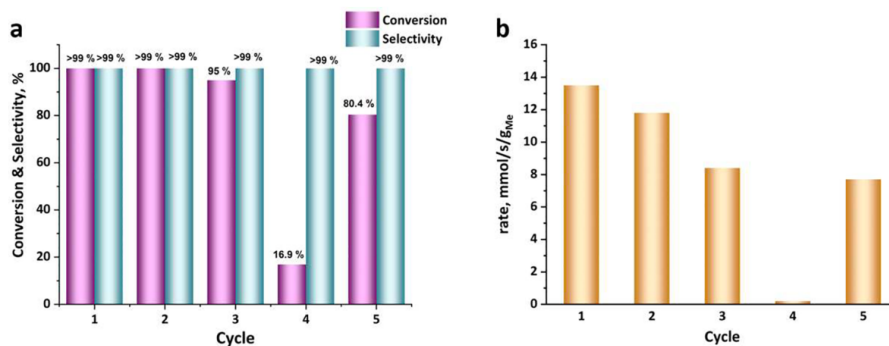


Fig. 6. Recycle study of Pt@MFI_ImILs catalyst in 4-nitrotoluene hydrogenation reaction. Conversion and selectivity (a), the corresponding initial reaction rate (b),

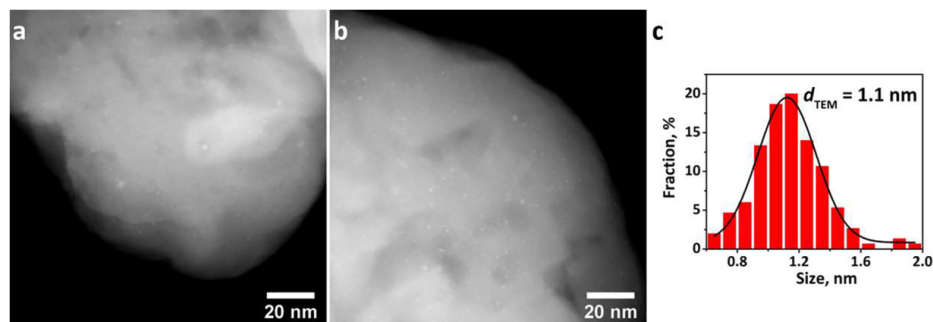


Fig. 7. STEM images of the 4-fold recycled and subsequently regenerated catalyst (a, b), and corresponding particle size histogram (c).

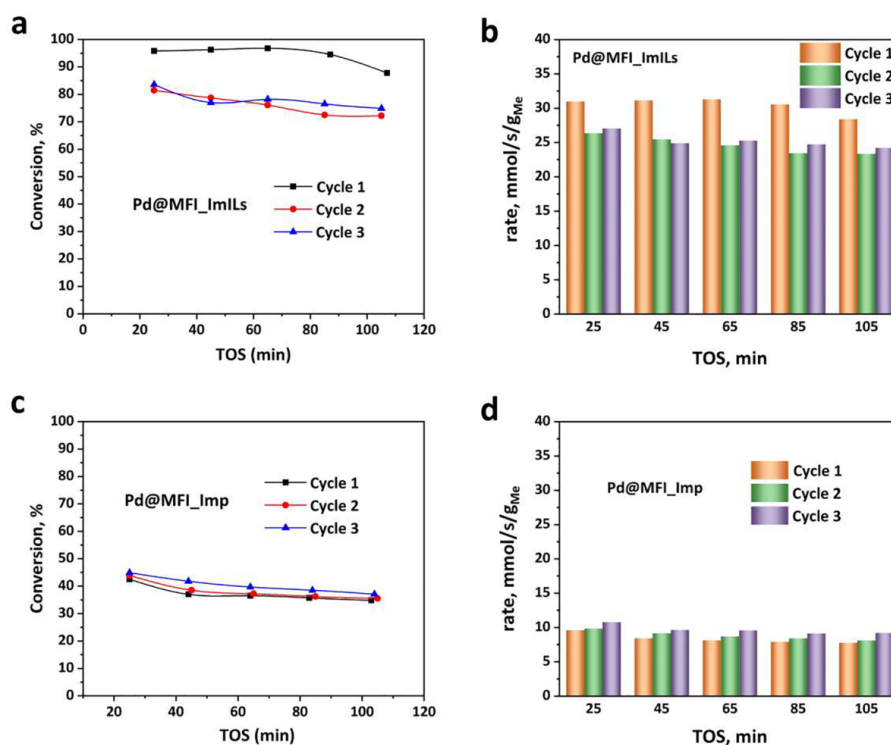


Fig. 8. Propene hydrogenation over Pd@MFI_Imls and Pd@MFI_Imp catalysts. Time-on-stream (TOS) plot of propene conversion at 20 °C used for three cycles over Pd@MFI_Imls (a) and Pd@MFI_Imp (c), rate of propene hydrogenation to propane as a function of TOS over Pd@MFI_Imls (b) and Pd@MFI_Imp (d).

catalysts with small and well-dispersed metal nanoparticles. Moreover, in principle, this approach can be used for any zeolite that can be prepared with ionic liquids, regardless of topology. Metal (Pt, Pd) NPs were encapsulated into the MFI zeolite using ImILs as an assistant agent via steam-assisted crystallization. This synthetic protocol synchronized zeolite crystallization with metal encapsulation.

The use of ImILs provides two key benefits: 1) protects the metal precursors through their electrostatic interactions with imidazolium groups, and 2) enables the participation of ImILs in zeolite crystallization through the alkoxy silane parts. The functional nature of ImILs

makes it possible to confine Pt and Pd NPs into the pore system of the MFI zeolite.

The resulting catalysts exhibited notable shape-selectivity in nitroarene hydrogenation over Pt@MFI_Imls and high activity in propene hydrogenation over Pd@MFI_Imls. Pt NPs encapsulated into MFI effectively reduced the nitro groups in 3-nitrotoluene, while the activity was significantly lower in the bulky 1,3-dimethyl-5-nitrobenzene. These shape-selectivity results also demonstrated the successful encapsulation of the metals. Pd@MFI_Imls exhibited higher activity and stability in propene hydrogenation than the impregnated sample. Furthermore, the

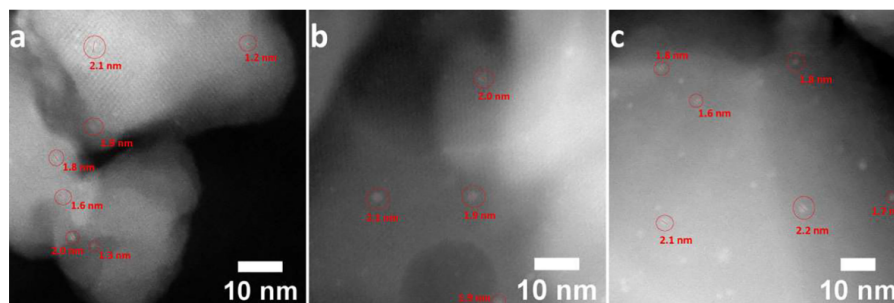


Fig. 9. STEM images of the spent Pd@MFI-ImILs after 1st cycle (a), 2nd cycle (b) 3rd cycle (c) of hydrogenation of propene.

recycle tests indicated that these zeolite-confined Pt and Pd NPs exhibited excellent stability. No nanoparticle sintering effect on the spent catalyst was observed in this study.

All data demonstrate that the ImIL-assisted synthetic strategy not only results in uniformly distributed, small metal NPs inside MFI zeolite, but also maintains the high catalytic activity, shape selectivity and good reusability of the catalysts. Accordingly, we expect that this strategy will be further extended to other metal precursors and zeolite frameworks as an alternative method for overcoming the challenges of sintering metal NPs into zeolite supports.

Declaration of Competing Interest

The authors declare that they have no known competing financial interests or personal relationships that could have appeared to influence the work reported in this paper.

Acknowledgements

This study is based upon work supported by the US Army DEVCOM-Atlantic under Award No. W911NF-17-S-0003. Authors would like to thank the OP VVV “Excellent Research Teams”, project no. CZ.02.1.01/0.0/0.0/15_003/0000417 – CUCAM. YZ would like to thank the GAUK project (No. 1372819). The authors thank Dr. Carlos V. Melo for editing the manuscript.

Appendix A. Supplementary data

Supplementary data to this article can be found online at <https://doi.org/10.1016/j.cej.2021.128599>.

References

- [1] Y. Li, J. Yu, New stories of zeolite structures: their descriptions, determinations, predictions, and evaluations, *Chem. Rev.* 114 (14) (2014) 7268–7316.
- [2] J. Prech, P. Pizarro, D.P. Serrano, J. Cejka, From 3D to 2D zeolite catalytic materials, *Chem. Soc. Rev.* 47 (22) (2018) 8263–8306.
- [3] W.J. Roth, P. Nachtigall, R.E. Morris, J. Cejka, Two-dimensional zeolites: current status and perspectives, *Chem. Rev.* 114 (9) (2014) 4807–4837.
- [4] D. Farrusseng, A. Tuel, Perspectives on zeolite-encapsulated metal nanoparticles and their applications in catalysis, *New J. Chem.* 40 (5) (2016) 3933–3949.
- [5] Y. Chai, W. Shang, W. Li, G. Wu, W. Dai, N. Guan, L. Li, Noble metal particles confined in zeolites: synthesis, characterization, and applications, *Adv. Sci.* 6 (16) (2019), 1900299 (1–19).
- [6] N. Wang, Q. Sun, J. Yu, Ultrasmall metal nanoparticles confined within crystalline nanoporous materials: a fascinating class of nanocatalysts, *Adv. Mater.* 31 (1) (2019), 1803966 (1–23).
- [7] S.B. Simonsen, I. Chorkendorff, S. Dahl, M. Skoglundh, J. Sehested, S. Helveg, Ostwald ripening in a Pt/SiO₂ model catalyst studied by in situ TEM, *J. Catal.* 281 (1) (2011) 147–155.
- [8] K. Wettergren, F.F. Schweinberger, D. Deiana, C.J. Ridge, A.S. Crampton, M. D. Rotzer, T.W. Hansen, V.P. Zhdanov, U. Heiz, C. Langhammer, High sintering resistance of size-selected platinum cluster catalysts by suppressed Ostwald ripening, *Nano Lett.* 14 (10) (2014) 5803–5809.
- [9] M. Shamzhy, M. Opanasenko, P. Concepcion, A. Martinez, New trends in tailoring active sites in zeolite-based catalysts, *Chem. Soc. Rev.* 48 (4) (2019) 1095–1149.
- [10] Z. Jin, L. Wang, E. Zuidema, K. Mondal, M. Zhang, J. Zhang, C. Wang, X. Meng, H. Yang, C. Mesters, F. Xiao, Hydrophobic zeolite modification for in situ peroxide formation in methane oxidation to methanol, *Science* 367 (6474) (2020) 193–197.
- [11] J. Deng, D. Deng, X. Bao, Robust catalysis on 2D materials encapsulating metals: concept, application, and perspective, *Adv. Mater.* 29 (43) (2017), 1606967 (1–23).
- [12] L. Liu, A. Corma, Metal catalysts for heterogeneous catalysis: from single atoms to nanoclusters and nanoparticles, *Chem. Rev.* 118 (10) (2018) 4981–5079.
- [13] L. Wang, S. Xu, S. He, F. Xiao, Rational construction of metal nanoparticles fixed in zeolite crystals as highly efficient heterogeneous catalysts, *Nano Today* 20 (2018) 74–83.
- [14] N. Kosinov, C. Liu, E.J.M. Hensen, E.A. Pidko, Engineering of transition metal catalysts confined in zeolites, *Chem. Mater.* 30 (10) (2018) 3177–3198.
- [15] R.J. White, R. Luque, V.L. Budarin, J.H. Clark, D.J. Macquarrie, Supported metal nanoparticles on porous materials. Methods and applications, *Chem. Soc. Rev.* 38 (2) (2009) 481–494.
- [16] Y. Shan, Z. Sui, Y. Zhu, J. Zhou, X. Zhou, D. Chen, Boosting size-selective hydrogen combustion in the presence of propene using controllable metal clusters encapsulated in zeolite, *Angew. Chem. Int. Ed.* 57 (31) (2018) 9770–9774.
- [17] K.H. Rasmussen, F. Goodarzi, D.B. Christensen, J. Mielby, S. Kegnes, Stabilization of metal nanoparticle catalysts via encapsulation in mesoporous zeolites by steam-assisted recrystallization, *ACS Appl. Nano Mater.* 2 (12) (2019) 8083–8091.
- [18] P. Gallezot, Preparation of metal clusters in zeolites, *Post-Synth. Modification I* (3) (2002) 257–305.
- [19] J. Shan, M. Li, L.F. Allard, S. Lee, M. Flytzani-Stephanopoulos, Mild oxidation of methane to methanol or acetic acid on supported isolated rhodium catalysts, *Nature* 551 (7682) (2017) 605–608.
- [20] X. Yang, X. Su, X. Chen, H. Duan, B. Liang, Q. Liu, X. Liu, Y. Ren, Y. Huang, T. Zhang, Promotion effects of potassium on the activity and selectivity of Pt/zeolite catalysts for reverse water gas shift reaction, *Appl. Catal. B* 216 (2017) 95–105.
- [21] L. Liu, U. Diaz, R. Arenal, G. Agostini, P. Concepcion, A. Corma, Generation of subnanometric platinum with high stability during transformation of a 2D zeolite into 3D, *Nat. Mater.* 16 (1) (2017) 132–138.
- [22] Y. Zhang, K. Fulajárová, M. Kubů, M. Mazur, M. Shamzhy, M. Hronec, J. Cejka, Controlling dispersion and accessibility of Pd nanoparticles via 2D-to-3D zeolite transformation for shape-selective catalysis: Pd@MWW case, *Mater. Today Nano* 8 (2019), 100056.
- [23] Y. Zhang, M. Kubů, M. Mazur, J. Cejka, Encapsulation of Pt nanoparticles into IPC-2 and IPC-4 zeolites using the ADOR approach, *Microporous Mesoporous Mater.* 279 (2019) 364–370.
- [24] J. Zhang, L. Wang, B. Zhang, H. Zhao, U. Kolb, Y. Zhu, L. Liu, Y. Han, G. Wang, C. Wang, D.S. Su, B.C. Gates, F.-S. Xiao, Sinter-resistant metal nanoparticle catalysts achieved by immobilization within zeolite crystals via seed-directed growth, *Nat. Catal.* 1 (7) (2018) 540–546.
- [25] J. Zhang, L. Wang, L. Zhu, Q. Wu, C. Chen, X. Wang, Y. Ji, X. Meng, F.S. Xiao, Solvent-free synthesis of zeolite crystals encapsulating gold-palladium nanoparticles for the selective oxidation of bioethanol, *ChemSusChem* 8 (17) (2015) 2867–2871.
- [26] T.L. Cui, W.Y. Ke, W.B. Zhang, H.H. Wang, X.H. Li, J.S. Chen, Encapsulating palladium nanoparticles inside mesoporous MFI zeolite nanocrystals for shape-selective catalysis, *Angew. Chem. Int. Ed.* 55 (32) (2016) 9178–9182.
- [27] Y. Yan, Z. Zhang, S.-M. Bak, S. Yao, X. Hu, Z. Shadice, C.-L. Do-Thanh, F. Zhang, H. Chen, X. Lyu, K. Chen, Y. Zhu, X. Lu, P. Ouyang, J. Fu, S. Dai, Confinement of ultrasmall cobalt oxide clusters within silicalite-1 crystals for efficient conversion of fructose into methyl lactate, *ACS Catal.* 9 (3) (2018) 1923–1930.
- [28] S. Goel, Z. Wu, S.I. Zones, E. Iglesia, Synthesis and catalytic properties of metal clusters encapsulated within small-pore (SOD, GIS, ANA) zeolites, *J. Am. Chem. Soc.* 134 (42) (2012) 17688–17695.
- [29] C. Wang, L. Wang, J. Zhang, H. Wang, J.P. Lewis, F. Xiao, Product selectivity controlled by zeolite crystals in biomass hydrogenation over a palladium catalyst, *J. Am. Chem. Soc.* 138 (25) (2016) 7880–7883.

- [30] N. Wang, Q. Sun, R. Bai, X. Li, G. Guo, J. Yu, In situ confinement of ultrasmall Pd clusters within nanosized silicalite-1 zeolite for highly efficient catalysis of hydrogen generation, *J. Am. Chem. Soc.* 138 (24) (2016) 7484–7487.
- [31] Q. Sun, N. Wang, Q. Bing, R. Si, J. Liu, R. Bai, P. Zhang, M. Jia, J. Yu, Subnanometric hybrid Pd-M(OH)₂, M = Ni Co, clusters in zeolites as highly efficient nanocatalysts for hydrogen generation, *Chem* 3 (3) (2017) 477–493.
- [32] M. Choi, Z. Wu, E. Iglesia, Mercaptosilane-assisted synthesis of metal clusters within zeolites and catalytic consequences of encapsulation, *J. Am. Chem. Soc.* 132 (26) (2010) 9129–9137.
- [33] T. Welton, Room-temperature ionic liquids. Solvents for synthesis and catalysis, *Chem. Rev.* 99 (8) (1999) 2071–2084.
- [34] F. Endres, S. Zein El Abedin, Air and water stable ionic liquids in physical chemistry, *Phys. Chem. Chem. Phys.* 8 (18) (2006) 2101–2116.
- [35] C.J. Mathews, P.J. Smith, T. Welton, A.J.P. White, D.J. Williams, In situ formation of mixed phosphine-imidazolylidene palladium complexes in room-temperature ionic liquids, *Organometallics* 20 (18) (2001) 3848–3850.
- [36] L.J.B. Lin, C.S. Vasam, Metal-containing ionic liquids and ionic liquid crystals based on imidazolium moiety, *J. Organomet. Chem.* 690 (15) (2005) 3498–3512.
- [37] T. Sasaki, C. Zhong, M. Tada, Y. Iwasawa, Immobilized metal ion-containing ionic liquids: preparation, structure and catalytic performance in Kharasch addition reaction, *ChemCommun* 19 (2005) 2506–2508.
- [38] E.R. Cooper, C.D. Andrews, P.S. Wheatley, P.B. Webb, P. Wormald, R.E. Morris, Ionic liquids and eutectic mixtures as solvent and template in synthesis of zeolite analogues, *Nature* 430 (7003) (2004) 10012–11016.
- [39] R.E. Morris, Ionic liquids and microwaves—making zeolites for emerging applications, *Angew. Chem. Int. Ed.* 47 (3) (2008) 442–444.
- [40] J.M. Martínez Blanes, B.M. Szyja, F. Romero-Sarria, M.A. Centeno, E.J. Hensen, J. A. Odriozola, S. Ivanova, Multiple zeolite structures from one ionic liquid template, *Chemistry* 19 (6) (2013) 2122–2130.
- [41] I. Capek, Noble Metal Nanoparticles, Springer, Tokyo, 2017.
- [42] H. Itoh, K. Naka, Y. Chujo, Synthesis of gold nanoparticles modified with ionic liquid based on the imidazolium cation, *J. Am. Chem. Soc.* 126 (10) (2004) 3026–3027.
- [43] J. Dupont, G.S. Fonseca, A.P. Umpierre, P.F. Fichtner, S.R. Teixeira, Transition-metal nanoparticles in imidazolium ionic liquids: recyclable catalysts for biphasic hydrogenation reactions, *J. Am. Chem. Soc.* 124 (16) (2002) 4228–4229.
- [44] B. Karimi, D. Enders, New N-heterocyclic carbene palladium complex/ionic liquid matrix immobilized on silica: application as recoverable catalyst for the Heck reaction, *Org. Lett.* 8 (6) (2006) 1237–1240.
- [45] Q. Dou, L. Liu, B. Yang, J. Lang, X. Yan, Silica-grafted ionic liquids for revealing the respective charging behaviors of cations and anions in supercapacitors, *Nat. Commun.* 8 (1) (2017), 2188 (1–9).
- [46] M. Matsukata, T. Osaki, M. Ogura, E. Kikuchi, Crystallization behavior of zeolite beta during steam-assisted crystallization of dry gel, *Microporous Mesoporous Mater.* 56 (1) (2002) 1–10.
- [47] C. Li, Y. Wang, B. Shi, J. Ren, X. Liu, Y. Wang, Y. Guo, Y. Guo, G. Lu, Synthesis of hierarchical MFI zeolite microspheres with stacking nanocrystals, *Microporous Mesoporous Mater.* 117 (1–2) (2009) 104–110.
- [48] H.J. Cho, D. Kim, J. Li, D. Su, B. Xu, Zeolite-encapsulated Pt nanoparticles for tandem catalysis, *J. Am. Chem. Soc.* 140 (41) (2018) 13514–13520.
- [49] D.H. Olson, G.T. Kokotailo, S.L. Lawton, W.M. Meier, Crystal structure and structure-related properties of ZSM-5, *J. Phys. Chem.* 85 (15) (1981) 2238–2243.
- [50] B.Y. Xia, H.B. Wu, J.S. Chen, Z. Wang, X. Wang, X.W. Lou, Formation of Pt-TiO₂-rGO 3-phase junctions with significantly enhanced electro-activity for methanol oxidation, *Phys. Chem. Chem. Phys.* 14 (2) (2012) 473–476.
- [51] L. Sun, S. Zhang, W. Bao, W. He, Catalytic properties of Pd nanoparticles supported on Cu₂O microspheres for hydrogen peroxide electroreduction, *RSC Adv.* 5 (66) (2015) 53320–53325.
- [52] J. Klinowski, T.A. Carpenter, L.F. Gladden, High-resolution solid-state n.m.r. studies of temperature-induced phase transitions in silicalite (zeolite ZSM-5), *Zeolites* 7 (1) (1987) 73–78.
- [53] C.J.H. Jacobsen, C. Madsen, T.V.W. Janssens, H.J. Jakobsen, J. Skibsted, Zeolites by confined space synthesis – characterization of the acid sites in nanosized ZSM-5 by ammonia desorption and 27Al/29Si-MAS NMR spectroscopy, *Microporous Mesoporous Mater.* 39 (1–2) (2000) 393–401.
- [54] P. Szazama, B. Wichterlova, J. Dedecek, Z. Tvaruzkova, Z. Musilova, L. Palumbo, S. Sklenak, O. Gonsiorova, FTIR and 27Al MAS NMR analysis of the effect of framework Al- and Si-defects in micro- and micro-mesoporous H-ZSM-5 on conversion of methanol to hydrocarbons, *Microporous Mesoporous Mater.* 143 (1) (2011) 87–96.
- [55] T. Yokoi, H. Mochizuki, S. Namba, J.N. Kondo, T. Tatsumi, Control of the Al distribution in the framework of ZSM-5 zeolite and its evaluation by solid-state NMR technique and catalytic properties, *J. Phys. Chem.* 119 (27) (2015) 15303–15315.
- [56] S. Cai, H. Duan, H. Rong, D. Wang, L. Li, W. He, Y. Li, Highly active and selective catalysis of bimetallic Rh3Ni1 nanoparticles in the hydrogenation of nitroarenes, *ACS Catal.* 3 (4) (2013) 608–612.
- [57] T. Iida, D. Zanchet, K. Ohara, T. Wakihara, Y. Roman-Leshkov, Concerted bimetallic nanocluster synthesis and encapsulation via induced zeolite framework demetallation for shape and substrate selective heterogeneous catalysis, *Angew. Chem. Int. Ed.* 57 (22) (2018) 6454–6458.
- [58] I. Sorribes, L. Liu, A. Corma, Nanolayered Co–Mo–S catalysts for the chemoselective hydrogenation of nitroarenes, *ACS Catal.* 7 (4) (2017) 2698–2708.
- [59] J. Zhang, L. Wang, Y. Shao, Y. Wang, B.C. Gates, F.S. Xiao, A Pd@zeolite catalyst for nitroarene hydrogenation with high product selectivity by sterically controlled adsorption in the zeolite micropores, *Angew. Chem. Int. Ed.* 56 (33) (2017) 9747–9751.
- [60] G.T. Kokotailo, S.L. Lawton, D.H. Olson, W.M. Meier, Structure of synthetic zeolite ZSM-5, *Nature* 272 (5652) (1978) 437–438.
- [61] C. Aaserud, A.-M. Hilmen, E. Bergene, S. Eri, D. Schanke, A. Holmen, Hydrogenation of propene on cobalt Fischer-Tropsch catalysts, *Catal. Lett.* 94 (3/4) (2004) 171–176.
- [62] M.A. El-Sayed, J.W. Yoo, Preparation of cubic Pt nanoparticles deposited on alumina and their application to propene hydrogenation, *ChemCatChem* 2 (3) (2010) 268–271.
- [63] N.M. Schweitzer, B. Hu, U. Das, H. Kim, J. Greeley, L.A. Curtiss, P.C. Stair, J. T. Miller, A.S. Hock, Propylene hydrogenation and propane dehydrogenation by a single-site Zn₂₊ on silica catalyst, *ACS Catal.* 4 (4) (2014) 1091–1098.
- [64] X.F. Yang, A. Wang, B. Qiao, J. Li, J. Liu, T. Zhang, Single-atom catalysts: a new frontier in heterogeneous catalysis, *Acc. Chem. Res.* 46 (8) (2013) 1740–1748.
- [65] B.C. Gates, M. Flytzani-Stephanopoulos, D.A. Dixon, A. Katz, Atomically dispersed supported metal catalysts: perspectives and suggestions for future research, *Catal. Sci. Technol.* 7 (19) (2017) 4259–4275.

Imidazolium-type ionic liquid-assisted formation of the MFI zeolite loaded with metal nanoparticles for hydrogenation reactions

Yuyan Zhang¹, Ang Li¹, Mehran Sajad², Katarína Fulajtárová³, Michal Mazur¹, Martin Kubů¹, Mariya Shamzhy¹, Milan Hronec³, Roman Bulánek², and Jiří Čejka¹

¹*Department of Physical and Macromolecular Chemistry, Faculty of Science, Charles University, Hlavova 2030/8, 128 43, Prague, Czech Republic*

²*Department of Physical Chemistry, Faculty of Chemical Technology, University of Pardubice, Studentská 573, 532 10 Pardubice, Czech Republic*

³*Department of Organic Technology, Slovak University of Technology, Radlinského 9, 812 37 Bratislava, Slovakia*

This file includes:

Figures S1 to S7

Table S1

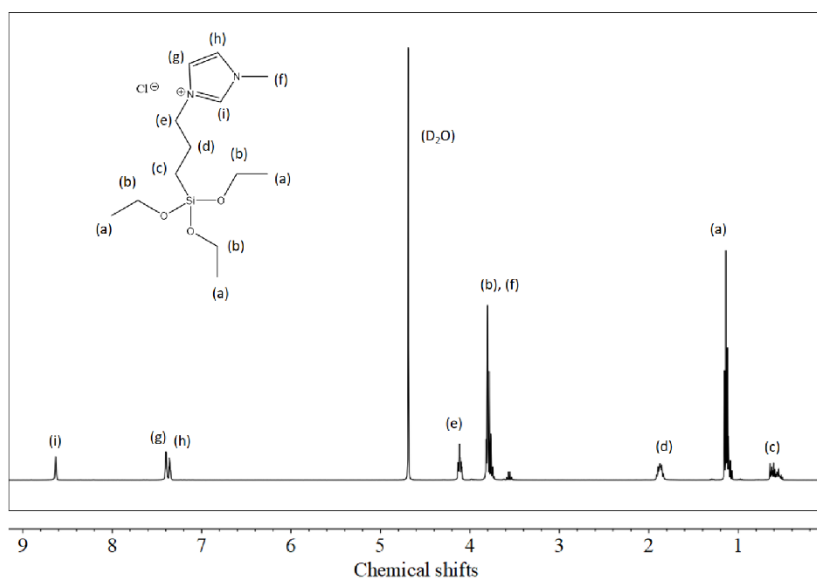


Figure S1. ¹H NMR spectra of IMLs.

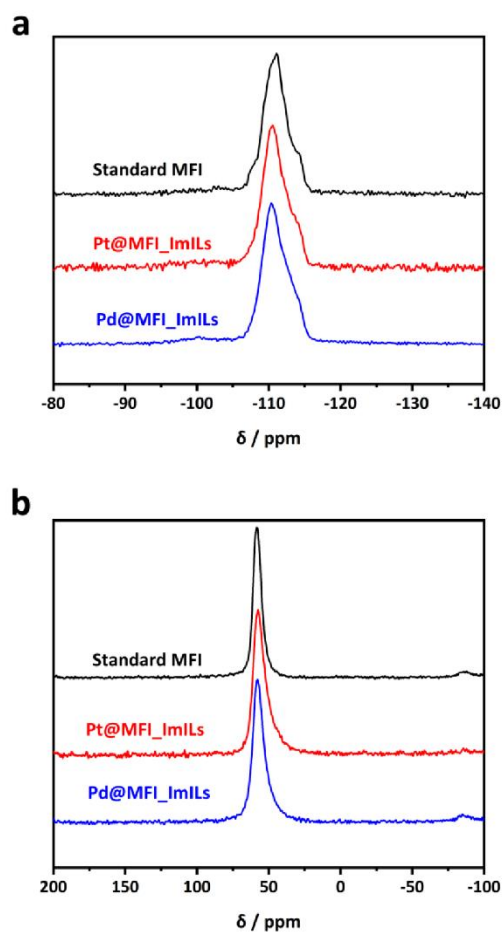


Figure S2. Solid ^{29}Si MAS NMR of Pt@MFI_Imls, Pd@MFI_Imls and standard **MFI** (a), Solid ^{27}Al MAS NMR of Pt@MFI_Imls, Pd@MFI_Imls and standard **MFI** (b).

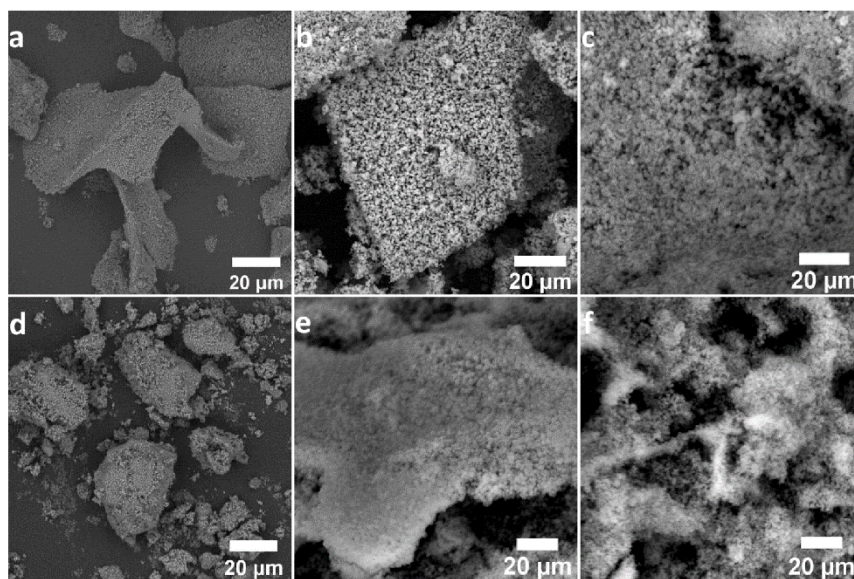


Figure S3. SEM images of Pt@MFI (a), Pt@MFI_ImlLs (b), Pt@MFI_Imp (c); Pd@MFI (d), Pd@MFI_ImlLs (e) and Pd@MFI_Imp (f).

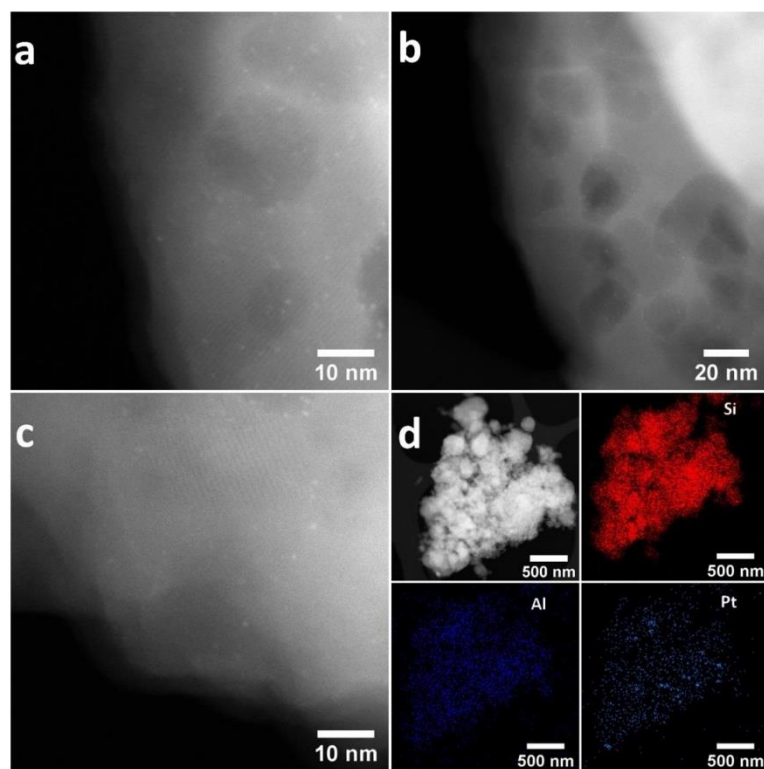


Figure S4. STEM images of Pt@MFI_lmls (a-c) showing zeolite structure (fringes) as well as Pt nanoparticles (bright spots), and STEM image with corresponding EDS maps of Si, Al, and Pt distribution (d).

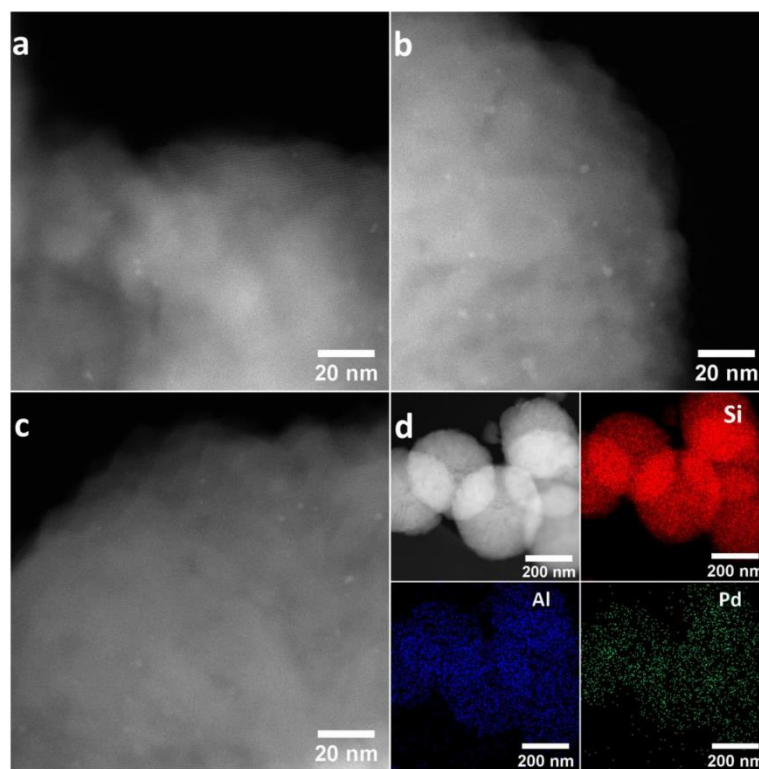


Figure S5. STEM images of Pd@MFI_ImILs (a-c) showing zeolite structure (fringes) as well as Pd nanoparticles (bright spots), and STEM image with corresponding EDS maps of Si, Al, and Pd distribution (d).

Table S1. Catalytic activities of various catalyst in the hydrogenation of 4-nitrotoluene according to the literature.

Catalyst	Type of support	Time	Conversion (%)	Yield (%)	Selectivity (%)	Ref
O-MoS ₂	--	1 h	>99	--	>99	1
rGO@Ag/Pd	Reduced graphene oxide	10 min	--	>99	--	2
MoO ₂ Cl ₂	--	48 h	--	100	--	3
Pd/HAM@γ-AIOOH	γ-AIOOH	90 min	100	--	100	4
colloidal nanoparticles	GA-Pt gum acacia	6 h	--	92	--	5
Pt@MIL-101	MIL-101	60 min	100	98.3	--	6
Ni ₅₀ Co ₅₀ BMNPs	--	1 h	--	96	--	7
Ni/CeO ₂ -CAS	CeO ₂	7 h	99.8	99.4	--	8
ALD Ni/SiO ₂	--	2 h	94.8	92.1	--	9
Ni ₂ P/PC-2	P-doped carbon	2 h	95	--	>99.9	10
ImmFe-IL	Ionic liquid	12 h	98	--	99	11
[Mo ₃ S ₄ (dnbpy) ₃]FB ₆	--	18 h	>99	>99	--	12
[FeF(L ₂)] [BF ₄]	--	2 h	>99	96	--	13
Fe-Ni NP	--	5 h	90	>99	94	14
rGO-Fe ₄₈ Pd ₅₂	Reduced graphene	10 min	>99	--	--	15

	oxide					
CuNi@MIL-101	MIL-101	4 min	--	>99	--	16
PdNi/mCN	N-doped carbon	60 min	96.8	--	100	17
Pd ⁰ -AmP-MCF	Mesocellular Foam	60 min	--	>99	--	18
Pd@NAC-800	N-doped carbon	2 h	>99	99	>99	19
Pd/N-CMK-3	Nitrogen- Doped Ordered Mesoporous Carbon	1 h	100	--	>99	20
micro-mesoporous iron oxide	--	50 min	>99	83	--	21
Rh ₃ Ni ₁	--	12 h	--	99	--	22
Co@NC-600	Nitrogen- doped carbon	5 h	>99	--	>99	23
Pt@MFI_1mILs	Zeolite	15 min	>99	--	>99	This work

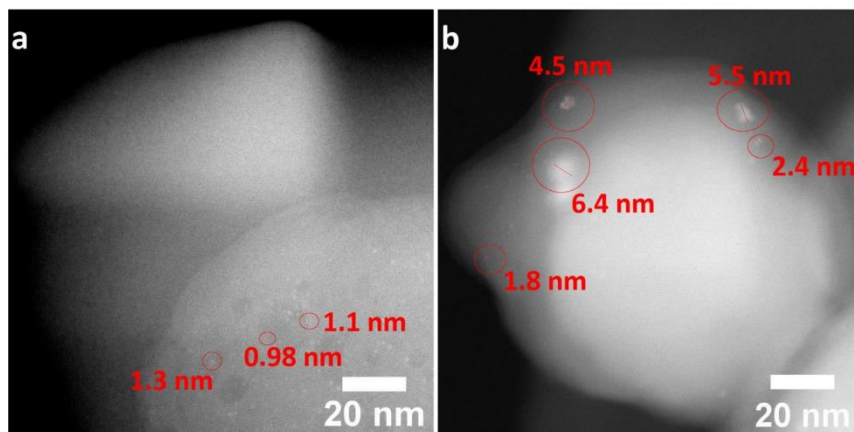


Figure S6. STEM images of Pt@MFI_Imls (a) and Pt@MFI_Imp (b) after one cycle of hydrogenation of 4-nitrotoluene.

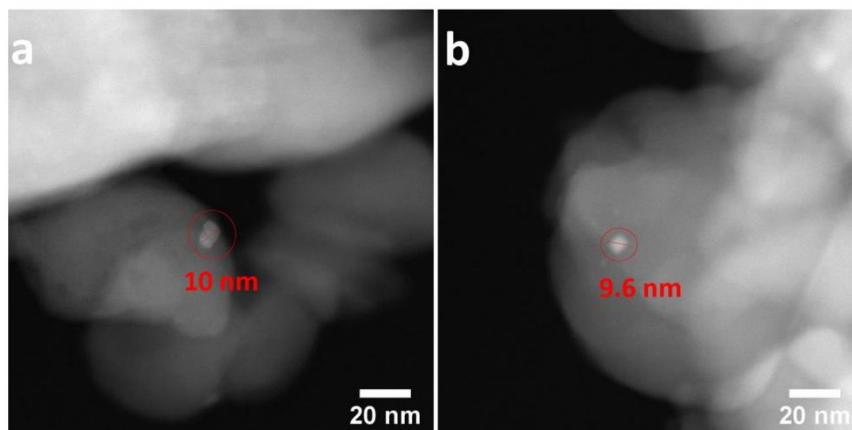


Figure S7. STEM images of the spent Pd@MFI_Imp after three cycles of hydrogenation of propene.

References

1. Zhang, C.; Zhang, Z.; Wang, X.; Li, M.; Lu, J.; Si, R.; Wang, F., Transfer hydrogenation of nitroarenes to arylamines catalysed by an oxygen-implanted MoS₂ catalyst. *Appl. Catal., A*. **2016**, *525*, 85-93.
2. Metin, O.; Can, H.; Sendil, K.; Gultekin, M. S., Monodisperse Ag/Pd core/shell nanoparticles assembled on reduced graphene oxide as highly efficient catalysts for the transfer hydrogenation of nitroarenes. *J. Colloid Interface Sci.* **2017**, *498*, 378-386.
3. Reis, P. M.; Royo, B., Chemoselective hydrogenation of nitroarenes and deoxygenation of pyridine N-oxides with H₂ catalyzed by MoO₂Cl₂. *Tetrahedron Lett.* **2009**, *50* (8), 949-952.
4. Tian, M.; Cui, X.; Dong, C.; Dong, Z., Palladium nanoparticles dispersed on the hollow aluminosilicate microsphere@hierarchical γ -AlOOH as an excellent catalyst for the hydrogenation of nitroarenes under ambient conditions. *Appl. Surf.* **2016**, *390*, 100-106.
5. Sreedhar, B.; Devi, D. K.; Yada, D., Selective hydrogenation of nitroarenes using gum acacia supported Pt colloid an effective reusable catalyst in aqueous medium. *Catal. Commun.* **2011**, *12*, 1009-1014.
6. Du, W.; Chen, G.; Nie, R.; Li, Y.; Hou, Z., Highly dispersed Pt in MIL-101: An efficient catalyst for the hydrogenation of nitroarenes. *Catal. Commun.* **2013**, *41*, 56-59.
7. Zhang, J.-w.; Lu, G.-p.; Cai, C., Chemoselective transfer hydrogenation of nitroarenes by highly dispersed Ni-Co BMNPs. *Catal. Commun.* **2016**, *84*, 25-29.
8. She, W.; Qi, T.; Cui, M.; Yan, P.; Ng, S. W.; Li, W.; Li, G., High Catalytic Performance of a CeO₂-Supported Ni Catalyst for Hydrogenation of Nitroarenes, Fabricated via Coordination-Assisted Strategy. *ACS Appl. Mater. Interfaces* **2018**, *10* (17), 14698-14707.
9. Jiang, C.; Shang, Z.; Liang, X., Chemoselective Transfer Hydrogenation of Nitroarenes Catalyzed by Highly Dispersed, Supported Nickel Nanoparticles. *ACS Catal.* **2015**, *5* (8), 4814-4818.
10. Gao, R.; Pan, L.; Wang, H.; Zhang, X.; Wang, L.; Zou, J.-J., Ultradispersed Nickel Phosphide on Phosphorus-Doped Carbon with Tailored d-Band Center for Efficient and Chemoselective Hydrogenation of Nitroarenes. *ACS Catal.* **2018**, *8* (9), 8420-8429.
11. Patil, N. M.; Sasaki, T.; Bhanage, B. M., Immobilized Iron Metal-Containing Ionic Liquid-Catalyzed Chemoselective Transfer Hydrogenation of Nitroarenes into Anilines. *ACS Sustain. Chem. Eng.* **2015**, *4* (2), 429-436.
12. Pedrajas, E.; Sorribes, I.; Gushchin, A. L.; Laricheva, Y. A.; Junge, K.; Beller, M.; Llugar, R., Chemoselective Hydrogenation of Nitroarenes Catalyzed by Molybdenum Sulphide Clusters. *ChemCatChem* **2017**, *9* (6), 1128-1134.
13. Wienhofer, G.; Baseda-Kruger, M.; Ziebart, C.; Westerhaus, F. A.; Baumann, W.; Jackstell, R.; Junge, K.; Beller, M., Hydrogenation of nitroarenes using defined iron-phosphine catalysts. *ChemComm* **2013**, *49* (80), 9089-91.
14. Petkar, D. R.; Kadu, B. S.; Chikate, R. C., Highly efficient and chemoselective transfer hydrogenation of nitroarenes at room temperature over magnetically separable Fe-Ni bimetallic nanoparticles. *RSC Adv.* **2014**, *4* (16), 8004-8010.
15. Metin, Ö.; Mendoza-Garcia, A.; Dalmızrak, D.; Gültekin, M. S.; Sun, S., FePd alloy nanoparticles assembled on reduced graphene oxide as a catalyst for selective transfer hydrogenation of nitroarenes to anilines using ammonia borane as a hydrogen source. *Catal. Sci.* **2016**, *6* (15), 6137-6143.
16. Zhou, Y. H.; Yang, Q.; Chen, Y. Z.; Jiang, H. L., Low-cost CuNi@MIL-101 as an excellent catalyst toward cascade reaction: integration of ammonia borane dehydrogenation with nitroarene

- hydrogenation. *ChemComm* **2017**, 53 (91), 12361-12364.
17. Cui, X.; Long, Y.; Zhou, X.; Yu, G.; Yang, J.; Yuan, M.; Ma, J.; Dong, Z., Pd-doped Ni nanoparticle-modified N-doped carbon nanocatalyst with high Pd atom utilization for the transfer hydrogenation of nitroarenes. *Green Chem.* **2018**, 20 (5), 1121-1130.
18. Verho, O.; Nagendiran, A.; Tai, C.-W.; Johnston, E. V.; Bäckvall, J.-E., Nanopalladium on Amino-Functionalized Mesocellular Foam as an Efficient and Recyclable Catalyst for the Selective Transfer Hydrogenation of Nitroarenes to Anilines. *ChemCatChem* **2014**, 6 (10), 205-211.
19. Li, Z.; Li, J.; Liu, J.; Zhao, Z.; Xia, C.; Li, F., Palladium Nanoparticles Supported on Nitrogen-Functionalized Active Carbon: A Stable and Highly Efficient Catalyst for the Selective Hydrogenation of Nitroarenes. *ChemCatChem* **2014**, 6 (7), 1333-1339.
20. Huang, H.; Wang, X.; Tan, M.; Chen, C.; Zou, X.; Ding, W.; Lu, X., Solvent-Free Selective Hydrogenation of Nitroarenes Using Nanoclusters of Palladium Supported on Nitrogen-Doped Ordered Mesoporous Carbon. *ChemCatChem* **2016**, 8 (22), 1485-1489.
21. Datta, K. J.; Rathi, A. K.; Gawande, M. B.; Ranc, V.; Zoppellaro, G.; Varma, R. S.; Zboril, R., Base-Free Transfer Hydrogenation of Nitroarenes Catalyzed by Micro-Mesoporous Iron Oxide. *ChemCatChem* **2016**, 8 (14), 2351-2355.
22. Cai, S.; Duan, H.; Rong, H.; Wang, D.; Li, L.; He, W.; Li, Y., Highly Active and Selective Catalysis of Bimetallic Rh₃Ni₁ Nanoparticles in the Hydrogenation of Nitroarenes. *ACS Catal.* **2013**, 3 (4), 608-612.
23. Yuan, M.; Long, Y.; Yang, J.; Hu, X.; Xu, D.; Zhu, Y.; Dong, Z., Biomass Sucrose-Derived Cobalt@Nitrogen-Doped Carbon for Catalytic Transfer Hydrogenation of Nitroarenes with Formic Acid. *ChemSusChem* **2018**, 11 (23), 4156-4165.

Paper IV



Direct dehydrogenation of propane over Pd nanoparticles encapsulated within IPC zeolites with tunable pore sizes

Mehran Sajad^a, Yuyan Zhang^b, Martin Kubů^b, Michal Mazur^b, Roman Bulanek^{a,*}, Jiří Čejka^{b,*}

^a Department of Physical Chemistry, Faculty of Chemical Technology, University of Pardubice, Studentska 573, 532 10 Pardubice, Czech Republic

^b Department of Physical and Macromolecular Chemistry, Faculty of Science, Charles University, Hlavova 2030/8, 128 43 Prague, Czech Republic

ARTICLE INFO

Keywords:
Dehydrogenation
Propane
Propene
IPC zeolites
Pd nanoparticles

ABSTRACT

Propane dehydrogenation (PDH) yields propene, a valuable feedstock in increasing global demand. Yet, despite recent advances in supported metal nanoparticles (NPs) for such catalytic applications, preventing nanoparticle agglomeration remains a challenge. In this study, we prepared well-dispersed Pd nanoparticles and encapsulated them within IPC-2 and IPC-4 zeolites using the Assembly, Disassembly, Organization, and Reassembly (ADOR) process based on the 3D-2D-3D transformation. By structural and textural analysis, we confirmed the synthesis of two 'ADORable' zeolites incorporated with Pd nanoparticles, namely Pd@IPC-2 and Pd@IPC-4. In the direct dehydrogenation of propane, Pd NPs encapsulated within IPC-2 and IPC-4 zeolites outperformed their impregnated counterparts (Pd/IPC-2 and Pd/IPC-4), with Pd@IPC-2 showing a higher catalytic activity than Pd@IPC-4. Accordingly, in addition to the number of surface Pd atoms, the size of the zeolite channels and the structure of the framework strongly affect the catalytic activity of encapsulated Pd. Moreover, confining Pd NPs inside zeolite channels prevented their sintering and agglomeration during the reaction as Pd NPs in impregnated catalysts expanded during the reaction. However, the structure of the zeolite encapsulated with Pd catalysts partly collapsed due to the harsh conditions of the dehydrogenation reaction, hindering access to Pd NPs, as observed in IR spectra. Therefore, palladium NPs are stable within zeolites and do not sinter, but their catalytic activity gradually decreases with the formation of carbon deposits. Although these deposits are removable by calcination, reactivation does not completely restore the original activity due to framework disruption and limited access to the active species.

1. Introduction

With the constant increase in the global demand for propene, new technologies have emerged for the production of this valuable feedstock, particularly propane dehydrogenation (PDH) [1,2]. Although PDH is an endothermic and equilibrium-limited reaction, which requires a relatively high temperature, catalysts decrease the reaction temperature with satisfactory conversion rates at high selectivity. C-H bond activation is the rate-determining step, but C-C bond breaking should be avoided in the catalytic dehydrogenation of propane to propene.

Several metal-based catalytic systems have been studied for PDH purposes [3–23]. Among them, supported Pt- and Cr-based catalysts have shown a strong ability to activate C-H bonds coupled with low C-C bond breaking [8,10,13,16–23]. However, in addition to the reactant and the product, metal particle size, shape, and chemical composition and interactions between the metal atoms and the support also strongly

affect the catalytic activity [24]. Considering these key factors and using new synthetic methods, significant advances have been recently made in the development of metal catalysts, including supported metal nanoparticles (NPs) [25–29].

Supported metal nanoparticles provide high efficiency for interactions between feed molecules and well-dispersed NPs. These NPs serve as active sites located on an appropriate support with a large surface area, thereby facilitating accessibility [30]. Despite these advantages, nanoparticle sintering and agglomeration under harsh reaction conditions are still major disadvantages [23,31]. In other words, nanoparticle stabilization against agglomeration remains a key challenge.

Improving NP stability and distribution may thus require encapsulating metal NPs within porous materials such as zeolites [31]. The unique properties of zeolites, including crystallinity, porosity, and hence, high surface area, make them highly suitable candidates for

* Corresponding author.

E-mail address: roman.bulanek@upce.cz (R. Bulanek).

<https://doi.org/10.1016/j.apmt.2022.101644>

Received 21 June 2022; Received in revised form 31 August 2022; Accepted 25 September 2022

Available online 6 October 2022

2352-9407/© 2022 Elsevier Ltd. All rights reserved.

confining metal NPs. The resulting catalysts have a higher activity and stability than catalysts prepared using conventional methods (i.e., impregnation and ion exchange) [26,31–35]. Moreover, we have recently combined a 2D-to-3D transformation of a layered zeolite with the Assembly, Disassembly, Organization, and Reassembly (ADOR) approach [36]. This 3D-2D-3D zeolite transformation has already enabled us to prepare metal nanoparticles encapsulated within zeolite pores, thereby protecting them against deactivation for the reasons mentioned above [36,37].

In this context, we studied the catalytic activity of Pd NPs encapsulated within IPC-2 and IPC-4 zeolites [36] in the direct dehydrogenation of propane. For this purpose, we prepared IPC-2 and IPC-4 zeolites from an IPC-1P precursor derived from UTL zeolite hydrolysis [38,39] using the ADOR approach to encapsulate metal NPs inside the zeolitic layers. After comparing the activity of these catalysts with that of their impregnated counterparts, we characterized all catalysts by combining scanning transmission electron microscopy-energy dispersive spectroscopy (STEM-EDS), X-ray diffraction measurements (XRD), scanning electron microscopy (SEM), and infrared spectroscopy (IR) with N_2 adsorption-desorption isotherm measurements to study the chemical composition, distribution and size of NPs and their crystallinity, textural properties, morphology and active sites, respectively. We compared and discussed the data on the structure and properties of Pd NPs together with catalytic results.

2. Experimental

2.1. Catalysts synthesis

2.1.1. Synthesis of UTL and IPC-1P

The UTL zeolite structure-directing agent (SDA) (6R,10S)-6,10-Dimethyl-5-anizosporo [4.5] decane hydroxide was synthesized as previously reported [38], confirming its purity by NMR spectroscopy. UTL germanosilicate zeolite was synthesized using procedures described in the literature [40,41]. The synthesis gel was prepared by dissolving amorphous GeO_2 (Alfa-Aesar) in the SDA solution in deionized water, adding a silica source (Cab-O-Sil M5) and stirring for 1 h at room temperature. The molar composition of the gel was 0.8 SiO_2 : 0.4 GeO_2 : 0.5 SDA: 30 H_2O . The resulting gel was transferred to a 90-mL, Teflon-lined, stainless-steel autoclave and heated at 175 °C for 7 days with agitation (60 rpm). The solid product was separated by filtration and washed with deionized water until neutral pH and dried at 65 °C overnight. To remove SDA, the solid product was calcined in air at 550 °C for 6 h while increasing the temperature at 1 °C min^{-1} .

The IPC-1P precursor was also prepared as previously described [40, 42]. Calcined UTL zeolite was hydrolyzed in 0.1 M HCl with a zeolite / solution ratio (w / w) of 1/150 at 95 °C overnight. The product was isolated by centrifugation, washed with deionized water and dried at 65 °C overnight.

2.1.2. IPC-2 and IPC-4 synthesis

To a 15-mL autoclave, 0.5 g of IPC-1P, 0.1 g of $Si(CH_3)_2(OCH_2CH_3)_2$ (Sigma Aldrich, 99.5%) and 10 mL of 1 M HNO_3 solution were added, subsequently heating at 170 °C for 16 hours. The product was isolated by centrifugation, washed and calcined at 540 °C for two hours with a temperature ramp of 1 °C min^{-1} and named IPC-2.

IPC-4 was prepared by mixing 0.5 g of IPC-1P with 34 g of pure octylamine (Sigma Aldrich, 99%), heating at 70 °C overnight and then stirring at room temperature overnight. The solid was isolated by centrifugation, washed, and calcined under the same conditions.

2.1.3. Pd@IPC-2 and Pd@IPC-4 synthesis

The solution of $Pd(en)_2(Ac)_2$ was prepared by dispersing 80 mg of palladium acetate (Sigma Aldrich, 99.9%) in 5 mL of ethanol containing 5 g of ethylenediamine (Sigma Aldrich, 99.5%). Sonication for 10 min resulted in a clear solution of $Pd(en)_2(Ac)_2$.

Pd@IPC-1P was synthesized by stirring 1 g of IPC-1P in the solution of $Pd(en)_2(Ac)_2$ prepared above overnight at room temperature.

Pd@IPC-4 was synthesized by calcination of Pd@IPC-1P in static air at 540 °C for 2 h (1 °C min^{-1} temperature ramp).

Pd@IPC-2 was synthesized by loading 0.5 g of Pd@IPC-1P, 10 mL of a 1 M HNO_3 solution and 0.1 g of $Si(CH_3)_2(OCH_2CH_3)_2$ (Sigma Aldrich, 99.5%) in a 15 mL autoclave and heating at 170 °C for 16 h. The solid product was recovered by centrifugation, washed with distilled water, and calcined under the same conditions.

2.1.4. Impregnated Pd/IPC-2 and Pd/IPC-4 synthesis

The solution of $Pd(en)_2(Ac)_2$ containing 40 mg of palladium acetate was mixed with 0.5 g of IPC-2 or IPC-4 and subsequently dried in the oven and calcined under the conditions mentioned above, thereby preparing Pd/IPC-2 and Pd/IPC-4.

2.2. Characterization

The structure and phase purity of the Pd-zeolite catalysts and zeolites were verified by powder X-ray diffraction on a Bruker D8 ADVANCE powder diffractometer. X-ray measurements were performed in continuous scan mode, in the range of 3 - 40° (2 θ).

The nitrogen adsorption isotherms of Pd-zeolite catalysts and zeolites were measured using the static volumetric apparatus of a Micromeritics ASAP 2020 adsorption analyzer at -196 °C. The surface area, S_{BET} , was calculated using adsorption data in the range of relative pressures $p/p_0 = 0.05 - 0.2$. The adsorbed amount at a relative pressure of $p/p_0 = 0.95$ reflects the total adsorption capacity (V_{tot}). Harkins-Jura equation for calculating the thickness of adsorbed layer was applied in Microactive data reduction software (Micromeritics, USA) to estimate the micropore volume (V_{mic}) and external surface area using the t -plot method.

Scanning transmission electron microscopy (STEM) images were recorded under a Jeol JEM-ARM200F NEOARM atomic resolution analytical electron microscope operated at 200 kV. The alignment was performed using the standard gold nanoparticles film method. Energy dispersive X-ray (EDS) mapping was performed on a JEOL JED-2300 EDS spectrometer.

The morphologies of the Pd-zeolite catalysts and zeolites were determined by scanning electron microscopy (SEM) under a TESCAN Vega microscope (TESCAN, Czech Republic).

The chemical composition, including Pd loading in Pd-zeolite catalysts, as well as the Si-to-Ge ratio, was determined under a LYRA 3 scanning electron microscope (TESCAN) equipped with an AZtec X-Max 20 EDS analyzer (Oxford Instruments).

TG-DSC analysis was performed on a NETZSCH STA 449 F5 Jupiter apparatus (Netzsch, Germany) with a TG sample Al holder (85 μ l open crucible in contact with a synthetic air stream (Linde Gas a.s., Czech Republic) at 50 $mL\ min^{-1}$). An empty crucible was used as a zero-line reference. The heating rate during the analysis was 5 °C min^{-1} within the temperature range of 25–600 °C.

DRIFT spectra of encapsulated and impregnated Pd-IPC-2 and Pd-IPC-4 catalysts were recorded through in situ measurements on a Thermo Nicolet FT-IR 6700 spectrometer (Thermo Fisher Scientific, Prague, Czech Republic) equipped with a DRIFT cell (Thermo Scientific) and an MCT/A detector cooled by liquid nitrogen. The background was measured using a metallic mirror under N_2 atmosphere in the reaction chamber (10 $mL\ min^{-1}$ flow rate). Step by step, the samples were heated to 450 °C in N_2 flow, reduced in H_2 (10 $mL\ min^{-1}$ flow rate) for 2 hours at 450 °C, and cooled to RT in N_2 . After CO adsorption for 30 min, desorption was performed in N_2 flow. During the experiments, spectra were collected in the 4000 – 650 cm^{-1} range at 1 cm^{-1} resolution with 256 scans. The spectra presented in this study were obtained by subtracting the sample spectrum before dosing CO and pure CO gas phase spectrum (measured independently under the same conditions).

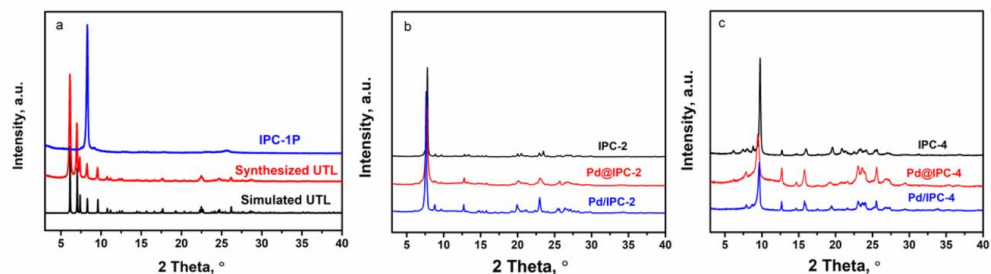


Fig. 1. a: XRD patterns of UTL and IPC-1P; b: IPC-2, Pd@IPC-2, and Pd/IPC-2; and c: IPC-4, Pd@IPC-4, and Pd/IPC-4.

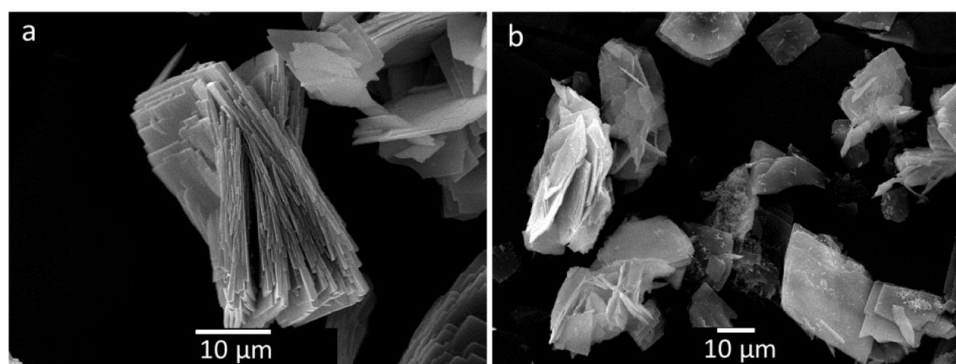


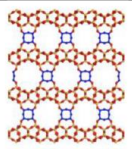
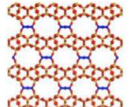
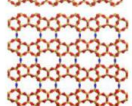
Fig. 2. a: SEM images of UTL, and b: IPC-1P

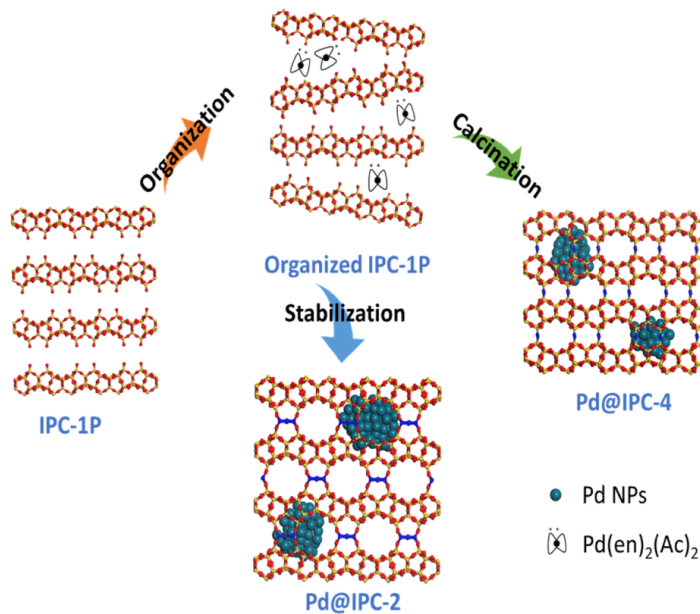
2.3. Catalytic tests

The catalytic activity of Pd catalysts in propane dehydrogenation was studied on a vertical, tubular, fixed-bed, plug-flow, quartz reactor 5 mm in inner diameter at atmospheric pressure for nearly three hours. For meaningful comparisons, we also measured the impregnated counterpart of each catalyst. The mass of the catalysts used in the tests was set to a constant palladium content in the reactor (approximately 1 mg),

with a desired grain size of 0.35 to 0.50 µm. Before each catalytic test, all samples were treated in hydrogen flow (10 mL min^{-1}) while heating to $600 \text{ }^\circ\text{C}$ at $5 \text{ }^\circ\text{C min}^{-1}$ and kept at this temperature for 2 hours. The catalytic tests were performed at $600 \text{ }^\circ\text{C}$ in a reaction mixture consisting of 2.5 mL min^{-1} propane and 10 mL min^{-1} helium. The products were analyzed on an online gas chromatograph (Agilent 7890A) equipped with a flame ionization detector (FID) and a thermal conductivity detector (TCD) connected in series. The 50-m-long GS-Alumina GC column

Table 1
Structural characteristics of UTL zeolite and UTL-derived IPC-2 and IPC-4 zeolites.

Zeolite	Structure	Interlayer connectivity	14-ring (Å)	12-ring (Å)	12-ring (Å)	10-ring (Å)	10-ring (Å)	8-ring (Å)
UTL		D4R	9.5×7.1	8.5×5.5				
IPC-2		S4R			6.6×6.2	5.4×5.3		
IPC-4		Oxygen					5.8×3.8	4.5×3.6



Scheme 1. Synthetic procedure of Pd@IPC-2 and Pd@IPC-4.

with a diameter of 530 μm was used to separate the component of the gas mixture. After almost three hours, the catalyst was regenerated at the same temperature (600 $^{\circ}\text{C}$) for 0.5 h in a mixture of helium (30 mL min^{-1}) and oxygen (1.5 mL min^{-1}). After its regeneration, the catalyst was reduced again with hydrogen, and another catalytic test was performed. Four tests were performed for each catalyst, and the resulting sample was named spent catalyst. Blank tests were conducted with an empty reactor, fumed silica, and IPC-2 and IPC-4 zeolites with no trace of Pd.

3. Results and discussion

3.1. Catalyst characterization

The phase purity of the starting zeolite UTL was evidenced by comparing the experimental and simulated powder XRD patterns of UTL zeolite (data taken from the IZA structure database, Fig. 1a). The UTL XRD pattern had a main reflection (200) at $\sim 6.2^{\circ} 2\theta$, indicating that the d spacing of the layers is 1.42 nm [26]. After selective removal of D4Rs by hydrolysis, the XRD pattern changed significantly, with a strong diffraction line at $\sim 8.3^{\circ} 2\theta$ (d spacing: 1.06 nm) [28]. The significant shift in the diffraction line (200) to higher angles and the disappearance of other peaks indicate that UTL was converted into IPC-1P (see Fig. 1a, blue pattern). Figs. 2a and b show SEM images of UTL and IPC-1P. UTL had a rectangular morphology of plate-shaped crystals 20–60 μm in size. No clear changes in crystal morphology were observed after UTL conversion into IPC-1P. The character of the crystallites was also preserved in the case of IPC-2 and IPC-4 materials prepared by the ADOR process from the parent UTL. It must be noted, that the pressing and granulation of the materials to the appropriate size of grain used in catalytic test and the influence of the reaction conditions led to the reduction in the size of the particles in used catalysts (see Fig. S4 in SI).

The IPC-1P precursor reassembled into two zeolites with targeted topologies, IPC-2 and IPC-4. The parent UTL and the resulting IPC-2, IPC-4 zeolites adopted the same layered structure and differed in the

linkers connecting individual layers, giving rise to different pore sizes, namely D4Rs for UTL and S4R and oxygen for IPC-2 and IPC-4, respectively (Table 1). The dominant peak attributed to (200) intra-layer reflection [23] is shifted to 7.6° and $9.7^{\circ} 2\theta$ in IPC-2 and IPC-4, respectively, evidencing a lower d spacing in IPC-2 and IPC-4 zeolites than in the parent UTL (cf. Fig. 1b and c).

To prepare target metal@zeolite catalysts with variable textural properties, Pd NPs were encapsulated into IPC-2 and IPC-4 using the ADOR strategy. Scheme 1 demonstrates different pathways for each zeolite based on the individual protocols provided in the experimental section.

After introducing Pd NPs into IPC-2 and IPC-4 zeolites, labelled as Pd@IPC-2 and Pd@IPC-4, respectively, the crystalline structures remained well preserved, without significant changes (cf. patterns in Fig. 1b and c). To compare the properties of encapsulated Pd catalysts with impregnated, Pd/IPC-2 and Pd/IPC-4 were also prepared by conventional impregnation. The XRD patterns of the Pd@IPC-2, Pd/IPC-2 catalysts and the IPC-2 zeolite exhibited a dominant diffraction peak at $2\theta = 7.6^{\circ}$, corresponding to a (002) reflection [36], thus indicating that the linker between layers is S4R. The remaining diffraction peaks at $2\theta = 8.8, 9.6, 12.7, 15.7, 20.0, 23.0, 25.7^{\circ}$ correlated with Si layers. However, the diffractions generated some overlap around 20.0° and 23.0° , most likely resulting from interactions between Pd NPs and the zeolite framework. After the linker was changed to oxygen, the dominant diffraction peak shifted to 9.4° in Pd@IPC-4 and to 9.7° in Pd/IPC-4 and IPC-4, showing that the Pd NPs increased the d spacing of the encapsulated sample. Because they had the same layer structure, the other diffraction peaks were located in the same position ($2\theta = 12.6, 15.8, 19.6, 23.3, 25.6$) as in IPC-2 samples. The XRD patterns of Pd@IPC-2, Pd/IPC-2, Pd@IPC-4, and Pd/IPC-4 matched the XRD patterns of IPC-2 and IPC-4, confirming that all structures maintained their integrity after introducing Pd NPs. No characteristic diffraction lines of Pd species were observed in Pd@IPC catalysts, e.g., at $2\theta = 39.9^{\circ}$ [43], most likely due to the low Pd loading and small size of the Pd NPs, which do not exceed 2.4 nm based on the STEM results.

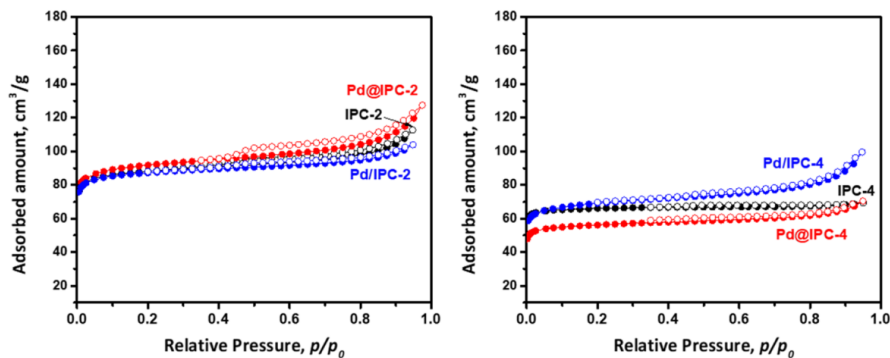


Fig. 3. N_2 adsorption-desorption isotherms of IPC-2, Pd@IPC-2, and Pd/IPC-2 (left panel), and IPC-4, Pd@IPC-4, and Pd/IPC-4 (right panel).

Table 2

Textural parameters, Pd content, Si/Ge ratio and average size of fresh and spent IPC-2, Pd@IPC-2, Pd/IPC-2 and IPC-4, Pd@IPC-4, and Pd/IPC-4.

	S_{BET} m^2/g		V_{mic} cm^3/g		S_{ext} m^2/g		V_{tot} cm^3/g		Pd content (wt%)		Si/Ge		NPs size ^a (nm)	
	Fresh	Spent	Fresh	Spent	Fresh	Spent	Fresh	Spent	Fresh	Spent	Fresh	Spent	Fresh	Spent
IPC-2	299	–	0.12	–	40	–	0.19	–	–	–	60.7±7.1	–	–	–
Pd@IPC-2	319	191	0.12	0.07	53	37	0.19	0.13	0.9±0.01	1.0±0.02	95±4.1	50.4±9.5	2.4±0.5	2.5±0.4
Pd/IPC-2	296	312	0.12	0.10	38	103	0.17	0.28	0.7±0.02	0.6±0.01	69.5±2.2	55.0±10.1	1.7±0.3	2.6±0.9
IPC-4	222	–	0.09	–	15	–	0.10	–	–	–	57.1±4.0	–	–	–
Pd@IPC-4	190	209	0.08	0.06	26	73	0.11	0.20	1.0±0.03	0.9±0.04	53.7±11.7	75.2±12.4	1.7±0.3	1.7±0.3
Pd/IPC-4	235	207	0.08	0.05	48	100	0.15	0.25	1.0±0.02	1.5±0.08	106.0±9.1	72.4±21.9	2.3±0.4	3.1±1.8

^a Average size of Pd NPs based on STEM images

IPC zeolites, Pd@IPC, Pd/IPC catalysts exhibited a type I isotherm (Fig. 3) typical of microporous materials according to the IUPAC classification [44]. These isotherms show the difference in micropore volumes caused by channel systems with different sizes. The micropore volumes of the IPC-2 sample set was ~ 0.12 cm^3/g and hence larger than that of the IPC-4 sample set (~ 0.09 cm^3/g), perfectly in line with the decreasing size of the pores. The S_{BET} surface area ranged from 296 to 319 m^2/g in IPC-2 samples with a larger channel system from 190 to 235 m^2/g in IPC-4 samples. The adsorption isotherms of all IPC-2 samples showed some hysteresis at higher p/p_0 values, indicating nitrogen condensation in the interparticle void space. The Si/Ge ratio of all IPC samples ranged from 53 to 106, which is significantly lower than the Si/Ge ratio of the parent UTL (Si/Ge=6). Pd loading had a different impact on the BET area based on zeolite structure, Pd amount and loading method. Table 2 outlines data on the ‘fresh’ catalysts before the reaction and without any further treatment (except degassing before adsorption measurement), whereas the data on ‘spent’ catalysts correspond to the catalysts after the cyclic reaction test.

The SEM images of Pd@IPC-2 (Fig. 4a) and Pd@IPC-4 (Fig. 5a) indicate that the crystal morphology of IPC-1P is preserved after stabilization and condensation. To assess the size and distribution of encapsulated Pd NPs prepared using the ADOR strategy and of impregnated Pd in IPC-2 and IPC-4 zeolites, STEM images and EDS maps of the catalysts were measured (see Fig. 4e and 5e). The white round spots visible in the images are Pd NPs. All encapsulated and impregnated samples show visible Pd NPs uniformly distributed across the zeolite crystals. The size distributions of Pd NPs were assessed by analyzing STEM images.

The average diameter of the Pd NPs in Pd@IPC-2 and Pd/IPC-2 was 2.4 and 1.7 nm, respectively (Fig. 4d and h). On average, Pd NPs in Pd@IPC-2 were larger than those in Pd/IPC-2, most likely because Pd@IPC-1P was treated with $Si(CH_3)_2(OCH_2CH_3)_2$ in a 1 M HNO_3 solution at 170 °C for 16 h. This high-temperature treatment unavoidably resulted in Pd NPs aggregation. The larger particle size of Pd@IPC-2

informed that the nanoparticles were located between layers in the encapsulated catalyst rather than in channels or channel intersections.

In Pd-IPC-4 samples, the average diameter of the Pd NPs in Pd@IPC-4 and Pd/IPC-4 was 1.7 and 2.3 nm, respectively (Fig. 5d and h), and the average size of the Pd NPs in Pd@IPC-4 was smaller than that of the impregnated sample. Due to the small pores of IPC-4 zeolite, Pd precursors can easily collect on the surface of the zeolite during the impregnating procedure (Pd/IPC-4), forming large Pd NPs with a non-homogeneous distribution (Fig. 5f).

Procedure used here for encapsulation of Pd NPs into IPC-2 and IPC-4 zeolites was applied previously also for encapsulation of Pt NPs into these zeolites [36]. In this study, we have demonstrated that the nanoparticles are located inside the zeolite lattice between the zeolite layers. In the case of the materials studied in this work, the encapsulation of Pd nanoparticles within the zeolite framework can be clearly seen in the side-view STEM images (see Fig. S5).

3.2. Catalytic activity

Catalytic performance in propane dehydrogenation was investigated over all Pd-IPC catalysts, regardless of pore size and preparation method. First, in an empty reactor without any catalyst, we assessed whether any gas phase reaction could occur without a catalyst, detecting approximately 4% propane conversion, with 51% selectivity to propene, 30% to ethylene, 16% methane, 2% ethane, and CO_2 traces (Table 3). These results indicated that the gas-phase reaction plays a role and must be taken into account. To determine the catalyst activity of Pd-IPC zeolites, the rate of propene production was calculated after subtracting the observed conversion of the empty reactor, which is considered the gas phase reaction.

In the next step, the catalytic activity of pure IPC-2 and IPC-4 zeolites was measured in the target reaction, measuring approximately 4.9% and 6.2% conversion, respectively. The catalytic behavior of the catalysts is

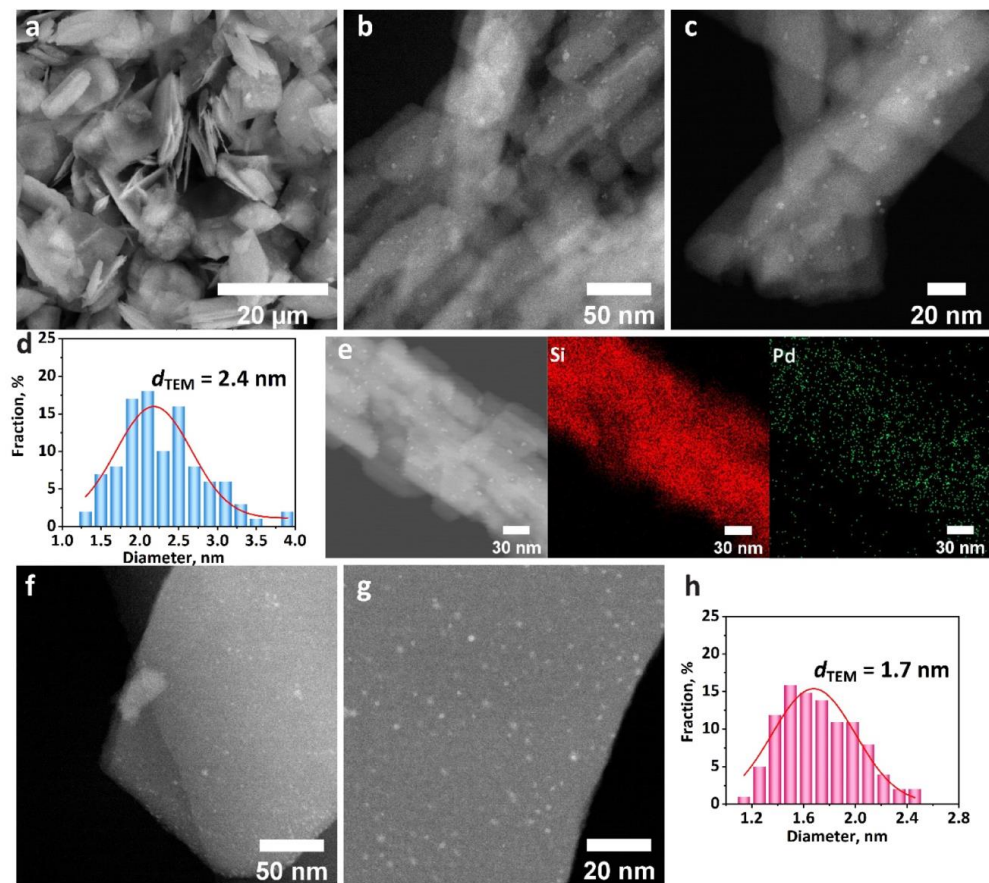


Fig. 4. SEM image (a), STEM images (b,c), size distribution (d) and EDS maps of Si and Pd elements (e) of fresh Pd@IPC-2; STEM images (f,g) and size distribution (h) of fresh Pd/IPC-2.

summarized in Table 3 and Fig. 6. IPC-2 and IPC-4 zeolites showed a selectivity to the products similar to that of the empty reactor. Moreover, the propane conversion of both zeolites did not differ considerably from that of the empty reactor, thus demonstrating that these supports alone are not able to participate in and catalyze the dehydrogenation of the propane reaction. In the following step, the activity of all Pd-IPC catalysts was tested, and as in all cases, conversion was lower than 20%. Therefore, conversion should be directly related to the reaction rate, and accordingly the catalysts can be compared directly.

Pd@IPC-2 exhibited the highest initial activity among all catalysts, with a rate of approximately $0.2 \text{ mmol}_{\text{C}_3\text{H}_6} \text{ g}_{\text{Pd}}^{-1} \text{ s}^{-1}$, and 15% propane conversion. By contrast, the activity of its impregnated counterpart (Pd/IPC-2) was less than half of that ($0.08 \text{ mmol}_{\text{C}_3\text{H}_6} \text{ g}_{\text{Pd}}^{-1} \text{ s}^{-1}$). This decreased activity could not have resulted from accessibility or diffusion constraints because, in the impregnated catalyst, the Pd NPs lie on the external surface of the zeolitic particles and are thus easily available and well distributed; instead, this difference is likely related to the intrinsic capacity of Pd NPs with different arrangements and sizes. Furthermore, propane conversion reached approximately 13% over Pd@IPC-4, whose rate of propene production ($0.14 \text{ mmol}_{\text{C}_3\text{H}_6} \text{ g}_{\text{Pd}}^{-1} \text{ s}^{-1}$) was more than 35% higher than that of its impregnated counterpart ($0.09 \text{ mmol}_{\text{C}_3\text{H}_6} \text{ g}_{\text{Pd}}^{-1} \text{ s}^{-1}$ for Pd/IPC-4). The reason for this increased catalytic activity could be

the smaller particle size of the encapsulated sample. As a result, the active Pd sites were more easily available because the accessible surface of NPs is larger than that of their impregnated counterparts. The initial activity related to the amount of surface Pd atoms (expressed as turnover frequency, which is defined by molar reaction rates per mole of surface Pd atoms) show the very similar turnover frequencies ($0.025 - 0.044 \text{ s}^{-1}$) for all catalysts, except for encapsulated IPC-2, which shows a TOF almost double (0.088 s^{-1}) (see Table S1).

In all encapsulated and impregnated IPC-2 and IPC-4 catalysts, the main product was propene, with less than 0.2% CO_2 . The main side products were methane and ethene, respectively. Clearly, selectivity to methane (4–21%) was significantly higher than to ethene (1–5%). Therefore, not only C_2 hydrocarbons generate methane but also C_3 hydrocarbons split into C_1 , and ethane is also found among the products.

Selectivity to propene increased significantly when using Pd NPs (69–87%) rather than pure supports or gas phase reaction (49–52%). Conversely, selectivity to ethene which was higher than 30% with an empty reactor or over pure supports due to C-C bond cracking, sharply decreased to values lower than 10% after applying Pd NPs. The selectivity to methane of both impregnated catalysts was the same (14%) and similar to that of the pure supports (16–17%), decreasing to only 4% over Pd@IPC-2 and increasing to 21% over Pd@IPC-4. This increase in

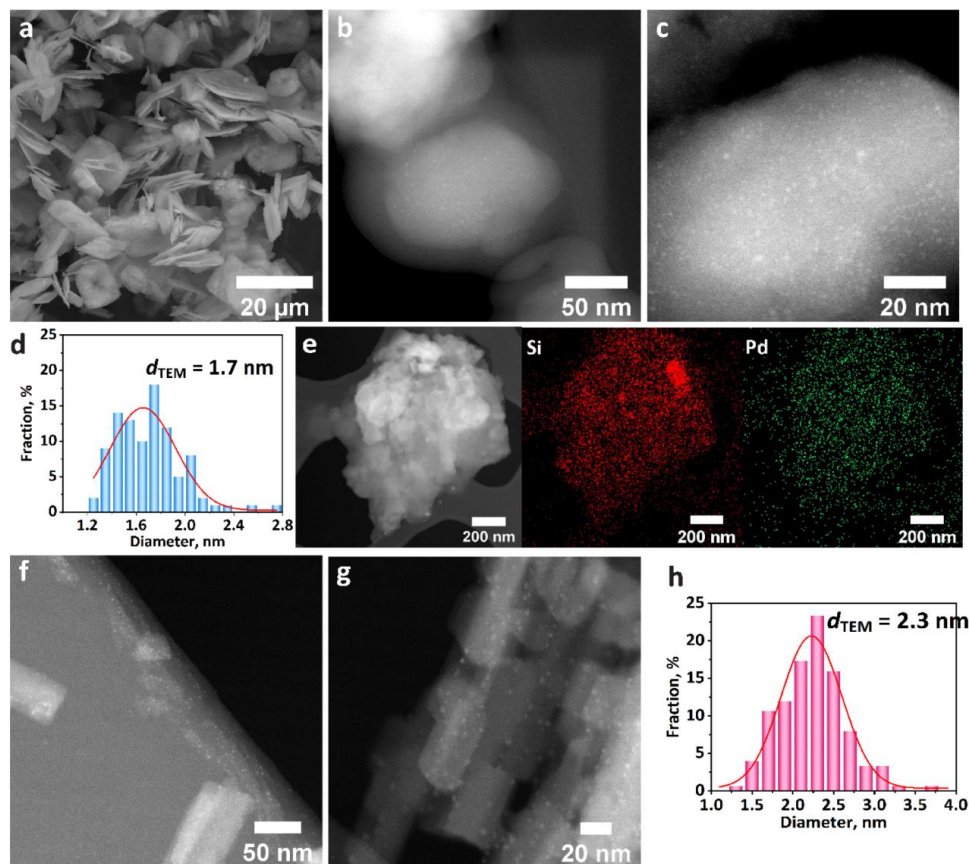


Fig. 5. SEM image (a), STEM images (b,c), size distribution (d) and EDS maps of Si, Pd elements (e) of Pd@IPC-4; STEM images (f,g) and size distribution (h) of Pd/IPC-4.

Table 3

Catalytic activity measured after 5 minutes under the stream, expressed as the rate of propene production, propane conversion, and selectivity to products.

Catalyst	Mass (mg)	Rate $\text{mol}_{\text{C}_3\text{H}_6} \text{kg}_{\text{cat}}^{-1} \text{h}^{-1}$	$\text{mmol}_{\text{C}_3\text{H}_6} \text{g}_{\text{Pd}}^{-1} \text{s}^{-1}$	Conversion (% C_3H_8)	Selectivity (%) C_3H_6	C_2H_4	CH_4	CO	CO_2	C_2H_6
Empty reactor	–	–	–	3.8	51	30	16	0	0	2
IPC-2	100	1.7	–	4.9	49	32	17	0	0	2
IPC-4	100	2	–	6.2	50	31	17	0	0	2
Fumed silica	100	1.3	–	3.8	52	30	16	0	0	2
Pd@IPC-2	100	8.7	0.20	15.0	87	2	4	6	0	1
Pd/IPC-2	131.4	3.3	0.08	9.3	71	9	14	2	0	4
Pd@IPC-4	88.5	7.1	0.14	13.3	71	4	21	2	0	2
Pd/IPC-4	91.1	5.2	0.09	10.3	69	10	14	2	0	5

selectivity to methane shows that the latter has a higher tendency to C-C cleavage, whereas the former prevents this undesired behavior. Selectivity to CO increased when using Pd NPs, albeit with negligible changes for CO_2 . Lastly, selectivity to C_2H_6 over Pd NPs differed from that of the pure supports, decreasing over encapsulated catalysts and increasing over impregnated catalysts.

Table 4 outlines a comparison between studies similar to this research. The results cannot be compared directly due to differences in conditions. Nevertheless, several systems have been tested as PDH

catalysts, including supported transition metals and noble metals, showing a wide range of catalytic activity, and promoters in bimetallic systems improve catalytic activity [3,8,9,13]. For PDH, Pd has been mostly supported on silica at different reaction temperatures as one of the noble metals capable of facilitating the non-oxidative activation of the C-H bond, with activity rates ranging from 1.3 to $15.4 \text{ mol}_{\text{C}_3\text{H}_6} \text{kg}_{\text{cat}}^{-1} \text{h}^{-1}$ depending on the reaction conditions and on the presence of promoters [3–5]. The selectivity of propane dehydrogenation over Pd-silica catalysts is usually very low (cf. data in Table 4) due to big competition

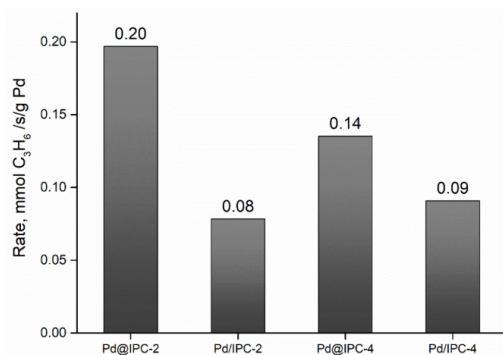


Fig. 6. Initial catalytic activity over different catalysts expressed as propene production rate at 5 min TOS.

with cracking and hydrogenolysis reaction. The reported selectivity toward propylene over encapsulated catalysts in our work range from 71% to 87% at similar conversion level (13–15%). Likewise, impregnated samples show similar selectivities (69–71%) with very comparable conversions (9.3–10.3%). These values are significantly higher than selectivity reported on Pd-silica catalysts in other works. (cf. Table 4). Childers et al. [4] reported very low selectivity for propane dehydrogenation (PDH) (11% at 15% conversion) as well as Yang et al. [5] reporting 30% of selectivity at 18% conversion. Rimaz et al. [3] reported little bit higher selectivity of PDH reaching 54% at 21% propane conversion. From this point of view, selectivity of our materials are quite good. The selectivity of Pd nanoparticles in the dehydrogenation of propane can be significantly increased by the addition of a secondary metal (Zn [4], Ge [3], Fe [5] and others) that forms an alloy with Pd, thereby changing the electronic properties (mainly the energy of the 4d orbital) and isolating palladium atoms (surrounded by secondary metal atoms). Unlike dehydrogenation, hydrogenolysis (side reaction of propane dehydrogenation) is a structure-sensitive reaction, which means that its kinetics is dependent on the size of the metal particles. The average size of Pd nanoparticles in our samples ranged between 1.7 and

Table 4

Catalytic activity and reaction conditions reported in similar studies found in the literature at TOS shorter than 15 min.

Catalyst	Hetero atom (wt.%)/TTC	Feed (molar ratio)	WHSV (h ⁻¹)	Conversion (C ₃ H ₈ , %)	Selectivity (C ₃ H ₆ , %)	Rate (mol _{C₃H₆} kg _{cat} ⁻¹ h ⁻¹)	Ref.
Pd@IPC-2	Pd: 0.92/600	C ₃ H ₈ :He 1:4	2.9	15	86.8	8.7	This work
Pd@IPC-4	Pd: 1.04/600	C ₃ H ₈ :He 1:4	3.3	13.3	70.9	7.1	This work
Pd ₂ /SiO ₂	Pd: 1.97/550	C ₃ H ₈ :H ₂ :N ₂ :Ar 1:1:5:18:24:1	3.78	21	53.6	9.6	[3]
Pd ₂ -Ge/SiO ₂	Pd: 2.13/575	C ₃ H ₈ :H ₂ :N ₂ :Ar 1:1:5:18:24:1	3.78	20	90	15.4	[3]
Pd-Zn/SiO ₂	Pd: 2/550	C ₃ H ₈ :Ar 1:49	0.6	35	98	4.6	[4]
Pd/SiO ₂	Pd: 2/550	C ₃ H ₈ :Ar 1:49	0.6	15	11	0.2	[4]
Pd ₃ Fe	Pd:2, Fe: 1.6/510	C ₃ H ₈ :H ₂ :Ar 1:1:133	4.2	14	90	12	[5]
Pd/SiO ₂	Pd: 1.8/600	C ₃ H ₈ :H ₂ :Ar 1:1:133	1.05	18	30	1.3	[5]
Ni-P/SiO ₂	Ni:2.6, P:2.35/600	C ₃ H ₈ :N ₂ 1:19	0.3	18	89	1.1	[6]
CrOx/Al ₂ O ₃	Cr ₂ O ₃ :22.5/600	C ₃ H ₈ :He 1:14	1.2	41.8	89.8	10	[10]
Pt-Sn/Al ₂ O ₃	Pt:0.35, Sn: 0.68/590	C ₃ H ₈ :H ₂ :N ₂ = 1: 1.25: 4	9.4	48.7	99.1	102.9	[22]
Pt-Cu/h-BN	Pt: 0.01, Cu: 1.0/600	C ₃ H ₈ :H ₂ :N ₂ 1:1:3.9	4.0	24	97.3	21.3	[8]
Pt-In/LaAlO ₃ /γ-Al ₂ O ₃	Pt: 0.6, In: 1.5/600	C ₃ H ₈ :H ₂ :N ₂ 8:7:35	3	47	96	26.6	[13]
Pt/TiO ₂ -Al ₂ O ₃	TiO ₂ : 10, Pt:1/600	C ₃ H ₈ :H ₂ :N ₂ 1:1:1.85	10	47.3	78	85.6	[16]
VO _x /Si-Beta	V: 7/600	C ₃ H ₈ :N ₂ 1: 19	0.6	40	90	4.8	[7]
VO _x -Mg/Al ₂ O ₃	V:12, Mg: 1/600	C ₃ H ₈ :H ₂ :N ₂ 1:1:1.6	3	33	83	20.5	[9]
V-DMSN ^a	V:Si= 4.8/600	C ₃ H ₈ :N ₂ 1:7.5	6.3	18.1	91	23.5	[11]
Sn-HMS ^b	Sn:5/600	C ₃ H ₈ :C ₃ H ₆ 99.87:0.13	0.4	40	90	3.2	[12]
ZnO@NC/silicalite-1	Zn: 2/600	C ₃ H ₈ :H ₂ :N ₂ 1:1:5	0.9	56	85	9.6	[14]
ZnO/H-ZSM-5	Zn: 10/600	C ₃ H ₈ : N ₂ 20:1	0.6	72.9	63	6.2	[15]
PF-MCN ^c	P: 0.032 /600	C ₃ H ₈ :Ar 1:19	0.6	33	85	3.8	[45]
CMSC ^d	-/600	C ₃ H ₈ :N ₂ 1:19	0.6	41	89	4.9	[46]

^a Vanadium-containing dendritic mesoporous silica nanoparticles

^b hexagonal mesoporous silica

^c P-modified microporous carbon nanospheres

^d castanea mollissima shell-derived carbon

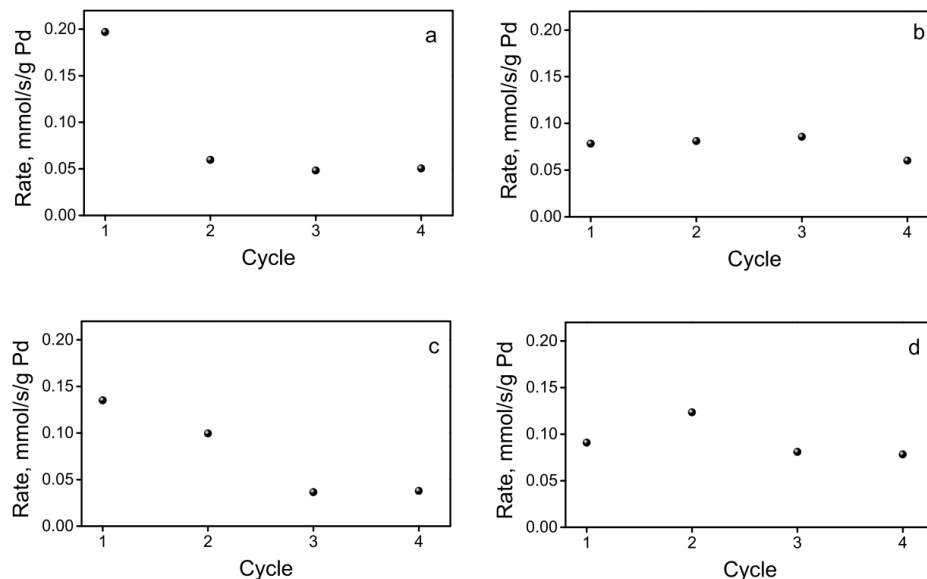


Fig. 7. Initial activity of the Pd@IPC-2 (a), Pd/IPC-2 (b), Pd@IPC-4 (c) and Pd/IPC-4 catalysts expressed as the rate of propene production for four cycles at 5 min TOS.

2.4 nm, thus very similar as in aforementioned studies (3.8 nm in [3], 2.5 nm in [4] and 1.7 nm in [5]). Thus, the effect of nanoparticle size should be similar in the mentioned studies and in our work. Chromium oxide and platinum-based catalysts are among the most successful systems for PDH that have been industrialized so far [10,22]. Several attempts have been made to improve the activity of Pt-based systems by introducing a second metal either as a catalyst promoter or a support modifier, with initial rates ranging from 21 to 103 mol_{C₃H₆} kg_{cat}⁻¹ h⁻¹ [8, 13,16,22]. Other catalysts, including vanadium, zinc, nickel, and tin, as well as non-metallic systems, have also been studied, but these catalysts are not as active as Pt- and CrO_x-based systems, as shown when comparing the initial rate of propene formation (Table 4).

Rapid catalyst deactivation was observed within 30 minutes because carbon deposits formed on Pd NPs covering them and/or block the pores of zeolite support. For this reason, the active sites were not exposed to

the feed and failed to catalyze the reaction. The TG-DSC profiles of the spent catalysts revealed that different amounts of carbon deposits were present in the materials (Fig. S1). In general, the amount of carbon deposited in the impregnated catalysts was significantly higher than that in the encapsulated catalysts possibly due to the confinement of the NPs in the zeolite. Under these conditions, the oligomers, which are coke precursors, cannot be easily generated; alternatively, less carbon can be deposited in the empty space of the channels of the encapsulated catalysts than on the outer surface opened to free space of the impregnated catalysts. Furthermore, IPC-4 support, having smaller pores compared to IPC-2, shows ca. 5 times more amount of carbon deposit than IPC-2 counterpart. As can be seen from the TG data (Fig. S1), the burn-off of the carbon deposit starts above 450 °C and is completed within 10 min at 600 °C. For a more detailed study of the nature of deactivation and the possibility of regeneration and reuse of the catalyst, the catalytic activity

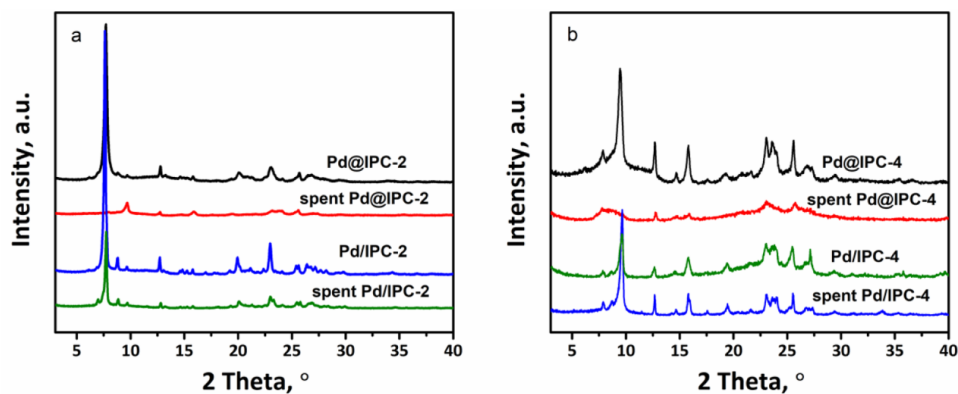


Fig. 8. XRD patterns of spent and fresh Pd@IPC-2 and Pd/IPC-2 (a), Pd@IPC-4 and Pd/IPC-4 (b).

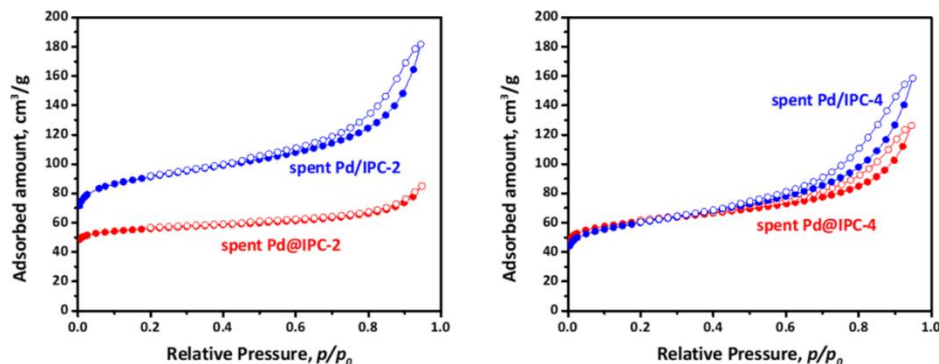


Fig. 9. N_2 adsorption-desorption isotherms of spent Pd@IPC-2 and Pd/IPC-2 catalysts (left panel), and Pd@IPC-4, and Pd/IPC-4 catalysts (right panel).

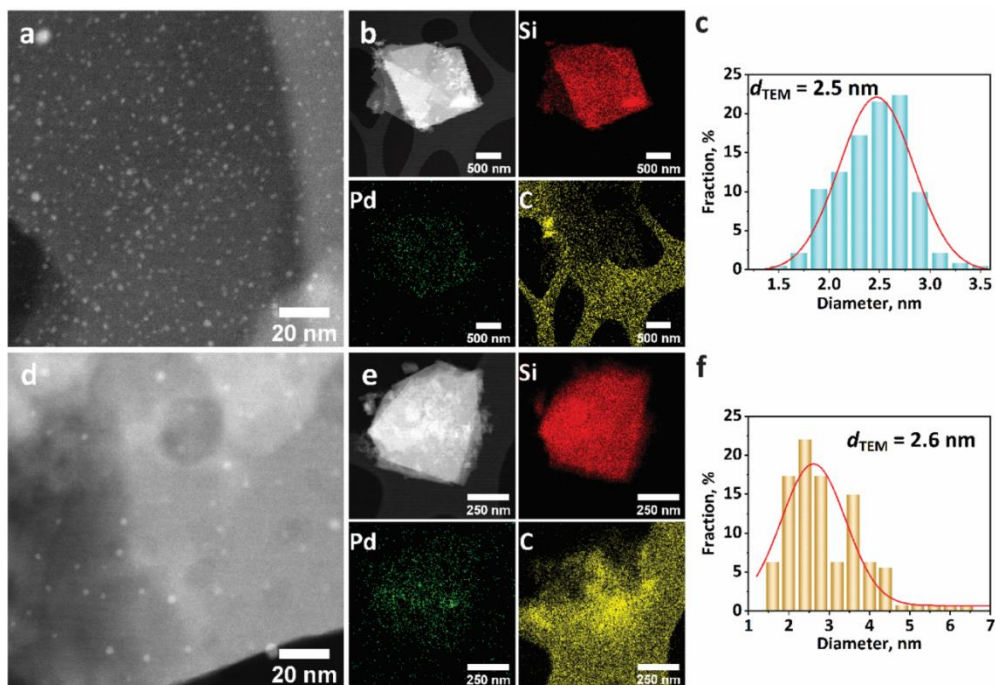


Fig. 10. STEM image, EDS maps of Si, Pd, and C elements, and size distribution of spent Pd@IPC-2 (a-c) and spent Pd@IPC-4 catalysts (d-f).

of the materials after regeneration in a He/O_2 mixture at $600\text{ }^\circ\text{C}$ for 0.5 h was studied.

Fig. 7 compares changes in the initial activity of the catalysts in the individual cycles. The encapsulated catalysts (Fig. 7a and c) showed a sharp decrease in initial activity after the first cycle, in contrast to their impregnated counterparts.

To identify the reason for decrease in activity of the catalysts, we characterized spent catalysts to elucidate possible changes in the structure and properties of the active Pd species or in the texture of the catalysts. The structure of the spent encapsulated catalysts collapsed, as confirmed by the disappearance of the dominant peaks around 7.6° and

9.7° 2θ in the XRD patterns of the spent IPC-2 and IPC-4 catalysts, respectively (Fig. 8a and b). This collapse did not occur in their impregnated counterparts (spent Pd/IPC-2 and spent Pd/IPC-4), whose structures remained well preserved. In spent Pd@IPC-2, the diffraction line at 9.6° 2θ appeared in the pattern while the intensity of the other peaks decreased in comparison with fresh Pd@IPC-2. These results indicate damage to the S4R linker and consequently disarrayed Si layers under harsh reaction conditions and decreased d spacing of the spent catalyst. In spent Pd@IPC-4, a broad band was generated in the range of $7\text{--}10^\circ$, and the intensity of the diffraction peaks corresponding to the layers also decreased, thus revealing that the structure collapsed due to

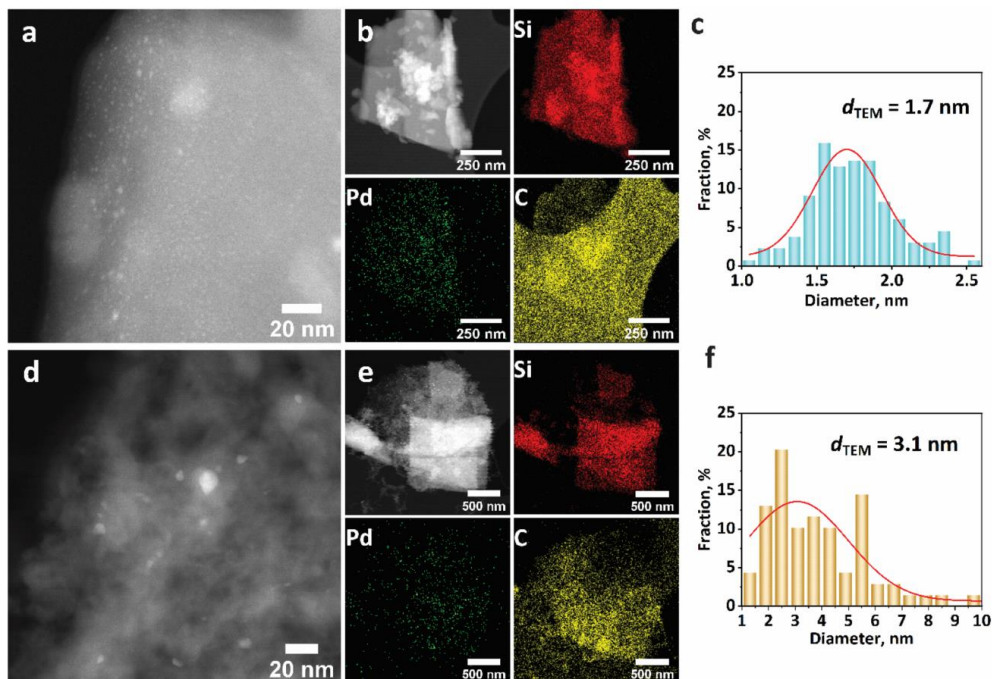


Fig. 11. STEM image, EDS maps of Si, Pd, and C elements, and size distribution of spent Pd@IPC-4 (a-c) and Pd/IPC-4 (d-f) catalysts.

the disorder of the layers. In the spent impregnated samples (spent Pd/IPC-2 and spent Pd/IPC-4), the structure remained well preserved (Fig. 8). Owing to coke on the catalyst, the intensity of all diffraction lines of Pd/IPC-2 decreased but remained at the original values of 20.

The EDS measurements did not show Pd leaching from the catalysts when comparing the Pd content of the samples before and after the reaction. The accuracy of EDS for low-content Pd is low; nevertheless, given the similar values, especially without any marked decrease, we confirmed that Pd atoms did not abandon the catalysts (Table 2). All catalysts also maintained their microporosity after the reaction, as shown in their N_2 adsorption-desorption isotherms because type I isotherms are typical of microporous materials, according to the IUPAC classification [44] (Fig. 9). And although the micropore volume decreased in all catalysts (Table 2), S_{BET} decreased significantly after the reaction only in the spent Pd@IPC-2, possibly due to the collapsed structure, in line with the XRD results. Yet, surprisingly, the S_{BET} Pd@IPC-4 was not similarly affected, remaining at a similar value despite the collapse of the structure. The spent catalysts exhibited a higher external surface area (Table 2) because the particle size decreased after the reaction, as shown in Fig. S2 and S3.

Figs. 10 and 11 show the STEM images, EDS mapping, and size distribution of spent Pd-IPC-2 and spent Pd-IPC-4, indicating that both encapsulated and impregnated samples contained uniformly visible Pd NPs. The average diameter of Pd NP in spent Pd@IPC-2 was 2.5 nm, which was similar to that of the fresh catalyst (2.4 nm). Therefore, the decrease in the initial activity of this catalyst after regeneration was likely caused by the collapse of the structure, as shown XRD patterns (Fig. 8).

The average diameter of the NPs in Pd/IPC-2 was approximately 2.6 nm and thus larger than that of the fresh catalyst (1.7 nm for the Pd/IPC-2). In this case, NP aggregation is a clear disadvantage of the impregnation, which may also account for the deactivation, in addition to

carbon deposition. In turn, the spent (Fig. 11) and fresh Pd@IPC-4 catalysts had similar Pd NP sizes, approximately 1.7 nm. However, the size distribution of spent Pd/IPC-4 revealed aggregation because the average diameter increased from 2.3 to 3.1 nm.

Fig. 12 shows acquired diffuse-reflectance FTIR spectra (DRIFT). Two absorption bands of carbonyl formed on metallic Pd are important in the studied region, namely one corresponding to linear carbonyls on the top of the well-dispersed metallic Pd, at a higher frequency around 2050 cm^{-1} , and another corresponding to bridged carbonyls at a lower frequency band between 1900 and 2000 cm^{-1} , probably involving 2-fold bridged carbonyls on metallic Pd [47]. The integral intensities of the linear and bridged carbonyls provided some information about changes in the active sites after the PDH reaction (Table 5). Among the impregnated catalysts (Pd/IPC-2 and Pd/IPC-4), the intensity of linear carbonyls decreased in the spent catalysts, but the intensity of bridged carbonyls increased during the reaction. As such, Pd NPs tend to form larger particles from unprotected Pd atoms after the reaction over impregnated catalysts, in line with the size of the NPs as assessed by STEM (Table 2), thereby decreasing the specific surface area of the particles and their catalytic activity. In turn, the intensity of both linear and bridged carbonyls of the spent Pd@IPC-2 and Pd@IPC-4 catalysts decreased, showing that Pd atoms are less accessible to the probe molecule (and subsequently to propane) after the reaction.

Cyclic reaction-regeneration experiments proved that the observed deactivation of catalysts consists of a reversible and an irreversible part. The reversible part is associated with the deposition of a carbon deposit, which is removable by burning at $600\text{ }^\circ\text{C}$ in the presence of oxygen, as documented in TG-DSC experiments (Fig. S1). From the characterization of the spent catalysts, it follows that the irreversible deactivation is not due to Pd leaching or a change in the size of Pd NPs (especially in the case of encapsulated catalysts) during the reaction, as confirmed by EDS and TEM (Table 2, Figs. 10 and 11). The partial inaccessibility of Pd NPs

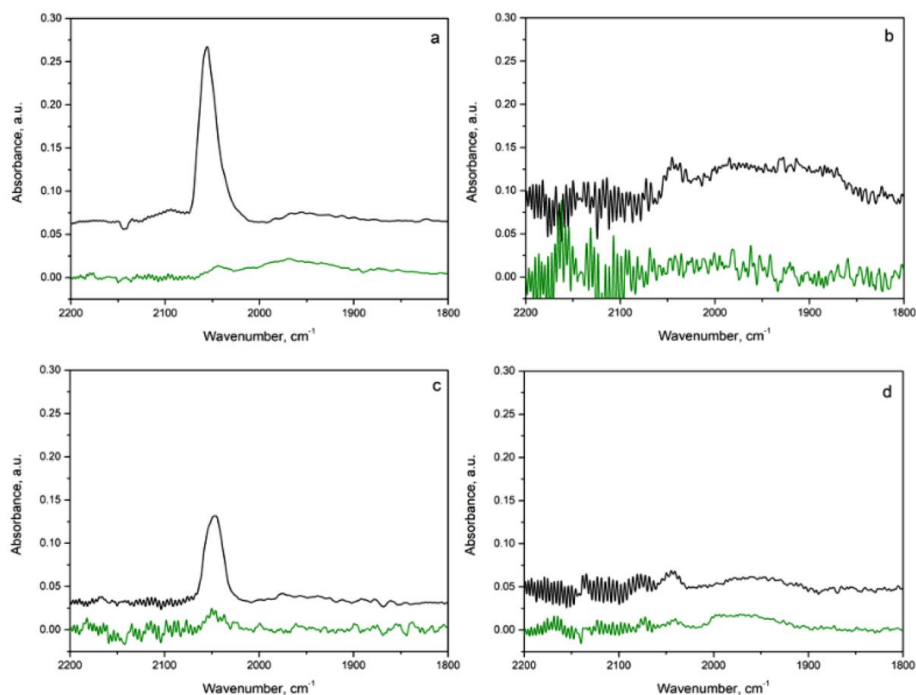


Fig. 12. DRIFT spectra of Pd@IPC-2 (a), Pd/IPC-2 (c), Pd@IPC-4 (b), and Pd/IPC-4 (d) before (black spectra) and after the reaction (green spectra). Note: The noisy section of the spectra in the range between 2200 and 2070 cm^{-1} is caused by an uncompensated contribution of gas phase CO vibrations.

Table 5

Integral intensities (in a.u.) of the C-O vibrational bands corresponding to the linear and bridged carbonyls in IR spectra (Fig. 12).

Catalyst	Linear	Bridged	L/B ^a
Pd@IPC-2	2.27	0.30	7.6
Spent Pd@IPC-2	0.41	0.07	5.9
Pd/IPC-2	4.49	0.54	8.3
Spent Pd/IPC-2	0.40	0.78	0.5
Pd@IPC-4	1.08	6.13	0.2
Spent Pd@IPC-4	0.48	0.62	0.8
Pd/IPC-4	0.40	1.07	0.1
Spent Pd/IPC-4	0.15	1.12	0.4

^aL/B refers to the Linear/Bridged carbonyls

is experimentally proven by observation of smaller amount of carbonyl complexes formed on Pd particles on spent catalysts after regeneration (see DRIFT spectra in Fig. 12). In our opinion, the lower accessibility of Pd NPs is related to the collapse of the zeolite framework, as evidenced by changes in XRD (see Fig. 8) and textural properties (decrease in the volume of micropores accompanied by increase in external surface area, see Fig. 9) of spent materials. It is assumed that the collapse of the zeolite matrix is due to harsh conditions during the catalytic reaction and/or regeneration and at the same time to the stress associated with the presence of Pd NPs between the individual lamellae. The lability of the zeolite frameworks of ADOR zeolites containing encapsulated metal particles under conditions of propane dehydrogenation reaction is not entirely expected, because zeolite materials are usually considered to be relatively thermally stable materials. This, from the point of view of propane dehydrogenation application, unsuitable behavior of catalysts brings new information about the behavior of a recently discovered

group of zeolites referred to as ADOR zeolites. In further research, it will be necessary to focus on finding ways to stabilize ADOR zeolite frameworks or to encapsulate metal nanoparticles in other zeolite structures, which will require other synthesis procedures, as was recently achieved using the imidazolium-type ionic liquid-assisted method applied to the MFI zeolite [26].

4. Conclusions

In the catalytic activity of Pd NPs encapsulated within IPC-2 and IPC-4 zeolites in the non-oxidative direct dehydrogenation of propane, the size of the zeolite channels and the structure of the framework play a critical role, with Pd@IPC-2 showing a higher activity than Pd@IPC-4 in PDH. Moreover, encapsulated Pd NPs exhibit a higher propane conversion and rate of propene formation than their impregnated counterparts possibly due to the smaller size or intrinsic properties of confined Pd NPs. Confining Pd NPs within a zeolite framework prevents undesired sintering, whereas their size increases in impregnated catalysts during this reaction. Moreover, encapsulated catalysts show decreased coke deposition inside the pores, but their structures collapse, rendering the Pd active sites inaccessible after the reaction and thus causing their deactivation during the cyclic catalytic tests.

Authors' contributions

M. S. and Y. Z. made equal contributions to this work.

CRediT authorship contribution statement

Mehran Sajad: Investigation, Data curation, Writing – original draft.

Yuyan Zhang: Data curation, Writing – original draft. **Martin Kubí:** Investigation. **Michal Mazur:** Investigation, Methodology. **Roman Bulánek:** Writing – review & editing, Supervision, Conceptualization. **Jiri Cejka:** Writing – review & editing, Supervision, Conceptualization.

Declaration of Competing Interest

The authors declare the following financial interests/personal relationships which may be considered as potential competing interests: Jiri Cejka reports financial support was provided by Czech Science Foundation. Michal Mazur reports financial support was provided by Ministry of Education Youth and Sports of the Czech Republic.

Data Availability

Data will be made available on request.

Acknowledgement

Y. Z. thanks the GAUK project (No. 1372819). J. Č. and M. K. acknowledge the support of the Czech Science Foundation (project EXPRO 19–27551X). The authors thank Carlos V. Melo for editing the manuscript. Jana Šánělová and Katerina Knotkova are kindly acknowledged for their help with TG-DSC and DRIFT measurements, respectively. M. M. would like to thank the OP VVV “Excellent Research Teams”, project no. CZ.02.1.01/0.0/0.0/15_003/0000417 – CUCAM. Y. Z. and J.C. thank the U.S. Army RDECOM Atlantic, U.S.A under Award No. W911NF-17-S-0003.

Supplementary materials

Supplementary material associated with this article can be found, in the online version, at doi:10.1016/j.apmt.2022.101644.

References

- J.J.H.B. Sattler, J. Ruiz-Martinez, E. Santillan-Jimenez, B.M. Weckhuysen, Catalytic dehydrogenation of light alkanes on metals and metal oxides, *Chem. Rev.* 114 (20) (2014) 10613–10653.
- J. Sheng, B. Yan, W.-D. Lu, B. Qiu, X.-Q. Gao, D. Wang, A.-H. Lu, Oxidative dehydrogenation of light alkanes to olefins on metal-free catalysts, *Chem. Soc. Rev.* 50 (2021) 1438–1468.
- S. Rimaz, M. Kosari, L. Chen, S. Kawi, A. Borgna, Enhanced catalytic performance of Pd nanoparticles during propane dehydrogenation by germanium promotion, *Mol. Catal.* 510 (2021), 111672.
- D.J. Childers, N.M. Schweitzer, S.M.K. Shahari, R.M. Rioux, J.T. Miller, R.J. Meyer, Modifying structure-sensitive reactions by addition of Zn to Pd, *J. Catal.* 318 (2014) 75–84.
- C. Yang, Z. Wu, G. Zhang, H. Sheng, J. Tian, Z. Duan, H. Sohn, A.J. Kropf, T. Wu, T. R. Krause, J.T. Miller, Promotion of Pd nanoparticles by Fe and formation of a Pd₃Fe intermetallic alloy for propane dehydrogenation, *Catal. Today* 323 (2019) 123–128.
- G. Zhang, C. Yang, J.T. Miller, Tetrahedral Nickel (II) phosphosilicate single-site selective propane dehydrogenation catalyst, *ChemCatChem* 10 (5) (2018) 961–964.
- C. Chen, M. Sun, Z. Hu, Y. Liu, S. Zhang, Z.-Y. Yuan, Nature of active phase of VOx catalysts supported on SiBeta for direct dehydrogenation of propane to propylene, *Chin. J. Catal.* 41 (2) (2020) 276–285.
- L. Wang, Y. Wang, C.-W. Zhang, J. Wen, X. Weng, L. Shi, A boron nitride nanosheet-supported Pt/Cu cluster as a high-efficiency catalyst for propane dehydrogenation, *Catal. Sci. Technol.* 10 (5) (2020) 1248–1255.
- T. Wu, G. Liu, L. Zeng, G. Sun, S. Chen, R. Mu, S. Agbotse Gbonfoun, Z.J. Zhao, J. Gong, Structure and catalytic consequence of Mg-modified VOx/Al₂O₃ catalysts for propane dehydrogenation, *AlChE J.* 63 (11) (2017) 4911–4919.
- A. Węgrzyniak, S. Jarczewski, A. Węgrzynowicz, B. Michorczyk, P. Kuśtrowski, P. Michorczyk, Catalytic behavior of chromium oxide supported on nanocasting-prepared mesoporous alumina in dehydrogenation of propane, *Nanomaterials* 7 (9) (2017) 249.
- Q. Liu, Z. Yang, M. Luo, Z. Zhao, J. Wang, Z. Xie, L. Guo, Vanadium-containing dendritic mesoporous silica nanoparticles: multifunctional catalysts for the oxidative and non-oxidative dehydrogenation of propane to propylene, *Microporous Mesoporous Mater.* 282 (2019) 133–145.
- G. Wang, H. Zhang, Q. Zhu, X. Zhu, X. Li, H. Wang, C. Li, H. Shan, Sn-containing hexagonal mesoporous silica (HMS) for catalytic dehydrogenation of propane: an efficient strategy to enhance stability, *J. Catal.* 351 (2017) 90–94.
- X. Chen, M. Ge, Y. Li, Y. Liu, J. Wang, L. Zhang, Fabrication of highly dispersed Pt-based catalysts on γ -Al₂O₃ supported perovskite Nano islands: High durability and tolerance to coke deposition in propane dehydrogenation, *Appl. Surf. Sci.* 490 (2019) 611–621.
- D. Zhao, Y. Li, S. Han, Y. Zhang, G. Jiang, Y. Wang, K. Guo, Z. Zhao, C. Xu, R. Li, C. Yu, J. Zhang, B. Ge, E.V. Kondratenko, ZnO nanoparticles encapsulated in nitrogen-doped carbon material and silicalite-1 composites for efficient propane dehydrogenation, *iScience* 13 (2019) 269–276.
- C. Chen, Z.-P. Hu, J.-T. Ren, S. Zhang, Z. Wang, Z.-Y. Yuan, ZnO supported on high-silica HZSM-5 as efficient catalysts for direct dehydrogenation of propane to propylene, *Mol. Catal.* 476 (2019), 110508.
- F. Jiang, L. Zeng, S. Li, G. Liu, S. Wang, J. Gong, Propane dehydrogenation over Pt/TiO₂-Al₂O₃ catalysts, *ACS Catal.* 5 (1) (2015) 438–447.
- M.D. Marcinkowski, M.T. Darby, J. Liu, J.M. Wimbly, F.R. Lucci, S. Lee, A. Michaelides, M. Flytzani-Stephanopoulos, M. Stamatakis, E.C.H. Sykes, Pt/Cu single-atom alloys as coke-resistant catalysts for efficient C–H activation, *Nat. Chem.* 10 (2018) 325–332.
- M.S. Kumar, D. Chen, J.C. Walmsley, A. Holmen, Dehydrogenation of propane over Pt-SBA-15: Effect of Pt particle size, *Catal. Commun.* 9 (5) (2008) 747–750.
- S. Vajda, M.J. Pellin, J.P. Greeley, C.L. Marshall, L.A. Curtiss, G.A. Ballentine, J. W. Elam, S. Catillon-Mucherie, P.C. Redfern, F. Mehmood, P. Zapol, Subnanometre platinum clusters as highly active and selective catalysts for the oxidative dehydrogenation of propane, *Nat. Mater.* 8 (2009) 213–216.
- L. Liu, U. Diaz, R. Arenal, G. Agostini, P. Concepcion, A. Corma, Generation of subnanometric platinum with high stability during transformation of a 2D zeolite into 3D, *Nat. Mater.* 16 (2017) 132–138.
- A. Iglesias-Juez, A.M. Beale, K. Maaßen, T.C. Weng, P. Glatzel, B.M. Weckhuysen, A combined in situ time-resolved UV-Vis, Raman and high-energy resolution X-ray absorption spectroscopy study on the deactivation behavior of Pt and PtSn propane dehydrogenation catalysts under industrial reaction conditions, *J. Catal.* 276 (2) (2010) 268–279.
- L. Shi, G.M. Deng, W.C. Li, S. Miao, Q.N. Wang, W.P. Zhang, A.H. Lu, Al₂O₃ nanosheets rich in pentacoordinate Al³⁺ ions stabilize Pt-Sn clusters for propane dehydrogenation, *Angew. Chem. Int. Ed.* 54 (47) (2015) 13994–13998.
- Y. Chen, S. Ji, C. Chen, Q. Peng, D. Wang, Y. Li, Single-atom catalysts: synthetic strategies and electrochemical applications, *Joule* 2 (7) (2018) 1242–1264.
- L. Liu, A. Corma, Metal catalysts for heterogeneous catalysis: from single atoms to nanoclusters and nanoparticles, *Chem. Rev.* 118 (10) (2018) 4981–5079.
- A. Wang, J. Li, T. Zhang, Heterogeneous single-atom catalysis, *Nat. Rev. Chem.* 2 (2018) 65–81.
- Y. Zhang, A. Li, M. Sajad, K. Fulajtárová, M. Mazur, M. Kubí, M. Shamzhy, M. Hronec, R. Bulánek, J. Cejka, Imidazolium-type ionic liquid-assisted formation of the MFI zeolite loaded with metal nanoparticles for hydrogenation reactions, *Chem. Eng. J.* 412 (2021), 128599.
- X. Li, X. Yang, J. Zhang, Y. Huang, B. Liu, In situ/operando techniques for characterization of single-atom catalysts, *ACS Catal.* 9 (3) (2019) 2521–2531.
- B.C. Gates, M. Flytzani-Stephanopoulos, D.A. Dixon, A. Katz, Atomically dispersed supported metal catalysts: perspectives and suggestions for future research, *Catal. Sci. Technol.* 7 (19) (2017) 4259–4275.
- Y. Du, H. Sheng, D. Astruc, M. Zhu, Atomically precise noble metal nanoclusters as efficient catalysts: a bridge between structure and properties, *Chem. Rev.* 120 (2) (2019) 526–622.
- J. Liu, Catalysis by supported single metal atoms, *ACS Catal.* 7 (1) (2017) 34–59.
- Z. Ou, Y. Li, W. Wu, Y. Bi, E. Xing, T. Yu, Q. Chen, Encapsulating subnanometric metal clusters in zeolites for catalysis and their challenges, *Chem. Eng. J.* 430 (2022), 132925.
- M. Shamzhy, M. Opanasenko, P. Concepción, A. Martínez, New trends in tailoring active sites in zeolite-based catalysts, *Chem. Soc. Rev.* 48 (4) (2019) 1095–1149.
- D. Farrusseng, A. Tuel, Perspectives on zeolite-encapsulated metal nanoparticles and their applications in catalysis, *New J. Chem.* 40 (5) (2016) 3933–3949.
- P. Gallezot, Preparation of Metal Clusters in zeolites. Post-Synthesis Modification I, Springer, 2002, pp. 257–305.
- S. Wang, Z.J. Zhao, X. Chang, J. Zhao, H. Tian, C. Yang, M. Li, Q. Fu, R. Mu, J. Gong, Activation and spillover of hydrogen on sub-1nm palladium nanoclusters confined within sodalite zeolite for the semi-hydrogenation of alkynes, *Angew. Chem. Int. Ed.* 58 (23) (2019) 7668–7672.
- Y. Zhang, M. Kubí, M. Mazur, J. Cejka, Encapsulation of Pt nanoparticles into IPC-2 and IPC-4 zeolites using the ADOR approach, *Microporous Mesoporous Mater.* 279 (2019) 364–370.
- M. Opanasenko, M. Shamzhy, Y. Wang, W. Yan, P. Nachtigall, J. Cejka, Synthesis and post-synthesis transformation of germanosilicate zeolites, *Angew. Chem. Int. Ed.* 59 (44) (2020) 19380–19389.
- O.V. Shvets, N. Kasian, A. Zukal, J. Pinkas, J. Cejka, The role of template structure and synergism between inorganic and organic structure directing agents in the synthesis of UTL zeolite, *Chem. Mater.* 22 (11) (2010) 3482–3495.
- M.V. Shamzhy, O.V. Shvets, M.V. Opanasenko, P.S. Yaremov, L.G. Sarkisyan, P. Chlubná, A. Zukal, V.R. Marthala, M. Hartmann, J. Cejka, Synthesis of isomorphously substituted extra-large pore UTL zeolites, *J. Mater. Chem.* 22 (31) (2012) 15793–15803.
- P. Chlubná, W.J. Roth, H.F. Greer, W. Zhou, O. Shvets, A. Zukal, J. Cejka, R. E. Morris, 3D to 2D routes to ultrathin and expanded zeolitic materials, *Chem. Mater.* 25 (4) (2013) 542–547.

- [41] O.V. Shvets, M.V. Shamzhy, P.S. Yaremov, Z. Musilová, D. Procházková, J. Čejka, Isomorphous introduction of boron in germanosilicate zeolites with UTL topology, *Chem. Mater.* 23 (10) (2011) 2573–2585.
- [42] W.J. Roth, O.V. Shvets, M. Shamzhy, P. Chlubná, M. Kubů, P. Nachtigall, J. Čejka, Postsynthesis transformation of three-dimensional framework into a lamellar zeolite with modifiable architecture, *J. Am. Chem. Soc.* 133 (16) (2011) 6130–6133.
- [43] L. Sun, S. Zhang, W. Bao, W. He, Catalytic Properties of Pd nanoparticles Supported On Cu₂O microspheres For Hydrogen Peroxide Electroreduction, *S, RSC Advances*, 2015, pp. 53320–53325.
- [44] M. Thommes, K. Kaneko, A.V. Neimark, J.P. Olivier, F. Rodriguez-Reinoso, J. Rouquerol, K.S.W. Sing, Physisorption of gases, with special reference to the evaluation of surface area and pore size distribution (IUPAC Technical Report), *Pure Appl. Chem.* 87 (9-10) (2015) 1051–1069.
- [45] S.-F. Pan, J.-L. Yin, X.-L. Zhu, X.-J. Guo, P. Hu, X. Yan, W.-Z. Lang, Y.-J. Guo, P-modified microporous carbon nanospheres for direct propane dehydrogenation reactions, *Carbon* 152 (2019) 855–864.
- [46] Z.-P. Hu, H. Zhao, C. Chen, Z.-Y. Yuan, Castanea mollissima shell-derived porous carbons as metal-free catalysts for highly efficient dehydrogenation of propane to propylene, *Catal. Today* 316 (2018) 214–222.
- [47] A. Tereshchenko, A. Guda, V. Polyakov, Y. Rusalev, V. Butova, A. Soldatov, Pd nanoparticle growth monitored by DRIFT spectroscopy of adsorbed CO, *Analyst* 145 (23) (2020) 7534–7540.

Supporting information

Direct dehydrogenation of propane over Pd nanoparticles encapsulated within IPC zeolites with tunable pore sizes

Mehran Sajad^a, Yuyan Zhang^b, Martin Kubů^b, Michal Mazur^b, Roman Bulanek^{a*}, and Jiří Čejka^{b*}

^aDepartment of Physical Chemistry, Faculty of Chemical Technology, University of Pardubice, Studentska 573, 532 10 Pardubice, Czech Republic

^bDepartment of Physical and Macromolecular Chemistry, Faculty of Science, Charles University, Hlavova 2030/8, 128 43 Prague, Czech Republic

Content

Figure S1. TG profile of the spent catalysts: a. Pd@IPC-2, b. Pd/IPC-2, c. Pd@IPC-4, d. Pd/IPC-4.

Figure S2. SEM images of the spent catalysts; Pd@IPC-2 (a), Pd/IPC-2 (b), Pd@IPC-4 (c), Pd/IPC-4 (d).

Figure S3. The zeolites particle size distribution for all of the fresh and spent catalysts obtained from SEM images.

Figure S4. High magnification SEM images of fresh (left column) and spent (right column) materials.

Figure S5: Side-view STEM images of encapsulated Pd nanoparticles within IPC- 2 (left) and IPC-4 (right) zeolite framework.

Table S1: Size and dispersion of Pd NPs in fresh catalysts and initial turnover rate

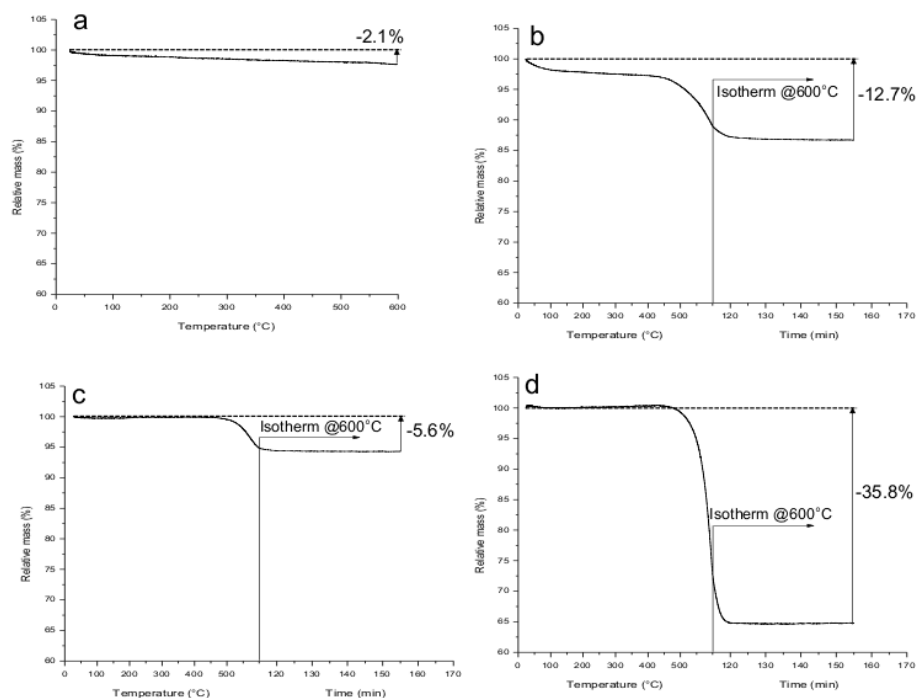


Figure S1. TG profile of the spent catalysts: a. Pd@IPC-2, b. Pd/IPC-2, c. Pd@IPC-4, d. Pd/IPC-4.

The TG-DSC profiles of the spent catalysts exhibited different mass losses, demonstrating the presence of different amounts of carbon deposits that have been burning out of the spent catalysts. In general, the amount of carbon content in the impregnated catalysts was significantly higher than that of the encapsulated ones. The spent Pd@IPC-2 exhibited the lowest amount of coke deposition among all catalysts, a weight loss of approximately 2.1% was observed throughout the heating process from 31 to 600 °C (Figure S1a), while it has been around 5.6% for its impregnated counterpart, Pd/IPC-2, from 415 °C to 600 °C (Figure S1b). On the other hand, Pd@IPC-4 showed a weight loss of approximately 2% in the range 25-183 °C assigned to the desorption of adsorbed water, then a larger mass loss of approximately 10.6% corresponded to

the coke deposition occurring between 323 °C and 600 °C (Figure S1c), while its impregnated counterpart, Pd/IPC-4, showed significantly higher carbon deposition around 35.8% starting at 426 °C and ending at 600 °C (Figure S1d).

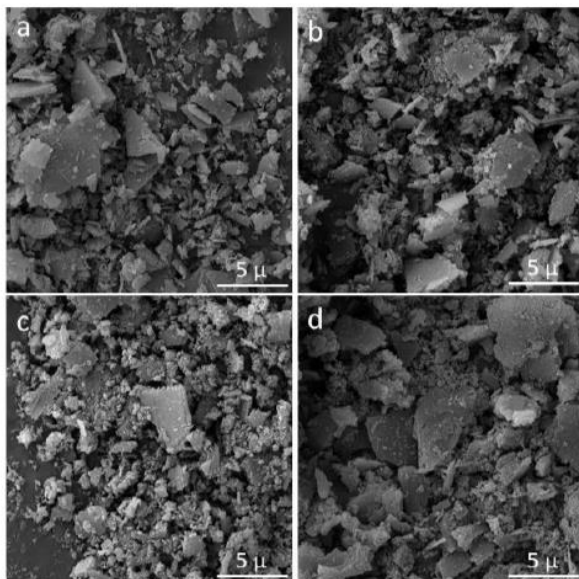


Figure S2. SEM images of the spent catalysts; Pd@IPC-2 (a), Pd/IPC-2 (b), Pd@IPC-4 (c), Pd\IPC-4 (d).

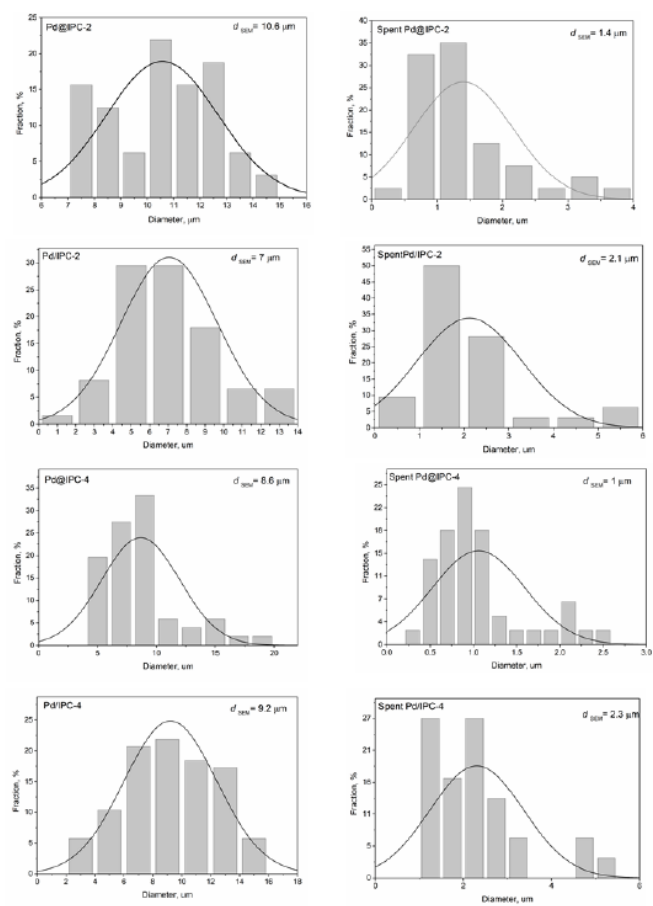


Figure S3. The zeolites particle size distribution for all of the fresh and spent catalysts obtained from SEM images.

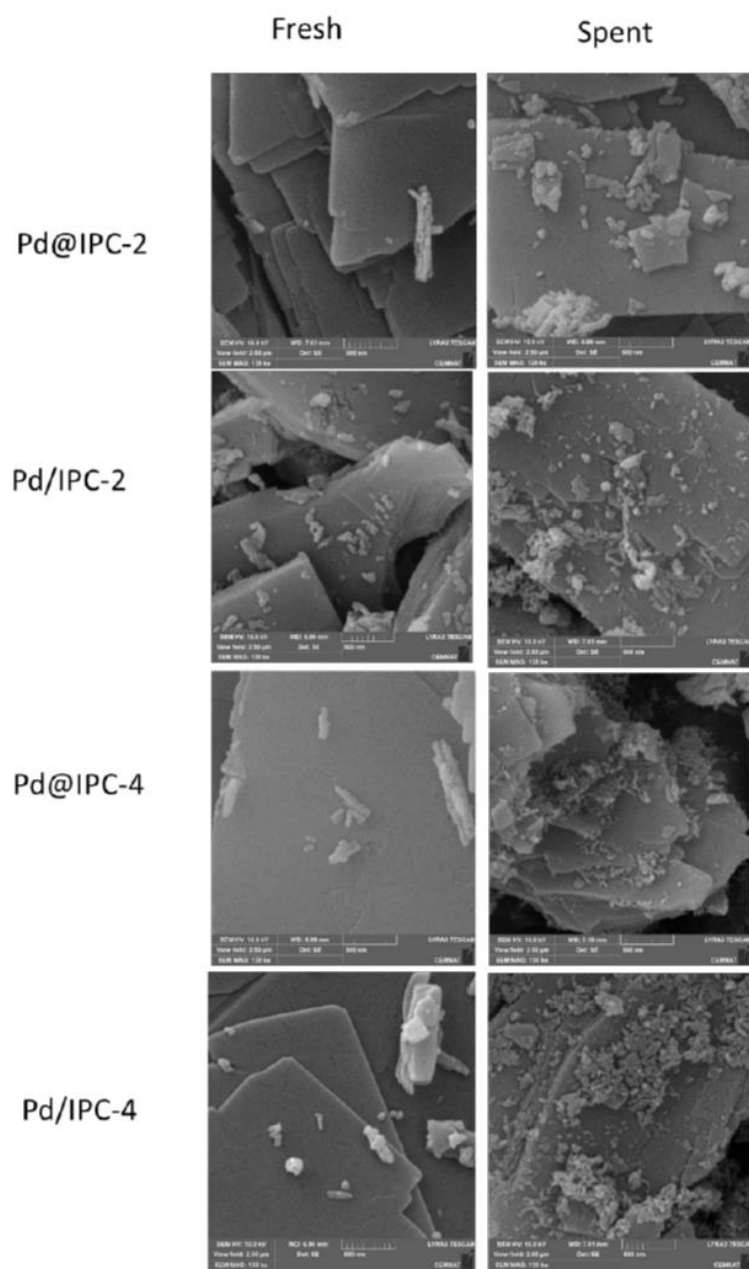


Figure S4. High magnification SEM images of fresh (left column) and spent (right column) materials.

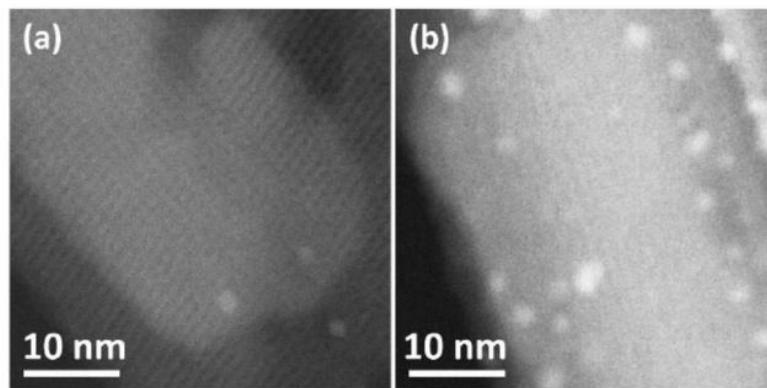


Figure S5: Side-view STEM images of encapsulated Pd nanoparticles within IPC- 2 (a) and IPC-4 (b) zeolite framework

Table S1: Size and dispersion of Pd NPs in fresh catalysts and initial turnover frequency

	NPs size ^a (nm) / dispersion (%) ^a	TOF (10 ⁻² s ⁻¹) ^b
IPC-2	-	-
Pd@IPC-2	2.4 / 24	8.8
Pd/IPC-2	1.7/ 34	2.5
IPC-4	-	-
Pd@IPC-4	1.7 / 34	4.4
Pd/IPC-4	2.3 / 25	3.8

^a – dispersion calculation is based on STEM images analysis and consideration of geometry of particles

^b - The TOF, i.e. turnover frequency, is defined by molar reaction rates per mole of surface Pd atoms

Paper V

Effect of the catalytic reactor arrangement and catalyst treatment in oxidative dehydrogenation of propane performance over hexagonal boron nitride

Mehran Sajad^{*1}, Roman Bulánek¹, Stanislav Šlang²

¹ Department of Physical Chemistry, Faculty of Chemical Technology, University of Pardubice, Studentska 573, 532 10 Pardubice, Czech Republic

² Center of Materials and Nanotechnologies, Faculty of Chemical Technology, University of Pardubice, nám. Čs. Legii 565, 532 10 Pardubice, Czech Republic

* Mehran.sajad@upce.cz

Abstract

A new promising nonmetallic catalyst, hexagonal boron nitride, was studied systematically in the oxidative dehydrogenation of propane to have a better understanding of the actual driver and the phenomena involved in this complicated system. This catalyst exhibited high activity and selectivity that was accompanied by the production of ethene as a valuable side product, along with low overoxidation of the products. Although the catalysts undergo substantial changes in chemical composition, textural properties, and crystallinity during the reaction, the activity and selectivity remain almost constant. Unlike previous studies that reported the oxygen content as the main factor, in this work it is shown that the reaction is driven mostly by gas-phase chemistry. Therefore, a longer residence time in a larger free space is essential for radical generation and propagation to improve productivity, while oxygen content does not play a key role. In fact, the change in oxygen content is the result of radical formation in the gas phase and not the cause for that. This catalyst is privileged because a coupled surface-mediated gas-phase mechanism is involved, resulting in higher activity and productivity compared with traditional metallic catalysts in the oxidative dehydrogenation of light alkanes suffering from overoxidation and low selectivity. It seems that one of the actual roles of hBN is to terminate the generated radicals or adsorption of water which are formed in the gas phase, and generate the in situ oxygenated species that eventually result in formation of products. It is hypothesized that in this system the initiation stage is in the gas phase and not on the surface of the catalyst.

Keywords: Oxidative dehydrogenation, propane, hexagonal boron nitride, olefin, gas phase, reactor.

Introduction

Recent breakthroughs in the metal-free catalyst for the oxidative dehydrogenation of propane (ODHP) have been dedicated to hexagonal boron nitride (hBN), with promising activity and selectivity for valuable olefins (propene and ethene), as well as negligible CO₂ formation^{1, 2}. First, Hermans et al. reported a 14% conversion of propane with ca. 90% selectivity to propene and ethene by commercial hBN, which changed

the common mindset about the inertness of this material ¹. Since then, the knowledge about the active sites and the mechanism in ODHP by hBN catalytic systems has continuously evolved. In situ functionalization of the surface has been reported to be essential for the formation of oxygenated boron species (BO_x), which act as initiators in the ODH of light alkanes ²⁻⁹. Moreover, it has recently been reported that hBN does not work with a typical redox mechanism similar to metal oxides, but instead, gas phase radical chemistry is the co-driver of ODH of light alkanes, while the catalyst is responsible for initiating the gas phase chemistry; therefore, the mechanism involves coupled catalytic and gas phase chemistry ¹⁰⁻¹³. It has been assumed that the hBN surface initiate the ODHP reaction by producing the radicals similar to allyl radicals generated in propene oxidation over bismuth oxide ¹⁴, or methyl radicals formed when methane was passed over magnesium oxide ¹⁵ at comparable temperatures to the ODHP reaction. Venegas et al. ¹³ reported some influence of changing reactor diameter and residence time. They realized that both parameters affect the hBN activity in ODH of propane. It was claimed that increasing the reactor size results in increasing in propane conversion and also the reaction progress exhibited a volcano type dependency to the catalyst mass. Moreover, the addition of SiC accelerated the extent of reaction even though the free space inside the reactor was filled by quartz chips. It was mentioned that mixing hBN with SiC lead to a higher rate of propane conversion compared to dilution as layered bed. Later, Zhang et al. explored the first direct experimental evidence of gas-phase which was methyl radicals formed during cleavage of the C-C bond ¹¹. It is said that the C₂ and C₁ products are generated through both surface-mediated and gas-phase reactions, while propene is produced mainly on the catalyst surface because no propyl radicals were observed. However, Venegas et al. ¹⁶ suggested that propyl radicals react in the gas phase and are not bound to the catalyst surface, which is not in agreement with the previous report, but again highlights the importance of gas phase chemistry and the crucial need to study more of this system. In another study, Najjafi et al ¹⁷ reported high propane conversion and olefin selectivity boron-based catalysts by empty quartz reactor via changing the reactor size, residence time, temperature etc. Also, the positive effect of increasing the post catalytic volume in the presence of hBN on the propane conversion was shown. They suggested that radicals desorbed from the surface of h-BN, react further with other species in the gas-phase and increase the conversion of propane. The possible influence of interaction from quartz reactor which exhibited similarity to hBN for production of radicals as well as the impurities from different supplier was studied as well.

In this contribution, it has been tried to disclose how the reported hypothesis in the literature could be confirmed or invalidated by experiments. The results revealed that the changes within the catalyst do not influence the activity and the oxygenated boron species are not the actual driving force, whereas the reaction productivity actually relies on the gas phase. Moreover, a systematic study of the possible effective parameters that interfere in the gas-phase reactions was studied, such as reactor geometry, catalyst bed, catalyst mass, catalyst dilution, free space, flowrates, and temperature, resulting in a better understanding of the important details in this reaction and improved knowledge of the hBN function in the ODHP reaction.

Experimental

2.1. Catalyst treatments

In this work, hexagonal boron nitride (h-BN with 98% purity and 1 μm particle size purchased from Sigma-Aldrich) was treated under various conditions at 490 °C, including treatment under different atmospheres for two hours (He, He/O₂, He/C₃H₈, He/O₂/C₃H₈), different time on the stream (TOS) in ODHP atmosphere (He/O₂/C₃H₈) from 15 minutes to 10 hours (0.25, 0.5, 1, 2, 3, 4, 5, 7, 10 h), different mass of catalyst (50,

100, 150 mg) under ODHP atmosphere with and without catalyst dilution (with SiC and quartz sand), different reactor diameter (internal diameter: 9, 10, 12.3, 14.5, 15.5 mm), direct and reverse direction of feeding, different total flowrates (15 to 35 ml min⁻¹) and lastly different temperature (470, 490, 510 and 530 °C). The porosity of quartz sand particles was calculated 45 %.

2.2. Catalyst preparation

The hBN was impregnated by boric acid for 5 wt.%. First boric acid was dissolved in water by stirring and then hBN was added to the solution and continued stirring at 75 °C until the solvent was evaporated. Then the obtained powder was dried at 110 °C over night and labeled as impregnated. Later, for measuring the catalytic activity of the washed sample, the impregnated hBN was stirred for one hour in methanol, filtered and dried at 110 °C over night and labeled as washed.

High surface area hBN was synthesized by using guanidine carbonate and boric acid as precursors. After dissolving the precursors in water, the solvent was evaporated at 80 °C over night, and then the white powder was treated at 1000 °C under N₂ atmosphere.

2.3. Catalytic test

Catalytic behavior of hBN in ODHP was investigated in plug-flow fixed-bed tubular shape glass reactors, using desired mass of catalyst with the grain size of 0.35 to 0.50 mm at the chosen temperature and under atmospheric pressure, in a reaction mixture consists of C₃H₈/O₂/He = 30/15/55 vol. % and total flow rate of 20 ml min⁻¹. Before each catalytic test, a pretreatment was performed by He (11 ml min⁻¹) at the reaction temperature with a heating rate of 5 °C min⁻¹ and was kept for 2 hours. The blank test was carried out with an empty reactor in the same conditions. The products were analyzed with an online gas chromatograph (Agilent 7890A) with a flame ionization detector (FID) and a thermal conductivity detector (TCD). The GS-Carbonplot GC column (60 m long with a diameter of 320 μm) was used for the separation of compounds. The injector and oven temperature were 150 °C and the detector temperature was 270 °C. Helium was used as carrier gas with a flow of 3 ml/min.

2.4. Characterization

All fresh and treated catalysts were characterized by N₂ physisorption isotherms, X-ray diffraction (XRD) patterns, X-ray photoelectron spectroscopy (XPS), energy dispersive X-ray spectroscopy (EDS), Raman, infrared (IR) and mass spectroscopy. N₂ physisorption isotherms at -196 °C were measured using a Gemini instrument. Before each adsorption measurement, the samples were degassed using a "Flow Prep 060 sample degas system" to allow slow removal of pre-adsorbed water at low temperatures. The temperature was increased with a temperature ramp of 10 °C min⁻¹ up to 250 °C. The samples were degassed at this temperature under an atmosphere of N₂ with the flow rate of 25 ml min⁻¹ for 5 h. The powder X-ray diffraction data were recorded on a Bruker D8 X-ray powder diffractometer equipped with a graphite monochromator and a position-sensitive detector (Vantec-1) using Cu K α radiation (at 40 kV and 30 mA) in Bragg–Brentano geometry. The surface chemical state of the samples was monitored by X-ray photoelectron spectroscopy (ESCA2SR, Scienta-Omicron) using a monochromatic Al K α (1486.7 eV) X-ray source. The binding energy scale was referenced to appendant carbon (284.8 eV). The quantitative elemental composition of the samples was further evaluated using a scanning electron microscope LYRA 3 (Tescan) equipped with an AZtec X-Max 20 (Oxford Instruments) at an acceleration voltage of 20 kV.

Raman Spectra of the samples were collected on a DXR2 Raman microscope (Nicolet, Thermo Fisher Scientific) equipped with the 785 nm excitation diode laser (30 mW, laser spot size 1.6 μm) and CCD detector. The experimental setup for the Raman measurements was 20 mW laser power on the sample, 5s duration of a single scan, 100 scans summed in one spectrum. Diffuse Reflectance Infrared Fourier Transform (DRIFT) spectra of the fresh and spent catalysts were recorded through in situ measurements on a Thermo Nicolet FT-IR 6700 spectrometer equipped with a DRIFT cell (Thermo Scientific) and an MCT/A detector cooled by liquid nitrogen. The background was measured using a metallic mirror under N_2 atmosphere in the reaction chamber (10 $\text{ml}\cdot\text{min}^{-1}$ flow rate). Step by step, the samples were heated to 450 $^\circ\text{C}$ in N_2 flow, dehydrated for 2 hours at 450 $^\circ\text{C}$, and cooled to 150 $^\circ\text{C}$ in N_2 , then the spectra were collected. During the experiments, spectra were collected in the 4000 – 650 cm^{-1} range at 2 cm^{-1} resolution with 1028 scans. Lastly, the products of the ODHP reaction were analyzed by a quadrupole mass spectrometer OmniStar GDS 300 (Pfeiffer Vacuum, Germany) under the flowrates of $\text{C}_3\text{H}_8/\text{O}_2/\text{He} = 30/15/55$ vol. % at 490 $^\circ\text{C}$ by 100 mg of hBN placed in the reactor with 15.5 mm diameter. After various time on stream, dosing of reaction mixture or oxygen was terminated and the changes in the output products were monitored.

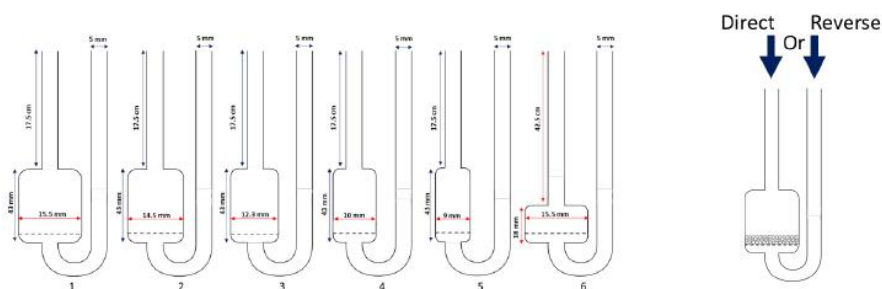
Results and discussion

Both theoretical and experimental studies on the catalytic activity of hBN have introduced the oxygenated boron species as the active sites^{2, 5}. Herein, we have observed that when different atmospheres (inert, oxidative, propane and ODHP) were applied at the reaction temperature (490 $^\circ\text{C}$), only the ODHP reaction atmosphere ($\text{He}/\text{O}_2/\text{C}_3\text{H}_8$), which contains propane and oxygen simultaneously, is able to make changes in the chemical composition, crystallinity, and surface area of hBN which is in agreement with Su et al¹⁸ work reporting that hBN materials could not be oxidized below 800 $^\circ\text{C}$ under an O_2 atmosphere. This indicates that with molecular O_2 alone it is not probable that the proposed B–O species could be formed at the surface of the catalyst under ODH reaction conditions. Figure S. 1. to S. 4. and table S. 1. show the changes in chemical composition on the surface and bulk, textural properties, and crystallinity of hBN treated under different atmospheres. It was observed that neither propane nor oxygen could modify the catalyst independently. Furthermore, it could be deduced that the change in catalyst at the reaction temperature under ODHP atmosphere comes from the interaction of generated radicals in the gas phase¹⁹ (from reaction between oxygen and propane) with catalyst surface, that stimulate the catalyst to generate oxygenated species.

According to our observation, all of the characterized physicochemical changes during the ODHP reaction over hBN (Figure S. 5. To Figure S. 9.) occur without noticeable impact on the catalyst activity, and the stable behavior of hBN was almost preserved in the course of 10 hours under the reaction stream (Figure S. 10). The catalytic activity of hBN showed propane conversion of approximately 25 % with selectivity of ca. 60% toward propene, approximately 17% for ethene and carbon monoxide, and less than 4 and 2% for methane and carbon dioxide, respectively. Thus, it could be said that the boron oxide species which play the main role, are maybe formed at the very initial stages and then the increase in oxygen content is due to the formation of unimportant oxygenated boron species that do not interfere in the reaction. On the other hand, it could be the gas phase that is controlling the reaction, and the extent of reaction is independent of the oxygen content which cause all the physicochemical changes occurring on the catalyst.

In our first step, to understand the influence of gas-phase chemistry, the ODHP reaction over hBN was studied by using different geometry of the reactors (Scheme 1) to provide various free space. Previously, the effect of post-catalytic volume in different systems including Mo-based for propene oxidation^{20, 21}, V-

Mg-O^{22,23} and hBN¹⁷ in ODHP, have been reported. It was shown that increasing the post-catalytic volume results in higher feed conversion because the generated free radicals via catalysts, proceed in the post catalytic volume and hence its size become important. Herein, the available free space is above the catalyst which makes it technically “pre-catalytic” volume (Scheme 1). It was observed that the propane conversion changes as a function of reactor diameter, where by increasing the free space step by step, the propane conversion increases (Figure 1). After that, two reactors with the same free volume but different diameter of the catalyst bed (Scheme 1, reactor 5 and 6) were used to study the effect of gas-solid interface against the gas-phase chemistry in ODHP reaction over hBN. These two reactors exhibited similar activity regardless of the differences in bed diameter, therefore it could be interpreted that the gas-solid interface does not play an important role, but in fact the available free space drives the reaction. This phenomenon is connected to the fact that a change in the reactor geometry impact the free volume and subsequently influences the residence time of the reaction mixture within the available space. Note that even though the interaction time with catalysts (contact time) remains the same, the residence time within the space is affected by changing the reactor size. Thus, it confirms the vital role of the gas-phase reactions. Later, more experiments were carried out where the reactor was fed by reverse direction (Scheme 1) to check the effect of post-treated free space in the gas-phase reactions, and it showed similar trend with a slightly higher propane conversion compared to the direct feeding pathway and confirmed the preliminary observations (Figure 1) but the catalytic activity decreased over time and the catalyst showed a slight deactivation which was not the case for the direct feeding with free space above the hBN catalyst (Figure 2). The chemical composition analysis of the spent catalysts after 3 hours under reaction by EDS revealed that in both feeding pathways, the oxygen content (which represents the oxygenated boron species) increased as the free space inside the reactor expanded (Table 1). In the direct feeding, the lowest amount of oxygen (3.2 at. %) was observed for the smallest reactor with 9 mm diameter, while this value increased step by step for each reactor by enlarging the container and reached 15.6 at. % for the largest reactor with 15.5 mm diameter. The amount of boron was almost constant, while the nitrogen content slowly decreased, probably due to the substitution with oxygen. In general, this trend was also valid for the reverse feeding direction, but with a lower oxygen content that changed from 2.6 to 7 at. % for the smallest and largest reactors, respectively. It seems that the content of oxygen correlate with the activity of the catalyst, because the lower activity of hBN under the stream due to the deactivation (Figure 2) seems corresponding for the lower content of oxygen in the reverse direction of feeding. Concerning this observation, it also can be deduced that the position of the catalyst bed could influence the activity, and the free space above the catalyst surface provide a better environment for the radicals to attack the catalyst surface and form the products, or maybe generates species that participate in the reaction and enhance the activity. Due to the interaction of feed molecules with each other in the gas phase that results in generation of radicals (probably oxygenated propyl radicals) the hBN surface is activated, but in the reverse feeding with post-treatment free space, the residence time in the empty space assist only in the formation and propagation of the radicals where not all of them will meet the catalyst surface eventually as the stream in reversed. Therefore, it was observed that the availability and the position of the free space and hBN catalyst is evidently crucial and have impact on oxygen content of the catalyst which is a representative of how much gas-surface interaction was involved.



Scheme 1. Schematic of the prepared reactors for ODHP over hBN (left) and the applied direct and reverse feeding lanes (right).

The free volume above the catalyst bed: Reactor number 1: 5.4 ml, 2: 4.9 ml, 3: 3.4 ml, 4: 2 ml, 5: 1.4 ml, 6: 1.4 ml.

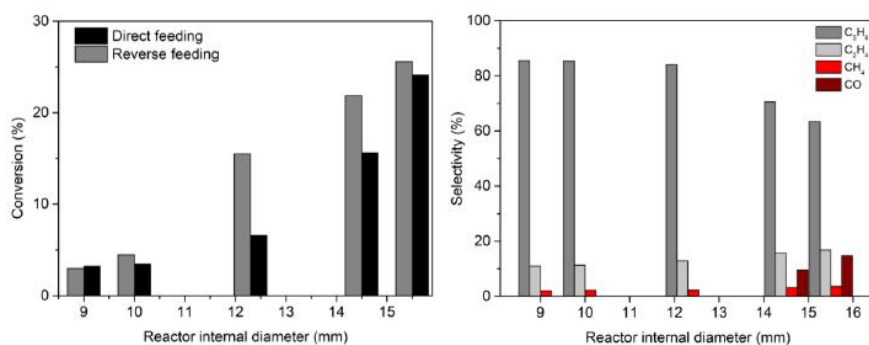


Figure 1. Propane conversion as a function of reactor size for ODHP in direct and reverse feeding direction (left), and products selectivity for the direct feeding (right), T: 490 °C, mass of catalysts: 100 mg, TOS: 15 min., He/O₂/C₃H₈ = 11/3/6 ml min⁻¹

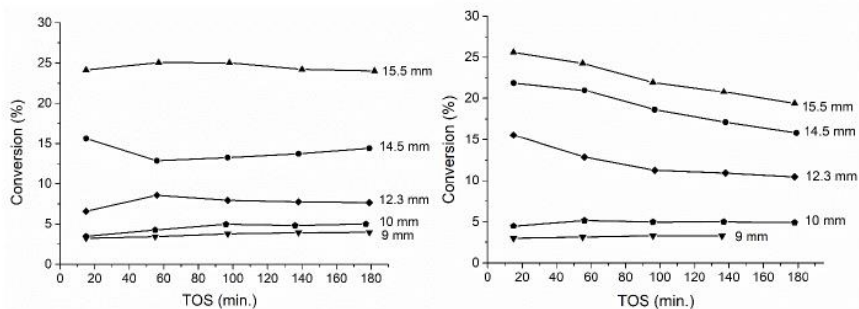


Figure 2. Propane conversion as a function of time on stream for different reactor sizes under the ODHP atmosphere, the direct direction of feeding (left), and the reverse direction of feeding (right). T: 490 °C, mass of catalysts: 100 mg, He/O₂/C₃H₈ = 11/3/6 ml min⁻¹

Table 1. Chemical composition (at. %) of spent hBN after the ODHP via different reactor sizes, TOS: 180 min, T: 490 °C.

	Reactor diameter (mm)	B	N	O
Direct	15.5	45.1	38.5	15.6
	14.5	47.2	46.0	5.9
	12.3	47.5	47.1	4.5
	10	47.5	47.7	3.7
	9	47.7	48.2	3.2
Reverse	15.5	47.1	45.1	7.0
	14.5	47.3	46.5	5.3
	12.3	47.4	47.2	4.4
	10	47.4	48.7	2.9
	9	47.9	48.9	2.6

The experimental evidence (EDS and XPS) of continuous increase in boron oxide formation during the ODHP (Figure S. 6.) as well as the enhanced conversion of propane by larger reactors (Figure 1) raised the questions whether the reaction is driven by in situ generated boron oxide, or the gas-phase chemistry that takes place inside the free space, or both. In addition, whether the free space controls the formation of oxygenated species and subsequently the catalyst activity, or the free space effect and the oxygenated species launch as individual phenomena. To answer these questions, two experiments were designed and carried out. The first experiment consisted of three steps: 1. The hBN catalyst was treated in ODHP using a small reactor (id: 9 mm), 2. then the spent catalyst from the small reactor was moved into a larger reactor (id: 15.5 mm), and 3. the spent catalyst from the larger reactor was moved back to the primary small reactor (id: 9 mm), and in each step the activity of the catalysts was measured in ODHP reaction (Figure 3). As discussed above (Table 1), the fresh catalyst in the smallest reactor generated much lower oxygen content (3.2 at. %) compared to the largest reactor (15.6 at. %). Therefore, the idea was to see whether the higher content of oxygenated species that were created in the largest reactor results in a higher activity of the catalyst in the smallest reactor or not. The results shown in Figure 3 disclosed that regardless of the amount of initial oxygen species, the reaction is driven by the free space because the oxygen content of the spent catalyst from the large reactor which was used in step 3 is five times higher than the oxygen content formed in step 1 using small reactor, but for both steps (1 and 3) the propane conversion is the same (ca. 3%) as the reactor size is identical (id: 9 mm) thus the role of the initial oxygenated species is not critical, while the actual driver force is the gas-phase reactions controlled by the free space.

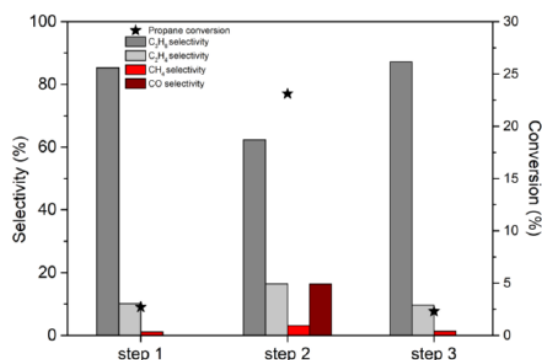


Figure 3. Propane conversion and product selectivity of step 1: fresh hBN in reactor with 9 mm diameter, step 2: the spent hBN from step 1 with O content of 3.2 at. % in reactor with 15.5 mm diameter, step 3: the spent hBN from step 2 with O content of 15.6 at. % in the reactor with 9 mm diameter. The O content after step 3 was measured as 13.7 at. %. T: 490 °C, mass of catalysts: 100 mg, TOS: 15 min., He/O₂/C₃H₈ = 11/3/6 ml min⁻¹

For the second test, the catalytic activity of hBN impregnated by boric acid (5 wt.%) was measured in ODHP. Then the catalyst was washed in order to remove the boron oxide and then the catalysts activities were compared (Figure 4). Surprisingly, the impregnated catalyst exhibited 36% less propane conversion compared to fresh hBN, meaning that the pre-formed boron oxide species not only did not improve the activity but also lessened it, probably due to covering the actual active sites or prevention of generating the genuine active sites. After washing the catalyst, the boron oxide was completely removed from the hBN surface and the activity was almost fully recovered. Thus, removing the preformed boron oxide made room for the catalyst to function with the typical access of the gaseous feed to the catalyst surface. The elemental composition obtained by EDS showed approximately 2 at. % and 12 at. % of oxygen content for the fresh and the impregnated catalyst which decreased to around 2 at. % after washing (Table 2). But interestingly both impregnated and washed catalysts exhibited ca. 12 at. % of oxygen after the reaction, which unveiled that the real active oxygenated species are formed in situ during the reaction and cannot be created by conventional impregnation of boron oxide in advance. It can be related to the nature of the species or to their sizes. Therefore, these experiments demonstrate that the structure of the active boron oxide is not the same as the preformed added bulk boron oxide. Also, the initial amount of boron oxide does not control the reaction pathway but, in fact, the gas-phase reaction is the decisive factor, meaning that the free space, permissible gas-phase reaction chains, and subsequently the interaction of feed with hBN surface for in situ generation of active sites, control the catalytic activity of this system.

It was also tried to compare the activity of commercial hBN (with 47 m²/g BET surface area) with a high surface area hBN (with 300 m²/g BET surface area) and the results showed comparable or even a bit lower propane conversion for the high surface area hBN, even though the later one with higher BET surface area exhibited ca. 25 at. % oxygen content (Figure 5). Under the same reaction condition, the propane conversion was ca. 18 and 25 % for the high surface area and the commercial hBN, respectively. Likewise, the selectivity toward products were similar. Therefore, these experimental results doubt the previous reports on considering importance of the catalyst surface (in sense how large surface area is) as the initiator of the gas-phase reaction and introduction of the boron oxide species as the main driver.

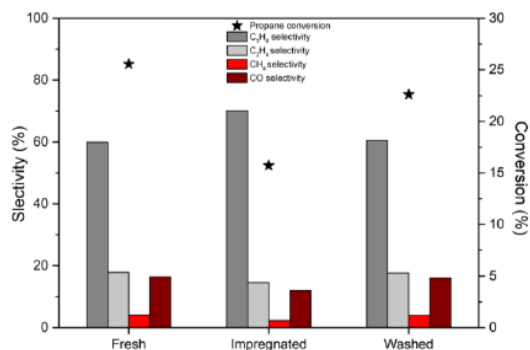


Figure 4. Propane conversion and products selectivity of impregnated BN by boric acid, and after washing, in ODHP, Reactor id: 15.5 mm, T: 490 °C, mass of catalysts: 100 mg, TOS: 15 min., He/O₂/C₃H₈ = 11/3/6 ml min⁻¹

Table 2. Chemical composition of impregnated and washed hBN before and after the ODHP reaction by EDS.

	Impregnated	washed	Spent impregnated	Spent washed
O at. %	12	2	12	12

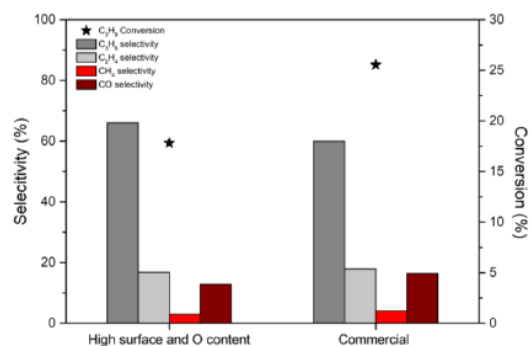


Figure 5. Propane conversion and products selectivity in ODHP over commercial hBN, and the synthesized hBN with higher surface area and oxygen content. T: 490 °C, mass of catalysts: 100 mg, TOS: 15 min., He/O₂/C₃H₈ = 11/3/6 ml min⁻¹

On the other hand, the activity of the empty reactors without hBN catalyst showed 3 to 5 % of propane conversion which are only due to the pure gas phase reactions and formation of the radical species. This experiment was measured in the reactor with 15.5 mm diameter without the catalyst, and exhibited 86 % of propene selectivity and 9 % of ethene selectivity. The CO, methane and CO₂ selectivity were observed as 0, 3 and 1 % respectively. In comparison with the hBN activity in the reactor of 9 mm diameter with similar propane conversion (ca. 3 %), under the same reaction condition, it could be seen that the selectivity toward products is just slightly different and almost comparable. Propene, ethene, CO, methane and CO₂ exhibited selectivity of 85, 11, 2, 0 and 2 % respectively. Therefore, it means in such a situation where there is not

enough space for an efficient radical propagation via coupled surface-mediated and gas-phase interaction, the reaction is driven only by the gas phase chemistry. Nevertheless, when hBN activity is measured in a larger reactor (id: 15.5 mm) under the same reaction condition, it is clearly visible that along with the increase in propane conversion to ca. 25 % (and O₂ conversion ca. 80 %), the selectivity to propene decreases to almost 60 % while the cracking products become more selective, such as ethene and CO with 17 % selectivity for both. There is no big change in selectivity toward methane and CO₂ as they stay with 4 and 2 %. Thus, these results show that under the same condition (reactor geometry, temperature, flow rate, etc.) the presence of hBN as the catalyst improve the propane conversion approximately five times. Therefore, it could be understood that after the interaction between generated radicals in the gas-phase with the hBN surface, some species are formed that enhance the reaction extent significantly.

The effect of dilution was studied in this work as well, and it was observed that the presence of SiC did not improve the activity but in contrary delayed reaching the final conversion level. This induction period was observed only in the presence of SiC, as the hBN catalyst without dilution exhibited stable activity from the beginning without showing induction time (Figure 6). The total volume of the bed (hBN diluted with SiC) was kept constant while changing the mass of hBN catalyst (the free space was 5.2 ml for all three experiments). Even though the initial activity of different masses of hBN catalyst were not the same, but they all reached similar conversion values after 3h under the stream which is in line with previous data showing that in a constant temperature the free space is the main driving force of the reaction, and as the free space was identical, the observed activity was similar. The presence of the induction period could be due to the existence of the diluent, because the radicals and intermediates are quenched on those sites. The slightly higher conversion of the hBN without dilution was probably due to the larger free space. The selectivity towards propene as the main product was a reverse trend of propane conversion and it decreased by time and at the end reached the value of 65 % for all the three diluted hBN catalysts (Figure 7). However, the ethene and CO selectivity increased over time with a similar trend as the propane conversion, and reached ca. 16 % for both after 225 minutes under the stream (Figure 7). The selectivity of the undiluted samples kept the same values due to no change in conversion (Figure 1). The presence of an induction period was reported in another work for ODH of ethane to ethene⁷, where the catalyst was also diluted as well, and the selectivity towards ethene decreased gradually by the increase in alkane conversion. In their work, it was claimed that the induction period indicate the B–O site needs to be formed under a certain activation and/or reaction condition, but the effect of the diluent was not considered by them. Because when we tried the ODH reaction over pure hBN without dilution, our observation did not show any induction period neither for propane nor ethane. Thus, as it was mentioned, the induction can be caused by quenching of the generated radicals on the diluent surface and delaying reaching the maximum efficiency.

Additionally, an experiment was carried out to demonstrate the activity of hBN in the presence of a fully packed reactor by SiC, to eliminate the entire possible free space of the reactor. The observed conversion was less than 2 % during 3 h of TOS whereas the empty reactor with the same geometry exhibited 3 to 5 % of propane conversion. Thus, it disclosed that the hBN without having available free space is almost inactive in ODH, and displayed again the critical role of the free space within the reactor for the gas phase reactions as the main driver. This result contradicts the report by Venegas et al.¹³ where addition of SiC improved the propane conversion while the remaining free volume of the reactor was filled by quartz chips. In fact, the presence of a diluent accelerates the radical quenching (based on the type of diluent) which means lowering the extent of reaction, even though the diluents or fillers are chemically inert and will not participate in the reaction. Another contradiction with their work stands against differences between dilution

by mixing hBN with SiC or use SiC as filler layers. In both cases our observation showed similar propane conversion of ca. 1 % which is less than empty reactor, while they have reported significant enhanced propane conversion by mixing compared to the layered SiC dilution. Hence accurate interpretation of the results is always important to not confuse the community working in the same field and we tried to clarify some of those.

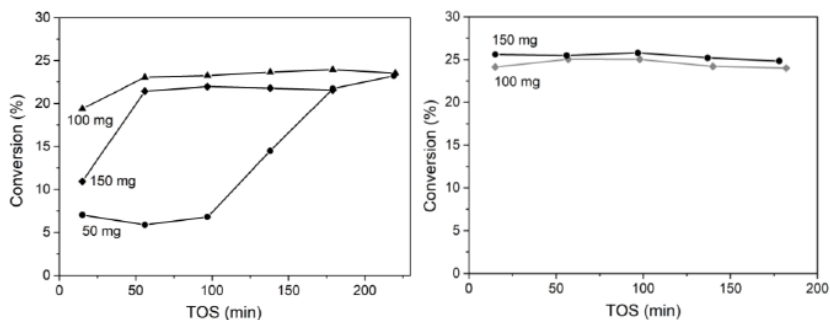


Figure 6. Propane conversion of different hBN masses as a function of time on stream, diluted by SiC (left), undiluted (right). The free volume above the catalyst in reactor with diluted hBN: 5.2 ml, and in reactor without dilution: 5.4 ml for 100 mg and 5.3 ml for 150 mg. Reactor id: 15.5 mm, T: 490 °C, He/O₂/C₃H₈ = 11/3/6 ml min⁻¹

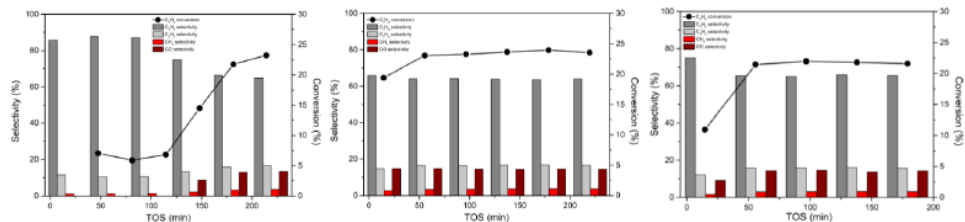


Figure 7. Selectivity towards products for different masses of hBN diluted by SiC, 50 mg (left), 100 mg (middle) and 150 mg (right). The free volume above the catalyst in reactor with diluted hBN: 5.2 ml. Reactor id: 15.5 mm, T: 490 °C, He/O₂/C₃H₈ = 11/3/6 ml min⁻¹

The effect of undiluted catalyst mass on this catalytic system was investigated in two different reactors with container diameters of 12.3 mm and 15.5 mm. For both of them, the results showed that the change in catalyst mass did not significantly influence conversion of propane, as shown in Figure 8. Note that changes in the free space were negligible with respect to the different masses of catalyst; therefore, it means the same diameter of catalyst bed provided identical interface between the gas and the solid phase in each reactor, and thus similar free space resulted in a comparable propane conversion. Even though the experiments involved adjusting the contact time between the gaseous feed and the catalyst surface by varying the mass of hBN, they provided confirmation that the reaction is primarily influenced by the available free space, rather than the quantity of catalyst. The selectivity toward products were similar in the same reactor. In the reactor with 12.3 diameter, for all three masses of hBN, the propene selectivity was kept approximately 74 % ± 2%, and for the ethene and CO ca. 13 ± 1 and 9 ± 1 %. Methane and CO₂ selectivity were less than 2%. In case of the reaction in the reactor with 15.5 mm diameter, both masses of hBN exhibited 61 % ± 2% of propene selectivity, while ethene, CO, and methane selectivity were 17 ± 1, 16 ± 1, and 4 ± 0.5 %. CO₂ selectivity was 1%.

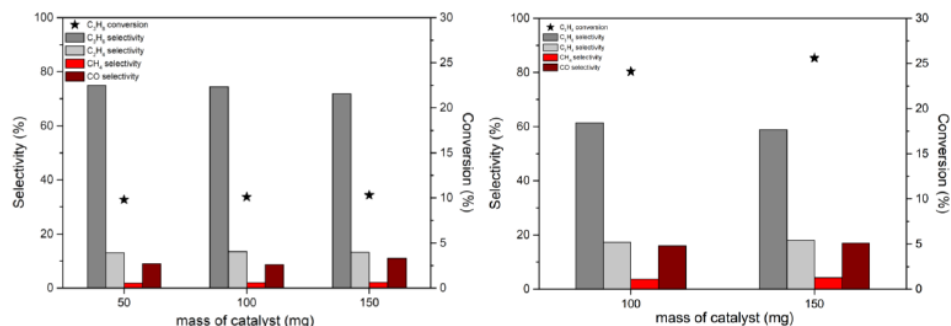


Figure 8. Propane conversion and products selectivity over hBN as a function catalyst mass, reactor diameter: 12.3 mm (left), 15.5 mm (right). The free volume above the catalyst in reactor with 12.3 mm diameter: 50 mg=3.6 ml, 100 mg= 3.4 ml, 150 mg= 3.3 ml, and in reactor with 15.5 mm diameter: 100 mg= 5.4 ml, and 150 mg= 5.3 ml. T: 490 °C, He/O₂/C₃H₈ = 11/3/6 ml min⁻¹

From the experiments described in the previous paragraphs, the essential role of the free space in the reactor emerges. Therefore, we performed another series of experiments with different values of the total flow rate of the reaction mixture, which affects the contact time with the catalyst as well as the total residence time of the gaseous mixture in the reaction zone of the reactor. It was observed that increasing the total flow rate, which is lowering the contact time and also the residence time of the gas in reactor, resulted in a decrease in the catalyst activity (Figure 9). Unlike catalyst mass, that did not play a crucial role in activity (due to not altering the free space), changing total flow within a constant free space, changed the time that the feed molecules (radical species) were able to interact with the hBN surface and/or with each other (residence time), therefore it affected the activity. It could be concluded that both larger free space and lower total flow rate increase the interactions between the gaseous species with each other and also with the catalyst surface and therefore push the ODHP reaction toward higher activity.

In another set of experiments, the propane conversion over the same amount of hBN in the same reactor was measured in the presence of quartz sands (particle size: 0.8-3 mm) as layers occupying one quarter, two quarters, three quarters and four quarters of the free space. The volume of the voids between the particles was calculated based on their porosity. The quartz sand particles occupied 0, 14, 31, 47 and 54 % of the space inside the reactor container. The results showed that by depressing the free space, the conversion rate decreased (Figure 10), which agrees with the observation of the change in the reactor size. Although the free space did not change to zero, because the porosity of the quartz sand layers inside the reactor was quite large, but still when the reactor was filled by quartz sands, the propane conversion dropped to 2.6 %, because the space between quartz particles as voids were not large enough to let the propagation chain of radicals be formed via gas phase chemistry, and in fact the filler particles turned to a place for termination of the radicals. As the propane conversion decreases by filling quartz sands, the propene selectivity increases from ca. 61 % for zero filling to 86 % with fully occupied reactor space. In contrary, the selectivity toward ethene and CO decreases from 17 to 11 and 16 to 0, respectively. Methane selectivity went through a smaller decrease from 4 to 1% while CO₂ selectivity was kept on 1%.

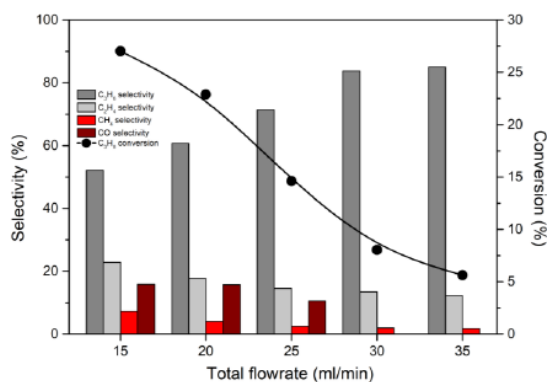


Figure 9. Propane conversion and product selectivity over hBN as a function total flow rate. Reactor id: 15.5 mm, T: 490 °C, mass of catalysts: 100 mg, He/O₂/C₃H₈ = 55/15/30 %

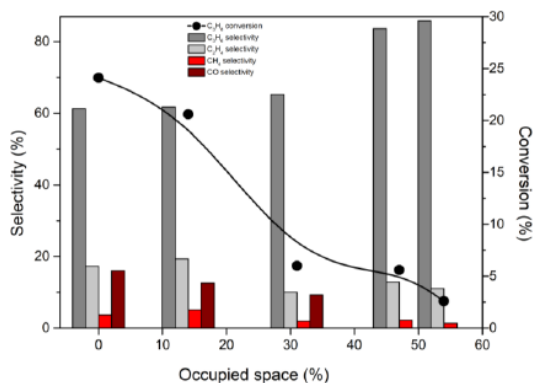


Figure 10. Propane conversion and product selectivity over hBN in ODHP reaction as a function of occupied reactor space by quartz sands. Reactor id: 15.5 mm, T: 490 °C, mass of catalysts: 100 mg, He/O₂/C₃H₈ = 11/3/6 ml min⁻¹

A combination of results from experiments with changing reactor size, free volume in the reactor by filler and change in flowrate revealed the dependency of reaction rate on residence time shown in Figure 11. It disclosed how propane conversion depends on residence time and supports the hypothesis mentioned above which showed the gas-phase is the main driving force the reaction in this system.

Furthermore, the change in reaction temperature (Figure S. 11.) as well as the changes of products selectivity as a function of conversion were investigated as well (Figure S. 12.). As it was expected, a higher reaction temperature resulted in higher propane conversion but it also revealed that regardless of how the propane conversion was changed, the selectivity to propene was always a reverse function of the propane conversion, irrespective of whether the size of the reactor was changed, or the temperature, or the amount of catalyst, or the gaseous feed flowrate, etc., the selectivity responded only to the conversion value and possibly took the same pathway. This trend was opposite for the other products which means in the case of ethene, methane and CO, the selectivity increases as the propane conversion was improved.

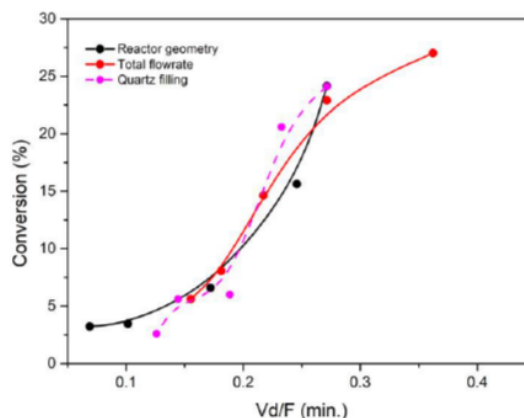


Figure 11. Propane conversion as a function of residence time (free space (or dead volume)/flowrate). Reactor id: 9, 10, 12.3, 14.5 and 15.5 mm, T: 490 °C, mass of catalysts: 100 mg, He: O₂: C₃H₈= 55/3/6 %, total flow: 15, 20, 25, 30, 35 ml min⁻¹, quartz filling: 0, 14, 31, 47, 54 %.

The experimental results obtained during this study from observation of different characterization of the hBN catalyst under various range of experiments that was discussed earlier let us disagree with some of the previous works and speculate a new pathway. It is clear that the oxygenated boron species are not the decisive parameter at least for the initiating the reaction, and the radicals are not formed on the boron oxide on the hBN surface at the beginning, but contrariwise, it seems that the oxygen and propane interactions in the gas-phase form radicals that attack the catalyst surface, and generate in-situ boron oxide moieties which enhance the extent of the reaction. To support this idea, it was shown that the empty reactor without catalyst exhibited some small activity in ODHP reaction. Additionally, the hBN catalyst was stable under oxidative atmosphere, therefore the reaction of surface with molecular oxygen is not probable at the reaction temperature. According to this research, the free space role is to provide environment for radical propagation and then one of the possible roles of hBN is to terminate those radicals on the catalyst surface that results in oxygenated moieties which could enhance the propane conversion.

Conclusions

The results obtained in this investigation revealed that the oxygen content does not control the reaction and in fact the gas-phase chemistry is the main driver in the oxidative dehydrogenation of propane over hBN. Thus, the available free space is a critical parameter because the residence time controls the radical formation/propagation in the gas phase. It could also be stated that the changes in the oxygen content of the catalyst are the result of interaction between activated oxygen in form of radicals and the hBN catalyst. According to our results we can hypothesize that one of the actual roles of hBN catalyst could be to terminate the generated radicals in the gas phase, and form the products. Also, it might result in formation of in situ oxygenated species that ultimately enhance formation of the products. On the other hand, the generated water in the gas phase also can be adsorbed on the hBN surface and produce oxygenated species which might participate in the reaction. Although a final precise mechanism cannot be proposed yet due to the complication of this system, but we have clarified that in contradiction with many reports in the literature, the initiation stage of the reaction in this system is not taking place on the surface of this catalyst, indeed it starts in the gas phase and then the surface contribution comes afterwards.

Author Contributions

Mehran Sajad: Conceptualization, data Curation, formal analysis, investigation, methodology, validation, visualization, writing – original draft, writing – review & editing

Roman Bulánek: Conceptualization, data Curation, formal analysis, investigation, methodology, validation, visualization, writing – original draft, writing – review & editing, project administration, Supervision, resources.

Stanislav Šlang: formal analysis, methodology, validation

Conflicts of interest

There are no conflicts to declare

Acknowledgements

M. S. and R. B. would like to acknowledge the support of the Czech Science Foundation (Project number: 22-23120S, Boron-containing catalysts for the oxidative dehydrogenation of alkanes).

References

1. J. T. Grant, C. A. Carrero, F. Goettl, J. Venegas, P. Mueller, S. P. Burt, S. E. Specht, W. P. McDermott, A. Chieregato and I. Hermans, *Science*, 2016, **354**, 1570-1573.
2. L. Shi, D. Wang, W. Song, D. Shao, W. P. Zhang and A. H. Lu, *ChemCatChem*, 2017, **9**, 1788-1793.
3. L. Shi, B. Yan, D. Shao, F. Jiang, D. Q. Wang and A. H. Lu, *Journal*, 2017, **38**, 389-395.
4. L. Shi, Y. Wang, B. Yan, W. Song, D. Shao and A.-H. Lu, *Chemical communications*, 2018, **54**, 10936-10946.
5. L. Shi, D. Wang and A.-H. Lu, *Chinese Journal of Catalysis*, 2018, **39**, 908-913.
6. J. M. Venegas, W. P. McDermott and I. Hermans, *Accounts of chemical research*, 2018, **51**, 2556-2564.
7. Y. L. Zhou, J. Lin, L. Li, X. L. Pan, X. C. Sun and X. D. Wang, *Journal of Catalysis*, 2018, **365**, 14-23.
8. S. Kumar, A. Lyalin, Z. Huang and T. Taketsugu, *ChemistrySelect*, 2022, **7**, e202103795.
9. J. H. Carter, T. Bere, J. R. Pitchers, D. G. Hewes, B. D. Vandegehuchte, C. J. Kiely, S. H. Taylor and G. J. Hutchings, *Green Chemistry*, 2021, **23**, 9747-9799.
10. P. Kraus and R. P. Lindstedt, *The Journal of Physical Chemistry C*, 2021, **125**, 5623-5634.
11. X. Zhang, R. You, Z. Wei, X. Jiang, J. Yang, Y. Pan, P. Wu, Q. Jia, Z. Bao and L. Bai, *Angewandte Chemie International Edition*, 2020, **59**, 8042-8046.
12. J. Sheng, B. Yan, W.-D. Lu, B. Qiu, X.-Q. Gao, D. Wang and A.-H. Lu, *Chemical Society Reviews*, 2021, **50**, 1438-1468.
13. J. M. Venegas and I. Hermans, *Organic Process Research & Development*, 2018, **22**, 1644-1652.
14. W. Martir and J. H. Lunsford, *Journal of the American Chemical Society*, 1981, **103**, 3728-3732.
15. D. J. Driscoll, W. Martir, J. X. Wang and J. H. Lunsford, *Journal of the American Chemical Society*, 1985, **107**, 58-63.

16. J. M. Venegas, Z. Zhang, T. O. Agbi, W. P. McDermott, A. Alexandrova and I. Hermans, *Angewandte Chemie International Edition*, 2020, **59**, 16527-16535.
17. M. Nadjafi, Y. Cui, M. Bachl, A. Oing, F. Donat, G. Luongo, P. M. Abdala, A. Fedorov and C. R. Müller, *ChemCatChem*, 2023, **15**, e202200694.
18. R. Huang, B. Zhang, J. Wang, K. H. Wu, W. Shi, Y. Zhang, Y. Liu, A. Zheng, R. Schlögl and D. S. Su, *ChemCatChem*, 2017, **9**, 3293-3297.
19. J. H. Knox, *Transactions of the Faraday Society*, 1960, **56**, 1225-1234.
20. C. Daniel and G. W. Keulks, *Journal of Catalysis*, 1972, **24**, 529-535.
21. C. Daniel, J. R. Monnier and G. W. Keulks, *Journal of Catalysis*, 1973, **31**, 360-368.
22. K. T. Nguyen and H. H. Kung, *Industrial & engineering chemistry research*, 1991, **30**, 352-361.
23. K. T. Nguyen and H. H. Kung, *Journal of Catalysis*, 1990, **122**, 415-428.

Effect of the catalytic reactor arrangement and catalyst treatment in oxidative dehydrogenation of propane performance over hexagonal boron nitride

Mehran Sajad^{*1}, Roman Bulánek¹, Stanislav Šlang²

¹ Department of Physical Chemistry, Faculty of Chemical Technology, University of Pardubice, Studentska 573, 532 10 Pardubice, Czech Republic

² Center of Materials and Nanotechnologies, Faculty of Chemical Technology, University of Pardubice, nám. Čs. Legii 565, 532 10 Pardubice, Czech Republic

* Mehran.sajad@upce.cz

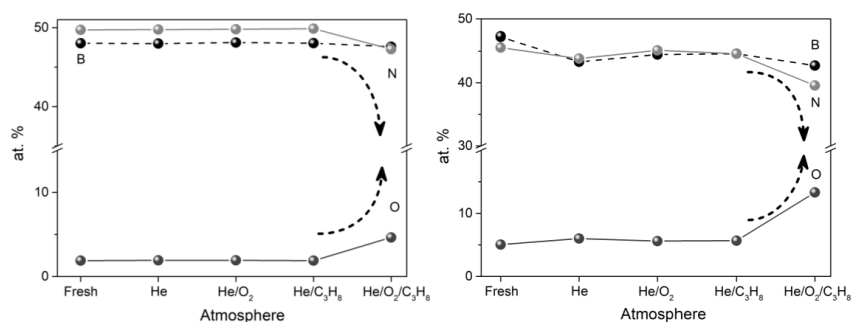


Figure S. 1. Chemical composition of BN treated under different atmospheres analyzed by EDS (left) and XPS (right).

When propane and oxygen were fed simultaneously to the reactor, an obvious increase in oxygen content occurred, accompanied by a decrease in nitrogen (Figure S. 1.). The oxygen content on the catalyst surface changes significantly from 5 to 13 at. % for the fresh and activated samples, respectively, confirmed by XPS, while the EDS results showed that it changed slightly from ca. 2 to 5 at. % inside the bulk, which is reasonable as diffusion is more difficult inside the hBN layers. Furthermore, the amount of nitrogen declined on the surface from 46 to 40 at. % (XPS) and inside the bulk from 50 to 47 at. % (EDS), whereas boron content was kept almost constant, 47 at. % on the surface and 50 at. % inside bulk.

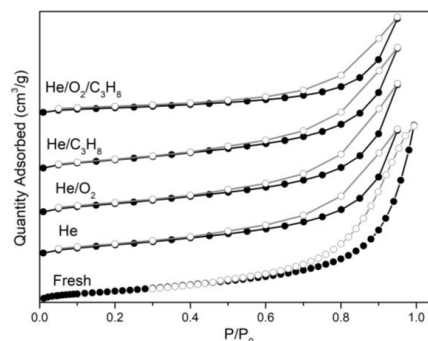


Figure S. 2. N₂ adsorption-desorption isotherms of fresh and treated BN under different atmospheres. The isotherms of treated samples are vertically shifted by 30 cm³/g STP.

The N₂ adsorption-desorption isotherms of the fresh and treated samples, shown in Figure S. 2., exhibited character similar to type II based on IUPAC classification for non-porous or macro-porous materials and also did not go through significant changes in different single atmospheres. Also, the BET surface area declined from 46 to 25 m² g⁻¹ (Table S. 1.). As the melting point of the boron oxide is lower than the ODHP reaction temperature, the accessibility of the gaseous probe molecule (nitrogen) to the catalyst surface had been reduced after the formation of liquid boron oxide species and caused the decrease in BET surface area.

Table S. 1. BET surface area and pore volume of the fresh and treated BN under different atmospheres

Sample	S _{BET} (m ² g ⁻¹)	Total pore volume (cm ³ g ⁻¹)
Fresh	46	0.19
He	48	0.14
He/O ₂	48	0.14
He/C ₃ H ₈	48	0.13
He/O ₂ /C ₃ H ₈	25	0.10

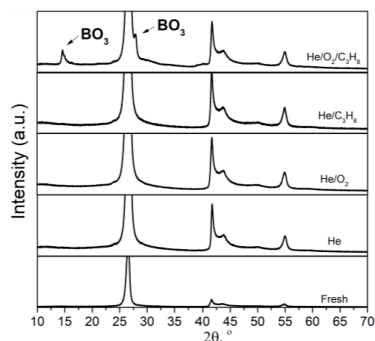


Figure S. 3. X-ray diffraction patterns of the treated BN under different atmospheres.

The XRD patterns of the fresh and the treated catalysts (Figure S. 3.) confirmed the formation of crystalline BO_3 only under a reaction atmosphere that agrees with the XPS and EDS results. The diffraction peaks at 14.6° and 27.9° 2θ correspond to BO_3 (Crystallography Open Database (COD) code: 2016172), while the peaks at 26.7° , 41.7° , 43.8° and 55° 2θ are related to the hexagonal structure of BN (COD database code: 9008997).

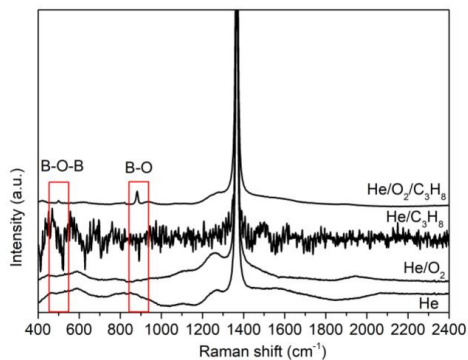


Figure S. 4. Raman spectra of the treated hBN under different atmospheres.

Raman spectra of the treated BN shown in Figure S. 4., confirmed the generation of B-O and B-O-B bonds, peaks at 882 and 500 cm^{-1} Raman shifts, respectively. Their presence is visible only when the treating atmosphere contains propane and oxygen concurrently. The peak at 1367 cm^{-1} that is related to B-N is clearly observable in all spectra.

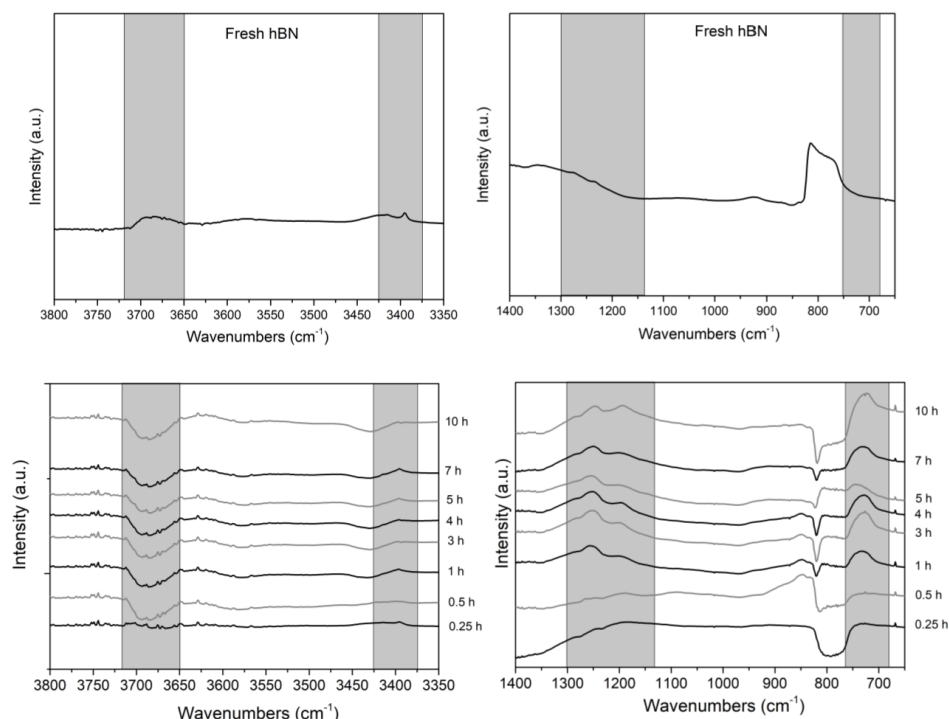


Figure S. 5. DRIFT spectrum of fresh hBN in the range 650-1400 cm^{-1} (above right) and 3350-3800 cm^{-1} (above left). The subtraction of DRIFT spectra collected through spent hBN from the fresh hBN for the corresponding ranges (below).

The functionalities and the skeletal vibration of the hBN catalyst before and after the reaction were identified by DRIFT spectroscopy. To make the comparison more visible, the spectra from the spent catalysts are subtracted from the spectra of the fresh hBN and shown in Figure S. 5. The intensity of the peaks at 732 cm^{-1} and 1200-1300 cm^{-1} , corresponding to B-O vibration, increases by reaction time, which confirms the generation of B-O bond. The vibration at 3400 cm^{-1} probably corresponds to N-H because this wavenumber is too low for the vibrational band between oxygen and hydrogen, and its intensity is constant over time. Hence, the O-H vibration is more likely to appear at a higher frequency. Therefore, in this research, the O-H vibration is considered at 3690 cm^{-1} . Moreover, the O-H vibration at 3690 cm^{-1} was interrupted in the initial step under the stream, and its intensity decreased from the beginning and not gradually, which could be due to the formation of the real active sites at the very first stages of the reaction. It could be possible that the O-H vibration was interrupted due to the interaction with the reaction feed or radicals produced in the feed, and thus, the O-H group on the surface of the hBN is involved in the reaction.

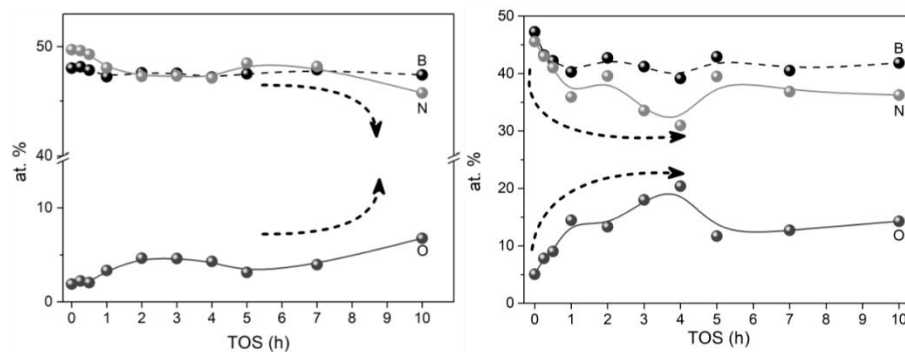


Figure 6. Chemical composition of BN under the ODHP reaction atmosphere as a function of time on stream analyzed by EDS (left) and XPS (right).

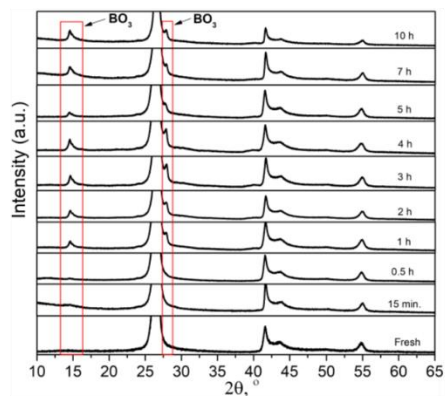


Figure 7. X-ray diffraction patterns of the treated BN under different times on stream

The EDS and XPS results (Figure S. 6.) show the increment in oxygen content of the catalyst. The XRD patterns (Figure S. 7.) exhibited the formation of a boron oxide crystalline phase during TOS, which is accompanied by an increase in boron oxide crystallite size while boron nitride crystallite size is almost constant (Figure S. 8.)

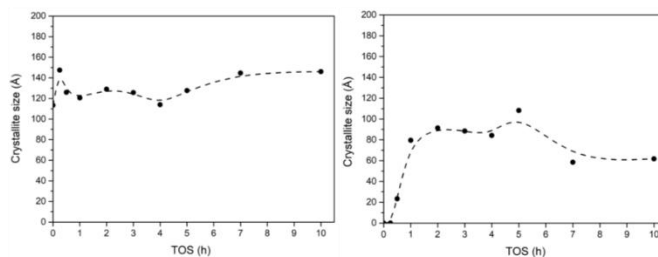


Figure S. 8. Crystallite size of hBN (left) and BO₃ (right), calculated by Scherrer equation for 2θ: 26.5 and 14.5, respectively.

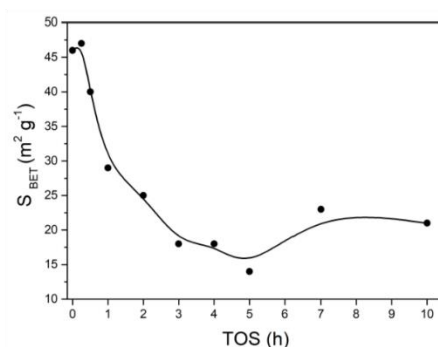


Figure S. 9. BET surface area of spent hBN over time on stream

It was seen that the BET surface decreased over time and leveled off almost after 3 hours under the stream.

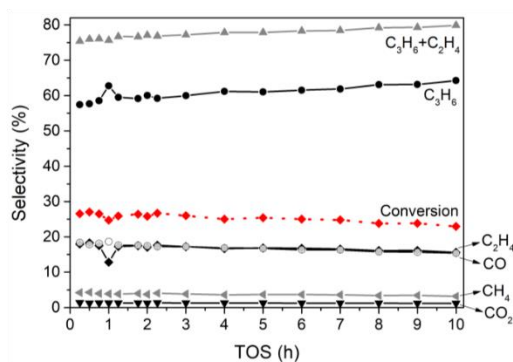


Figure 10. Propane conversion and product selectivity toward products over hBN in ODHP reaction as a function of TOS

The free volume above the catalyst bed: Reactor number 1= 6.4 ml, 2= 5.5 ml, 3= 3.9 ml, 4=2.5 ml, 5= 1.8 ml, 6= 1.8 ml.

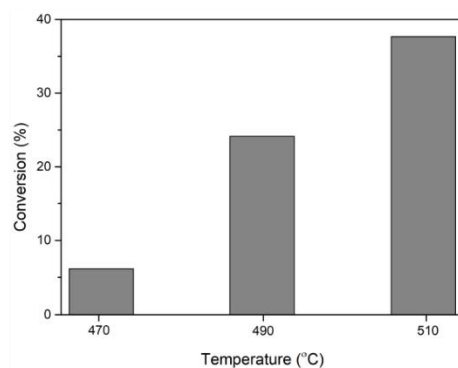


Figure 11. Change of propane conversion in different reaction temperatures. Reactor id: 15.5 mm, mass of catalysts: 100 mg, $\text{He}/\text{O}_2/\text{C}_3\text{H}_8 = 11/3/6 \text{ ml min}^{-1}$

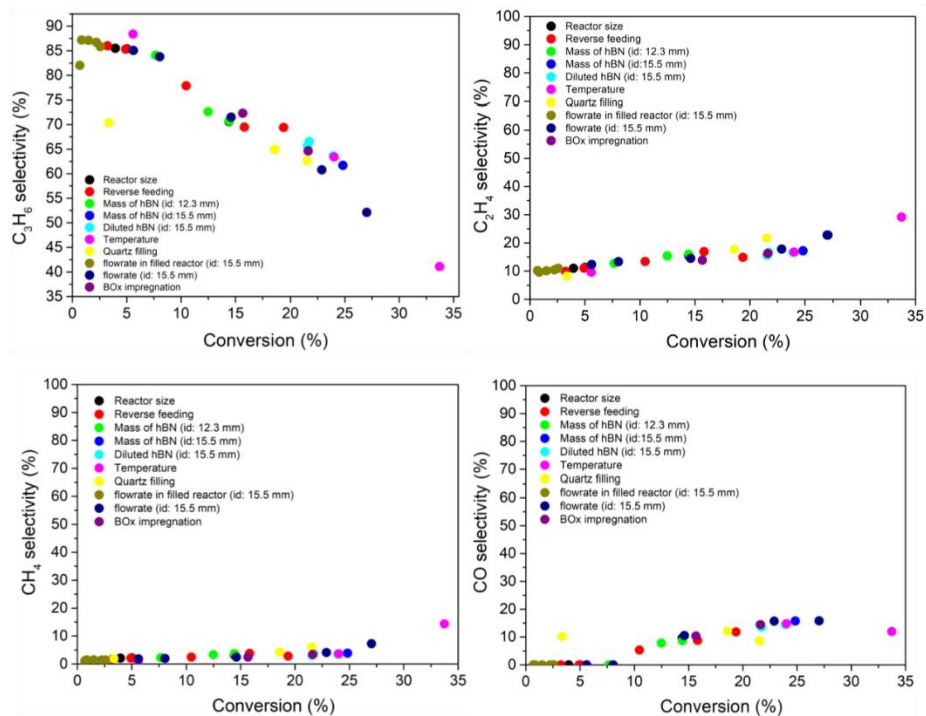


Figure 12. Selectivity towards products as a function of propane conversion.